Università degli Studi di Torino
Scuola di Dottorato

Dottorato in Fisica ed Astrofisica

Probing the Milky Way gravity with hypervelocity stars

Arianna Gallo

Tutor: Dr. Luisa Ostorero

Contents

Thesis content

The Lambda Cold Dark Matter (ΛCDM) cosmological model can successfully explain the homogeneous and isotropic Universe and the formation and dynamics of cosmic structures. In the ΛCDM scenario, halos of cold dark matter (CDM) are predicted to surround the Milky Way (MW) and the other galaxies. Thus, in the last decades, the predictions of ΛCDM on the properties of dark matter (DM) halos have been largely tested on our Galaxy.

Even though the CDM model explains a number of observational properties of galaxies, it faces persistent challenges on galaxy scales, as illustrated in Chpt. 1 of this Thesis and in our review de Martino et al. (2020). Possible solutions to these challenges can be found within the CDM scenario, by including in CDM simulations physical processes that involve baryons and that were previously neglected. Other solutions come from the assumption of DM candidates different from the weakly interacting, non-relativistic, collisionless particles that constitute CDM. Finally, the challenges of the ΛCDM model on the scale of galaxies may also be interpreted as a breakdown of the law of gravity, and another way to face them is thus to assume a different theory of gravity.

The shape of the halos is one of the testable predictions of the ΛCDM model. DM-only numerical simulations find globally triaxial DM halos with a tendency to prolateness in the center. When the physics of baryons is accounted for, cosmological hydrodynamic simulations predict rounder DM halos in the inner regions. The predicted triaxiality parameters of the DM halos are subject to changes if alternative DM candidates are considered. Constraining the shape of the DM halo of the MW is thus instrumental to test the predictions of the standard cosmological model on galaxy scales and to unveil the nature of the DM particles. The fact that, to date, none of the elementary particles suggested as candidates of dark matter has been detected may suggest a failure of Newtonian gravity on galaxy scales, calling for a modification of the law of gravity. In this perspective, one of the most explored and successful alternative theories of gravity on galaxy scales is MOdified Newtonian Dynamics (MOND).

In this Thesis, we investigate the MW gravity following two different approaches: (i) assuming that the Milky Way is embedded in a DM halo and that Newtonian gravity holds on Galactic scales, in Chpt. 2 we propose a new method to determine the shape of the DM halo of the MW; (ii) accounting for the possibility that Newtonian gravity may not be the correct theory of gravity, in Chpt. 3 we propose a novel test to discriminate between Newtonian gravity and MOND. In both approaches, we perform our investigations by means of hypervelocity stars (HVSs), that we use as test particles to probe the Galactic gravitational potential well. Indeed, these stars are ejected from the Galactic center on purely radial trajectories and may reach the outer regions of the Galaxy. During their travel, they acquire non-null tangential velocities due to the non-spherical components of the Galactic gravitational potential.

Following approach (i), in Chpt. 2, based on our work Gallo et al. (2022), we use Newtonian gravity and assume the presence of a DM halo surrounding the MW. In this

model, for a given distribution of the baryonic matter in the Galactic bulge and disk, the magnitude of the HVS tangential velocities proves to be a powerful indicator of the shape of the DM halo. We thus propose a new method to determine the shape of the gravitational potential of the DM halo of the MW with the galactocentric tangential velocities of a sample of HVSs. We compute the trajectories of different samples of HVSs in a MW where the baryon distribution is axisymmetric and the DM potential either is spherical or is spheroidal or triaxial with radial-dependent axis ratios. We create ideal observed samples of HVSs with known latitudinal component of the tangential velocity, v_ϑ, and azimuthal component of the tangential velocity, v_φ. Axisymmetric potentials only affect the latitudinal components of HVSs, while non-null azimuthal components originate from non-axisymmetric matter distributions. Therefore, we determine the shape of the DM potential with the distribution of $|v_\vartheta|$, when the Galactic potential is axisymmetric, or with the distribution of $|v_\vartheta|$ and of a function, $\bar{v}_\varphi$, of v_φ when the Galactic potential is non-axisymmetric. We recover the correct shape of the DM potential by comparing the distribution of $|v_\vartheta|$ and $\bar{v}_\varphi$ of the ideal observed sample against the corresponding distributions of mock samples of HVSs that traveled in DM halos of different shapes. We use ideal observed optimal samples of ~ 800 HVSs, which are the largest samples of 4 $M_\odot$ HVSs ejected with the Hills mechanism at a rate $\sim 10^{-4}$ yr^{-1}, currently outgoing, and located at more than 10 kpc from the Galactic center. In our ideal case of galactocentric velocities with null uncertainties and no observational limitations, the method recovers the correct shape of the DM potential with a success rate $S \gtrsim 89\%$ when the Galactic potential is axisymmetric, and $S > 96\%$ in the explored non-axisymmetric cases.

The unsuccessful cases yield axis ratios of the DM potential that are off by ± 0.1. The success rate decreases with decreasing size of the HVS sample: for example, for a spherical DM halo, S drops from $\sim 98\%$ to $\sim 38\%$ when the sample size decreases from ~ 800 to ~ 40 HVSs. Accurate estimates of the success rate of our method applied to real data require more realistic samples of mock observed HVSs. Nevertheless, our analysis suggests that a robust determination of the shape of the DM potential requires the measure of the galactocentric velocity of a few hundred HVSs with robustly confirmed galactocentric origin.

Following approach (ii), in Chpt. 3, based on our work Chakrabarty et al. (2022), we account for the possibility that Newtonian gravity is not the correct theory of gravity, and we show that measuring the velocity components of HVSs can discriminate between MOND and Newtonian gravity. As anticipated above, HVS azimuthal velocities only appear in non-axisymmetric matter distributions. We find that, for HVSs with sufficiently high ejection speed, the azimuthal velocity components are proportionate to the deviation of the gravitational potential from axial symmetry. The ejection velocity threshold is ~ 750 km s^{-1} for 4 $M_\odot$ stars and increases with decreasing HVS mass. We determine the upper limit of v_φ as a function of the galactocentric distance for these high-speed HVSs if MOND, in its quasi-linear formulation QUMOND, is the correct theory of gravity and either the triaxial Galactic bulge or a non-spherical hot gaseous halo is the primary source of the azimuthal component, v_φ. In Newtonian gravity, the HVSs within 60 kpc of the Galactic center may easily have v_φ values higher than the QUMOND upper limit if the DM halo is triaxial or if the DM halo and the baryonic components are axisymmetric but their two axes of symmetry are misaligned. Therefore, even a limited sample of high-speed HVSs could in principle enable us to distinguish between the QUMOND scenario and the DM model.

A critical issue of both our new method to constrain the DM halo shape and our novel test to distinguish between MOND and Newtonian gravity is the uncertainty on the HVS tangential velocities used to probe the MW gravitational potential. Currently available

velocities from the *Gaia* Early Data Release 3 are affected by relative uncertainties that can exceed 100%. These errors need to be reduced by at least a factor ~ 10 to make our gravity test decisive. On the other hand, the impact of the velocity uncertainties on the success rate of our method to determine the shape of the DM halo of the MW is currently under investigation. Indeed, the high success rate of our method in recovering the correct DM halo shape is obtained for the ideal case of null uncertainties. To preserve a high success rate, the uncertainties on the HVS tangential velocities need to be as small as possible. Because proper motion is the main source of uncertainty on the tangential velocity for distant HVSs, and significantly contributes to this uncertainty for nearby HVSs, improving the precision on the measures of HVS proper motion is a crucial step to significantly constrain the shape of the DM halo of our Galaxy. A *Theia*-like future astrometric mission should reach an end-of-mission uncertainty on proper motions of a few microarcseconds per year, namely ~ 100 times smaller than that of *Gaia*. Our work is contributing to the definition of the scientific goals and of the technical requirements of this mission.

The Thesis is organized as follows. In Chpt. 1, based on our works de Martino et al. (2020), Gallo et al. (2022), and Chakrabarty et al. (2022), we introduce the general context of the Thesis: In Sect. 1.1 we discuss the missing mass problem, which led to the introduction of the concept of DM; in Sect. 1.2 we explore the ΛCDM cosmological model; in Sect. 1.3 we present the challenges faced by the ΛCDM model on galaxy scales (Sect. 1.3.1) and we explore possible solutions under the assumption of either different DM candidates (Sect. 1.3.2) or a different theory of gravity (Sect. 1.3.3); in Sect. 1.4 we investigate the theoretical predictions on the shape of DM halos made by the ΛCDM model (Sect. 1.4.1) and by models that assume alternative DM particles (Sect. 1.4.2), and we explore the current observational constraints on the shape of the DM halo of the MW (Sect. 1.4.3); finally, in Sect. 1.5 we focus on HVSs: we explore the mechanisms that can lead to their ejection (Sects. 1.5.1 and 1.5.2) and discuss their observations (Sect. 1.5.3).

In Chpt. 2, based on our work Gallo et al. (2022), we present our new method to constrain the shape of the MW DM halo using a statistical sample of HVSs whose galactocentric tangential velocities are known. In Sect. 2.1 we describe our numerical simulations of the initial velocity distribution of a sample of HVSs ejected according to the Hills mechanism, and the simulations of the HVS trajectories in a Galactic gravitational potential generated by DM halos with different shapes; we also illustrate the construction of our HVS phase space mock catalogs. In Sect. 2.2 we show how the asphericity of the DM halo mostly affects the HVS tangential velocity: we identify this velocity as the key variable to statistically discriminate between different shapes of the DM halo, and we select the appropriate HVS sample to pursue this goal. In Sect. 2.3 we present our statistical method to recover the shape of the DM halo from a distribution of HVS tangential velocities. In Sects. 2.4 and 2.5 we show the results of the application of our method to an ideal sample of mock observed HVSs with null uncertainties and no observational limitations that traveled in an axisymmetric and non-axisymmetric Galactic gravitational potential, respectively. In Sect. 2.6 we investigate the effect of the size of the ideal sample of mock observed HVSs on the success rate of our method. We discuss our results and conclude in Sects. 2.7 and 2.8.

In Chpt. 3, based on our work Chakrabarty et al. (2022), we propose a novel test to discriminate between MOND and Newtonian gravity by means of the measurement of the azimuthal component of the galactocentric tangential velocity of even few HVSs observed in the MW. In Sect. 3.1 we illustrate the quasi-linear formulation of MOND (QUMOND)

that we adopt in this work. Sect. 3.2 describes our model of the distribution of the MW baryonic matter that generates the QUMOND gravitational potential. In Sect. 3.3 we illustrate the model of DM halo we adopt for comparison with the QUMOND predictions. In Sect. 3.4 we illustrate and discuss our simulations of the HVS kinematics in MOND and in Newtonian gravity. In Sect. 3.5 we show the galactocentric tangential velocities of the HVSs in QUMOND and in Newtonian gravity, and detail our QUMOND predictions. We conclude in Sect. 3.6.

We present our final remarks and future prospects in Sect. 4.

Chapter 1

Introduction [1]

1.1 The missing mass problem and the idea of dark matter halos

> "*Dark matter, in an astronomical sense, is introduced to explain the difference between how objects in the sky ought to move, according to some preconceived notion, and how they are actually observed to move.*"
>
> (R. H. Sanders (2010), The Dark Matter Problem: A Historical Perspective)

The concept of invisible or dark matter (DM) developed during the last century to what is the current connotation.

In 1932, Oort first introduced the concept of invisible matter after having pointed out in the Milky Way (MW) a discrepancy of a factor of up to two between the amount of the visible stellar populations near the Sun and the total matter density estimated from dynamical data. Although this result is often considered to be the first evidence of the existence of dark matter, the discrepancy has now been alleviated by more accurate observations of the stellar disk population (Kuijken and Gilmore, 1989a,b; Holmberg and Flynn, 2004).

In 1933, F. Zwicky pointed out a discrepancy between the observed velocity dispersion of about 1000 km s^{-1} along the line of sight of eight galaxies in the Coma cluster (Fig. 1.1) and the velocity dispersion expected in a system of N massive galaxies in dynamical equilibrium ($\sim$ 80 km s^{-1}). In order to explain this discrepancy, the average density of the Coma cluster needed to be at least 400 times greater than that derived from the observation of the luminous matter. Part of this huge density difference was due to the underestimate of the cluster distance of a factor ~ 8. The remaining part was due to the underestimate of the baryonic mass of the cluster by a factor of about ten: indeed the presence of a hot X-ray emitting gas component was unknown at that time. However, even though the distance and baryonic mass of the cluster are properly computed, a mass discrepancy between five and ten subsists (Jones and Forman, 1984; David et al., 1990).

This discrepancy implied the presence of a large amount of invisible mass: this was the first time that the dark matter concept was introduced in an extragalactic context. Although this mass was still thought to be in the form of stars and/or gas which were not yet observable, this result of Zwicky traditionally marks the birth of the dark matter problem.

A new era began in the 1970s, when V. C. Rubin and W. K. Ford measured the rotation curve of the Andromeda galaxy (M31) out to 110 arcminutes away from the

[1] Part of the content of this chapter is published in our works de Martino et al. (2020), Gallo et al. (2022), and Chakrabarty et al. (2022).

Figure 1.1. The Coma galaxy cluster. Image credits: NASA, ESA, and the Hubble Heritage Team (STScI/AURA).

galactic center, and estimated a mass-to-light ratio of $13 \pm 0.7\ M_\odot/L_\odot$ at $R = 24$ kpc (Rubin and Ford, 1970). In the same years, measures of the 21-cm line emission of neutral hydrogen also suggested that the rotation curves of spirals fall off at large radii less rapidly than they should when most of the galaxy mass is concentrated in the optically luminous component (Freeman, 1970; Roberts and Rots, 1973). This flatness of the rotation curves led to the conclusion that galaxies are embedded in massive halos extending to large radii, as was suggested by theoretical studies of the stability of disk against the development of a bar (Hohl, 1971; Ostriker and Peebles, 1973).

In the 1980s the idea of DM halos surrounding the galaxies and becoming dynamically more important at increasing distances from the galactic center was accepted by the majority of the astronomers.

The presence of a mass discrepancy in the Universe continued to be, up to the present day, the constant result of independent observations from the galactic to the cosmological scales.

On the scale of galaxies, evidence of missing mass results from:

- the nearly flat rotation curves of disk galaxies at large radii (see Fig. 1.2) (e.g., Rubin and Ford, 1970; Freeman, 1970; Rogstad and Shostak, 1972; Roberts and Rots, 1973; Bosma, 1978; Rubin et al., 1982, 1985; van Albada and Sancisi, 1986; Persic et al., 1996; Martinsson et al., 2013; Bhattacharjee et al., 2014);

- the stability of dynamically cold stellar disks (e.g., Hohl, 1971; Ostriker and Peebles, 1973; Fall and Efstathiou, 1980; Sellwood, 2014);

- the dynamics of the outer regions of elliptical galaxies (e.g., Franx et al., 1991; Cappellari et al., 2006; Cappellari, 2016; Pulsoni et al., 2018);

- the large mass-to-light ratios of dwarf galaxies (e.g., Kormendy, 1987; Irwin and Hatzidimitriou, 1995; Wechsler and Tinker, 2018);
- the discrepancy between the expected gravitational acceleration given the baryonic matter and the gravitational acceleration observed thanks to weak gravitational lensing measurements (e.g., Brouwer et al., 2021).

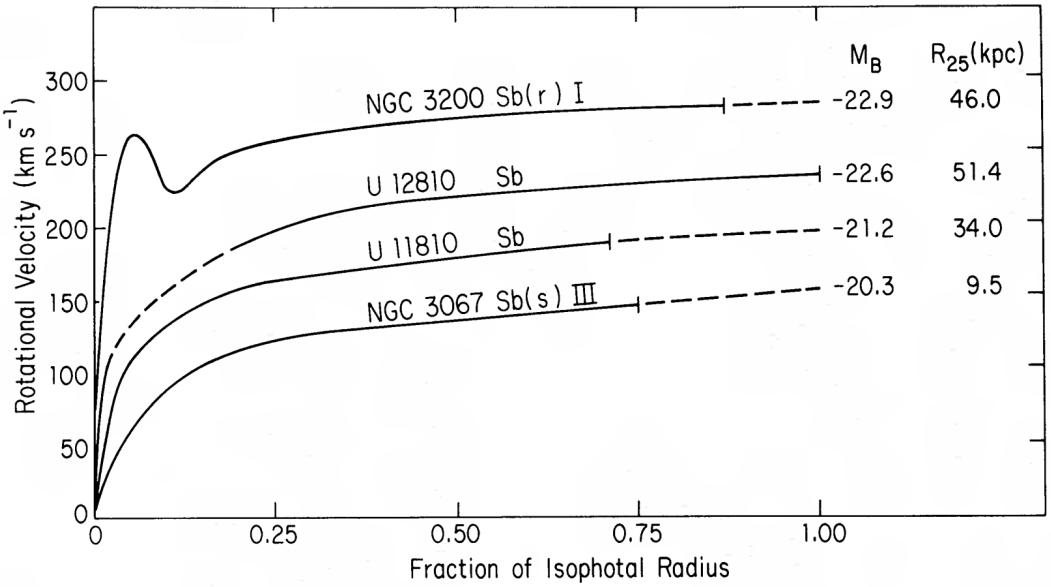

Figure 1.2. Rotation velocity for four Sb galaxies as a function of the fraction of the isophotal radius, R_{25}, for each galaxy. The figure is reproduced from Rubin et al. (1982).

On the scale of galaxy clusters (Biviano, 2000; Voit, 2005; Diaferio et al., 2008; Walker et al., 2019), mass-to-light ratios of $\sim 100 - 400\, M_\odot/L_\odot$ were found (Girardi et al., 2002; Rines et al., 2004; Proctor et al., 2015). However, these high values are not indicative of the real mass discrepancy in the galaxy clusters, because the clusters are characterized by a major hot gas component. Thus, on the scale of galaxy clusters, the mass discrepancy can be more meaningfully quantified by the ratio between the total mass of the cluster, $M_{\rm tot}$, and the sum of the stellar and gaseous mass, $M_{\rm stars} + M_{\rm gas}$. Typical values of the mass discrepancy are in the range $\sim 5 - 15$ (Blumenthal et al., 1984) and result from:

- the dynamics of the member galaxies (e.g., Kneib et al., 1996; Łokas and Mamon, 2003; Giodini et al., 2009; Geller et al., 2013; Rines et al., 2013; Sohn et al., 2017; Tian et al., 2021);
- the X-ray emission of the intracluster gas (e.g., Sarazin, 1986; Rosati et al., 2002; Böhringer and Werner, 2010; Sohn et al., 2019; Clerc et al., 2020);
- gravitational lensing (e.g., Tyson et al., 1990; Clowe et al., 2006; Postman et al., 2012; Sereno et al., 2018; Meneghetti et al., 2020; Umetsu, 2020).

Initially the dominant idea was that the dark matter consists of baryonic matter and the search for dark matter focused on sub-luminous compact objects, such as planets, brown dwarfs, white dwarfs, neutron stars, and black holes. These Massive Astrophysical Compact Halo Objects (MACHOs) are now believed to form only a small fraction of dark matter. Microlensing surveys have been used to set an upper limit of 8% to the contribution of MACHOs to the mass fraction of the DM halo of the Milky Way (Lasserre

et al., 2000; Tisserand et al., 2007). Nevertheless, there is the possibility that Primordial Black Holes (PBHs), which formed before the Big Bang nucleosynthesis and have masses below the sensitivity range of microlensing surveys, may form a substantial fraction of the total dark matter density. This idea was originally discussed by Carr and Hawking in 1974. However, generating a relevant abundance of primordial black holes requires a substantial degree of non-Gaussianity in the power spectrum of the primordial density perturbations (Motohashi and Hu, 2017; Passaglia et al., 2019). Recently, the detection of gravitational waves has set a tight upper limit to the abundances of these black holes. This limit suggests that the black hole contribution to the dark matter abundance is at the level of a few per cent (Wang et al., 2018), as allowed by the constraints on non-Gaussianity obtained from the Planck satellite (Young and Byrnes, 2015; Clark et al., 2017; Planck Collaboration et al., 2020c).

Meanwhile, a novel idea was growing: that the dark matter consists of non-baryonic subatomic particles only weakly interacting with baryons and photons. Indeed, on cosmological scales, the structure formation from the nearly homogeneous matter distribution implied by the small temperature anisotropies of the cosmic microwave background (CMB) requires a stronger gravitational pull than that provided by the baryonic matter alone (Silk, 1967; Davis et al., 1985; Spergel et al., 2007; Planck Collaboration et al., 2020a).

The evidence of a mass discrepancy in both galaxies and clusters of galaxies, together with the cosmological arguments for a substantial non-baryonic component of the Universe, lead to the emergence of a new paradigm: the standard Cold Dark Matter (CDM) model of the Universe. This paradigm is now replaced by the Lambda Cold Dark Matter (ΛCDM) model, with the inclusion of a negative-pressure fluid, the dark energy, that explains the Universe expansion.

1.2 The ΛCDM model

Over the last decades, the standard model for the evolution of the Universe, the ΛCDM or concordance model (Ostriker and Steinhardt, 1995), was established by many independent observations; among them:

- the CMB temperature fluctuations (Hinshaw et al., 2013; Planck Collaboration et al., 2020a,b,c,d,e);
- the power spectrum of the matter density perturbations (Percival et al., 2001; Pope et al., 2004; Tegmark et al., 2004);
- the luminosity distances to supernovae SNIa (Riess et al., 1998; Perlmutter et al., 1999; Riess et al., 2004; Astier et al., 2006; Davis et al., 2007; Kowalski et al., 2008; Amanullah et al., 2010; Suzuki et al., 2012);
- the expansion rate of the Universe (Jimenez et al., 2003; Simon et al., 2005; Stern et al., 2010; Moresco et al., 2012a,b).

The current constraints on the cosmological parameters have reached unprecedented accuracy (Génova-Santos, 2020).

In this model, the present period of accelerated expansion is driven by the cosmological constant Λ, that provides an energy density $\Omega_{\Lambda,0} = 0.686 \pm 0.020$ in units of the critical density $\rho_c = 3H_0^2/8\pi G$ (Planck Collaboration et al., 2020a). The cosmological constant can be identified with a perfect fluid with an equation of state $p = w\rho$, between pressure p and energy density ρ, with the constant parameter $w = -1$. The second largest

contribution to the total energy-density budget of the Universe is dark matter, which is needed to explain the dynamics of galaxies and the large-scale structure. Its energy density is $\Omega_{\rm DM,0} = 0.314 \pm 0.020$ (Planck Collaboration et al., 2020a). The present density of ordinary, or baryonic, matter is $\Omega_{\rm b,0}h^2 = 0.02207 \pm 0.00033$ (Planck Collaboration et al., 2020a). Summing the contributions of the cosmological constant, dark matter, and baryonic matter yields the curvature of the Universe $\Omega_{\rm k,0}h^2 = -0.037^{+0.044}_{-0.042}$ (Planck Collaboration et al., 2020a), where h is the Hubble constant in units of 100 km s^{-1} Mpc^{-1}. This curvature makes the Universe spatially flat.

The concordance model successfully describes the homogeneous and isotropic Universe, and the dynamics of cosmic structures (see, however, Sect. 1.3.1).

Dark matter is expected to consist of stable massive particles beyond the Standard Model of elementary particle physics. Dark matter can thus clump in self-gravitating structures embedding galaxies and clusters of galaxies. Once General Relativity is assumed to be the correct theory of gravity, evidence of the DM existence is based on its gravitational effects that solve the mass discrepancy problem on both galaxy scales and galaxy cluster scales.

Dark matter also allows the primordial perturbations in the density field of the baryonic matter to grow and form the cosmic structures we observe today (e.g., Kuhlen et al., 2012). Indeed, in the history of cosmic expansion, for models where the dark matter and dark energy are not separated from the other components of the Universe, dark matter decouples from the primordial plasma much earlier than baryons; the primordial fluctuations in the DM density field thus start growing earlier and, at recombination epoch, they are larger than the baryon density perturbations that are still coupled to the perturbations of the background radiation field that generates the CMB anisotropies. After the recombination epoch, baryonic matter falls into the gravitational potential wells of the DM halos and forms the cosmic structure (see e.g., Bertone et al., 2005; Boyarsky et al., 2009; Feng, 2010; Bertone and Hooper, 2018).

In these models, DM particles are thus in thermal equilibrium with the cosmic plasma before the decoupling epoch, when they get out of kinetic equilibrium, as they become non-relativistic, at temperature $T = T_{\rm d} \ll m_{\rm DM}$, where $m_{\rm DM}$ is the mass of the DM particle. In the standard CDM model, the DM particles are so massive that $T_{\rm d} \gg T_0$, where T_0 is the plasma temperature at recombination epoch. They thus decouple from other particles and start moving freely at non-relativistic speeds in the early Universe. The comoving number density of DM particles freezes out when the creation and annihilation of the DM particles are inhibited. In general, the freeze-out cosmic temperature $T_{\rm f} \gg T_{\rm d}$. The comoving number density of DM particles is thus set by their annihilation cross section at this epoch (Jungman et al., 1996)

$$\Omega_\chi h^2 = (3 \times 10^{-27} {\rm cm}^3/{\rm sec}) / \langle \sigma v \rangle_{\rm ann} \, . \tag{1.1}$$

Intriguingly, for Weakly Interacting Massive particles (WIMPs), with mass in the range $\sim$ 1GeV - 10TeV, the annihilation cross section $\langle \sigma v \rangle_{\rm ann}$ gives $\Omega_\chi h^2$ comparable to the observed dark matter density $\Omega_{\rm DM,0} \sim 0.3$ (Planck Collaboration et al., 2020a). This coincidence is usually called "the WIMP miracle". WIMPs are expected in the theory of supersymmetry, which dates back to the 1970s and supposes that, for any given fermion, there is a boson with the same quantum numbers, and vice versa (Martin, 1998). In this case, there would be many electrically neutral and weakly interacting massive particles that could be cosmologically abundant and could play the role of dark matter. Nowadays, direct and indirect searches for WIMPs as well as other DM particle candidates are ongoing (see e.g., Tanabashi et al. (2018) for a comprehensive review).

1.3 Beyond the ΛCDM model

The ΛCDM model, that successfully describes the formation and dynamics of cosmic structures and the homogeneous and isotropic Universe, still faces important challenges at all scales. Among the difficulties faced the on cosmological scales, there are the cosmological constant problem (e.g., Weinberg, 1989; Del Popolo and Le Delliou, 2017) and the cosmic coincidence problem (e.g., Velten et al., 2014; Del Popolo and Le Delliou, 2017). The cosmological constant problem consists in a huge difference between value of the cosmological constant obtained in quantum field theory, when interpreting the constant as the present energy density of the vacuum, and the value resulting from observations: quantum field theory predicts $\rho_\Lambda = 10^{71}\,\mathrm{GeV}^4$, while the cosmological upper bound is $\rho_\Lambda = 10^{-47}\,\mathrm{GeV}^4$. The coincidence problem is connected to the fact that the dark energy and dark matter energy densities are of the same order of magnitude at the present epoch ($\Omega_\Lambda \approx 0.7$ and $\Omega_{\mathrm{DM}} \approx 0.3$, respectively), thus requiring very special initial conditions in the primordial Universe. Other challenges of ΛCDM involve the discrepancy between the observations at early and late cosmological time of some cosmological parameters: one example is the Hubble tension, namely the disagreement at 5σ between the values of the Hubble parameter, H_0, derived from the CMB data, that are cosmological model dependent, and the values obtained from the direct local distance ladder measurements. Another example is the tension at 3σ on the strength of matter clustering S_8 (for a comprehensive review see, e.g., Abdalla et al., 2022).

Nevertheless, the most severe challenges of the ΛCDM model appear at the scale of galaxies as detailed in Sect. 1.3.1.

1.3.1 Challenges of the ΛCDM model on the scale of galaxies

In the standard cosmological model, DM consists of massive particles that weakly interact with ordinary matter and that decoupled from the primordial plasma when they were non-relativistic. This CDM scenario encounters some difficulties in describing structures at galactic scales (see e.g., Moore, 1994; Boylan-Kolchin et al., 2011; Bullock and Boylan-Kolchin, 2017; Del Popolo and Le Delliou, 2017; Salucci, 2019). These difficulties include the cusp/core problem (CCP), the missing satellites problem (MSP), the too-big-to-fail (TBTF) problem, and the planes of satellite galaxies problem (PSP).

- The CCP is the discrepancy between the flat DM density profile observed at the centers of low surface brightness (LSB), dwarf and ultra-faint galaxies, and the cuspy profile predicted in collisionless N-body simulations (e.g., Navarro et al., 1997; Ferrero et al., 2012; Genina et al., 2018). In particular, N-body simulations show cuspy density profiles for DM halos of galaxy size; the halo density increases with decreasing radius r as $r^{-\beta}$, with β in the range $\sim [1 - 1.5]$. These slopes do not match the cores favored by the observed rotation curves (Davis et al., 1985; Flores and Primack, 1994; Moore, 1994; Navarro et al., 1997). Nevertheless, modeling the kinematics of stars in dwarf galaxies does not lead to a clear conclusion to whether these galaxies are dominated by a core or a cusp in their innermost regions (Walker et al., 2009). Figure 1.3 illustrates the cusp/core problem. A "modern" approach to the CCP problem consists in facing the *diversity of rotation curves* problem (e.g., Oman et al., 2015; Ghari et al., 2019), that is the difference between the shape of the theoretical rotation curves obtained in DM only simulations and the shape of the observed rotation curves. Indeed, for a fixed maximum circular velocity, the theoretical circular velocity profiles are substantially invariant, while the shapes of the observed rotation curves display large differences (especially for dwarf galaxies)

and only part of them are in agreement with the simulations. Typically, the rotation curves that do not match the theoretical predictions have a lower circular velocity in the inner part of the galaxy that indicates an inner mass deficit. Although this mass deficit can be the result of an inner core of the DM density profile, approaching the problem as a deficit in the mass eliminates the uncertainties of the decomposition of the inner mass profile in its baryonic and DM contributions, and enables a direct comparison between simulations and observations.

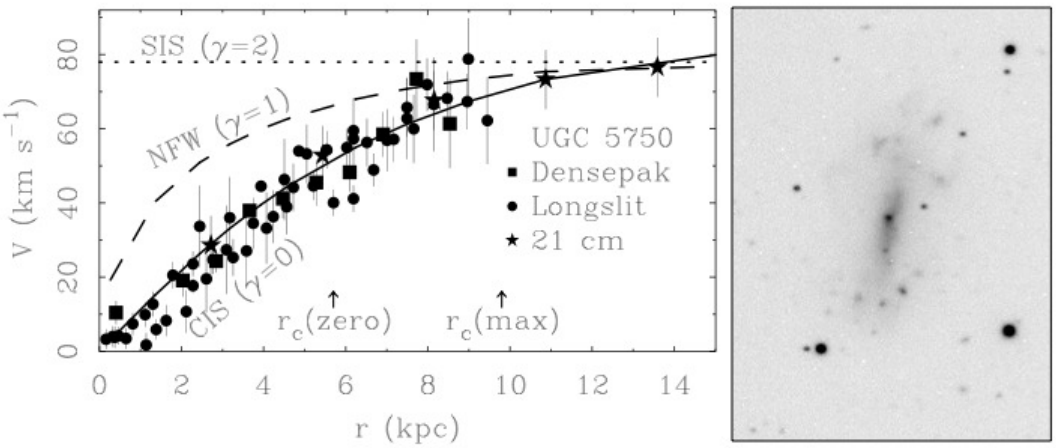

Figure 1.3. Rotation curve (left panel) of UGC 5750 (the LSB galaxy, showed in the right panel). The data of the rotation curve are obtained with the integrated field Hα spectroscopy (squares) (Kuzio de Naray et al., 2006), long slit optical observations of the Balmer transition (circles) (McGaugh et al., 2001; de Blok and Bosma, 2002), and radio observations of the 21 cm atomic hydrogen spin flip transition (stars) (van der Hulst et al., 1993). The isothermal sphere with a core (CIS) profile (solid line) fits the data. r_c(zero) and r_c(max) are the values of the core radius obtained from the fit in the no disk and maximum disk case, respectively; the solid line is the case of no disk. Neither the Navarro-Frenk-White (NFW) profile (dashed line), whose parameters are fixed and given by the ΛCDM cosmology, nor the singular isothermal sphere (SIS) profile can describe the DM halo of this LSB galaxy. The figure is reproduced from Chen and McGaugh (2010).

- The MSP, illustrated in Fig. 1.4, is the fact that the DM halos of galaxies like the Milky Way are predicted to have a number of dark matter subhalos which is an order of magnitude larger than the number of satellites observed around the Milky Way or other comparable galaxies (Kauffmann et al., 1993; Klypin et al., 1999).

- The TBTF problem (Read et al., 2006; Boylan-Kolchin et al., 2011, 2012; Garrison-Kimmel et al., 2014), illustrated in the right panel of Fig. 1.4, manifests in the central densities of the most massive DM subhalos formed in ΛCDM simulations; these densities are systematically larger than the central densities of the brightest classical Milky Way satellites, as inferred from their stellar kinematics. In principle, associating the classical satellites to dark matter subhalos with smaller central densities and smaller mass would erase the discrepancy; however, this association would clearly imply that the most massive subhalos would not host a galaxy. In other words, these subhalos "failed" to form stars even though less massive subhalos succeeded in doing so.

- The PSP refers to the fact that, in the galaxy systems of the Milky Way (see Fig. 1.5), of M31, and of Centaurus A, the satellite galaxies reside in a thin plane and they generally corotate. This satellite configuration appears unlikely in the simulations of the standard CDM model (Pawlowski et al., 2014).

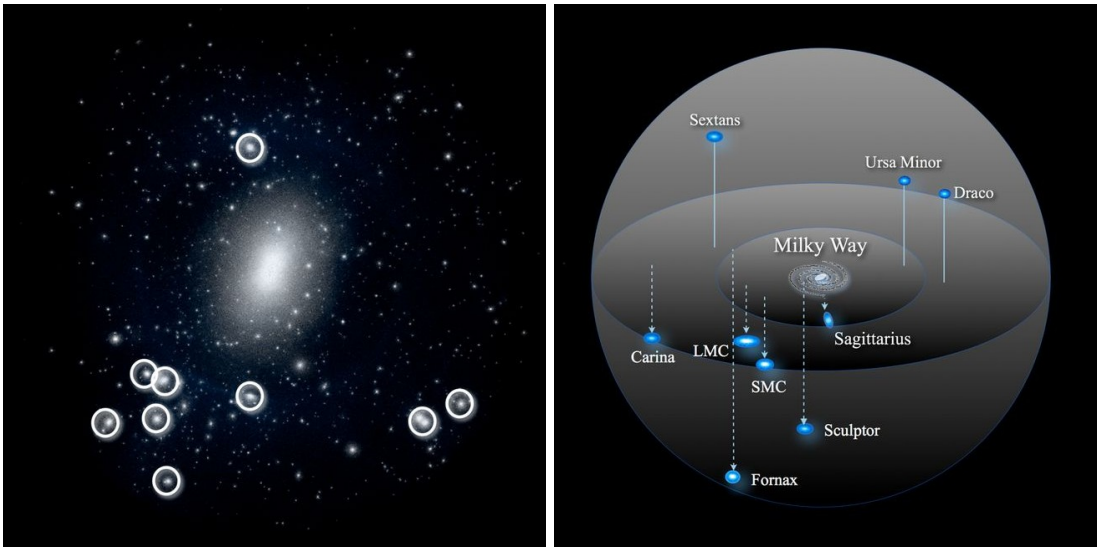

Figure 1.4. *Left panel*: Projected dark matter distribution (600 kpc on a side) of a $10^{12}\,M_\odot$ DM halo from the ELVIS ΛCDM simulations (Garrison-Kimmel et al., 2014). The number of small subhalos strongly exceeds the number of known Milky Way satellites (missing satellites problem). The circles highlight the nine most massive subhalos. *Right panel*: Spatial distribution of the closest nine of the eleven most luminous (classical) satellites of the Milky Way (the diameter of the outer sphere is 300 kpc). For these satellites, the central mass inferred from stellar kinematics is a factor of ~ 5 lower than the mass predicted for the central regions of the subhalos highlighted in the left panel, preventing the association of the classical satellites to the most massive subhalos of the DM halo of Milky Way-like galaxies (too-big-to-fail problem). The figure is reproduced from (Weinberg et al., 2015).

Possible solutions to some of the above mentioned challenges can be found within the context of the CDM scenario. For example, including in the CDM simulations physical processes that mostly affect the baryonic matter and that are usually neglected, may alleviate some of the problems (see e.g., de Martino et al. (2020) for a comprehensive review).

Possible solutions within the CDM paradigm to the cusp/core problem can involve processes as supernova feedback and dynamical friction. Winds driven by supernovae (Navarro et al., 1996a; Mashchenko et al., 2006) or stellar winds (Gnedin and Zhao, 2002; Mashchenko et al., 2008) can be an effective mechanism to transform the cusp of the dark matter density profiles into a core. In both cases the winds produce energy feedback that can drastically modify the shape of the dwarf galaxies by forcing the gas and the DM particles to move outwards, change the gravitational potential well, and flatten the density profile (Mashchenko et al., 2008). Moreover, the dynamical friction between gas clumps with masses of $10^5 - 10^6 M_\odot$ can transfer angular momentum from the gas to the DM particles that would move away from the central region of the halo, flattening its density profile. This effect should be efficient in the early phase of the galaxy formation when the halo size is smaller (El-Zant et al., 2001; Romano-Díaz et al., 2008). However, gas clumps in dwarf galaxies are usually less massive than $10^5 - 10^6 M_\odot$; thus, the mechanism is not sufficient to solve the cusp/core problem (Jardel and Sellwood, 2009). Moreover, when approaching the diversity of rotation curves problem, cored DM density profiles do not offer a natural explanation for the large range of values of the mass deficit inferred from the observed rotation curves; indeed, at a given mass scale, the size of the cores should be similar. Although there are uncertainties in the inference of the rotation curve of a galaxy due to instrumental complexities and to the difficulties of modeling non-circular and random motions, it is unlikely that their effect can be so

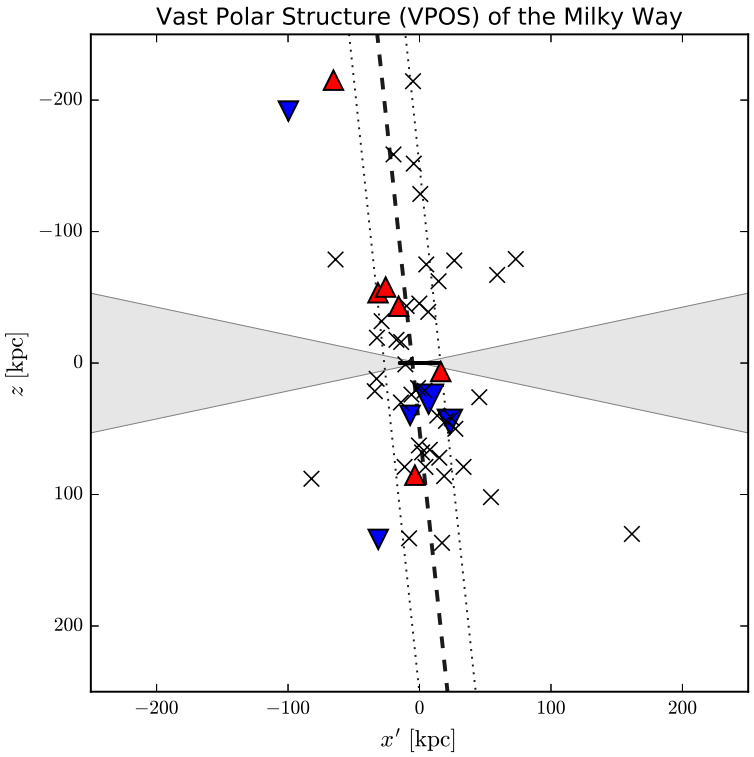

Figure 1.5. Edge-on view of the *vast polar structure* (VPOS) around the Milky Way and the disk (solid black line at the center). The orientation and the width of the best fit satellite plane are indicated by the dashed and dotted lines, respectively. The colored triangles, red upward (blue downward) for receding from (approaching towards) an observer at rest with respect to the host galaxy, indicate coherent kinematics of the co-orbiting satellites. The satellites with no proper motion measurements are plotted as crosses. The grey area corresponds to the region ±12° from the Milky Way disk which is obscured by galactic foreground. The figure is reproduced from Pawlowski (2018).

high to provide the explanation for the diversity of rotation curves problem (Oman et al., 2015).

The MSP can be addressed within the CDM model with the abundance matching technique, that matches the cumulative distribution of an observed property of galaxies with the predicted cumulative distribution of the mass of their DM halos (Bullock and Boylan-Kolchin, 2017). For example, by adopting the mean star formation rate as the observed property, the MSP in the MW appears to be solved for satellite masses larger than 10^9 $M_\odot$ (Read and Erkal, 2019), for which the cumulative mass function within 280 kpc from the MW center is consistent with the results from ΛCDM simulations that account for sub-halo depletion by the MW disk. For satellites with halo masses $\lesssim 10^9 M_\odot$, the MSP might be explained by the suppression of star formation caused by UV reionisation (Bullock and Boylan-Kolchin, 2017), but this issue requires further investigation.

An overestimate by about a factor two of the mass of the DM halo of the Milky Way can in principle solve the TBTF problem for the Galaxy. Indeed, in this scenario, the number of massive dark sub-halos not corresponding to observed dwarf satellites would be of the order of three; this number can be attributed to statistical fluctuations (Boylan-Kolchin et al., 2012). However, there are currently no indications of the existence of systematic errors that can reduce the estimate of the Milky Way mass by the required

factor. In addition, the TBTF problem appears in M31 and in other galaxies; therefore, the overestimate of the Milky Way mass would not fully remove the tension. One way to solve this problem would be to account for baryonic physics in simulations (Brooks and Zolotov, 2014; Dutton et al., 2016; Buck et al., 2019), even though the results depend on the mass resolution of baryonic particles.

Concerning the planes of satellite galaxies problem, although several solutions have been proposed within the CDM model, none of them has been unanimously accepted, because they either fail to reproduce all the observational aspects or they are based on poorly-investigated assumptions. For example, some mechanisms can reproduce the planar structures observed in M31 and Centaurus A (Libeskind et al., 2015) but not in the Milky Way (Libeskind et al., 2014; Pawlowski, 2018).

Besides the above mentioned solutions, some of the challenges faced by the ΛCDM model on galaxy scale can be solved under the assumption of either a different DM candidate (see Sect. 1.3.2) or a different theory of gravity (see Sect. 1.3.3).

1.3.2 Alternative dark matter candidates

Besides WIMPs, among the hypothetical elementary particles beyond the Standard Model that can make up for the non-baryonic dark matter, quantum chromodynamics (QCD) axions and fuzzy dark matter (FDM) are strongly motivated candidates (Hu et al., 2000; Amendola and Barbieri, 2006). QCD axions are suggested by the solution of the Strong CP problem in the Standard Model (Weinberg, 1978; Wilczek, 1978), while fuzzy dark matter arises from the compactification of extra dimensions in the String Theory landscape (Arvanitaki et al., 2010). Moreover, some of the small scale issues of the CDM scenario can be solved assuming a warm dark matter (WDM) model or a self-interacting dark matter (SIDM) model.

QCD axions

QCD axions have the double virtue of solving the Strong CP problem in the Standard Model (SM) of particle physics (Peccei and Quinn, 1977a,b; Weinberg, 1978; Wilczek, 1978) and of being a potential candidate for dark matter (Abbott and Sikivie, 1983; Preskill et al., 1983; Dine and Fischler, 1983): it was indeed shown that they could be abundantly produced in the early Universe and their energy density behaves as that of CDM. Ultra-light axion-like particles (ULALPs) with a mass of $\sim 10^{-22}$ eV might solve both the cusp/core problem, resulting in DM density profiles with a ~ 1 kpc extended core, and the missing satellites problem. An attempt to solve the CCP with QCD axions by simply extrapolating the ULALPs scenario does not work, because the DM core they produce would be too small: of the size of $\mathcal{O}(1)$ km (Marsh and Pop, 2015). Whether QCD axions can address the small-scale problems requires further investigations.

Fuzzy dark matter

Another excellent alternative to CDM is Fuzzy Dark Matter, which consists of ultra-light bosons with mass in the range $10^{-23} - 10^{-20}$ eV (Hu et al., 2000; Amendola and Barbieri, 2006). These light bosons are naturally generated from symmetry breaking due to the misalignment mechanism (Preskill et al., 1983; Abbott and Sikivie, 1983; Svrcek and Witten, 2006), and are very common in string theory (for more details see Arvanitaki et al., 2010). FDM is considered to be a real scalar field ϕ with mass m_ϕ which is minimally coupled to the metric (Hui et al., 2017).

The field ϕ is initially massless until the Universe cools down to some critical temperature (Luu et al., 2020). It acquires the mass by rolling down and oscillating about the minimum of a potential generated non-perturbatively (Luu et al., 2020). The typical de Broglie wavelength of a FDM particle is a few kpc:

$$\frac{\lambda_{\rm dB}}{2\pi} = \frac{\hbar}{m_\phi v} = 1.92\,{\rm kpc}\left(\frac{10^{-22}\,{\rm eV}}{m_\phi}\right)\left(\frac{10\,{\rm km/s}}{v}\right)\,. \tag{1.2}$$

Therefore, the physics of FDM on length scales below $\lambda_{\rm dB}$ differs from that of the standard CDM. In particular, small density fluctuations unstable for masses larger than the Jeans mass (see Eq. 42 in Hui et al., 2017) lead to a minimum halo mass of $\sim 10^7\,{\rm M}_\odot$ for a boson mass of $\sim 10^{-22}$ eV. On the contrary, on scales above $\lambda_{\rm dB}$, the large scale structure of FDM is indistinguishable from CDM (Schive et al., 2014).

In 2014, novel N-body simulations with unprecedented high resolution showed the rich small scale structures of FDM halos (Schive et al., 2014). The uniqueness of these N-body simulations was their ability to capture the quantum nature of the DM particles by combining Schrödinger's and Poisson's equations (Widrow and Kaiser, 1993). Each virialized halo has a core of dark matter in the innermost part, which represents the ground state solution of the Schrödinger-Poisson equations. This core is surrounded by an interference pattern represented by fluctuations in the velocity and density fields of the particles. The cores, more often called solitons, exhibit flat density profiles that can naturally explain the wide cores in dwarf galaxies, and match the Navarro-Frenk-White (NFW) density profiles (Navarro et al., 1996b) in the outer regions of the halos.

Since solitons have a constant central density thanks to pressure support, they may potentially solve the CCP. To shed light on this issue, independent analyses used stellar kinematics data of dwarf spheroidal galaxies by carrying out a Markov Chain Monte Carlo fitting procedure of the projected velocity dispersion profiles (Marsh and Pop, 2015; Calabrese and Spergel, 2016; González-Morales et al., 2017; Chen et al., 2017). These analyses found that the data prefer soliton-generated cores (with boson mass $\sim 10^{-22}$ eV) over cuspy NFW profile.

N-body simulations also show the suppression of the halo number density for mass $\leq 10^{10}\,{\rm M}_\odot$, and how this cut-off depends upon the mass of the FDM particle (Marsh and Silk, 2014). Such suppression may provide a solution to the MSP (Du et al., 2017).

The debate on whether or not FDM may be a viable DM candidate is still ongoing. The presence of the soliton in every virialized halo can affect the dynamics of the disk by enhancing the circular velocity in the inner part of the rotation curve; this feature can provide a way to probe the model (Bar et al., 2019). However, many pieces of evidence, like the contribution of baryons or the constraints on FDM mass, still need to be explored.

Warm dark matter

In contrast to CDM, WDM particles decouple when they are still relativistic; they thus erase primordial fluctuations on sub-galactic scales, and produce a cut-off in the primordial power spectrum (Smith and Markovic, 2011). WDM particles can play the role of CDM in the cosmological evolution of the Universe (Schneider et al., 2014) and may also alleviate some of the problems of the CDM model at galactic scales.

To investigate the suppression of the primordial power spectrum on small scales, one of the most powerful tools is the Lyman-α forest. A lower limit to the mass of the WDM particles were initially set to $m_\chi > 750$ eV (Narayanan et al., 2000) by fitting the Lyman-α forest in quasar spectra. More recent analyses of the Lyman-α forest and of the Milky Way satellites have increased the lower limit to several keV (e.g., Seljak et al., 2006; Abazajian, 2006; Kennedy et al., 2014).

The most promising candidate of WDM is sterile neutrino, with mass m_s, which is mixed with an ordinary neutrino (Dodelson and Widrow, 1994; Dolgov and Hansen, 2002). For small mixing angles such as $\sin^2 2\theta \sim 10^{-7}$, the total amount of sterile neutrinos is only a small fraction of the ordinary neutrinos.

The claimed detections are based on the so-called 3.55 keV line emission, which is attributed to the decay of DM particles, and are obtained by using Chandra X-ray observations of galaxies in the Local Group (Horiuchi et al., 2014), studies on dwarf galaxies (Malyshev et al., 2014), and Suzaku observations of the Perseus galaxy cluster (Tamura et al., 2015). These investigations imply a sterile neutrino of mass ~ 7 keV.

In contrast to these results, the full-sky Fermi Gamma-ray Burst Monitor data (Ng et al., 2015) do not reveal any significant signal for sterile neutrino decay lines in the energy spectrum.

Additional constraints have been obtained by using gravitationally lensed quasars: under the assumption of a thermal relic DM particle, modeling the image positions and the flux-ratios of several gravitationally lensed quasars implies a lower limit (Hsueh et al., 2019) of $m_\chi > 5.58$ keV or $m_\chi > 5.2$ keV, consistent with the lower limits $m_\chi > 5.3$ keV or $m_\chi > 3.5$ keV, depending on the assumed thermal history of the intergalactic medium, derived from the analysis of the Lyman-α forest (Bolton et al., 2008; Iršič et al., 2017; Garzilli et al., 2019).

WDM particles can lead to possible solutions of some of the CDM observational challenges. Since WDM particles are moving freely when they are relativistic, they can travel distances of the order of the horizon size, suppressing density fluctuations on scales below the inverse of a characteristic comoving wavenumber (Bode et al., 2001):

$$k_{\rm WDM} \sim 15.6 \frac{h}{\rm Mpc} \left(\frac{m_X}{\rm keV}\right)^{4/3} \left(\frac{0.12}{\Omega_{\rm DM} h^2}\right)^{1/3}, \tag{1.3}$$

with obvious meaning of the symbols. This suppression of the density perturbations may lead to a solution of some of the problems that the CDM model encounters at galactic scales. The matter power spectrum drops below a certain length scale k^{-1} depending upon the mass of the WDM particles. For example, the power spectrum is suppressed below $k^{-1} \sim 100$ kpc for a particle mass of $\sim$1 keV (Viel et al., 2005). Therefore, the subhalo mass function can be brought into agreement with satellite counts and the MSP would be solved (Smith and Markovic, 2011; Zavala et al., 2009; Papastergis et al., 2011).

In addition, the gravitational collapse leads to a cuspy halo profile with a lower central concentration compared to CDM halos (Smith and Markovic, 2011). Moreover, the existence of a relic thermal velocity distribution for the WDM particles may convert the cusp in the density profile into a core, providing a solution to the CCP (Tremaine and Gunn, 1979). Nevertheless, the cores appear to be smaller than required to explain the data on LSB galaxies (Villaescusa-Navarro and Dalal, 2011; Macció et al., 2012).

These results have been widely validated by many N-body simulations of structure formation within the WDM scenario (e.g., Bode et al., 2001; Polisensky and Ricotti, 2011; Macció et al., 2012; Anderhalden et al., 2012; Schneider et al., 2012; Angulo et al., 2013).

Finally, a WDM particle with mass in the range $1.5 - 2$ keV can potentially solve the TBTF problem for satellite dwarf galaxies, as Milky Way-sized DM halos have fewer and less dense massive subhalos in WDM than in CDM (Lovell et al., 2012; Schneider et al., 2014). Furthermore, the TBTF problem for field dwarf galaxies can also be solved by a WDM particle with mass of ~ 1 keV (Papastergis et al., 2015). However, WDM particles with such small masses are in conflict with a number of observational constraints; masses of the WDM particles that are consistent with the largest estimate of ~ 7 keV enable

WDM simulations to alleviate the TBTF problem only when baryonic feedback and tidal process are accounted for, similarly to CDM simulations.

Self-interacting dark matter

A model of WDM and SIDM was firstly introduced in 1992 (Carlson et al., 1992), and subsequently constrained a few years later (Machacek, 1994; de Laix et al., 1995). In 2000, Spergel and Steinhardt proposed the idea of cold and self-interacting dark matter to solve two small scale issues of CDM: the cusp/core and the missing satellites problems. The newly proposed SIDM particles behave like collisionless CDM at larger length scales, where the rate of collisions becomes negligible due to the smaller density.

SIDM models are commonly parametrized by the cross-section per unit mass, σ/m, which, in general, is a function either of the relative velocity $v_{\rm rel}$ of the DM particles, or of the total mass of the virialized halo, $M_{\rm halo}$. In addition, $v_{\rm rel}$ and $M_{\rm halo}$ are related by the fact that the velocity dispersion of the DM particles is larger in more massive halos.

Cosmological simulations of SIDM halos without the baryonic feedback predict constant density cores (Dave et al., 2001; Yoshida et al., 2000; Rocha et al., 2013; Elbert et al., 2015) contrary to the cuspy profiles from the simulations of collisionless CDM. The SIDM simulations solve the cusp-core problem if $\sigma/m \gtrsim 0.5$ cm^2/g for galactic halos with $M_{\rm halo} \sim 10^{11}\,{\rm M}_\odot$ (Firmani et al., 2000; Elbert et al., 2015). However, galaxy clusters with $M_{\rm halo} \sim 10^{14}\,{\rm M}_\odot$ require $\sigma/m \sim 0.1$ cm^2/g (Meneghetti et al., 2001; Firmani et al., 2000, 2001; Tulin and Yu, 2018). The difference in σ/m at galaxy and cluster scales implies velocity-dependent cross-sections which is a crucial aspect of the SIDM models.

Although SIDM with large scattering rates tends to reduce the number of subhalos, the MSP is not easily solved by SIDM (Rocha et al., 2013; Colin et al., 2002; Vogelsberger et al., 2012; Zavala et al., 2013), unless non-minimal SIDM interactions are assumed (Tulin and Yu, 2018). From SIDM-only simulations, the values of σ/m required to solve the MSP are most likely ruled out by constraints from the measured ellipticities of DM halos (see Tulin and Yu (2018) and references therein). However, the baryonic contributions may significantly change this scenario on galaxy scales. On the scale of galaxy clusters, values of σ/m in the range 0.3 to 10^4 cm^2/g are excluded based on the fact that, unlike the number of satellite galaxies, the number of galaxies in a cluster is comparable to the number found in the simulations of the formation of the large-scale structure (Gnedin and Ostriker, 2001; Rocha et al., 2013).

The self-interactions between the DM particles also alleviates the TBTF problem for satellite and field dwarf galaxies. Even though self-interaction has little effect on the abundance or total mass of the subhalos, it effectively decreases the central density of the most massive subhalos by removing mass from these regions, characterized by cuspy density profiles. Velocity-independent SIDM models are consistent with the kinematics of the Milky Way dwarf spheroidal galaxies (dSphs) for values of the cross-section per unit mass $\sigma/m \approx 1$ cm^2/g (Zavala et al., 2013; Dooley et al., 2016); lower values of σ/m generate a population of subhalos too dense to be consistent with the observations. On the other hand, velocity-dependent SIDM models successfully solve the TBTF (Loeb and Weiner, 2011; Vogelsberger et al., 2012; Dooley et al., 2016). However, the class of velocity-dependent SIDM models remains largely unconstrained.

In principle, SIDM with dissipative or inelastic scattering may also alleviate the problem of the planes of satellite galaxies by allowing the observed satellites to be dark matter dominated tidal dwarfs (Foot and Silagadze, 2013; Randall and Scholtz, 2015). In CDM simulations, dwarf galaxies formed due to tidal disruption during the merging

of two galaxies are baryon dominated. On the contrary, a dissipative dark matter scenario allows a thin dark matter disk in a halo, and merging galaxies with such dark disks may produce dark matter dominated dwarf galaxies with strong phase-space correlations. However, the presence of a dark matter disk in the Milky Way is not currently supported (Schutz et al., 2018; Buch et al., 2019).

1.3.3 Alternative theories of gravity: MOND

The observational challenges of the CDM model on galactic scales may also be interpreted as a breakdown of the law of gravity. Modifications of the law of gravity conceived to explain the observed kinematics of visible matter started to be systematically investigated back in the 1980s (Bekenstein and Milgrom, 1984; Sanders, 1986, 1990; Sanders and McGaugh, 2002), although some suggestions were put forward much earlier (e.g., Finzi, 1963). On cosmological scales, observational data from the Planck mission do not seem to provide statistical evidence in favor of any particular theory of gravity (Planck Collaboration et al., 2020a). Also at galactic scales, where the physics is complicated by the relevant role of baryons, the issue remains open.

In the following, we focus on MOdified Newtonian Dynamics (MOND), the alternative theory of gravity for which we conceived a novel test in Chakrabarty et al. (2022) (see Chpt. 3).

MOND

In 1983, Milgrom suggested to explain the mass discrepancy in cosmic structures with a modification of the law of gravity rather than with the presence of dark matter (Milgrom, 1983a,b,c). His phenomenological proposal rests upon the hypothesis that there is an acceleration scale $a_0 \simeq 1.2 \times 10^{-10}$ m s^{-2} above which Newtonian gravity holds and below which Newtonian gravity breaks down. This idea goes beyond the naive idea that gravity should be modified simply beyond a length scale (Finzi, 1963; McGaugh and de Blok, 1998b).

According to Milgrom's suggestion, the magnitude a of the acceleration experienced by a test particle in a gravitational field is

$$a = \nu \left(\frac{a_N}{a_0} \right) a_N \ , \tag{1.4}$$

where a_N is the magnitude of the gravitational acceleration, estimated in Newtonian gravity, originated by the distribution of the baryonic matter alone, as dark matter is assumed to be nonexistent; ν is an interpolation function whose asymptotic behaviors are $\nu \to 1$ when $a_N \gg a_0$ (and thus $a = a_N$) and $\nu \to (a_N/a_0)^{-1/2}$ when $a_N \ll a_0$ (and thus $a = \sqrt{a_N a_0}$).

A number of interpolation functions has been proposed in the literature; one of them is that of McGaugh (2008):

$$\nu \left(\frac{a_N}{a_0} \right) = \left(1 - e^{-\sqrt{a_N/a_0}} \right)^{-1} \ . \tag{1.5}$$

Rather than as a modification of the law of gravity, the introduction of an acceleration scale can be alternatively interpreted as a modification of the law of inertia $F = ma$, where the inertial mass differs from the gravitational mass when $a_N \ll a_0$ (Milgrom, 1994, 1999, 2006). In both cases, Milgrom's suggestion yields a MOdified Newtonian Dynamics (MOND) (see Famaey and McGaugh (2012) for an extensive review).

The introduction of an acceleration scale makes the MOND formulation manifestly purely phenomenological: in General Relativity, the acceleration is linked to the affine connection $\Gamma^{\mu\nu}_{\lambda}$ which is not a tensor; therefore, the formulation of a covariant version of MOND, which is required to test the theory against the properties of the large-scale structure on cosmic scales, is not unique and remains difficult. As a consequence, in the MOND framework we can neither build a cosmological model, which is the most relevant success of the ΛCDM model, nor quantify the phenomenology of gravitational lensing, which is an important probe of the mass distribution on large scale. An additional shortcoming is that MOND is unable to explain the observed mass discrepancy on the scale of galaxy clusters and on larger scales, although the amount of required dark matter is substantially reduced (Milgrom, 1983c).

Attempts to provide MOND with a covariant formulation include, for example, AQUAL (Bekenstein and Milgrom, 1984), TeVeS (Bekenstein, 2004), and bimetric MOND (Milgrom, 2009). These theories introduce additional scalar, vector or tensor fields and reduce to MOND in the non-relativistic limit (Cardone and Radicella, 2009). Recently, Hernandez et al. (2019) concluded that a covariant equivalence between the MOND acceleration scale a_0 and the scalar quantity K_b, constructed at galaxy level, yields a cosmic expansion history of the Universe in agreement with ΛCDM predictions; with:

$$\mathcal{K}_b = K\frac{r^4}{M} = \frac{28Ga_0}{c^4}\,, \tag{1.6}$$

where M is the total mass of the baryonic component in a galactic system, K is the Kretschmann curvature scalar for a Schwarzschild metric, G is the universal gravitational constant and c is the speed of light. Skordis and Złośnik (2021) present a relativistic version of MOND in which a scalar field plays the role of DM in the early-Universe; this MOND version successfully explains the CMB and matter power spectrum in the linear regime.

The number of different theories shows that a covariant theory that reduces to MOND is not uniquely determined. Therefore, invalidating one of these theories does not necessarily invalidate MOND. For example, the detection of gravitational waves originating from the merging of two neutron stars (LIGO Scientific Collaboration and Virgo Collaboration, 2017) combined with the observation of a gamma-ray burst within a few seconds (Goldstein et al., 2017; Savchenko et al., 2017) implies that the speed of light and the speed of gravitational waves coincide within one part in 10^{-15}. In the original formulation of TeVeS, the speed of gravitational waves in general is different from the speed of light and therefore TeVeS appears to be ruled out (Gong et al., 2018). Nevertheless, there is a family of tensor-vector-scalar theories that still reduce to MOND in the non-relativistic limit, where the speed of gravitational waves equals the speed of light (Skordis and Złośnik, 2019).

The idea of a hybrid model that merges the success of MOND on small scales with the properties of the large-scale structure provided by the presence of dark matter was suggested by Angus in 2009. He assumed MOND as the theory of gravity and added a Hot Dark Matter (HDM) component made of sterile neutrinos of mass ~ 11 eV. The existence of a sterile neutrino still appears to be a solution to the detection of the excess of electron-like events in short-baseline neutrino experiments (Aguilar-Arevalo et al., 2018). HDM has the advantage of clumping on scales larger than the scale of galaxies. The MOND phenomenology would thus be preserved on small scales, whereas dark matter starts becoming relevant on larger scales, where MOND apparently disagrees with observations (see Diaferio and Angus (2012) for a review). Unfortunately, this hybrid model is unable to reproduce the mass function of galaxy clusters (Angus and Diaferio, 2011; Angus et al.,

2013, 2014).

On the other hand, on the scale of galaxies, MOND has proved not only to successfully describe most of the observed phenomenology, but actually to be predictive (e.g., Merritt, 2020). The predictions of MOND on the scales of galaxies are so distinctive that it has become customary to collect them in the so-called MOND phenomenology. These observational facts are clearly independent of the theory of gravity; therefore, other theories, alternative to the standard model, must mimic the MOND phenomenology on these scales.

Confirmed MOND predictions include:

- the Baryonic Tully-Fisher Relation (BTFR; McGaugh et al., 2000) of disk galaxies. The BTFR is the correlation between the total baryonic mass of the galaxy ($M_{\rm bar}$) and the asymptotic flat velocity of its rotation curve, $V_{\rm c}$, that behaves as $M_{\rm bar} = AV_{\rm c}^4$, where the normalization constant is $A = 47 \pm 6$ $\mathrm{M_\odot\ km^{-4}\ s^4}$ (McGaugh, 2012). A can also be written as $A \sim (Ga_0)^{-1}$, the product between the gravitational constant G and an acceleration scale $a_0 = 1.2 \times 10^{-10}$ m s^{-2}. The intrinsic scatter of the BTFR reaches a minimum of $\sim$0.10 dex for $\Upsilon_{[3.6]} \gtrsim 0.5$ $\mathrm{M_\odot/L_\odot}$ (Lelli et al., 2016b). MOND predicts this correlation with virtually no systematic scatter over ~ 5 orders of magnitude in baryonic mass (Lelli et al., 2016a; McGaugh, 2020);

- the Mass Discrepancy-Acceleration Relation (MDAR; Sanders, 1990; McGaugh, 2004). MDAR is the anti-correlation between the Newtonian acceleration due to the mass density of baryons and the squared ratio of the total and the baryons-induced galaxy velocity, $(V/V_{\rm bar})^2$, that coincides with the mass discrepancy, $(M/M_{\rm bar})$ under the assumption of spherical symmetry. In the standard model, we dynamically estimate the total mass with $M \sim rv^2/G$; from the luminosity we can estimate the baryonic mass $M_{\rm bar}$. In MOND, Newtonian gravity holds when the Newtonian gravitational acceleration generated by the baryonic mass is larger then a_0, therefore we expect $M/M_{\rm bar} \sim 1$ in this regime and $M/M_{\rm bar}$ increasingly larger than 1 at increasingly smaller accelerations. This mass discrepancy-acceleration relation, predicted in 1983 (Milgrom, 1983b), implies increasingly large mass-to-light ratios for galaxies with increasingly fainter surface brightness, as it was confirmed years later with the observations of dwarf spheroidals galaxies and LSB disks galaxies (Mateo et al., 1991; McGaugh and de Blok, 1998a). The MDAR can also be interpreted as a discrepancy between the Newtonian gravitational acceleration generated by the baryonic mass distribution, $g_{\rm bar}$, and the observed centripetal acceleration derived from the rotation curves of disk galaxies, $g_{\rm obs}$. The tight correlation between $g_{\rm obs}$ and $g_{\rm bar}$ was found by McGaugh et al. (2016) and is called radial acceleration relation (RAR): the deviation from the one-to-one relation appears at Newtonian accelerations smaller than a_0 and the relation is described by the interpolation function of Eq. (1.5) (McGaugh, 2008). Accurate spectroscopic measures of the disk galaxies in SPARC (Lelli et al., 2016a) and other data sets (e.g., Lelli et al., 2013) support this relation;

- the Freeman limit. When the introduction of massive DM halos was thought to be necessary to make the disks dynamically stable and explained the flat rotation curves, Freeman noted that the mean central surface brightness of disk galaxies is $\mu_F = 21.65$ mag arcsec^{-2} in the B-band with a little scatter of 0.30 mag arcsec^{-2}: this relation became known as the Freeman law (Freeman, 1970). However, the Freeman law was the result of an observational bias, as it became clear a few years later (Allen and Shu, 1979). In fact, disks appear in a wide range of central surface brightness

(van der Kruit and Freeman, 2011). In addition, LSB galaxies are actually more than half of the total galaxy population and the number of galaxies with central surface brightness brighter than $\mu_F = 21.65$ mag arcsec^{-2} drops substantially faster than for a normal distribution (McGaugh et al., 1995): the Freeman law actually is a Freeman limit. The Freeman limit is a property of the baryonic matter, whereas dark matter dominates the dynamics of disk galaxies in the standard model. Therefore, the Freeman limit must originate from the interplay between dark matter and baryonic matter. The CDM model has not yet an obvious solution for deriving this limit (Dalcanton et al., 1997). On the other hand, in MOND, the origin of the Freeman limit simply derives from gravitational dynamics. Without dark matter, disks are unstable in Newtonian gravity. However, if MOND is the theory of gravity, the disk becomes stable against the development of bars (Milgrom, 1989; Brada and Milgrom, 1999; Tiret and Combes, 2008b; Jiménez and Hernandez, 2014; Thies et al., 2016; Sánchez-Salcedo et al., 2016; Banik et al., 2018). It follows that disks without any dark matter are gravitationally stable only if they are in the MOND regime, $a_N < a_0$. If mass is proportional to luminosity, we have the acceleration $a_N \sim 2\pi G\Sigma$, in Newtonian gravity, where Σ is the surface mass density. The limit $a_N < a_0$ becomes $a_N \sim 2\pi G\Sigma < a_0$; in other words, gravitationally stable disks must have $\Sigma < a_0/(2\pi G)$: this limit $a_0/(2\pi G) \approx 143$ M$_\odot$ pc^{-2} neatly returns the Freeman limit $\mu_F = 21.65$ mag arcsec^{-2} (Milgrom, 1983b, 1989);

- the dependence of the shape of the rotation curves on the surface brightness of the galaxy. High surface brightness (HSB) galaxies are expected to have steeply rising rotation curves that flatten at small radii, whereas LSB galaxies are expected to have slowly rising rotation curves that converge to the asymptotic constant velocity at large radii (McGaugh, 2020);

- the large mass-to-light ratios of dwarf galaxies when interpreted in Newtonian gravity (Aaronson, 1983; Kormendy, 1987; Mateo et al., 1991; Mateo, 1998). MOND can explain the velocity dispersion profiles of dwarf spheroidals with mass-to-light ratios M/L consistent with stellar population synthesis models for the classical dwarfs, except Carina (Angus, 2008; Serra et al., 2010). Carina is the closest dwarf spheroidal to the Milky Way and detailed N-body simulations in MOND show that tidal forces and the external field effect, an effect that lacks in Newtonian gravity, can only partly alleviate the tension (Angus et al., 2014): the best-fit M/L in the V-band required to match the observed velocity dispersion profile is $M/L \sim 5.3-5.7$ M$_\odot$/L$_\odot$, a value $\sim 10\%$ higher than the upper limit of ~ 5 M$_\odot$/L$_\odot$ for the old stellar population of Carina (Maraston, 2005). However, there might still be the possibility to alleviate this tension both observationally and theoretically: more accurate measurements of the proper motion of the dwarf spheroidals and larger samples of stars with accurate photometry can provide a better understanding of the physical properties of the dwarf spheroidals; similarly, the modeling of these systems can be improved by considering a triaxial three-dimensional stellar distribution, more sophisticated treatments of stellar binaries and even more accurate stellar population synthesis models.

Many of the observational challenges described in Sect. 1.3.1 were predicted by MOND many years before they were actually observed and posed unexpected challenges to the traditional dark matter framework. This feature is specific to MOND and makes it fundamentally different from the other suggested theories of modified gravity: these latter theories attempt to describe these observations only after they become available and never anticipate them.

Because in MOND no dark matter is present, MOND provides a natural solution to all the DM-related challenges of the ΛCDM model illustrated in Sect. 1.3.1, namely the cusp/core problem, the missing satellites problem and the too-big-to-fail problem. Finally, MOND might present a viable mechanism for the formation of the plane of satellites. In the standard model, the problem of the plane of satellites would be most easily solved if these satellites were collapsed tidal debris formed during galaxy interactions (Weilbacher et al., 2000; Bournaud and Duc, 2006; Wetzstein et al., 2007). Unfortunately, the dwarf galaxies appear to be dark matter dominated, whereas these Tidal Dwarf Galaxies (TDGs) are expected to be dark-matter free. In fact, the DM halo of the parent galaxy is supported by the velocity dispersion of the DM particles and it is dynamically hot, unlike the dynamically cold baryonic galactic disk supported by rotation. Therefore the DM halo does not participate in the formation of the TDGs orbiting in a dynamically cold plane: this tidal tail can only originate from the galactic disk. In MOND, this mechanism would work without the complication of the existence of the dark matter, as shown by N-body simulations (Tiret and Combes, 2008a; Renaud et al., 2016); the mechanism is actually favored by the enhanced self-gravity of the baryons.

1.4 The shape of dark matter halos

1.4.1 Theoretical predictions in the ΛCDM model

The ΛCDM cosmological model predicts the existence of DM halos surrounding the Milky Way and the external galaxies.

Although at first order the spherically symmetric NFW profile (Navarro et al., 1997) can provide a good approximation to the shape of the DM halos, the first numerical N-body simulations (Frenk et al., 1988; Dubinski and Carlberg, 1991; Warren et al., 1992; Cole and Lacey, 1996) found the shape of the DM halos to be triaxial, and subsequent works (e.g., Jing and Suto, 2002; Bailin and Steinmetz, 2005; Hayashi et al., 2007; Vera-Ciro et al., 2011) confirmed this results.

The triaxiality coefficient, T, is defined as:

$$T = \frac{1 - \left(\frac{b}{a}\right)^2}{1 - \left(\frac{c}{a}\right)^2} \ , \tag{1.7}$$

where, a, b, and c are the ellipsoidal parameters of the DM halo, with $a > b > c$; thus, b/a and c/a are the intermediate-to-major axis ratio and the minor-to-major axis ratio, respectively. If the DM halo is purely prolate ($a > b = c$) the triaxiality parameter is $T = 1$. If the DM halo is purely oblate ($a = b > c$) the triaxiality parameter is $T = 0$. The DM halo is triaxial for $0 < T < 1$; usually, a DM halo with $0 < T < 1/3$ is considered nearly-oblate and a DM halo with $2/3 < T < 1$ is considered nearly-prolate (Warren et al., 1992).

In particular, DM halos in CDM simulations are triaxial with a tendency to prolateness in the center, while they become more triaxial in the outer part. For example, Dubinski and Carlberg (1991) find that the halos are strongly triaxial and very flat, with an average density minor-to-major axis ratio $(c/a)_\rho = 0.50$ and an average density intermediate-to-major axis ratio $(b/a)_\rho = 0.71$, that corresponds to a triaxiality parameter $T = 0.66$. Within the inner 25 kpc, they find that the DM halos become more prolate with average density axis ratio $(c/a)_\rho = 0.42$ and $(b/a)_\rho = 0.56$, that lead to $T = 0.83$. This behavior is as a consequence of an accretion history that is more anisotropic at early times, when halos are fed through narrow filaments, and becomes more isotropic at later times (Vera-Ciro et al., 2011).

The results obtained from these DM-only simulations are affected by the absence of the baryonic component, whose inclusion is of fundamental importance to properly describe the formation of small scale systems like the MW and the other galaxies. The inclusion of the gas dynamics in the simulations was the first attempt to account for the baryonic effects on the shape of the DM halo in the 1990's (e.g., Katz and Gunn, 1991; Katz and White, 1993; Dubinski, 1994).

In the following years, cosmological hydrodynamic simulations were used to investigate the impact of radiative cooling, star formation, and supernova feedback on the final shape of the DM halos (e.g., Gnedin et al., 2004; Kazantzidis et al., 2004; Gustafsson et al., 2006; Tissera et al., 2010; Abadi et al., 2010; Zemp et al., 2012; Bryan et al., 2013; Butsky et al., 2016).

The inclusion of these effects leads to a larger sphericity of the DM halos, that are now predicted to be, in the central regions of galaxies, rounder than previously thought. For example, Butsky et al. (2016) find that, for masses of $\approx 10^{12}\,M_{\odot}$, the inner halo becomes more spherical with an average density minor-to-major axis ratio $(c/a)_{\rho} = 0.8$, while in the DM-only simulations of Dubinski and Carlberg (1991) an axis ratio $(c/a)_{\rho} = 0.42$ is obtained within 25 kpc from the galactic center.

1.4.2 Theoretical predictions for alternative dark matter candidates

The dependence of the shape of the DM halo on the type of DM particle candidate is still a poorly investigated field.

Among the alternative DM candidates illustrated in Sect. 1.3.2, only self-interacting dark matter (SIDM) has been explored in this perspective.

Chua et al. (2020) explored the effects of inelastic DM self-interactions on the internal structure of a simulated MW-size halo. They found that the central density of the MW halo is reduced by the energy injection from inelastic self-interactions on a timescale shorter than that of the elastic scale; this results in a larger size for the core of the DM halo. Inelastic collisions also isotropize the orbits, causing an overall lower velocity anisotropy for the inelastic MW halo.

All SIDM models lead to more spherical halos (i.e., larger b/a and c/a) than CDM for a significant fraction of the halo. This increase in sphericity is stronger in the inner regions and decreases towards the virial radius (see Fig. 1.6). In particular, when the primordial fraction of DM in the excited state is $\chi^2_{init} = 100\%$, in the inner 10 kpc from the center of the galaxy, the DM halo is more spherical in the case of inelastic SIDM ($(c/a)_{\rho} \approx 0.65$) than in the case of CDM ($(c/a)_{\rho} \approx 0.4$), but less spherical than in the case of elastic SIDM ($(c/a)_{\rho} \approx 0.75$).

In order to incorporate the effects of both baryonic and SIDM elastic interactions, Vargya et al. (2021) studied a set of cosmological-baryonic simulations of MW-mass galaxies from the FIRE-2 project by varying the SIDM self-interaction cross-section, σ/m. Using the same initial conditions, they compared the shape of the DM halo at redshift $z = 0$ predicted by SIDM simulations (at $\sigma/m = 0.1, 1$, and 10 $\mathrm{cm^2\,g^{-1}}$) with that obtained in CDM simulations; they found that, when the baryonic feedback effects are included, the SIDM models do not produce the large differences in the inner structure of MW-mass galaxies predicted by SIDM-only models.

1.4.3 Observational constraints for the Milky Way

In the last decades, a large number of studies has been conducted with the aim of testing model predictions on the shape of the DM halo of the MW with available observations.

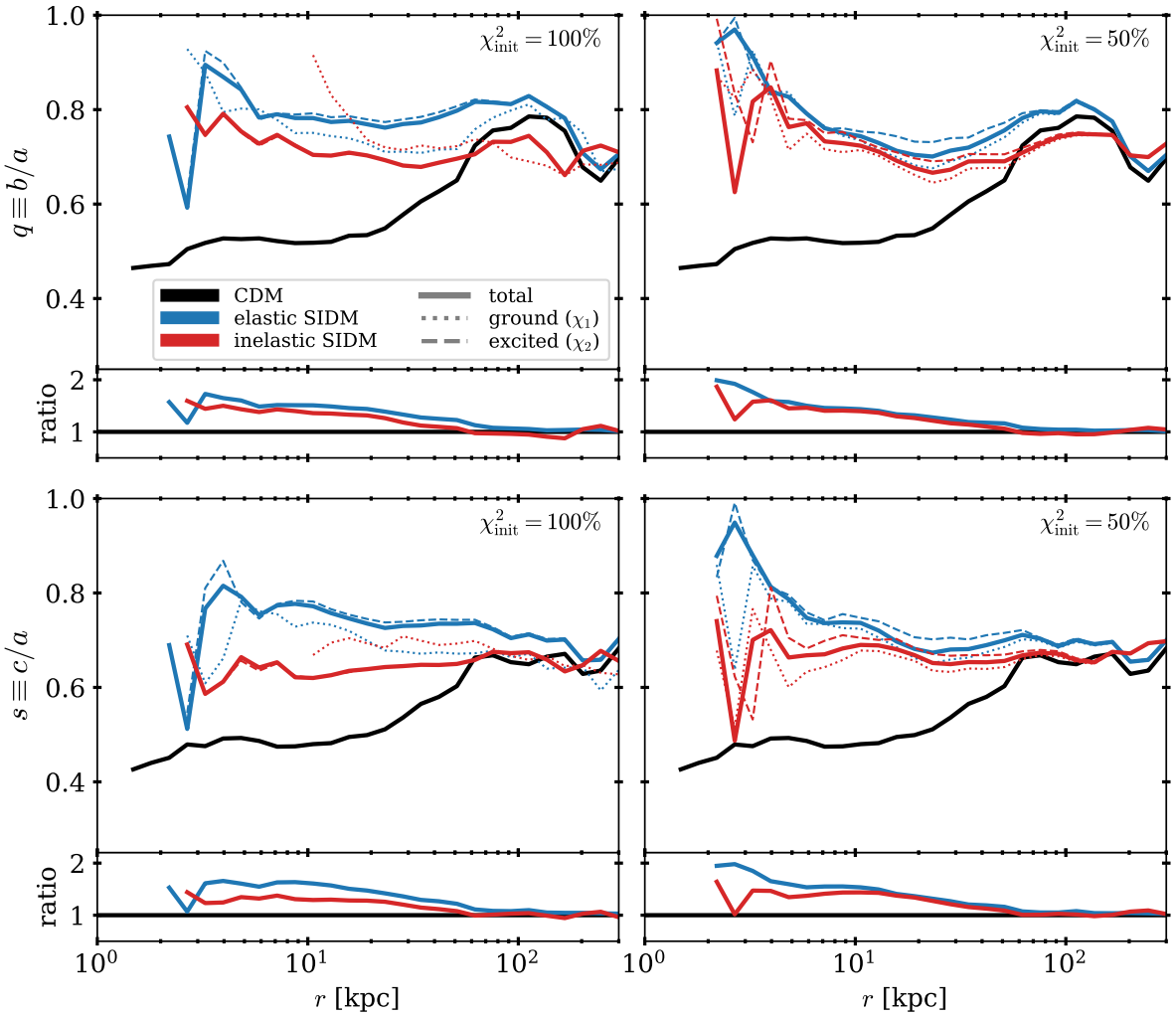

Figure 1.6. *Top panels*: intermediate-to-major (b/a) density axis ratio as a function of galactocentric distance, r. *Bottom panels*: minor-to-major (c/a) density axis ratio as a function of galactocentric distance, r. The left panels show the results from simulations in which the primordial fraction of dark matter in the excited states is $\chi^2_{init} = 100\%$, while the right panels show the results for $\chi^2_{init} = 50\%$. The bottom plots attached to each panel show the ratio of the SIDM profiles relative to CDM. The figure is reproduced from Chua et al. (2020).

Those tests used different tracers of the Galactic gravitational potential, such as:

- the distribution and kinematics of halo stars (e.g., Smith et al., 2009a; Loebman et al., 2014);
- the kinematics of disk stars in the Solar neighborhood (Olling and Merrifield, 2000);
- the tidal streams from satellite galaxies and from globular clusters (e.g., Helmi, 2004; Johnston et al., 2005; Fellhauer et al., 2006; Růžička et al., 2007; Law et al., 2009; Koposov et al., 2010; Law and Majewski, 2010; Vera-Ciro and Helmi, 2013; Küpper et al., 2015; Bovy et al., 2016; Malhan and Ibata, 2019);
- the distribution of globular clusters (e.g., Posti and Helmi, 2019);
- the distribution of the MW satellite galaxies (Zentner et al., 2005);
- the flaring of the HI distribution (e.g., Olling and Merrifield, 2000; Banerjee and Jog, 2011).

Because of the use of different tracers, the results of these studies hold on different spatial scales. However, even on comparable scales, these results are not all consistent with one another, partly because of the use of different techniques and partly because of the different working assumptions.

The Galactic DM halo is suggested to be overall close to spherical on the basis of the tilt of the velocity ellipsoid of a sample of halo subdwarf stars located at galactocentric cylindrical radii of 7-10 kpc and depth $\lesssim 4.5$ kpc below the Galactic plane, in the 250 deg^2 sky area covered by SDSS Stripe 82 (Smith et al., 2009a).

Under the assumptions that the MW DM halo is a spheroid and the full Galactic gravitational potential is axisymmetric, a variety of results are found. The GD-1 stellar stream excludes a significantly oblate DM halo at the GD-1 location, $r \sim 14$ kpc, where the vertical-to-planar axis ratio (hereafter referred to as "flattening") of the gravitational equipotential surfaces is constrained to $q_\Phi > 0.89$, according to Koposov et al. (2010); the same stellar stream is found to provide a stronger constraint, yielding a prolate DM halo with mass density flattening $q_\rho = 1.27$, by Bovy et al. (2016). On the other hand, the stellar stream Pal 5 constrains the DM halo to be mildly oblate at $r \sim 19$ kpc, with either potential flattening $q_\Phi = 0.95$ (Küpper et al., 2015) or density flattening $q_\rho = 0.9$ (Bovy et al., 2016), suggesting a radial-dependent flattening for the DM halo. Finally, the combination of Pal 5 and GD-1, together with constraints on the force field near the Galactic disk, return a nearly spherical DM halo, with $q_\rho = 1.05$, (Bovy et al., 2016) within the inner 20 kpc.

These results are at odds with those found with different probes on similar scales: the combination of the kinematics of disk stars in the vicinity of the Sun with the flaring of the HI disk is found to consistently constrain the DM halo to be oblate, with density flattening $q_\rho \sim 0.8$ (Olling and Merrifield, 2000); the kinematics of halo stars also constrains the dark halo to be significantly oblate, with flattening $q_\rho = 0.4$ (or, equivalently, $q_\Phi = 0.7$; Loebman et al. 2014). Conversely, the distribution of globular clusters suggests a prolate DM halo with density flattening $q_\rho = 1.3$ (Posti and Helmi, 2019).

At larger galactocentric distances, $20 \lesssim r \lesssim 60$ kpc, the tidal streams of the Sagittarius dwarf spheroidal (Sgr dSph) galaxy lead to conclude that the DM halo potential has to be mildly oblate ($q_\Phi = 0.90-0.95$; Johnston et al. 2005) or nearly spherical ($q_\Phi = 0.92-0.97$; Fellhauer et al. 2006) to explain the precession of Sgr dSph's orbit, while extremely oblate halos with density flattening $q_\rho < 0.7$ are ruled out (Ibata et al., 2001); on the other hand, the potential of the dark halo has to be prolate, with $q_\Phi = 1.25-1.5$ to explain the kinematics of Sgr dSph's older, leading stream (Helmi, 2004). Finally, on scales $r \lesssim 200$ kpc, the modeling of the Magellanic stellar streams generated by the interaction of the MW with the Magellanic system favors a DM halo that has a globally oblate potential with $q_\Phi < 1$ (Růžička et al., 2007). The uncertainties on the quoted flattening range from $\sim 5\%$ to $\sim 20\%$.

Some of the apparent inconsistencies among the results on the shape of the dark halo can be solved by assuming that the DM halo is triaxial, so that the Galactic potential is globally non-axisymmetric. For instance, a triaxial DM potential with intermediate-to-major axis ratio $(b/a)_\Phi = 0.99$ and a minor-to-major axis ratio $(c/a)_\Phi = 0.72$ on scales $20 \lesssim r \lesssim 60$ kpc enables Law and Majewski (2010) to explain, at the same time, both the angular precession and the radial velocities of the stars in the Sgr dSph leading stream (see also Law et al., 2009).

Other inconsistencies on the shape of the dark halo, especially those on different spatial scales, may in principle be relieved by discarding the simplifying assumption of a radial-independent shape for the halo: although common to all the above-mentioned models, this assumption is not supported by the results of N-body simulations. In this context,

by assuming an axisymmetric dark halo to model the flaring of the HI disk, Banerjee and Jog (2011) find the halo to be prolate, with a density flattening q_ρ increasing from 1 to 2 in the range $9 \lesssim r \lesssim 24$ kpc. Conversely, with a non-axisymmetric model applied to the Sgr dSph's streams, and accounting for the effects of the Large Magellanic Cloud (LMC), Vera-Ciro and Helmi (2013) constrain the DM halo potential to be mildly oblate at $r \lesssim 10$ kpc, where $q_\Phi = 0.9$, and smoothly translating to a triaxial shape at larger radii, where the intermediate-to-major axis ratio is $(b/a)_\Phi = 0.9$ and the minor-to-major axis ratio is $(c/a)_\Phi = 0.8$, in agreement with cosmological simulations.

All these results clearly show that, despite the large efforts, the shape of the MW DM halo remains uncertain and that further work is necessary.

1.5 Hypervelocity stars

In this Thesis we will use hypervelocity stars (HVSs) as tracers of the MW gravitational potential. These stars are ejected from the Galactic center and may reach the outer regions of the Galaxy within their lifetime: this property makes them exceptional tools to investigate the MW gravity on a wide range of scales.

1.5.1 The Hills mechanism

The existence of hypervelocity stars was postulated by Hills in 1988, who defined as an HVS a star ejected from the Galactic center after a close encounter between a binary star system and the supermassive black hole (SMBH) at the center of our Galaxy associated with SgrA*; if the binary system experiences a sufficiently close passage near the SMBH, it can be tidally disrupted: one of the binary member is ejected as hypervelocity star and maybe characterized by a present-day speed exceeding the Galactic escape velocity, while the companion star becomes gravitationally bound to the SMBH (Hills, 1988).

A SMBH of mass $M_{\rm BH}$ tidally disrupts a stellar binary of mass $m_{\rm b}$ and semi-major axis $a_{\rm b}$ at distances smaller than the binary tidal disruption radius, r_{bt}, at which the SMBH gravitational tidal force exceeds the force that binds the binary (Miller et al., 2005):

$$r_{\rm bt} = a_{\rm b} \left(\frac{3M_{\rm BH}}{m_{\rm b}}\right)^{\frac{1}{3}} \simeq 14\,{\rm AU} \left(\frac{a_{\rm b}}{0.1\,{\rm AU}}\right) \left(\frac{{\rm M}_\odot}{m_{\rm b}}\right)^{\frac{1}{3}} \left(\frac{M_{\rm BH}}{10^6\,{\rm M}_\odot}\right)^{\frac{1}{3}} . \tag{1.8}$$

The orbital velocity of the stars in a binary system is:

$$v_{\rm b} = \sqrt{\frac{Gm_{\rm b}}{a_{\rm b}}}, \tag{1.9}$$

that corresponds to $v_{\rm b} \simeq 10^2$ km s^{-1} for, e.g., an equal mass system of $m_{\rm b} = 4 + 4\,M_\odot$ with semi-major axis $a_{\rm b} = 0.5$ AU. For a SMBH of $4 \times 10^6 M_\odot$ (Gillessen et al., 2017), the orbital velocity of the same stellar binary at the disruption radius is:

$$v = \sqrt{\frac{GM_{\rm BH}}{r_{\rm bt}}} \simeq 10^4\,{\rm km\,s^{-1}} . \tag{1.10}$$

Thus, when the binary is tidally disrupted, the stars have a relative motion of order $v_{\rm b}$ and their specific energy changes by $\delta E = 1/2(v + v_{\rm b})^2 - 1/2v^2 \simeq v v_{\rm b}$ (Hills, 1988; Yu and Tremaine, 2003). Because of the conservation of energy, the ejected star gets a final velocity at infinite distance from the SMBH of $v_{\rm ej} = \sqrt{2 v v_{\rm b}}$ that, for the example here considered, corresponds to $\simeq 10^3$ km s^{-1}.

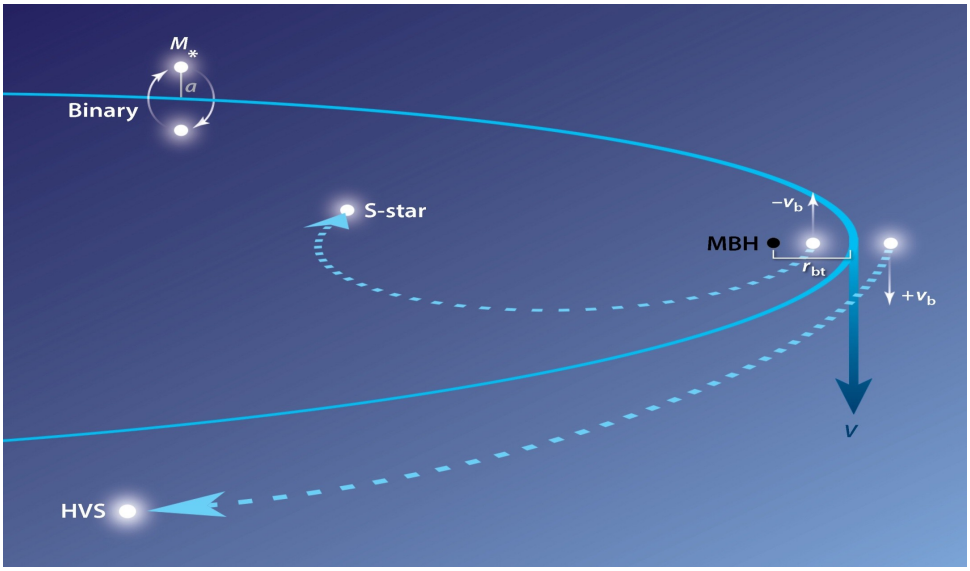

Figure 1.7. Schematic illustration of the Hills mechanism. The Figure is reproduced from Brown (2015).

HVS ejection velocities at infinite distance from the SMBH can be predicted with higher detail with numerical simulations. Simulating HVSs ejected after a 3-body encounter between an equal mass binary and a SMBH, Bromley et al. (2006) obtain a final velocity distribution at infinite distance from the black hole whose mean value is:

$$v_{\rm ej} = 1{,}370\,{\rm km\,s^{-1}} \left(\frac{a_{\rm b}}{0.1\,{\rm AU}}\right)^{-1/2} \left(\frac{m_{\rm b}}{{\rm M}_\odot}\right)^{1/3} \left(\frac{M_{\rm BH}}{4\times10^6\,{\rm M}_\odot}\right)^{1/6} f_R, \tag{1.11}$$

where f_R is a factor of order unity that depends on $R_{\rm p}$, the periapse distance to the SMBH. For an unequal-mass binary, the ejection velocities of the primary star (with mass m_1) and secondary star (with mass m_2) are respectively:

$$v_1 = v_{\rm ej}\left(\frac{2\,m_2}{m_1+m_2}\right)^{1/2}, \quad v_2 = v_{\rm ej}\left(\frac{2\,m_1}{m_1+m_2}\right)^{1/2}. \tag{1.12}$$

The Hills mechanism is illustrated in Fig. 1.7.

The periapse distance to the SMBH and the semi-major axis of the stellar binary determine on the probability of ejection,

$$P_{\rm ej} = 1 - D/175, \tag{1.13}$$

where

$$D = \left(\frac{R_{\rm p}}{a_{\rm b}}\right)\left(\frac{10^6\,m_{\rm b}}{2M_{\rm BH}}\right)^{1/3} \tag{1.14}$$

and $0 \leq D \leq 175$ (Hills, 1988; Bromley et al., 2006). For D $\geq$ 175, the binary does not approach close enough to the SMBH to produce an ejection. The ejection probability as a function of D parameter is shown in Fig. 1.8.

The stellar binaries encounter the SMBH with a rate that depends on the timescale at which they are scattered into the SMBH "loss cone", namely the subset of Galactic center orbits with low angular momentum that pass close to the SMBH. The stars in the loss cone are rapidly eliminated and, thus, the steady-state encounter rate between the SMBH and the stars depends on the dynamical processes that refill the "empty loss

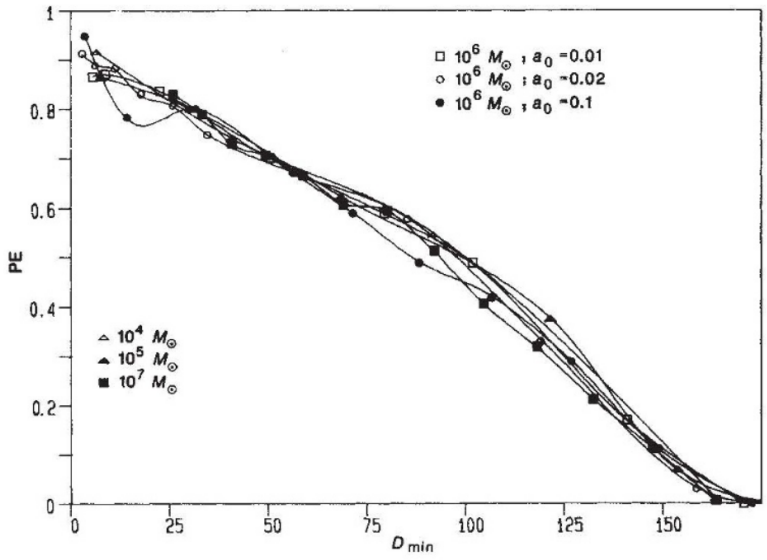

Figure 1.8. Ejection probability, PE, as a function of D parameter. The curves are labeled by the mass of the SMBH and the semi-major axis of the binary. An equal mass binary of mass $m_{\rm b} = 2\,M_{\odot}$ is used in all simulations. The Figure is reproduced from Hills (1988).

cone". The rate, R, at which HVSs are ejected from the Galactic center is then affected by the rate of the encounters between the binaries and the SMBH.

In his work of 1988, Hills finds a theoretical HVSs ejection rate of $\sim 10^{-3} - 10^{-4}\,{\rm yr}^{-1}$ from the simulated number of stellar binaries, with semi-major axis $a_{\rm b} = 0.1 - 1$ AU, that encounter the SMBH in a full loss cone. This ejection rate decreases when an empty loss cone is considered. Assuming that the loss cone is replenished by the two-body relaxation, namely the gravitational encounter in which a star orbit is altered due to the gravitational interaction with another star, Yu and Tremaine (2003) estimate an HVS ejection rate $R \sim 10^{-5}(\eta/0.1)\,{\rm yr}^{-1}$, with η the fraction of stars in binaries with semi-major axis $a_{\rm b} \lesssim 0.3$ AU. However, because other processes can also fill the loss cone (e.g., Merritt and Poon, 2004; Hopman and Alexander, 2006; Perets et al., 2007), the above estimate likely represents a lower limit. Bromley et al. (2012) assume continuous star formation and steady, random scattering of binary stars toward the Galactic center: they estimate an ejection rate $R \approx 1 - 2 \times 10^{-3}$ yr^{-1} when integrating over all the mass spectrum of the ejected stars considered. However, if the assumption of continuous star formation is dropped, the ejection rate decreases to $\sim 2 - 8 \times 10^{-5}$ yr^{-1}. Zhang et al. (2013) consider different origins of the injected binaries (both from stellar disks and from infinity) and different models of the Initial Mass Function of the primary stars. Comparing their simulations with the observed S-stars in the Galactic Center and the B-type HVSs in the Galactic halo, they find the best match for models with HVS ejection rates of $10^{-5} - 10^{-4}\,{\rm yr}^{-1}$.

HVSs are ejected isotropically from the Galactic center in the pure radial direction. Then, they start their travel through the MW gravitational potential, during which they are decelerated and they acquire non-null tangential velocities. Indeed, their radial trajectory is bent by the non-spherical components of the Galactic potential or by satellite galaxies orbiting the MW (Kenyon et al., 2018; Boubert et al., 2020). HVSs thus represent a powerful tool to investigate the MW gravity. However, not all the stars ejected according to the Hills mechanism are unbound to the MW; there is a population of stars whose ejection velocity is not high enough to enable them to escape the gravitational field of the Galaxy: these stars are called "bound HVSs" (Bromley et al., 2006; Kenyon

et al., 2008). For bound HVSs, lower ejection velocities and longer lifetimes imply larger number of orbits traced by the stars around the Galactic center. Thus, in order to use HVSs to investigate the MW gravity, proper selection criteria must be applied to exclude bound HVSs whose acquired tangential velocities can be extremely high independently from the non-spherical components of the Galactic potential that bent their trajectory (See Sects. 2.2.2 and 3.4.2).

1.5.2 Alternative mechanisms

After the formulation of the Hills mechanism and the prediction of the existence of hypervelocity stars (Hills, 1988), alternative scenarios for the generation of HVSs were proposed:

- three-body interactions between a single star and a binary BH can lead to the ejection of stars as HVSs (Yu and Tremaine, 2003). Differently from the Hills mechanism, in this scenario, the HVS ejection is not isotropic and it is flattened along the plane of the orbital motion of the binary black holes. However, ejections are expected to become more and more isotropic as the binary SMBH hardens (Sesana et al., 2006). A variant of the binary SMBH is a binary system composed of an intermediate mass black hole (IMBH) and a SMBH; observations in the Galactic center cannot exclude the presence of an IMBH less massive than $10^4 M_\odot$ orbiting Sgr A* (Reid and Brunthaler, 2004). A study of Rasskazov et al. (2019) shows that, on average, the ejection velocities of HVSs produced by this mechanisms are slower than that obtained according to the Hills mechanism.

- the scattering of a star off a stellar-mass BH orbiting a SMBH can lead to the ejection of HVSs (O'Leary and Loeb, 2008); the stars within 0.1 pc from Sgr A* are expected to encounter a cluster of stellar-mass BHs that have segregated to that region. Ejections occurs when a star is scattered off an orbiting BH and kicked out of the Galactic center; the ejection velocities can reach the ~ 2000 km s^{-1}.

- the interaction between a globular cluster and a SMBH binary can produce HVSs (Fragione and Capuzzo-Dolcetta, 2016); in this scenario some stars of the cluster can reach high velocities as the combined result of the extraction of their gravitational binding energy and the slingshot due to the interaction with the SMBH binary.

- a four-body interaction between a binary star and a binary SMBH can eject both single HVSs and binary HVSs. The HVS ejection rate is enhanced for the largest mass ratio SMBH-SMBH binaries (Wang et al., 2018).

- the production of HVSs in the interaction of an active galactic nucleus (AGN) jet from the central SMBH with a dense molecular cloud has been proposed as an alternative to the above mentioned stellar dynamical mechanisms for the production of HVSs (Silk et al., 2012);

However, as noted by Brown (2015), among the mechanisms proposed for the HVS production, the Hills mechanism has a unique ability in generating a large number of unbound main-sequence stars and in explaining the presence of the so-called S-stars (see Fig. 1.9) in close orbit around the central SMBH (e.g., Ghez et al., 2003, 2005; Gillessen et al., 2009, 2017; Genzel et al., 2010).

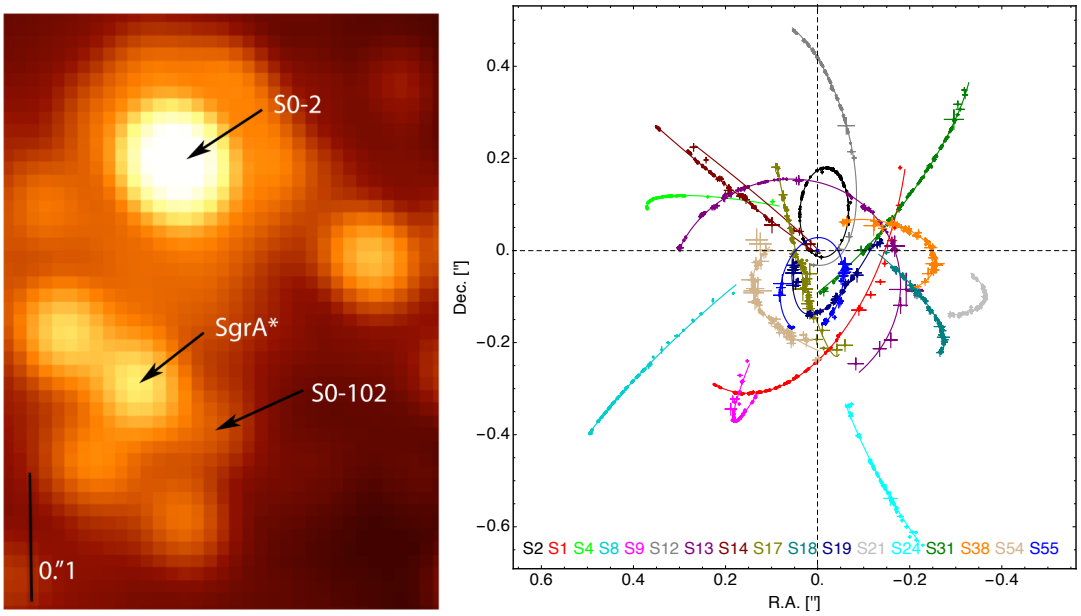

Figure 1.9. *Left panel*: S-stars S0-2 and S0-102 near Sgr A*. The image was taken at a wavelength of 2.12 μm. The Figure is reproduced from Meyer et al. (2012). *Right panel*: The astrometric data for the 17 stars used for the multi-star fit, shown together with the best-fitting orbits from the multi-star fit (solid lines). The Figure is reproduced from Gillessen et al. (2017).

1.5.3 Observations: state of the art and challenges

On the observational side, it was W. R. Brown who serendipitously discovered the first HVS candidate (HVS1): a B-type star escaping the MW with a heliocentric radial velocity of 831 ± 6 km s^{-1}, corresponding to a galactocentric velocity of at least 673 km s^{-1}, that enables the star to escape the MW gravitational potential (Brown et al., 2005).

Many HVS candidates were later found in both targeted and not targeted surveys (e.g., Hirsch et al., 2005; Edelmann et al., 2005; Brown et al., 2006a,b, 2007a,b, 2009, 2012, 2014; Tillich et al., 2011; Li et al., 2012, 2015; Pereira et al., 2013; Zheng et al., 2014; Huang et al., 2017; Neugent et al., 2018; Du et al., 2019; Luna et al., 2019; Koposov et al., 2020; Li et al., 2021). The fastest star, S5-HVS1, has a heliocentric radial velocity of 1017 km s^{-1} corresponding to a galactocentric velocity of 1755 km s^{-1}(Koposov et al., 2020), while other observed stars have speeds smaller than the Galactic escape velocity and are, thus, bound HVSs.

For example, the Hypervelocity Star Survey (Brown et al., 2006a,b, 2007a,b, 2009, 2012, 2014) is a spectroscopic survey of halo stars complete over 12,000 deg^2 of sky that selects for B-type stars by broadband color only, while no kinematic selection criteria are applied to the sample. The HVS Survey identifies 21 unbound late B-type stars in the halo that are significantly unbound from the Galaxy in radial velocity alone and that are traveling in an outward trajectory (consistently with an ejection from the Galactic center). These unbound stars are identified as $2.5 - 4\,M_\odot$ main-sequence stars at a galactocentric distances of $50 - 120$ kpc: stars of this mass should not be found at faint magnitudes in the outer halo, unless they were ejected as hypervelocity stars. The HVS Survey also includes a comparable number of bound HVS candidates with galactocentric velocities of ~ 300 km s^{-1} in the outer halo. Figure 1.10 shows the Galactic rest frame velocity of the stars in the HVS Survey as a function of the galactocentric distance: unbound HVSs are marked by magenta stars, while possible bound HVSs are marked by blue circles. Other HVS candidates are classified as A type stars or as F, G, or K type stars like those found

by Li et al. (2015).

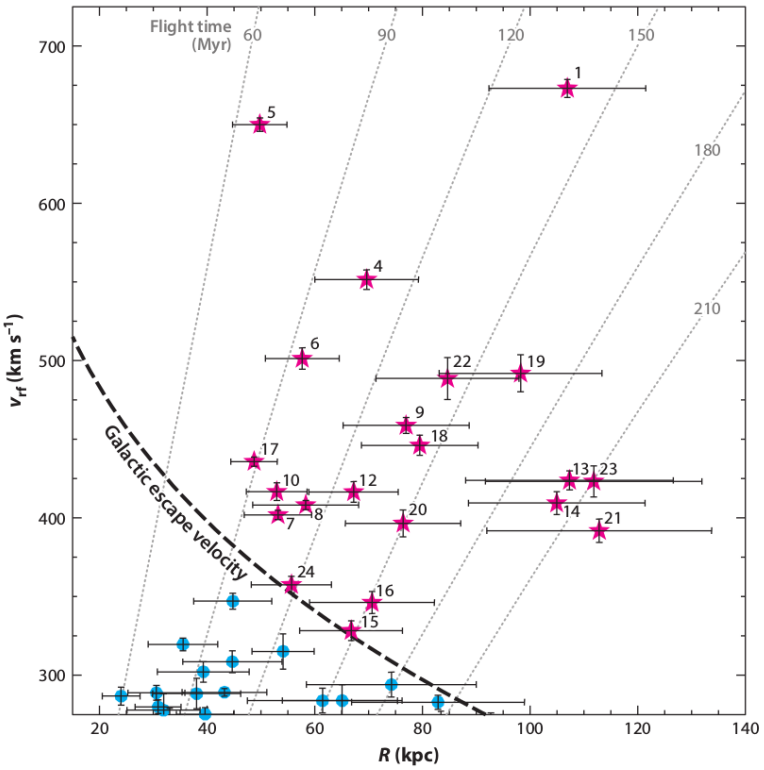

Figure 1.10. Observed Galactic rest frame velocity $v_{\rm rf}$ and galactocentric distance R of late B-type stars in the Hypervelocity Star Survey. The dashed line is the Galactic escape velocity from the model by Kenyon et al. (2008). Dotted grey lines are isochrones of flight time from the Galactic Center. Unbound HVSs are marked by magenta stars, while possible bound HVSs are marked by blue circles. The Figure is reproduced from Brown (2015).

We live in the Gaia era (e.g., Gaia Collaboration, 2016b,c,a, 2018b,a, 2021) and in the last years several studies have been conducted to forecast the number of HVSs that Gaia can detect by the end of the mission (Marchetti et al., 2018), search for new HVSs candidates (e.g., Marchetti et al., 2017; Bromley et al., 2018; Marchetti et al., 2019; Marchetti, 2021), and revalue the classification of a star as HVS candidate based on the improved accuracy on proper motions provided by Gaia (e.g., Boubert et al., 2018; Brown et al., 2018; Irrgang et al., 2018; Erkal et al., 2019; Kreuzer et al., 2020; Irrgang et al., 2021). The birth place of the HVS candidates is indeed uncertain and some of them may actually be:

- runaway stars ejected from the Galactic disk. There are two proposed mechanisms for the ejection of runaways: (i) the supernova ejection mechanism, in which the runaway is ejected from a binary stellar system when its former companion explodes as a supernova; in this scenario, the maximum possible ejection velocity is given by the sum of the supernova kick and the orbital velocity of the progenitor binary (Blaauw, 1961); (ii) the dynamical ejection mechanism, according to which the runaway is ejected by dynamical 3-body or 4-body interactions in a young star cluster (Poveda et al., 1967) with a maximum possible ejection velocity set by the escape velocity of the most massive star (Leonard, 1991);
- halo stars outliers whose velocities can reach 450 km s^{-1} (Smith et al., 2009b);
- fast halo stars, that can be unbound to the MW, produced by a tidal interaction

between a dwarf galaxy and the MW near the Galactic center (Abadi et al., 2009). For example, the star J1443+1453, with a velocity larger than the escape speed at its position, may have been tidally stripped from the Sgr dSph (Huang et al., 2021);

- stars of extragalactic origin ejected as either HVSs or runaway stars from the nearest satellite galaxies of the MW, as the Large Magellanic Cloud (LMC) (Boubert and Evans, 2016; Boubert et al., 2017). For example, the high galactocentric rest frame velocity of the star J1443+1453 may also be explained with an ejection from the Sgr dSph due to a gravitational slingshot effect involving a SMBH, an IMBH or a massive PBH (Huang et al., 2021).

To confirm the genuine HVS nature of a candidate, it is thus of the utmost importance to prove its galactocentric origin. The metallicity of the HVS candidates or their spatial distribution may be used, together with their high speed, to prove a galactocentric origin. Indeed, for example, the fastest runaways stars are ejected in the direction of Galactic rotation, with simulations predicting 90% of hyper-runaways (i.e., runaways unbound to the Galaxy) at Galactic latitudes $b < 30^\circ$ (Bromley et al., 2009); on the contrary, the Hills mechanism predicts an isotropic ejection. Moreover, runaway star velocities are limited to the escape velocity from the surface of the stars, while HVS velocities can, in certain cases, exceed this limit. The origin of an HVS candidate is usually investigated through a backtracking of the star trajectory in a chosen gravitational potential (e.g. Brown et al., 2014, 2018; Marchetti et al., 2019; Irrgang et al., 2018; Koposov et al., 2020; Kreuzer et al., 2020; Irrgang et al., 2021). Thus, the identification of genuine HVSs depends on the gravitational potential assumed for the Galaxy. For this reason, the use of HVSs to constrain the MW gravitational potential generates a circularity problem (see Sects. 2.7, 3.5.3, and 4).

From the available literature, we estimate a sample of $\sim$ 70 HVS candidates whose galactocentric origin has not been unambiguously ruled out. This sample includes both unbound and bound HVS candidates, that make up $\sim$ 40% and $\sim$ 60% of the full sample, respectively. These HVS candidates are the result of heterogeneous classification methods, and the number of true HVSs remains uncertain until the galactocentric origin of these stars is unambiguously confirmed.

Chapter 2

Probing the shape of the Milky Way dark matter halo with hypervelocity stars: a new method [1]

The shape of DM halos that surround galaxies in the ΛCDM model is one of the testable predictions of this model, as illustrated in Sect. 1.4. As reviewed in Sect. 1.4.3 this prediction has been largely tested on our Galaxy, in the last decades, through a number of projects aimed at constraining the shape of its DM halo. Those tests use different tracers of the Galactic gravitational potential, hold on different spatial scales, and are not all consistent with one another. Among the tracers that can be used to probe the MW DM halo, there are hypervelocity stars (HVSs) As described in detail in Sect. 1.5, HVSs are ejected from the Galactic center and their present-day speeds can exceed the Galactic escape velocity. HVSs may reach the outer regions of the Galaxy and are thus powerful probes of the MW mass distribution. Since the discovery of the very first HVS candidate (Brown et al., 2005), the HVSs have been recognized as a powerful tool to probe either the shape of the Galactic DM halo (Gnedin et al., 2005; Yu and Madau, 2007), or its mass (Rossi et al., 2017; Fragione and Loeb, 2017), or both (Contigiani et al., 2019). They were also used to discriminate among different models of the Galactic potential in Newtonian gravity (Perets et al., 2009) and between different theories of gravity (Perets et al. 2009; see also our work Chakrabarty et al. 2022, presented in Chpt. 3).

In this Chapter, we use HVSs as tracers of the shape of the MW DM halo. We assume that Newtonian gravity holds on Galactic scales, we fix the mass of the DM halo, and we use the kinematical properties of the HVSs to constrain the triaxiality parameters of the dark halo. We account for neither the gravitational effects of the LMC on the HVS trajectories (Kenyon et al., 2018) nor the time dependence of the gravitational potential of the MW due to its interaction with the LMC (Boubert et al., 2020). Because the HVSs are ejected radially with high speed and may cross the entire Galaxy before dying out, in an isolated MW, the small, typically a few per cent, deviations from straight lines of their trajectories are determined by the asphericity of the MW gravitational potential well, dominated by the DM halo at large galactocentric distances.

Previous studies aimed at constraining the shape of the gravitational potential of the dark halo with HVSs made use of (i) sufficiently accurate ($\sigma_\mu \lesssim 10$ μas yr^{-1}) proper motion measurements of either one observed HVS with known distance or a set of two or

[1] The results presented in this chapter are published in our work Gallo et al. (2022)

more HVSs with unknown distance, with the constraints becoming tighter for larger samples of observed HVSs (Gnedin et al., 2005); (ii) a triaxiality estimator that is a function of the components of the specific angular momentum of HVSs located at galactocentric distances $r \gtrsim 50$ kpc (Yu and Madau, 2007); (iii) a likelihood function constructed by back-propagating the phase-space position of each HVS to the Galactic center, in order to reproduce its observed phase-space coordinates and mass (Contigiani et al., 2019).

The above methods have been applied to triaxial (Gnedin et al., 2005; Yu and Madau, 2007) or axysimmetric (Contigiani et al., 2019) DM halos. The techniques used by Gnedin et al. (2005) and Contigiani et al. (2019) do not depend on the model of the potential assumed for the DM halo, but require the integration of the HVS trajectories; conversely, the angular-momentum technique designed by Yu and Madau (2007) does depend on the dark halo potential, but does not require the trajectory integration. In all these models, the shape of the DM halo potential is constant with radius. Furthermore, all the techniques require intermediate steps that involve each HVS of the sample individually, even though the final result depends on the contribution of all the HVSs of the sample.

Here we present a new statistical method to constrain the axis ratios of a distance-dependent, triaxial DM halo potential from the distributions of the HVS observables that are mostly affected by the asphericity of this potential, namely the components of the galactocentric tangential velocities. Differently from the techniques illustrated above, our method does not require intermediate steps that involve each star of the sample, such as the trajectory integration or the evaluation of the angular momenta of the HVSs; it can be applied to different models of the MW gravitational potential (as it is the case for the methods by Gnedin et al. (2005) and Contigiani et al. (2019)); it is not degenerate in the axis ratios.

The Chapter is organized as follows. In Sect. 2.1, we describe our numerical simulations of the initial velocity distribution of a sample of HVSs ejected according to the Hills mechanism, and the simulations of the HVS trajectories in a Galactic gravitational potential generated by DM halos with different shapes; we also illustrate the construction of our HVS phase space mock catalogs. In Sect. 2.2, we show how the asphericity of the DM halo mostly affects the HVS tangential velocity: we identify this velocity as the key variable to statistically discriminate between different shapes of the DM halo, and we select the appropriate HVS sample to pursue this goal. In Sect. 2.3, we present our statistical method to recover the shape of the DM halo from a distribution of HVS tangential velocities. In Sects. 2.4 and 2.5, we show the results of the application of our method to an ideal sample of mock observed HVSs with null uncertainties and no observational limitations that traveled in an axisymmetric and non-axisymmetric Galactic gravitational potential, respectively. In Sect. 2.6, we investigate the effect of the size of the ideal sample of mock observed HVS on the success rate of our method. We finally discuss our results and conclude in Sects. 2.7 and 2.8.

2.1 Numerical simulations and mock catalogs

In Sect. 2.1.1, we illustrate the generation of the distribution of the initial velocities of HVSs ejected with the Hills mechanism, illustrated in Sect. 1.5.1. In Sect. 2.1.2, we describe our model for the gravitational potential of the MW, generated by the baryonic components and a DM halo with different shapes, and in Sect. 2.1.3 we illustrate the simulation of the trajectories of the ejected HVSs across the Galaxy. Finally, in Sect. 2.1.4, we describe the mock catalogs that we built from the HVS phase space distribution.

2.1.1 Ejected stars: velocity distribution

Following Hills (1988) (see also Bromley et al., 2006), we simulated the ejection of stars from the Galactic Center with a 3-body numerical code which reproduces the gravitational interaction of a binary star system with the SMBH associated with SgrA*. For the ejected stars, our code provides the distribution of the ejection velocities, $v_{\rm ej}$. A detailed description of the code will be provided in a separate paper.

We set the mass of the SMBH to $4 \times 10^6 M_\odot$, consistent with different estimates (e.g., Boehle et al., 2016; Gillessen et al., 2017). For simplicity, we restricted our simulations to equal-mass stellar binaries of $4 + 4$ $M_\odot$ on hyperbolic orbits. The mass of 4 $M_\odot$ is representative of the upper end of the mass distribution of the HVS candidates observed in currently available surveys (see references in Sect. 1.5.3). We will further discuss our mass choice in Sect. 2.7.

For a fixed mass of the binary members, the velocity distribution of the ejected stars depends upon a series of parameters: (i) the stellar binary semi-major axis, a; (ii) the minimum approach distance, $R_{\rm min}$, between the center of mass of the binary and the SMBH; (iii) the inclination angle, i, between the orbital plane of the binary star and the orbital plane of the binary's center of mass and the SMBH; (iv) the initial phase, ϕ, of the binary star. We randomly sample i and ϕ in the interval $[0, 2\pi]$ with uniform probability density function. As for a and $R_{\rm min}$, which determine the probability of ejection of the primary star, we randomly sampled a from the interval $0.05 - 4$ AU with probability density function $p(a) \propto 1/a$, and we randomly drew $R_{\rm min}$ from the interval $1 - 700$ AU with probability density function $p(R_{\rm min}) \propto 1/R_{\rm min}$ (Bromley et al., 2006, and references therein).

Figure 2.1 shows the ejection velocity distribution for a simulation of $N_{\rm int} \sim 240{,}000$ 3-body interactions that produces $N_{\rm ej} = 60{,}000$ ejection events. Most of the ejected stars possess ejection velocities in the range $\sim 250{-}4{,}000$ km s^{-1}; the velocity distribution has a major peak at $v_{\rm ej} \sim 510$ km s^{-1} and has positive skewness. A minority of stars are ejected with speeds lower than ~ 250 km s^{-1}: these stars are the result of rare, double-ejection events, where neither of the binary members becomes gravitationally bound to the SMBH, and both stars are ejected. Because we assumed that the binary system starts its approach trajectory towards the SMBH with a velocity at infinity $v_{\rm inf} = 250$ km s^{-1} (Hills, 1988), energy conservation requires that one of these stars is ejected with velocity lower than 250 km s^{-1}. Our distribution of ejection velocities is comparable to the ejection speed distribution obtained from the analytical prescription by Bromley et al. (2006).

We note that the ejection velocity $v_{\rm ej}$ is defined as the speed that an ejected star would have at infinite distance from the SMBH, in absence of other gravitational sources (Hills, 1988; Bromley et al., 2006), as in our 3-body simulation. However, the ejection velocity distribution shown in Fig. 2.1 can be used as a distribution of initial velocities when simulating the trajectories of the HVSs from the Galactic center to the outer halo, as we explain in Sect. 2.1.3.

2.1.2 Milky Way gravitational potential

We modeled the Milky Way gravitational potential Φ as the superposition of the potentials generated by three distributions of baryonic matter and one distribution of dark matter:

$$\Phi = \Phi_{\rm BH} + \Phi_{\rm b} + \Phi_{\rm d} + \Phi_{\rm h}, \tag{2.1}$$

where $\Phi_{\rm BH}$ is the potential generated by the SMBH located in the Galactic Center, $\Phi_{\rm b}$ is generated by the Galactic bulge, $\Phi_{\rm d}$ is the disk potential, and $\Phi_{\rm h}$ is the potential of the

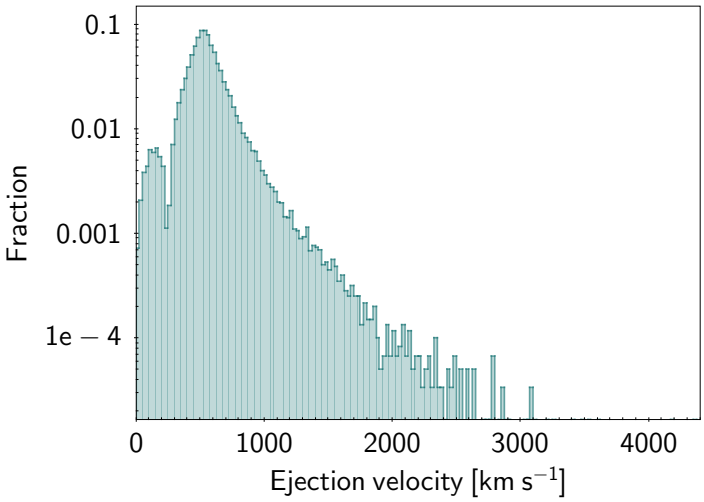

Figure 2.1. Distribution of ejection velocities for the ejected star(s) of a $4 + 4\ M_\odot$ binary star system, after a close encounter with a $4 \times 10^6\ M_\odot$ SMBH. The distribution consists of $N_{\rm ej} = 60{,}000$ stars ejected in $N_{\rm int} \sim 240{,}000$ 3-body interactions.

dark matter halo embedding the Galaxy. We consider the Galaxy as isolated, neglecting both the presence of the LMC (Kenyon et al., 2018) and any time dependence of the Galactic potential deriving from the interaction of the MW with the LMC (Boubert et al., 2020).

In a reference frame with the origin at the Galactic Center, we used spherical coordinates (r, ϑ, φ) for the spherically symmetric components of the potential (with $-90° \leq \vartheta \leq 90°$), cylindrical coordinates (R, φ, z) for the axisymmetric components, and Cartesian coordinates (x, y, z) for the triaxial component. We took the x-y plane as the equatorial plane of the disk, with the x-axis corresponding to the direction from the Sun to the Galactic center, and we took the z-axis as the vertical axis.

We included the contribution of the SMBH to the gravitational potential as:

$$\Phi_{\rm BH}(r) = -\frac{G\, M_{\rm BH}}{r}, \tag{2.2}$$

where $M_{\rm BH}$ is the mass of the SMBH.

For the bulge component, we adopted the Hernquist (1990) potential:

$$\Phi_{\rm b}(r) = -\frac{G\, M_{\rm b}}{r + r_{\rm b}}, \tag{2.3}$$

where $M_{\rm b} = 3.4 \times 10^{10}\ M_\odot$ and $r_{\rm b} = 0.7$ kpc (Kafle et al., 2014; Price-Whelan et al., 2014; Rossi et al., 2017; Contigiani et al., 2019) are the scale mass and the scale radius of the model, respectively.

For the disk component, we adopted the axisymmetric potential by Miyamoto and Nagai (1975):

$$\Phi_{\rm d}(R, z) = -\frac{G\, M_{\rm d}}{\sqrt{R^2 + \left(a_{\rm d} + \sqrt{z^2 + b_{\rm d}^2}\right)^2}}, \tag{2.4}$$

where $M_{\rm d} = 1.0 \times 10^{11}\ M_\odot$, $a_{\rm d} = 6.5$ kpc and $b_{\rm d} = 0.26$ kpc (Kafle et al., 2014; Price-Whelan et al., 2014; Rossi et al., 2017; Contigiani et al., 2019) are the scale mass and the scale lengths of the model, respectively.

Finally, we modeled the contribution of the DM halo with the triaxial generalization of the spherically symmetric NFW (Navarro et al., 1997) potential proposed by Vogelsberger et al. (2008):

$$\Phi_{\rm h}(\tilde{r}) = -\frac{G\,M_{200}}{f(C_{200})}\,\frac{\ln\left(1+\frac{\tilde{r}}{r_{\rm s}}\right)}{\tilde{r}}\,, \tag{2.5}$$

where $f(w) = \ln(1+w) - w/(1+w)$, $M_{200} = 8.35\times10^{11} M_{\odot}$ is the DM halo mass enclosed within r_{200},[2] $C_{200} = r_{200}/r_s = 10.82$ is the halo concentration parameter, and $r_{\rm s} = 18$ kpc is a generalized scale radius. For the above parameters, we adopted the values used by Hesp and Helmi (2018), that are consistent with the values derived from halo stars (Xue et al., 2008), blue horizontal branch stars (Deason et al., 2012a), the massive satellite population of the MW (Cautun et al., 2014), and Cepheids (Ablimit et al., 2020). The coordinate $\tilde{r}$ is a generalized radius that replaces the radius r of the NFW spherical potential,

$$\tilde{r} = \frac{(r_{\rm a}+r)\,r_{\rm E}}{r_{\rm a}+r_{\rm E}}\,. \tag{2.6}$$

Here, $r_{\rm E}$ is an "ellipsoidal radius",

$$r_{\rm E} = \sqrt{\frac{x^2}{a^2}+\frac{y^2}{b^2}+\frac{z^2}{c^2}}\,, \tag{2.7}$$

where the three ellipsoid parameters, a, b, and c have to fulfill the condition $a^2+b^2+c^2 = 3$, and their combination defines the degree of triaxiality of the potential well. Specifically, the axis ratio of the equipotential surfaces on the x-y plane is $q_y = b/a$, whereas the axis ratio of the equipotential surfaces on the x-z plane is $q_z = c/a$. The parameter $r_{\rm a}$ is the scale length where the smooth transition from a triaxial potential to a nearly spherical potential occurs; we took it to be $1.2r_{\rm s}$, as in Hesp and Helmi (2018): the halo is triaxial ($\tilde{r} \approx r_E$) in the inner region ($r \ll r_a$), whereas it is approximately spherical ($\tilde{r} \approx r$) in the outer region ($r \gg r_a$).

In general, the potential $\Phi_{\rm h}(\tilde{r})$ given by Eq. 2.5 is triaxial with $q_y \neq 1$, $q_z \neq 1$, and $q_y \neq q_z$. However, this potential becomes spheroidal when either q_y or q_z are equal to 1 or when $q_y = q_z \neq 1$: when $q_y = 1$, the potential is axisymmetric about the z-axis; when $q_z = 1$, the potential is axisymmetric about the y-axis; when $q_y = q_z \neq 1$ the potential is axisymmetric about the x-axis. When both q_y and q_z are equal to 1, the DM halo potential is spherically symmetric.

Because $\Phi_{\rm BH}$ and $\Phi_{\rm b}$ are spherically symmetric, and $\Phi_{\rm d}$ is axisymmetric about the z-axis, our gravitational potential Φ (Eq. 2.1) is globally axisymmetric about the z-axis when the DM halo is either spherical or spheroidal and axisymmetric about the z-axis. On the other hand, the Galactic gravitational potential is non-axisymmetric when the DM halo is either triaxial or spheroidal with a symmetry axis misaligned with respect to the z-axis.

In all of our simulations, we adopted the same parameters for the SMBH, the bulge, and the disk potentials (Eqs. 2.2-2.4). We also adopted the same parameters for the potential of the DM halo (Eq. 2.5), with the exception of (i) the triaxiality parameter q_z, which was set to a different value in each of the simulations of the axisymmetric Galactic potential, while q_y was kept fixed to 1, and (ii) both triaxiality parameters, q_y and q_z, in simulations of a non-axisymmetric Galactic potential. By varying the triaxiality

[2] r_{200} is the radius of a spherical volume whose mean mass density is 200 times the critical density of the Universe

parameter of the DM halo q_y and q_z in appropriate ranges of values, we explored the effect of the halo shape on the HVS observables.

Figure 2.2 shows the magnitude of the radial gravitational acceleration in the plane of the disk associated with our MW potential Φ as a function of the cylindrical coordinate R, for a spherical DM halo ($q_y = 1, q_z = 1$). The chosen gravitational potential generates masses enclosed within 120 pc and within 100 kpc that agree with the observed values derived by Launhardt et al. (2002) and reported in Dehnen and Binney (1998), respectively. It also reproduces a circular velocity of 235 km s^{-1} at the solar neighborhood, in agreement with the observational values of 231 ± 6 km s^{-1} by Bobylev (2017) and of 230 ± 12 km s^{-1} by Bobylev and Bajkova (2016).

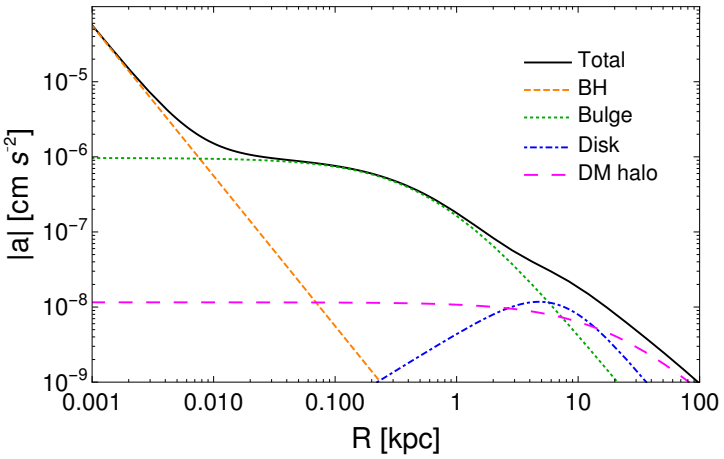

Figure 2.2. Magnitude of the radial gravitational acceleration in the plane of the disk due to our MW potential Φ (Eq. 2.1), as a function of the radial cylindrical coordinate R. The black solid line represents the total gravitational acceleration. The dashed and dotted lines represent the contributions of the SMBH (dashed orange line), the bulge (dotted green line), the disk (blue dot-dashed line), and a spherical DM halo (magenta long-dashed line).

2.1.3 Orbit integration

In the Galactic gravitational potential illustrated in Sect. 2.1.2, we simulated the time evolution of the position, velocity, and acceleration of a sample of stars ejected from the Galactic Center according to the Hills mechanism (see Sect. 2.1.1). For each star, we numerically integrated Newton's equation of motion in a galactocentric reference frame and in Cartesian coordinates, using the Velocity Verlet algorithm (e.g., Frenkel and Smit, 2001). We traced the star trajectory until the star death. In our simulations, the total energy of a star is conserved with a relative accuracy of $\sim 10^{-8}$.

In Sect. 2.1.1, we showed that our sample of ejected star consists of $N_{\rm ej} = 60{,}000$ HVSs; we adopted this sample as our full sample of initial velocity magnitudes. This choice is legitimate: even though $v_{\rm ej}$ is defined as the speed that an ejected star would have at infinite distance from the SMBH in a 3-body interaction (see Sect. 2.1.1), our SMBH is embedded in the Galactic mass distribution; thus, the ejected stars can be assumed to move at $v_{\rm ej}$ at the outer edge of the sphere of influence of the SMBH, just before the Galactic gravitational potential starts to overcome the SMBH potential. The Hills ejection mechanism yields an isotropic distribution of ejected stars. We thus assigned each of the $N_{\rm ej}$ stars an initial position $(r_0, \vartheta, \varphi)$, with $r_0 = 3$ pc the radius of the sphere of influence of the SMBH (Genzel et al., 2010), and (ϑ, φ) randomly drawn from a uniform distribution over the surface of a sphere; we assigned each star a velocity direction $\hat{n}(\vartheta, \varphi)$. We end up with a sample of $N_{\rm ej}$ initial conditions.

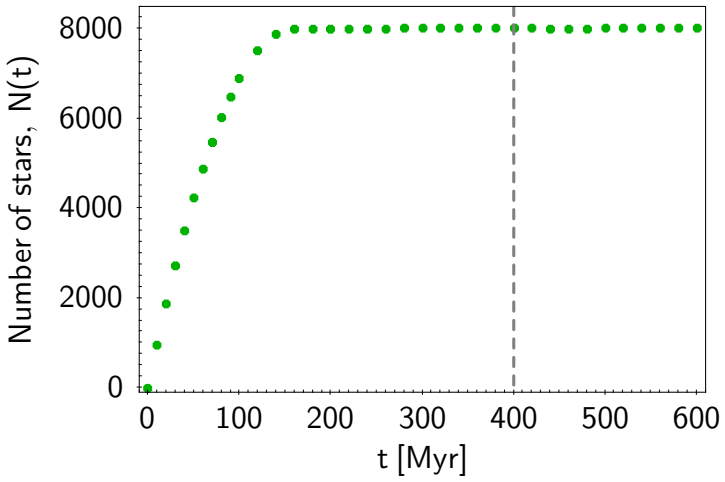

Figure 2.3. The number of 4 $M_\odot$ observable HVSs, that started to be ejected at $t = 0$ at a rate 10^{-4} yr^{-1}, stops increasing beyond $t \simeq \tau_{\rm L} = 160$ Myr. The vertical, dashed line marks the time of the steady state when we chose to observe the system, $t_{\rm obs} = 400$ Myr.

In our simulations below, we computed the trajectories of the HVSs in a large number of different subsamples of size smaller than $N_{\rm ej}$. Each subsample was generated by adopting a random subsample of the $N_{\rm ej}$ initial conditions. Each subsample was selected as follows.

At an average rate $R = 10^{-4}$ yr^{-1}, roughly consistent with the estimate by Bromley et al. (2012) and Zhang et al. (2013) (see also Hills, 1988; Yu and Tremaine, 2003), all the $N_{\rm ej}$ HVSs would be ejected in 600 Myr. We thus assigned the i-th HVS of each subsample an ejection time $t_{\rm ej,i}$ uniformly sampled in the range $0 - 600$ Myr. The stars have a finite lifetime and each star can thus have a different residual lifetime at $t_{\rm ej,i}$. A 4 $M_\odot$ star with Solar metallicity has a main sequence lifetime $\tau_{\rm ms} \simeq 160$ Myr (Schaller et al., 1992; Brown et al., 2006b): we took this lifetime as the total lifetime of the star, $\tau_{\rm L}$. Thus, at the time of ejection, the i-th star is also assigned an age $\tau_{\rm ej,i}$ randomly sampled from a uniform distribution between 0 and $\tau_{\rm L}$.

Figure 2.3 shows that the number $N(t)$ of observable stars, whose lifetime is $\tau_{\rm L}$, reaches a steady state $N(t) \simeq N_{\rm s} \simeq 8000$ at $t \simeq \tau_{\rm L}$. The steady state is the result of the combination of (i) a continuous ejection of stars, with average rate R, and (ii) the finite lifetime of the stars, $\tau_{\rm L}$. We chose to observe our star sample at the observation time, $t_{\rm obs} = 400$ Myr. All the stars whose ejection time was larger than $t_{\rm obs}$ were discarded from the sample. Among the remaining HVSs, we selected the $N_{\rm obs}$ stars that are alive at the observation time $t_{\rm obs}$, namely the stars that satisfy the condition $t_{\rm obs} - t_{\rm ej,i} + \tau_{\rm ej,i} < \tau_{\rm L}$. For these stars, we computed the trajectory through the Galaxy for a travel time $t_{\rm travel,i} = t_{\rm obs} - t_{\rm ej,i}$.

We computed the orbits of the sample of $N_{\rm obs} \simeq N_{\rm s} \simeq 8000$ HVSs in a series of 64 simulations, each of them corresponding to a different combination (q_y, q_z) of the triaxiality parameters of the DM halo (see Sect. 2.1.2). The different combinations were obtained by varying both q_y and q_z in the range $0.7 - 1.4$ in steps of 0.1. A summary of the simulated shapes of the DM halo is reported in Table 2.1.

2.1.4 Mock catalogs A and B

With the simulations described in Sect. 2.1.3, we created two series of mock catalogs, hereafter referred to as mock catalogs A and B. In both series, each mock catalog includes

Table 2.1. Summary of the shapes of the DM halo gravitational potential used to simulate the HVS trajectories.

Shape of the DM halo	Axis of symmetry	Axial ratios	Number of combinations
Spherical	–	$q_y = q_z = 1$	1
Spheroidal	z	$q_y = 1$ & $q_z \neq 1$	7
Spheroidal	y	$q_y \neq 1$ & $q_z = 1$	7
Spheroidal	x	$q_y = q_z \neq 1$	7
Triaxial	none	$q_y \neq q_z$ & $q_y \neq 1$ & $q_z \neq 1$	42

the phase space distribution of $N_{\rm obs}$ HVSs at the observation time $t_{\rm obs}$ in a DM halo with a given shape. However, the two series differ in the initial conditions of the HVSs.

Each mock catalog A was generated with the same set of $N_{\rm obs}$ initial conditions. In other words, all the stars with the same identification index i in all catalogs A are given the same combination $S^i = \{v_{\rm ej},\ \hat{n}(\vartheta,\varphi),\ t_{\rm ej},\ \tau_{\rm ej}\}^i$ of initial conditions, namely the same ejection velocity, ejection time $t_{\rm ej}$, and age $\tau_{\rm ej}$ at ejection. The only difference among these mock catalogs is the set of triaxiality parameters of the DM halo, (q_y, q_z). We used mock catalogs A to highlight the effect of the degree of triaxiality of the DM halo on the distribution of the phase space coordinates of the HVSs, and to identify the phase space coordinates that can serve as shape indicators (Sect. 2.2.1). On the other hand, mock catalogs B were generated with different sets of $N_{\rm obs}$ initial conditions. In other words, the i-th stars in different catalogs B are given a different combination S^i of initial conditions. Therefore, mock catalogs B differ from one another not only for the shape of the DM halo, but also for the sample of ejected stars. We used mock catalogs B to explore the effect of the variation of the initial conditions on the detection of deviations from spherical symmetry of the shape of the DM halo potential (Sect. 2.2.3). We also used catalogs B to implement our method to recover the shape of the DM halo of the MW from real HVS samples (Sect. 2.3).

Each mock catalog A or B includes the positions and the velocities of the $N_{\rm obs}$ bound and unbound HVSs in the galactocentric, the Galactic heliocentric, and the equatorial reference frames, at the observation time $t = t_{\rm obs}$. In our simulations, the star position in the galactocentric reference frame is (r, ϑ, φ) in spherical coordinates and (x, y, z) in Cartesian coordinates, with $\varphi = 0°$ on the x-axis, and $\vartheta = 0°$ on the x-y plane; the star galactocentric velocity is $(v_r, v_\vartheta, v_\varphi)$, with v_r the radial velocity, v_ϑ the latitudinal velocity, and v_φ the azimuthal velocity. We defined as tangential velocity the vector whose components are the latitudinal and the azimuthal velocities: $\vec{v}_{\rm t} = (v_\vartheta, v_\varphi)$; its magnitude is $v_{\rm t} \equiv |\vec{v}_{\rm t}| = (v_\vartheta^2 + v_\varphi^2)^{\frac{1}{2}}$. We show the distribution of the galactocentric distance, as well as the distributions of the galactocentric radial, latitudinal, and azimuthal velocities of the HVSs for one of our mock catalogs in Appendix 2.9.1.

As will be shown at the end of Sect. 2.2.1, we evaluated the possible use of galactocentric, heliocentric, and equatorial phase space coordinates to infer the shape of the dark halo. To this aim, we converted the star phase space coordinates from the galactocentric to the Galactic heliocentric reference frame, by choosing the Sun to be located at $(x, y, z) = (-R_\odot, 0, 0)$ and to have velocity $(U_\odot, V_\odot + \Theta_0, W_\odot)$ in the galactocentric reference frame. We used $R_\odot = 8.277$ kpc (Gravity Collaboration et al., 2022), and our model's rotational velocity at $R_\odot$, $\Theta_0 = 235$ km s^{-1}, in agreement with Bobylev (2017) and Bobylev and Bajkova (2016) (see Sect. 2.1.2). For the velocity of the Sun with respect to the local standard of rest, we used $U_\odot = 11.1$ km s^{-1}, $V_\odot = 12.24$ km s^{-1}, and $W_\odot = 7.25$ km s^{-1} (Schönrich et al., 2010). The equations for the transformation of coordinates and velocities from the galactocentric to the Galactic heliocentric reference

frame, and from the Galactic heliocentric to the equatorial reference frame, are reported in Appendix 2.9.2.

2.2 Indicators of the shape of the DM halo

We used mock catalogs A described in Sect. 2.1.4 to investigate the effect of the triaxiality parameters of the gravitational potential of the DM halo on the HVS phase space distribution. Our final goal was to identify the HVS phase space coordinates (Sect. 2.2.1) and define the HVS samples (Sects. 2.2.1 and 2.2.2) that are best suited to discriminate between different shapes of the DM halo.

2.2.1 Effect of the shape of the DM halo on the HVS phase space distribution

We explored the effect of the triaxiality parameters of the gravitational potential of the DM halo on the phase space distribution of the simulated HVSs, with the goal of identifying the phase space coordinates that are most sensitive to the shape of the DM halo, and can thus be identified as triaxiality indicators. For this purpose, we resorted to mock catalogs A: because these catalogs are all generated with a specific sample of stars, characterized by fixed distributions of initial conditions (Sect. 2.1.4), any significant difference among two of these mock catalogs can only be ascribed to the different triaxiality parameters of the gravitational potential of the DM halo.

For our investigation, from each mock catalog A of $N_{\rm obs}$ stars (see Sect. 2.1.4), we selected a subsample of stars that, at the time of observation $t_{\rm obs}$, are located at galactocentric distances $r > 10$ kpc, where the gravitational effect of the DM halo starts to be relevant (see Fig. 2.2). We also required the stars to possess positive galactocentric radial velocity, $v_{\rm r} > 0$, to match the observational HVS selection criterion. Applying these selection criteria returns, for each mock catalog, a subsample of $N \simeq N_{\rm obs}/10 \simeq 800$ stars. In Sect. 2.2.2 we demonstrate that this reasonable sample selection turns out to be the best selection on the basis of kinematic arguments.

We performed our analysis by means of a statistical approach. Specifically, we made use of the two sample Kolmogorov-Smirnov test (Press et al., 2007), hereafter referred to as "KS test", to check whether the null hypothesis H_0 is true, namely whether the distribution of a given phase space coordinate in a spherical DM halo and the distribution of the same coordinate in a non-spherical DM halo are consistent with being drawn from the same parent population, and are thus indistinguishable. If the p-value of the KS test is $p \leq \alpha$, then H_0 is rejected at the adopted significance level α: in this case, we considered the two distributions as significantly different from each other, and we investigated the use of that phase space coordinate as an indicator of the shape of the DM halo. We adopted a significance level $\alpha = 5\%$.

For our KS tests, we considered the distributions of the components of the star position and velocity in the galactocentric reference frame, in both spherical and Cartesian coordinates, for a series of pairs of DM halos; each halo pair is composed of a spherical DM halo and a non-spherical DM halo with different triaxiality parameters. For the sake of simplicity, we illustrate here the details of our investigation for spheroidal DM halos with $q_y = 1$, namely for spheroidal halos that are axisymmetric about the z-axis and yield a global axisymmetric Galactic potential; we only comment on the case of a non-axisymmetric Galactic potential. This restriction will not imply a loss of generality of our main result. Both the axisymmetric and the non-axisymmetric cases are carefully explored in Sects. 2.4 and 2.5.

We created 50 series of mock catalogs A. Each series consisted of a spherical DM halo and six spheroidal DM halos axisymmetric about the z-axis and with q_z ranging from $q_z = 0.7$ (extremely oblate halo) to $q_z = 1.4$ (extremely prolate halo). The set of initial conditions is the same for each halo in the same series, and differs from one series to the other. We computed the p-values of the KS tests between the distributions of the phase-space coordinates in the spherical halo and those in the spheroidal halos of the same series. Table 2.2 shows the range of these p-values for the 50 series of mock catalogs.

The distributions of the magnitude of the latitudinal velocity, $|v_\vartheta|$,[3] are the only distributions to be significantly different in a spherical DM halo and in a spheroidal DM halo axisymmetric about the z-axis: for DM halos whose gravitational potential well displays a deviation from the spherical shape $|q_z - 1| \geq 0.1$, we always got $p < \alpha$, implying that the null-hypothesis of the KS test could be rejected at the significance level α. In particular, for the largest deviations from the spherical DM halo considered in this work, the p-value is $< 10^{-10}$. On the other hand, for a very mild deviation of the potential well of the DM halo from the spherical shape (i.e., for $|q_z - 1| \leq 0.05$) the distributions of $|v_\vartheta|$ are never significantly different from the spherical case. Finally, for DM halos whose potential well displays a deviation from the spherical shape $|q_z - 1|$ in the range $(0.05 - 0.1)$, the distributions of $|v_\vartheta|$ can either be or not be significantly different from the spherical case, depending on the set of stars' initial conditions used for the generation of mock catalogs A. For example, when $|q_z - 1| = 0.075$, we found p in the range $0.01 - 0.14$ for the case of spherical vs. oblate (with $q_z = 0.925$) DM halo, and p in the range $0.01 - 0.11$ for the case of spherical vs. prolate (with $q_z = 1.075$) DM halo.

For all the distributions of phase space coordinates different from $|v_\vartheta|$, we found $p > 0.7$: we could not reject the null-hypothesis of the KS test at the significance level $\alpha = 5\%$, regardless of the shape of the DM halo. Therefore, we conclude that the magnitude of the HVS latitudinal velocity, $|v_\vartheta|$, is the only phase space coordinate whose distribution can be used to discriminate between a spherical and a spheroidal DM halo axisymmetric about the z-axis.

This result is not surprising. HVSs are ejected radially outward from the Galactic center, but they attain non-zero tangential velocities, $\vec{v}_\mathrm{t}$, as they travel through a non-spherically symmetric potential. In our model (see Eq. 2.1), the potentials of both the SMBH and the bulge are spherically symmetric (see Eqs. 2.2 - 2.3). However, the disk potential (see Eq. 2.4) is axially symmetric about the z-axis. Hence, it contributes to the component of the tangential velocity along the polar angle, that is the latitudinal velocity v_ϑ. When the DM halo is either spherical or spheroidal with axial symmetry about the z-axis, v_ϑ is still the only non-null component of the tangential velocity. In particular, when the DM halo is spherical, only the gravitational pull of the disk induces non-null v_ϑ; on the other hand, when the DM halo is spheroidal with axial symmetry about the z-axis, the gravitational pull of the disk combines with that of the DM halo: in the case of prolate spheroidal DM halo ($q_z > 1$) the pull of the disk is opposite to that exerted by the DM halo, while in the case of oblate spheroidal DM halo ($q_z < 1$) both the disk and the halo attract the stars towards the Galactic plane, leading to higher tangential velocities.

[3] $|v_\vartheta|$ is equivalent to the magnitude of the tangential velocity, v_t, in a spheroidal DM halo axisymmetric about the z-axis.

Table 2.2. Ranges of the p-values of the KS tests between the distribution of the HVS phase space coordinates in a spherical DM halo and those in different spheroidal halos. Each entry shows the ranges of p-values obtained from a sample of 50 series of mock catalogs A. Each series is made of a spherical halo and spheroidal halos with axial symmetry about the z-axis with six different values of the triaxiality parameter q_z. Column 1: HVS phase space coordinate in the galactocentric reference frame. Columns 2-4: p-value of the KS test for a spherical halo compared against a prolate halo (with $q_z = 1.4$, $q_z = 1.1$, $q_z = 1.05$). Columns 5-7: p-value of the KS test for a spherical halo compared against an oblate halo (with $q_z = 0.7$, $q_z = 0.9$, $q_z = 0.95$). A single p-value is shown instead of a p-value range when the relative difference between the limits of the p-value interval is smaller than 10^{-2}. With the adopted 5% significance level, p-values smaller than 5% indicate that the compared distributions are not drawn from the same parent distribution, implying that the corresponding phase space variable can be an indicator of the shape of the DM halo.

Phase space coordinate	p-value (sph. vs. prolate)			p-value (sph. vs. oblate)		
	$q_z = 1.4$	$q_z = 1.1$	$q_z = 1.05$	$q_z = 0.7$	$q_z = 0.9$	$q_z = 0.95$
x	1.00	1.00	1.00	1.00	1.00	1.00
y	1.00	1.00	1.00	1.00	1.00	1.00
z	[0.99 - 1.00]	1.00	1.00	[0.88 - 1.00]	1.00	1.00
r	1.00	1.00	1.00	1.00	1.00	1.00
ϑ	[0.94 - 1.00]	1.00	1.00	[0.71 - 0.99]	1.00	1.00
v_x	[0.98 - 1.00]	1.00	1.00	1.00	1.00	1.00
v_y	[0.98 - 1.00]	1.00	1.00	1.00	1.00	1.00
v_z	[0.93 - 1.00]	1.00	1.00	[0.76 - 0.99]	1.00	1.00
v_r	1.00	1.00	1.00	1.00	1.00	1.00
$v_{\rm t} = \lvert v_\vartheta \rvert$	[6×10^{-22} - 5×10^{-14}]	[2×10^{-4} - 0.01]	[0.06 - 0.44]	[7×10^{-21} - 6×10^{-11}]	[8×10^{-4} - 0.04]	[0.11 - 0.47]

This situation is illustrated in Fig. 2.4, where we show a comparison of the distributions of the magnitude of the latitudinal velocity, $|v_\vartheta|$, for simulated HVSs in a Galaxy with a spheroidal DM halo which is axisymmetric about the z-axis and characterized by an extremely prolate ($q_z = 1.4$), spherical ($q_z = 1$), and extremely oblate ($q_z = 0.7$) shape. The fraction of HVSs with higher $|v_\vartheta|$ is larger in the case of the oblate DM halo (green histogram) than in the case of the spherical DM halo (grey, shaded histogram), because of the concordant gravitational pull of disk and DM halo. Conversely, the fraction of stars with lower $|v_\vartheta|$ is larger in the case of the prolate DM halo (blue histogram) than in the case of the spherical DM halo, because of the opposite pull of disk and DM halo.

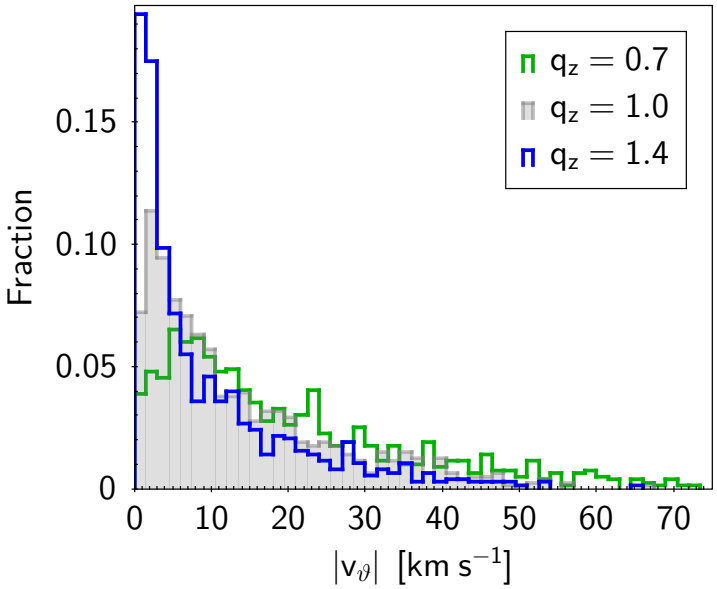

Figure 2.4. Distribution of the magnitude of the HVS galactocentric latitudinal velocity, $|v_\vartheta|$, in a Galaxy with an extremely prolate DM halo ($q_z = 1.4$; blue histogram), a spherical DM halo ($q_z = 1$; grey, shaded histogram), and an extremely oblate DM halo ($q_z = 0.7$; green histogram). The distributions were generated with the same initial conditions (mock catalogs A), to highlight the effect of the different geometries of the DM halo.

The results reported in Table 2.2 show that, while the latitudinal velocity v_ϑ is an indicator of the shape of the DM halo, the polar angle ϑ is not, even though any difference in the distributions of ϑ for stars that have traveled in different DM halos is only determined by the halo shape, as v_ϑ is. This higher sensitivity of v_ϑ to the changes of the shape of the DM halo has two explanations: (i) v_ϑ is the time derivative of ϑ; any variation in v_ϑ implies a variation $\Delta\vartheta$ of the coordinate ϑ over a finite time interval Δt; however, significant $\Delta\vartheta$ can be achieved only over Δt that, on average, are larger than the HVS travel time; (ii) the v_ϑ's are null at the ejection, and the final distribution of v_ϑ is determined by the gravitational potential alone; instead, the distribution of ϑ is uniform in $\cos\vartheta$ at the start: hence, its final distribution is the result of the combination of the initial randomness and of the action of the gravitational potential.

Table 2.2 also shows that neither the Cartesian spatial coordinates nor the Cartesian components of the HVS velocity are significantly affected by the deviation from spherical of the shape of the DM halo; therefore, they are not useful indicators of the triaxiality of the DM halo. This result is expected for the Cartesian spatial coordinates x and y, as well as for the velocity components v_x and v_y, because the gravitational potential is symmetric about the z-axis. On the other hand, for the same reason, the result is not fully expected for z and v_z. However, our simulations show that the projection, on

the z-axis, of any non-null v_ϑ induced by a non-spherical gravitational potential in the star motion is overwhelmed by the projection, on the same axis, of the radial velocity component of the star. If v_z is not a good indicator of the triaxiality of the DM halo, the spatial coordinate z cannot be a good indicator either: as ϑ is less sensitive than v_ϑ to the shape of the DM halo, z is less sensitive to the halo shape than v_z.

The results that we obtained for a spheroidal DM halo symmetric about the z-axis (i.e., for a DM halo with $q_y = 1$ and $q_z \neq 1$) can be extended to the more complex cases of a fully triaxial DM halo and of a spheroidal DM halo with a symmetry axis misaligned with respect to the z-axis (i.e., for a DM halo with $q_y \neq 1$). In those cases, the stars acquire both a non-null latitudinal velocity, v_ϑ, and a non-null azimuthal velocity, v_φ. Therefore, both components of $\vec{v}_\mathrm{t} = (v_\vartheta, v_\varphi)$ can be used as indicators of the triaxiality parameters of the DM halo.

We note that significant differences between the distributions of HVS tangential velocity components in a spherical and in a non-spherical DM halo only emerge when those velocity components are computed in the galactocentric reference frame. In the Galactic heliocentric reference frame, no phase space coordinate is characterized by distributions that significantly differ in the cases of spherical and non-spherical DM halos, according to the KS test. Specifically, this is the case for each of the components of the star velocity. Indeed, all the components of the heliocentric velocity (v_d, v_l, v_b) are a composition of v_r and $\vec{v}_\mathrm{t} = (v_\vartheta, v_\varphi)$ (see Eqs. 2.11-2.13), and the information on the triaxiality parameters stored in the galactocentric $\vec{v}_\mathrm{t}$'s is diluted in the velocity transformation from the galactocentric to the heliocentric system. The same results hold for the phase space coordinates in the equatorial reference frame.

2.2.2 Star kinematics and sample selection

As illustrated in Sect. 2.2.1, the components v_ϑ and v_φ of the tangential velocity of the HVSs can effectively probe the non-spherical components of the gravitational potential. This result was demonstrated for a subsample of mock HVSs characterized by $r > 10$ kpc and $v_\mathrm{r} > 0$. Here, we show that these sample selection criteria turn out to be the most suitable selection criteria also on the basis of the star kinematics, for HVSs of $4\,M_\odot$. Indeed, these criteria enable us to select those stars whose tangential velocity is not affected by effects other than the shape of the gravitational potential well. We adopted an analogous HVS sample selection based on stellar kinematics in Chakrabarty et al. (2022) (see Sect. 3.4.2).

In our model of the Galactic potential (see Sect. 2.1.2), stars with ejection speed $v_\mathrm{ej} \gtrsim 800$ km s^{-1} always possess tangential velocities that are independent of their radial velocities, and are induced only by the non-spherical shape of the gravitational potential well. Those stars are robust indicators of the shape of the DM halo in any stage of their trajectory. Conversely, for stars with ejection speed $v_\mathrm{ej} \lesssim 800$ km s^{-1}, the tangential velocity, v_t, can be strongly coupled with the radial velocity, v_r, for a significant fraction of their trajectory, and v_t can be very high regardless of the shape of the DM halo. Indeed, if any of these stars is sufficiently young at ejection, it may experience the outer turnaround before dying out. At the outer turnaround, the star starts falling back toward the Galactic center, its radial velocity becomes negative, and its tangential velocity starts growing; this growth continues until the star experiences the inner turnaround, and then starts a new outward trajectory, with positive radial velocity and a tangential velocity that decreases with time. Therefore, those stars may serve as indicators of the halo shape only in specific parts of their outward trajectory, namely only during specific periods of their lifetime.

The situation is illustrated in Fig. 2.5 for the case of a spherical DM halo, and for a set of HVSs ejected radially outward in the direction $\hat{n}(\vartheta, \varphi) = \hat{n}(45°, 45°)$ and with representative values of the ejection speed, $|v_{\rm ej}| = \{700, 720, 740, 800, 900\}$ km s^{-1}. All the stars are ejected with null age, $\tau_{\rm ej} = 0$, to illustrate the evolution of the stars' observables during the largest possible travel time (i.e., 160 Myr, for the 4 $M_\odot$ stars considered in this work). Stars not ejected with null age would experience only part of the evolution shown in the figure. We note that the choice of the ejection direction of the HVSs does not affect any of the results that are presented in the following.

Panel *a* of Fig. 2.5 shows the relation between the magnitude of the tangential velocity, $v_{\rm t} = |v_\vartheta|$, and the radial velocity, $v_{\rm r}$, for the above set of stars. We note that the magnitude of the tangential velocity, $v_{\rm t} = (v_\vartheta^2 + v_\varphi^2)^{\frac{1}{2}}$ is equivalent to the magnitude of the latitudinal velocity $|v_\vartheta|$ because the DM halo is spherical: since the axisymmetric disk potential is the only source of non-zero $v_{\rm t}$, the azimuthal velocity v_φ is null.

Panel *b* of Fig. 2.5 shows the relation between the radial velocity, $v_{\rm r}$, and the distance to the Galactic center, r, for the same set of HVSs. Both the vertical dashed line in panel *a*, and the horizontal dashed line in panel *b* correspond to a null radial velocity, $v_{\rm r} = 0$, that the star possesses at its outer and inner turnaround radii.

For the HVSs generated with ejection speeds $v_{\rm ej} \gtrsim 800$ km s^{-1} (blue and purple lines), both panels *a* and *b* show that these stars can never reach their outer turnaround radius ($r = r_{\rm out}$) before dying out. Indeed, they never cross the line $v_{\rm r} = 0$ from right to left in panel *a*, and the line $v_{\rm r} = 0$ from top to bottom in panel *b*.

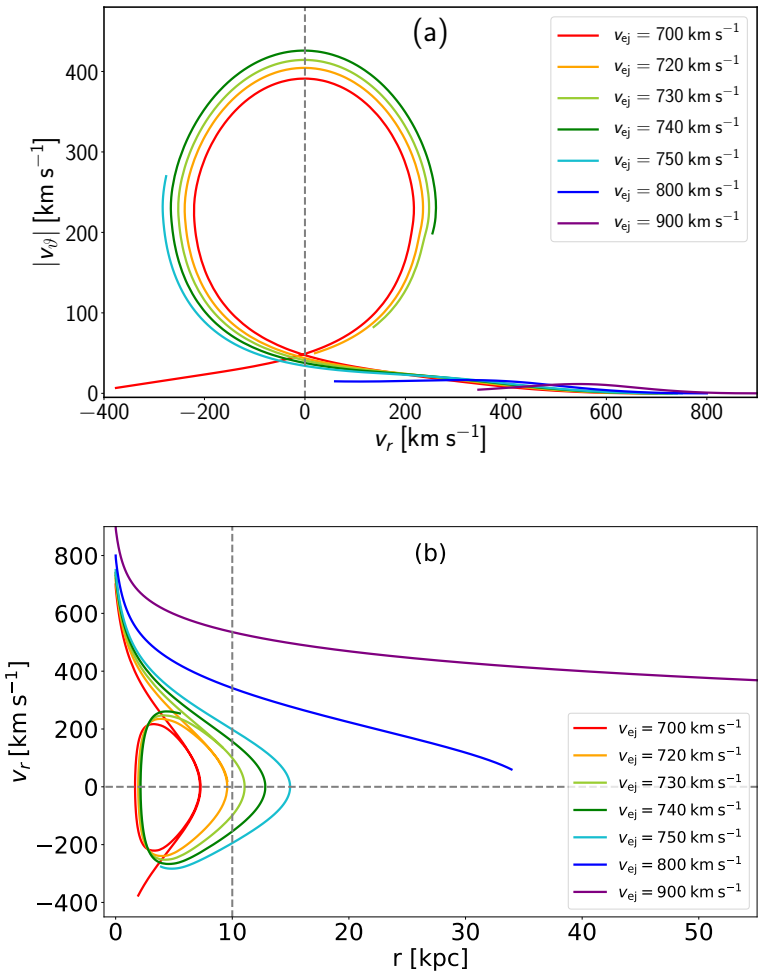

Figure 2.5. *Panel a*: Magnitude of the galactocentric latitudinal velocity, $|v_\vartheta|$, as a function of the galactocentric radial velocity v_r, for HVSs ejected with different speed $v_{\rm ej}$ and traveling in a spherical DM halo. Initially, the star velocity is purely radial, and $|v_\vartheta| = 0$; as time goes on, $|v_\vartheta|$ becomes non-null due to the non-spherical potential of the Galactic disk (see Eq. 2.4). For stars with smaller ejection speed ($v_{\rm ej} \lesssim 800$ km s^{-1}), radial and angular dynamics are coupled: this coupling results into a fast growth of $|v_\vartheta|$ after the first turnaround of the star. However, such couplings are not manifested for stars with larger ejection speed. *Panel b*: galactocentric radial velocity v_r as a function of the galactocentric distance r, for HVSs ejected radially outward with different ejection velocities $v_{\rm ej}$. The vertical dashed line of panel a and the horizontal dashed line of panel b corresponds to $v_r = 0$, while the vertical dashed line of panel b corresponds to $r = 10$ kpc. In both panels, HVSs are ejected in the direction $\hat{n}(\vartheta, \varphi) = \hat{n}(45°, 45°)$ with a travel time of 160 Myr, which is the largest possible travel time for a 4 $M_\odot$ star.

For these stars, panel a shows that $|v_\vartheta|$ is always $\lesssim$ few 10 km s^{-1}, regardless of $v_{\rm r}$: these values of v_ϑ are entirely determined by the deviation from the spherical symmetry of the gravitational potential. This deviation is due to the axisymmetric disk alone, in the case of the spherical DM halo considered here; it is due to a combination of disk and triaxial DM halo when the DM halo is non-spherical, as discussed in Sect. 2.2.1. At any stage of the stars' trajectories, the distributions of $|v_\vartheta|$ for these stars can be used as an indicator of the shape of the DM halo.

On the contrary, for the HVSs with ejection speed $v_{\rm ej} \lesssim 800$ km s^{-1} (cyan, dark green, green, orange, and red lines), both panels a and b show that these stars may undergo at least the first, outer turnaround before dying out. Indeed, these stars may

cross both the line $v_r = 0$ from right to left in panel a, and the line $v_r = 0$ from top to bottom in panel b at the outer turnaround radius, $r = r_{out}$, if they are ejected with sufficiently low age. When $v_{ej} \lesssim 740$ km s^{-1}, the stars may also experience the second, inner turnaround. In this case, they cross again the line $v_r = 0$ from left to right in panel a, and correspondingly cross the line $v_r = 0$ from bottom to top in panel b, at the inner turnaround radius, $r = r_{in}$. Finally, when $v_{ej} \lesssim 720$ km s^{-1}, the stars may also undergo subsequent turnarounds.

For the HVSs with $v_{ej} \lesssim 800$ km s^{-1}, panel a shows that, after an initial phase where the star velocity is almost purely radial, with $|v_\vartheta| \lesssim$ few 10 km s^{-1} regardless of v_r, $|v_\vartheta|$ quickly increases after the outer turnaround and becomes very large for those stars that undergo the inner turnaround. These large values of $|v_\vartheta|$ are determined by the exchange of kinetic energy between radial and angular degrees of freedom, rather than by the shape of the gravitational potential well, especially close to the inner turnaround. Therefore, the tangential velocity of these stars could in principle be used as an indicator of the shape of the DM halo only in specific parts of the star's trajectory.

To perform our investigation on the shape of the DM halo by means of the HVS tangential velocities, we needed to select only the stars that, at $t = t_{obs}$, were on their first outward trajectory from the Galactic center, namely the stars that had not experienced an inner turnaround yet. Therefore, we first excluded the stars that, at $t = t_{obs}$, were on an inward trajectory ($v_r < 0$) toward the Galactic center: we thus required $v_r > 0$ for the stars of our sample. From all the outgoing stars, we then excluded those that had already experienced the inner turnaround and may thus had uninterestingly large $|v_\vartheta|$. To do so, we note that panel b of Fig. 2.5 shows that stars characterized by ejection velocities $v_{ej} \lesssim 740$ km s^{-1} may live long enough to experience at least one inner turnaround. However, panel b of Fig. 2.5 also shows that these stars can never go back to galactocentric distances $r > 10$ kpc, after having undergone the inner turnaround. We thus required a galactocentric distance $r > 10$ kpc for the stars of our sample. This detailed analysis of the star kinematics thus supports our choice of the two preliminary selection criteria, $v_r > 0$ and $r > 10$ kpc, adopted in Sect. 2.2.1.

The case of a non-spherical DM halo is slightly more complicated than the case of the spherical halo explored so far. Here, both the disk and the DM halo generate a non-null latitudinal velocity, v_ϑ; furthermore, fully triaxial or spheroidal DM halos with a symmetry axis misaligned with respect to the z-axis are also sources of a non-null azimuthal velocity, v_φ, because the axial symmetry of the Galactic potential is broken.

However, we again find that both v_ϑ and v_φ are strongly coupled with v_r for the stars with $v_{ej} \lesssim 800$ km s^{-1}, as it happened for v_ϑ in the case of a spherical DM halo. As an example, for the case of a $(q_y, q_z) = (0.8,1)$ DM halo, Fig. 2.6 shows the relation between the azimuthal and radial velocity components. The stars' travel time is again 160 Myr, namely the largest possible travel time for 4 $M_\odot$ stars. The figure shows that for stars with $v_{ej} \lesssim 800$ km s^{-1}, $|v_\varphi|$ starts increasing after the outer turnaround, and reaches very large values close to the inner turnaround, irrespective of the shape of the DM halo that generated the non-null v_φ's. To exclude all the stars that had acquired large v_φ and correspondingly large v_θ after the outer turnaround, we again selected stars with $v_r > 0$ and $r > 10$ kpc, as we did in the case of a spherical DM halo.

We note that these two selection criteria, illustrated for both a spherical DM halo (see Fig. 2.5) and a non-spherical DM halo with $(q_y, q_z) = (0.8,1)$ (see Fig. 2.6), actually hold for a DM halo with any combination of axis ratios among those investigated in this work, as illustrated in Fig. 2.7. This figure shows the radial velocity, v_r, as a function of the galactocentric distance, r, for a star ejected at $v_{ej} = 740$ km s^{-1} and traveling in a Galaxy with DM halos of different shapes: a spherical DM halo, an extremely oblate

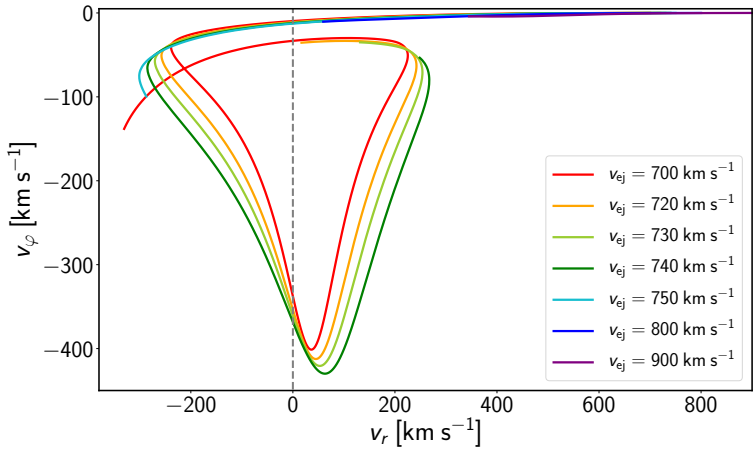

Figure 2.6. The HVS galactocentric azimuthal velocity v_φ as a function of the radial velocity v_r, for HVSs ejected with different speed v_ej and traveling for 160 Myr. Here, the gravitational potential of the MW is non-axisymmetric, with a $q_y = 0.8$ and $q_z = 1.0$ DM halo potential. Initially, the star velocity is purely radial, and $v_\varphi = 0$; as time goes on, v_φ becomes non-null due to the DM halo asymmetry with respect to the z-axis (see Eq. 2.5). Radial and angular dynamics are coupled for stars with smaller ejection speed ($v_\mathrm{ej} \lesssim 800$ km s^{-1}); these stars start acquiring significant v_φ values after the outer turnaround. However, stars with larger ejection speed die before this increase of v_φ can happen. The grey dashed line corresponds to $v_r = 0$.

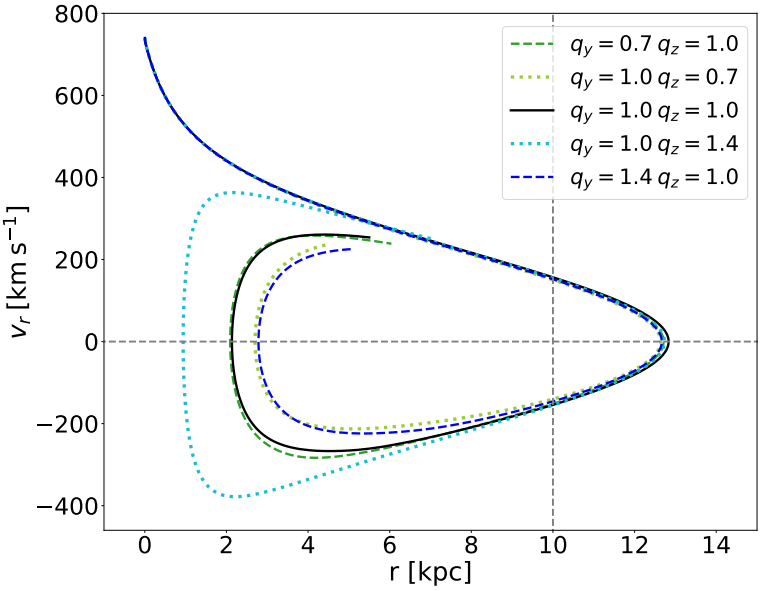

Figure 2.7. galactocentric radial velocity v_r as a function of the galactocentric distance r for HVSs ejected radially outward with an ejection velocity of $v_\mathrm{ej} = 740$ km s^{-1} in the direction $\hat{n}(\vartheta, \varphi) = \hat{n}(45°, 45°)$, for different shapes of the DM halo. The triaxiality parameters (q_y, q_z) of the DM halos are listed in the inset. The travel time is 160 Myr. The vertical and the horizontal dashed lines correspond to $r = 10$ kpc and $v_r = 0$, respectively.

or prolate DM halo which is axisymmetric about the z-axis, and an extremely oblate or prolate DM halo which is axisymmetric about the y-axis. Regardless of the axis ratios, stars ejected at $v_\mathrm{ej} = 740$ km s^{-1} can never reach a galactocentric distance $r > 10$ kpc,

after having experienced the inner turnaround.

We emphasize that the stars' outer and inner turnaround radii depend on the gravitational potential chosen for the computation of the trajectories (see also Chakrabarty et al. (2022) or Sect. 3.4.2). Thus, the kinematic selection criteria derived in this work would differ in different models of the Galactic gravitational potential. In addition, the kinematic selection criteria depend on the mass of the HVSs. In particular, HVSs with $M < 4\,M_\odot$ would have longer lifetimes, and thus a higher probability to reach the outer turnaround, undergo the inner turnaround, and go back to large galactocentric distances before dying out; this would result in a threshold radius larger than 10 kpc.

2.2.3 Effect of the initial conditions on the distributions of the shape indicators

In Sect. 2.2.1, we identified the distribution of the magnitude of the HVS latitudinal velocity, $|v_\vartheta|$, as the only distribution of HVS phase space coordinates to be significantly affected by a change of shape of the DM halo from spherical to spheroidal with axis of symmetry about the z-axis. Based on this finding, and extending the argument to a more general, non-axisymmetric Galactic potential, we identified the components of $\vec{v}_\mathrm{t}$ (i.e., v_ϑ and v_φ) as indicators of the triaxiality parameters of a DM halo. Hereafter, we generally refer to ω as each of the quantities used as an indicator of the shape of the DM halo; we define the distribution of the shape indicator ω as D_ω.

In Sect. 2.2.1 we presented results obtained for simulated HVSs from mock catalogs A, that are unambiguously determined by the shape of the DM halo because the set of stars is ejected with the same initial conditions in halos of different shapes. If a set of real HVSs were ejected with the initial conditions used to generate our mock catalogs A, recovering the shape of the MW DM halo from the distributions D_ω of real stars would be straightforward. In reality, however, the situation is more complex. At any given time t, we can observe the phase space distribution of a sample of HVSs that are traveling in a DM halo whose unknown shape we want to recover. Furthermore, the ejection conditions of these stars are also unknown: even assuming an ejection mechanism (e.g., the Hills mechanism, in our case), we do not know the initial conditions of the stars' trajectories, which are subject to statistical fluctuations. Therefore, recovering the shape of the DM halo requires the comparison of the distributions D_ω of the real HVS sample with mock D_ω's that were generated with all possible combinations of initial conditions and shape of the DM halo. In the following, we illustrate the impact of the statistical fluctuations of the initial conditions of the ejected stars on the distributions D_ω and on our ability to detect deviations from spherical of the shape of the DM halo.

When simulating the trajectories of a sample of HVSs, a different set of initial conditions for the trajectories yields a different distribution of the HVS phase space coordinates at $t = t_\mathrm{obs}$. Consequently, the results of the KS test, that compares the distribution D_ω of the shape indicators against a reference set of D_ω's of DM halos with different degrees of triaxiality, depend on the initial conditions. In Sect. 2.2.1, we already explored the effect of using different sets of initial conditions, each of them applied to all mock catalogs A generated for a series of spheroidal DM halos with different shapes. These different sets are responsible for the fluctuations of the p-value of the KS test within the ranges reported in Table 2.2 for some of the HVS phase space coordinates. As a result, mild deviations from spherical of the shape of the DM halo (i.e., $0.05 < |q_z - 1| < 0.1$) may not be recognized.

The situation becomes more complex when different sets of initial conditions are applied to each mock catalog. To investigate this case, we resorted to our HVS mock

catalogs B (see Sect. 2.1.4): these catalogs differ from one another both for the shape of the DM halo, as catalogs A, and for the set of the stars' initial conditions.

Depending on the combination of initial conditions and triaxiality parameters that characterizes each mock catalog B, the comparison of the resulting D_ω's for any of these catalogs with a catalog of a spherical halo, based on the KS test, may lead to two different incorrect conclusions: (i) $p < \alpha$ (with $\alpha = 5\%$), suggesting a deviation from the spherical halo, at the significance level α, even though both star samples have traveled in the same, spherical DM halo; (ii) $p > \alpha$, suggesting that both the DM halos crossed by the two star samples are spherical, even though one of the two halos is not.

Situation (i) would never occur in the comparison of two catalogs A, with the same initial conditions: the KS test for two D_ω's from different catalogs A would always yield $p = 100\%$ for identical halo shapes. Conversely, for two mock catalogs B, situation (i) can occur as a consequence of a fundamental property of the p-value: when we compare two D_ω's with the KS test, if the null hypothesis is true (i.e., if the two D_ω's are drawn from the same parent distribution), the value of the KS test statistics will be at least as large as the observed value in a fraction p of the cases (e.g., Press et al., 2007). Because the p-value of the KS test is a random variable itself, and because for a true null hypothesis it is uniformly distributed in the range $[0; 1]$ (e.g., Hung et al., 1997; Donahue, 1999; Bhattacharya and Habtzghi, 2002), one time out of 20 the p-value will be $\leq 5\%$ for D_ω's that are drawn from the same parent distribution. At the significance level $\alpha = 5\%$, this probability implies that a null hypothesis that is actually true (i.e., the shapes of the two DM halos are equal) will be rejected in 5% of the cases. [4]

Situation (ii) can instead occur also for catalogs A, when the shapes of the DM halos are only mildly different. However, our success in detecting actual deviations from the spherical shape with the KS test applied to the D_ω's is lower for catalogs B because of the additional effect of the statistical fluctuations of the initial conditions. Indeed, whereas in catalogs A we cannot distinguish a spherical DM halo from a spheroidal DM halo, symmetric about the z-axis, whose deviation from spherical is $|q_z - 1| < 0.1$, with catalogs B the range of non-detectable deviations widens to $|q_z - 1| \lesssim 0.2$. The failure to detect the different shapes of DM halos is a failure to reject a null hypothesis that is actually false. [5]

We note that false negatives may significantly hamper the recovery of the halo shape, especially for mild deviation from spherical of the shape of a spheroidal DM halo axisymmetric about the z-axis. As an example, we mention that comparing the D_ω's obtained in a spheroidal DM halo axisymmetric about the z-axis and with $q_z = 0.9$ (i.e., $|q_z - 1| = 0.1$) against those obtained in a spherical DM halo yields a rate of false negatives of $\sim 20\%$: in other words, we are not able to distinguish the shapes of the two DM halos in $\sim 20\%$ of the cases. Even though the rate of false negatives decreases with an increasing deviation from the spherical shape, and it becomes null for $|q_z - 1| \gtrsim 0.2$, it is important to reduce the rate of false negatives to improve the efficiency of the shape recovery of the DM halo.

Summarizing, when the initial conditions of the trajectories of a set of HVSs are unknown, as it happens for real HVSs, comparing the D_ω's of real stars with mock D_ω's with a KS test may yield results on the shape of the DM halo which are significantly affected by the initial conditions of real HVSs, especially for mild deviations of the shape of the DM halo from spherical. Therefore, it is important to design a method that

[4] In statistical hypothesis testing, this incorrect rejection is known as "type I error", or "false positive".

[5] In statistical hypothesis testing, this failure to reject a false null hypothesis is known as "type II error", or "false negative".

optimizes the recovery of the shape of the DM halo, minimizing the effects of the statistical fluctuations of the stars' initial conditions. We propose this optimized method in the following.

2.3 A new method to constrain the shape of the DM halo

Our final goal is to recover the shape of the DM halo from the distribution D_ω of the shape indicators ω of a real sample of HVSs, properly accounting for the effects of the unknown initial conditions of the stars' trajectories. To this aim, we designed a method based on (i) the use of the KS test to compare the D_ω of the sample of real HVSs with the corresponding distributions generated with a series of DM halos of different shape; (ii) the property of the KS test's p-value mentioned in Sect. 2.2.3: its uniform probability density function for a true null hypothesis which, in our case, occurs when two D_ω's are drawn from the same parent distribution.

To implement the method and evaluate its efficiency, we resorted to our HVS mock catalogs B (see Sect. 2.1.4), that differ from one another for the shape of the DM halo and/or the set of the stars' initial conditions. We also constructed a sample of synthetic HVSs, hereafter referred to as the "observed sample": the stars of this sample are ejected from the Galactic center, according to the Hills mechanism, with a statistically random set of initial conditions, and move across a Galaxy whose DM halo has a known shape. In our analysis, the observed sample mimics a real sample of HVSs: we used it to test the efficiency of our method in recovering the correct, known shape of the DM halo from its D_ω at $t = t_{\rm obs}$. The distributions of the kinematic properties of one of our observed samples is highlighted in green color in Fig. 2.20 of the Appendix. We emphasize that our HVS observed samples are ideal: we include neither observational uncertainties nor observational cuts imposed by the star observability, like its magnitude or position within the Galaxy. The method success rates that we estimate in Sects. 2.4.2 and 2.5.3 are thus valid for these samples alone and not for the HVS samples that might actually be observed.

We illustrate the basic concepts of our method in Sect. 2.3.1, and the method implementation in Sect. 2.3.2.

2.3.1 Fundamentals of the method

In our approach, recovering the shape of the DM halo crossed by an observed sample of HVSs requires the comparison of the D_ω of the observed sample with a series of corresponding D_ω's generated in mock catalogs characterized by a different shape of the DM halo and by a different set of initial conditions. We considered the shape of the DM halo of the mock sample that best matches the observed sample as the actual shape of the DM halo crossed by the HVS observed sample.

In principle, the comparison could be performed by means of a KS test, whose null hypothesis H_0 states that the two compared D_ω's are drawn from the same parent distribution. At the significance level α, we would accept H_0 in those cases where the test returns $p > \alpha$, and we would reject it otherwise. Accepting H_0 would correspond to considering the D_ω of the observed sample indistinguishable from the mock D_ω selected for the comparison, thus associating to the observed sample a DM halo with the same shape of the mock sample's DM halo. However, because of the effect of the statistical fluctuations of the initial conditions of the stars' trajectories (see Sect. 2.2.3), the D_ω of the observed sample may either turn out to be indistinguishable from a significant number of mock D_ω's obtained in DM halos with different shapes (false negatives), or

turn out to be significantly different from mock D_ω's obtained in DM halos with identical shapes (false positives).

To select the "best match" between observed and mock sample, we resorted to a property of the p-value, already mentioned in Sect. 2.2.3. When the null hypothesis H_0 is true, the p-value is uniformly distributed in the range $[0; 1]$ (e.g., Hung et al., 1997; Donahue, 1999); thus, its median value is $p_{\rm med} = 0.5$. On the other hand, when the alternative hypothesis, $H_{\rm a}$, is true, the distribution of the p-values is markedly skewed towards low p-values, because small values of p are more likely; thus, the median p-value under $H_{\rm a}$ will be $p_{\rm med} \ll 0.5$.

As a consequence, performing the KS test for a number $n_{\rm t}$ of D_ω pairs that are randomly drawn from the same parent distribution, namely from the ensemble of the D_ω obtained from mock catalogs B that are characterized by the same shape of the DM halo but by different initial conditions, yields a uniform distribution of p-values. Conversely, performing the KS test for a number $n_{\rm t}$ of D_ω pairs that are randomly drawn from different parent distributions, namely from different mock catalogs B, each of them characterized by a different shape of the DM halo and different initial conditions, yields a distribution of p-values which is markedly skewed towards small p-values. The larger is the difference in shape, the more skewed is the distribution.

The situation becomes more complex when we pick a specific distribution of ω, say $\tilde{D}_\omega$, as that of the observed sample, and we compare it against a series of mock distributions, performing a number $n_{\rm t}$ of KS tests. Even though both the HVS observed sample and the mock samples have traveled in the same DM halo, the distributions of the p-values is not necessarily uniform. It may be approximately uniform over the range $[0; 1]$, skewed towards low p-values, or skewed towards high p-values, with a corresponding median p-value $p_{\rm med} \simeq 0.5$, $p_{\rm med} < 0.5$, and $p_{\rm med} > 0.5$, respectively. This situation is illustrated in Fig. 2.8, that shows the distributions of the p-values obtained from $n_{\rm t} = 5{,}000$ KS test comparisons of $\tilde{D}_\omega$ for each of $n = 3$ different observed samples against all the D_ω's of a mock catalog B generated with a spherical DM halo. In each of the three cases, the observed sample and all the mock samples of HVSs have traveled in the same, spherical DM halo; however, the p-value distributions are markedly different: the black histogram shows the case of an approximately uniform distribution, with $p_{\rm med} \simeq 0.5$; the olive histogram shows the case of a distribution skewed towards low p-values, with $p_{\rm med} \simeq 0.3$; the purple histogram shows the case of a distribution skewed towards high p-values, with $p_{\rm med} \simeq 0.7$.

The fact that a uniform distribution of p-values is not guaranteed even for the same shapes of the DM halo is a consequence of the random selection of the observed sample's $\tilde{D}_\omega$ that we compare against all of the mock D_ω's. If we repeat the exercise of Fig. 2.8 with a series of $n > 3$ observed samples, we find n different distributions of p, each of them with a different median p-value. However, for sufficiently large n, the sum of all these distributions yields a uniform distribution. Moreover, the distribution of the n median p-values is markedly skewed towards high $p_{\rm med}$'s, as the one shown in Fig. 2.9: here, the grey histogram is obtained assuming in turn as observed sample each of the $n_{\rm t} = 5{,}000$ mock catalogs B with a spherical DM halo and comparing its $\tilde{D}_\omega$ against all the D_ω's of the remaining mock catalogs, for a total of $n = n_{\rm t} = 5{,}000$ KS tests per observed sample, and $n_{\rm t}$ corresponding p-values whose distribution has a median $p_{\rm med}$. Repeating the exercise $n = n_{\rm t} = 5{,}000$ times yields a distribution of $n = n_{\rm t} = 5{,}000$ median p-values. In this distribution, $\sim 80\%$ of the $p_{\rm med}$'s are in the range $0.3 - 0.7$, and the median is $M_0 \simeq 0.55$.

We note that the characteristics of the distribution of the median p-values primarily depend on the validity of H_0; indeed, the distribution is independent of the shape of the

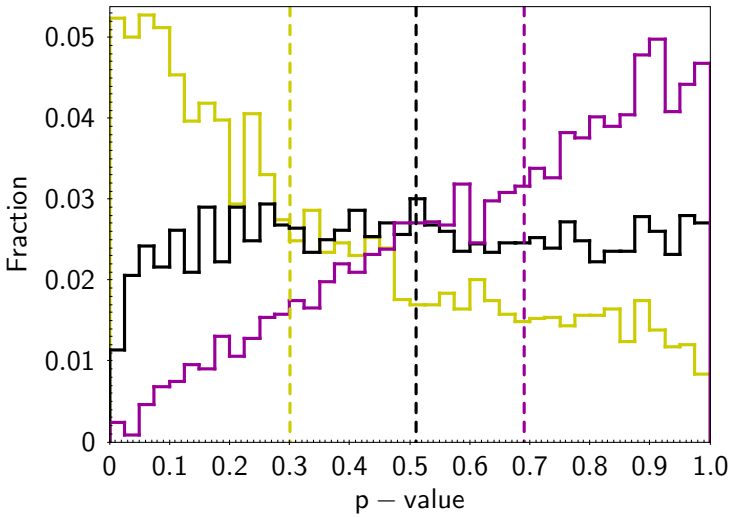

Figure 2.8. Distributions of the p-values obtained by comparing $\tilde{D}_\omega$ from each of $n = 3$ observed samples of HVSs against the D_ω's of a series of $n_\mathrm{t} = 5{,}000$ mock samples. The observed samples and the mock samples have all crossed a spherical DM halo. The black histogram shows an approximately uniform distribution of p, with a median value $p_\mathrm{med} \simeq 0.5$; the olive histogram shows the case of a skewed distribution with $p_\mathrm{med} \simeq 0.3$; the purple histogram shows the case of a skewed distribution with $p_\mathrm{med} \simeq 0.7$. The median p-values of the three distributions are marked by the vertical dashed lines.

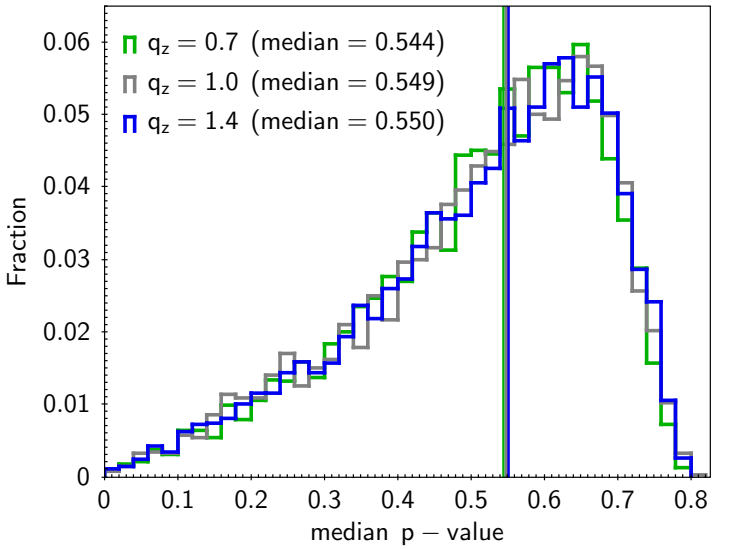

Figure 2.9. Distribution of the median p-values obtained from the KS test comparison of $\tilde{D}_\omega$ from all possible observed samples against the D_ω's from mock catalogs B generated in the same DM halo; the DM halo is spherical (grey histogram) or spheroidal with axis of symmetry about the z-axis with an oblate (q_z=0.7; green histogram) or prolate ($q_z = 1.4$; blue histogram) shape. The grey, green, and blue solid lines are the medians of the corresponding distributions.

DM halo under test. As shown in Fig. 2.9, the p_med's have indistinguishable distributions for extremely prolate ($q_z = 1.4$; blue histogram), spherical ($q_z = 1$; grey histogram), and extremely oblate ($q_z = 0.7$; green histogram) DM halos. The compatibility of the three distributions is also confirmed by a KS test. For all of the distributions, the median p_med is $M_0 \simeq 0.55$.

Summarizing, Figs. 2.8 and 2.9 show how the KS test comparison of the $\tilde{D}_\omega$ of an observed sample of HVSs with a series of n_t mock D_ω's may yield a p-value distribution different from uniform even though the observed sample and the mock sample crossed DM

halos with the same shape. This variety of p-value distributions corresponds to a variety of $p_{\rm med}$'s. Higher $p_{\rm med}$'s are more likely than lower $p_{\rm med}$'s, implying that a distribution of p-values skewed towards higher p's is more likely to occur under the null hypothesis H_0. Conversely, a distribution of p-values skewed towards lower p's, and thus characterized by a lower $p_{\rm med}$, is a more likely outcome under the alternative hypothesis $H_{\rm a}$ that the DM halos have different shapes.

Therefore, to select the "best match" between the observed sample and the mock sample, we chose the p-value distribution characterized by the largest $p_{\rm med}$. The DM halo crossed by the HVS observed sample was then assigned the shape of the mock sample that yielded the "best match".

2.3.2 Implementation of the method

To implement our method, we first explored the case of an axisymmetric Galactic potential, that includes the case of a spherical DM halo and that of a spheroidal DM halo axisymmetric about the z-axis; we then explored the more complex case of a non-axisymmetric Galactic potential, that includes the case of a spheroidal DM halo with a symmetry axis misaligned with respect to the z-axis, and that of a fully triaxial DM halo.

In both the axisymmetric and non-axisymmetric case studies, we resorted to mock catalogs B (Sect. 2.1.4), that we constructed as follows. We defined a series of $n_{\rm s}$ reference shapes for the DM halo, characterized by: (i) triaxiality parameters $q_y = 1$ and q_z that varied in steps of 0.1 within the range $0.7 - 1.4$, for the axisymmetric Galactic potential; (ii) triaxiality parameters q_y and q_z that both varied in steps of 0.1 within the range $0.7 - 1.4$, and $q_y \neq 1$, for the non-axisymmetric Galactic potential. For each of the $n_{\rm s}$ shapes of the DM halo, we generated an ensemble of $n_{\rm t} = 5{,}000$ HVS mock catalogs B, each of them including the phase space coordinates of a sample of HVSs characterized by a different random set of initial conditions. We also generated one observed sample of HVSs, randomly drawn from one of the mock catalogs B: this sample plays the role of a real HVS sample, and was used to evaluate the efficiency of the method in recovering the known shape of the DM halo crossed by the observed sample.

For each of the $n_{\rm s}$ simulated shapes of the DM halo, we performed a number $n_{\rm t} = 5{,}000$ of KS test comparisons of the $\tilde{D}_\omega$ of the observed sample against the D_ω's of the mock samples. From these $n_{\rm t}$ KS tests, we got a distribution of $n_{\rm t}$ p-values, whose median is $p_{\rm med}$. We repeated the procedure for all the $n_{\rm s}$ simulated shapes, and eventually obtained a set of $n_{\rm s}$ $p_{\rm med}$'s. We selected the mock sample corresponding to the largest value of $p_{\rm med}$ as the sample that "best matched" the observed sample, and we associated the shape of its DM halo to the DM halo of the observed sample.

To evaluate the success rate of our method in recovering the shape of the DM halo crossed by the observed sample, we generated a series of $n = n_{\rm t}$ observed samples corresponding to the same shape of the DM halo, by randomly varying the set of the HVS initial conditions, and we computed the fraction of cases where the method correctly recovers the known shape of the DM halo crossed by the observed sample. Finally, to study the dependence of the success rate of our method on the shape of the DM halo, we repeated our analysis for the observed samples of HVSs drawn from DM halos of different shapes.

In Sect. 2.4 we illustrate the application of our method to a series of observed samples generated in an axisymmetric Galactic potential, where the shape indicator ω is $|v_\vartheta|$. The test used for our analysis is the two-sample, one-dimensional KS test that we also used in the previous sections. In Sect. 2.5 we illustrate the application of our method to a series of observed samples generated in a non-axisymmetric Galactic potential, where

the shape indicators ω are $|v_\vartheta|$ and a function of v_φ. The test used for our analysis is the two-sample, two-dimensional KS test.

A possible alternative to the KS test chosen for our method is represented by the Anderson-Darling (AD) test (Anderson and Darling, 1952, 1954). However, the AD test currently exists only in its one-dimensional formulation; the use of this test would thus be limited to the case of axisymmetric Galactic potentials, when the shape of the DM halo can be recovered from the distribution of one shape indicator only, $|v_\vartheta|$. In the comparison of two one-dimensional distributions of $|v_\vartheta|$, the AD test is more sensitive to the tails of the distributions than the KS test. These tails are sensibly affected by the shape of the DM halo, as can be seen from Fig. 2.4. Therefore, the use of the AD test for our method is expected to improve our method success rate (see Sect. 2.4.2) in recovering the correct shape of an axisymmetric DM halo. Consequently, our choice of the KS test as the statistical test of our method represents a conservative choice in terms of method success rate.

Unlike the AD test, the KS test is available also in its two-dimensional formulation. We can thus also apply the method to non-axisymmetric Galactic potentials, where the comparison of the distributions of the two shape indicators, $|v_\vartheta|$ and a function of v_φ, is required. Adopting the same statistical test guarantees a consistent comparison of the success rate in axisymmetric and non-axisymmetric scenarios.

We remind that, from mock catalogs B and for the observed sample, we always selected subsamples of stars that fulfill the criteria defined in Sect. 2.2.2, namely subsamples composed of $N \simeq N_{\rm obs}/10 \simeq 800$ stars located at $r > 10$ kpc and with $v_r > 0$.

2.4 Constraining the shape of the DM halo in an axisymmetric Galactic potential

If the DM halo of our Galaxy is either spherical (i.e., with triaxiality parameters $q_y = q_z = 1$) or spheroidal with axial symmetry about the z-axis (i.e., with triaxiality parameters $q_z \neq q_y = 1$), the total gravitational potential of the Galaxy (Eq. 2.1) is axisymmetric about the z-axis. For an axisymmetric Galactic potential, we show that the method presented in Sect. 2.3 can effectively recover the axial ratio q_z of the DM halo from the distribution $\tilde{D}_\omega$ of the shape indicator ω of an observed sample of HVSs (Sect. 2.4.1). We also present the evaluation of the success rate of the method (Sect. 2.4.2).

As demonstrated in Sect. 2.2.1, if the Galactic potential is axisymmetric, there is only one shape indicator ω of the DM halo: the magnitude of the latitudinal velocity of the HVSs, $|v_\vartheta|$. We refer to its distribution as $D_{|v_\vartheta|}$. A few examples of $D_{|v_\vartheta|}$ for DM halos with different shapes were shown in Fig. 2.4.

2.4.1 Shape recovery

We defined a series of $n_{\rm s} = 8$ reference shapes for the DM halo by varying q_z in steps of 0.1 in the range $0.7 - 1.4$, For each shape, we generated an ensemble of $n_{\rm t} = 5{,}000$ mock catalogs B, one per different set of initial conditions of the star trajectories. We thus got $n_{\rm t}$ mock samples of stars, and $n_{\rm t}$ corresponding distributions $D_{|v_\vartheta|}$ for each of the $n_{\rm s}$ shapes of the DM halo.

As a first test, we chose as the HVS observed sample one random mock sample of HVSs that have crossed a spherical DM halo (with $q_z = q_y = 1$). We now show that our method successfully recovers the axis ratio $q_z = 1$.

For each of the $n_{\rm s} = 8$ reference shapes, we performed a set of $n_{\rm t} = 5{,}000$ KS test comparisons of the observed sample's $\tilde{D}_{|v_\vartheta|}$ against each of the $n_{\rm t}$ $D_{|v_\vartheta|}$'s of the mock

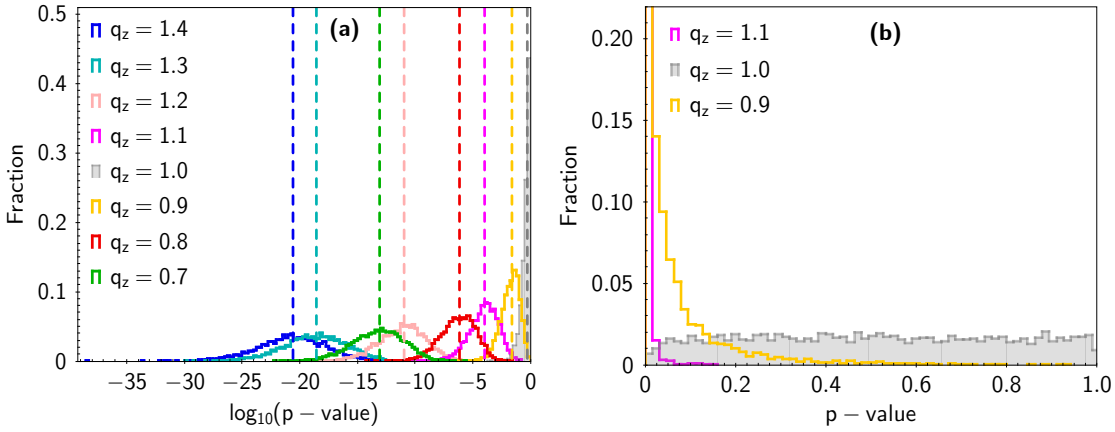

Figure 2.10. *Panel a:* Distributions of the p-values (in logarithmic scale) obtained from the KS test comparison of the distribution $\tilde{D}_{|v_\vartheta|}$ of one HVS observed sample generated in a spherical DM halo, against each of the $n_\mathrm{s} = 8$ ensembles of $n_\mathrm{t} = 5{,}000$ mock distributions $D_{|v_\vartheta|}$ generated in DM halos with different shapes, as listed in the panel. The vertical, dashed lines mark the median p-value of each distribution. *Panel b*: Enlargement of the right-most part of panel a with the p_med axis in linear scale. The difference in shape of the distributions in panels a and b are due to the different size of the histogram bins in the logarithmic and linear scales.

samples associated to that reference shape. Figure 2.10 shows the outcome of this test. Specifically, panel b of Fig. 2.10 shows the test result for three of these n_s sets of comparisons: the n_t KS test comparisons of the $\tilde{D}_{|v_\vartheta|}$ of the observed sample against the $D_{|v_\vartheta|}$'s of the mock star samples that traveled in the spherical DM halo yields a uniform distribution of p-values (filled, grey histogram) whose median is $p_\mathrm{med} \simeq 0.5$; the comparison of $\tilde{D}_{|v_\vartheta|}$ against a mock sample generated either in a slightly oblate ($q_z = 0.9$; yellow histogram) or in a slightly prolate ($q_z = 1.1$; magenta histogram) DM halo yields a distribution of p-values which is markedly skewed towards very low p's; the median p-values are $p_\mathrm{med} = 2 \times 10^{-2}$ for the observed vs. oblate comparison, and $p_\mathrm{med} = 10^{-4}$ for the observed vs. prolate comparison.

As shown in panel a of Fig. 2.10, the median p-value becomes smaller and smaller for increasing departure from spherical of the shape of the DM halo of the mock catalogs used for the comparison: it reaches $p_\mathrm{med} \simeq 10^{-13}$ for the comparison against the most oblate DM halo case ($q_z = 0.7$; green histogram) considered in this work, and $p_\mathrm{med} \simeq 10^{-21}$ for the comparison against the most prolate DM halo case ($q_z = 1.4$; blue histogram). We thus confirm that the largest p_med, that we obtained in the observed vs. spherical comparison, identifies the correct shape of the DM halo crossed by the observed sample (i.e., the spherical shape, with $q_z = q_y = 1$).

2.4.2 Success rate S of the method

Even though the result shown in the above test is a likely result, it is not guaranteed. Indeed, as pointed out in Sect. 2.3, the p-value distributions of Fig. 2.10 are not unique, and depend on the specific observed sample that we pick for the comparison (i.e., from the set of random initial conditions of the simulated HVSs). Therefore, it may happen that only in a fraction of cases the largest p_med is the correct indicator of the shape of the DM halo. We defined this fraction as the success rate S of our method in recovering the correct axis ratio of the DM halo. We now illustrate the evaluation of the method success rate, S, for the case of a spherical DM halo (Sect. 2.4.2), and the investigation of the dependence of S on the shape of the DM halo (Sect. 2.4.2).

The case of a spherical DM halo

To evaluate the success rate S of our method in recovering the correct axis ratio $q_z = 1$, we constructed the distributions of all possible $p_{\rm med}$'s that could be obtained by comparing the observed sample against the mock samples corresponding to the reference shapes of the DM halo. To generate these distributions, we simulated a series of $n = n_{\rm t}$ HVS observed samples in a spherical DM halo, by randomly varying the set of the stars' initial conditions. For each observed sample, we performed the $n_{\rm t}$ KS test comparisons against all the mock samples of a given shape, and we obtained a $p_{\rm med}$; performing the procedure for $n = n_{\rm t}$ observed samples yields a distribution of $n = n_{\rm t}$ values of $p_{\rm med}$ for each comparison of the observed samples against the mock samples of a given shape of DM halo. Repeating this exercise for each of the $n_{\rm s} = 8$ shapes of DM halo yields the $n_{\rm s}$ distributions of $p_{\rm med}$'s that we show in Fig. 2.11.

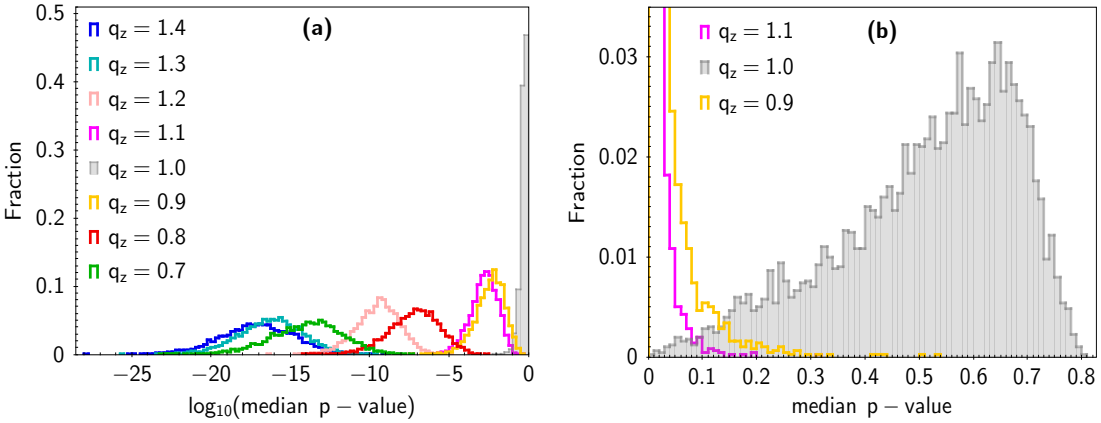

Figure 2.11. *Panel a:* Distributions of the median p-values, $p_{\rm med}$ (in logarithmic scale), obtained from the KS test comparison of the HVS observed sample generated in a spherical halo against each of the $n_{\rm s} = 8$ ensembles of mock HVS samples generated in a DM halo with different shape. Each distribution is the result of the KS test comparison of the $\tilde{D}_{|v_\vartheta|}$'s of the $n = n_{\rm t}$ observed samples against the $n_{\rm t} = 5{,}000$ mock samples generated in a DM halo with different shape as listed in the panel. *Panel b*: Enlargement of the right-most portion of panel a, with the $p_{\rm med}$ axis in linear scale. The yellow and pink distributions are the only distributions with non-null overlap with the grey distribution. The different shape of the distributions in panels a and b are due to the different size of the histogram bins in the logarithmic and linear scales.

Panel a of Fig. 2.11 shows that the comparison of the observed samples (generated in a spherical DM halo) against the samples generated in a spherical DM halo returns a distribution (the grey histogram) where most of the $p_{\rm med}$'s are larger than the $p_{\rm med}$'s of the other distributions, confirming that the method correctly recovers the shape of the DM halo crossed by the observed sample in most of the cases. However, panel a also shows that the distribution corresponding to the comparison of the observed samples against the samples generated in the spherical DM halo displays a non-null overlap with the two distributions of $p_{\rm med}$ that correspond to the comparison of (i) the observed samples against the samples generated in a slightly oblate DM halo ($q_z = 0.9$; yellow histogram), and (ii) the observed samples against the samples generated in a slightly prolate DM halo ($q_z = 1.1$; magenta histogram). This non-null overlap, that can be better appreciated in panel b, implies that, for an observed sample generated in a spherical DM halo, the shapes that mildly deviate from spherical ($|\Delta q_z| = 0.1$, in our mock catalogs) might be erroneously associated to the observed sample of HVSs, based on our method. The moderate, non-null overlap, however, does not necessarily imply that erroneous associations do occur with a rate proportional to the overlapping areas.

To illustrate this concept, let us consider two overlapping distributions of $p_{\rm med}$, one which is right-skewed and the other which is left-skewed, with a non-null overlap (as, e.g., the grey and yellow distributions of Fig. 2.11). Each value of $p_{\rm med}$ of the distributions is contributed by a specific HVS observed sample, characterized by a specific random set of initial conditions and a specific $\tilde{D}_{|v_\vartheta|}$ (see Sect. 2.4.1 for details). Only when the $p_{\rm med}$ that contributes to the left-skewed distribution ($p_{\rm med,ls}$) is higher than the $p_{\rm med}$ that contributes to the right-skewed distribution ($p_{\rm med,rs}$) for the same random observed sample, the erroneous association does occur. Other similar pairs ($p_{\rm med,ls}, p_{\rm med,rs}$), that can be randomly drawn from the overlapping portion of the two distributions, may never occur in reality. Therefore, whereas a null overlap ensures a null rate of erroneous shape associations, the existence of a non-null overlap of two distributions is only an indication that some erroneous associations may occur, without quantifying their rate of occurrence. However, the larger is the overlap, the higher is the probability of erroneous associations.

To evaluate the rate of success of our method in recovering the shape of a spherical DM halo, for each distribution of $p_{\rm med}$'s (as the yellow and magenta distributions in Fig. 2.11) that has a non-null overlap with the $p_{\rm med}$ distribution corresponding to the observed vs. spherical comparison (i.e., the grey distribution in Fig. 2.11), we computed the rate of occurrence of pairs ($p_{\rm med,ls}, p_{\rm med,rs}$) where $p_{\rm med,ls} > p_{\rm med,rs}$, thus providing an erroneous shape recovery. We found that in 1.16% of the cases (i.e., in 58 cases out of 5,000) the KS test comparison of the $\tilde{D}_{|v_\vartheta|}$ of the observed sample against the $n_{\rm t} = 5{,}000$ $D_{|v_\vartheta|}$'s of a mildly oblate ($q_z = 0.9$) DM halo yields a $p_{\rm med}$ value larger than that obtained in the comparison against the $n_{\rm t} = 5{,}000$ $D_{|v_\vartheta|}$'s of a spherical DM halo (i.e., $p_{\rm med,ls} > p_{\rm med,rs}$), leading to erroneously classify as mildly oblate a spherical halo; this result is equivalent to a success rate $S = 98.84\%$. The fraction of erroneous associations drops to 0.4% for the comparison against a mildly prolate ($q_z = 1.1$) DM halo, yielding $S = 99.6\%$. For $|\Delta q_z| \geq 0.2$, the overlap of the $p_{\rm med}$ distributions with the distribution corresponding to the spherical DM halo is null, implying a null rate of erroneous associations, and a success rate of our method $S = 100\%$.

Overall, for an observed sample generated in a spherical DM halo, our method enables to recover the correct axis ratio $q_z = 1$ of the DM halo in more than 98% of the cases; in other words, the method has a success rate $S \gtrsim 98\%$. We stress that, in the rare cases of an erroneous shape association, the recovered axis ratio q_z is off by only $|\Delta q_z| = 0.1$.

Dependence of the success rate S on the shape of the DM halo of the observed sample

The success rate S of our method displays a weak, non obvious dependence on the actual shape of the DM halo crossed by the HVS observed sample. Indeed, repeating the exercise of Sect. 2.4.2 for an HVS observed sample that traveled in each of our $n_s = 8$ reference DM halos (with $q_z = 0.7 - 1.4$), returned a success rate that varies from 89% to 99%, as listed in Table 2.3.

The success rate is slightly higher for spherical ($q_z = 1.0$) or mildly prolate ($q_z = 1.1$) DM halos than for oblate and markedly prolate DM halos; in other words, our method recovers more easily the shape of a DM halo crossed by an observed sample of HVSs when this DM halo is not too different from spherical. In addition, S is slightly lower for markedly prolate than for markedly oblate DM halos; this result indicates that the method recovers more easily the shape of an oblate DM halo than the shape of a prolate DM halo.

To illustrate this effect, Fig. 2.12 shows the analogs of the distributions of Fig. 2.11 for the case of an HVS observed sample that traveled in a prolate DM halo with $q_z = 1.2$. Panel *a* shows that the comparison of the HVS observed sample against the mock

Table 2.3. Success rate S of our method in recovering the axis ratio q_z of the DM halo of an axisymmetric Galactic potential from the distribution of the magnitudes of the azimuthal velocities, $D_{|v_\vartheta|}$, of an observed sample of HVSs.

q_z	1.4^a	1.3	1.2	1.1	1.0	0.9	0.8	0.7^a
S	88.9%	92.6%	96.6%	99.2%	98.4%	97.4%	97.2%	96.6%

Notes. $^{(a)}$ To properly compute the success rate in recovering the shape of DM halos with $q_z = 1.4$ and $q_z = 0.7$ we generated also reference sets of $n_t = 5{,}000$ HVS mock catalogs for DM halos of $q_z = 1.5$ and $q_z = 0.6$, respectively.

sample that traveled in a DM halo with the same shape returns a distribution (the pink histogram) where most of the $p_{\rm med}$'s are larger than the $p_{\rm med}$'s of the other distributions. This result confirms that the correct shape is recovered also for non-spherical DM halos.

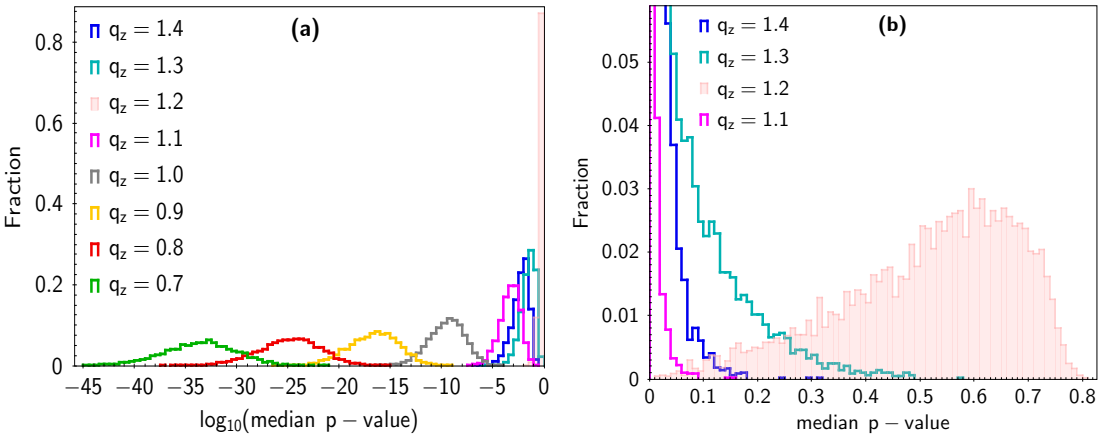

Figure 2.12. *Panel a:* Distributions of the median p-values, $p_{\rm med}$ (in logarithmic scale), obtained from the KS test comparison of the HVS observed sample against each of the $n_s = 8$ ensembles of mock HVS samples generated in a DM halo with different shape. Each distribution is the result of the KS test comparison of the $\tilde{D}_{|v_\vartheta|}$'s of the $n = n_t$ observed samples obtained in a prolate DM halo with $q_z = 1.2$ against the $n_t = 5{,}000$ mock samples generated in a DM halo with different shape as listed in the panel. *Panel b*: Enlargement of the right-most part of panel a with the $p_{\rm med}$ axis in linear scale. The cyan, blue, and magenta distributions are the only distributions with non-null overlap with the pink distribution. The difference in shape of the distributions in panels a and b are due to the different size of the histogram bins in the logarithmic and linear scales.

However, panel a and the corresponding enlargement in panel b also show that three distributions of $p_{\rm med}$ display a non-null overlap with the distribution corresponding to the correct shape: two of these distributions correspond to the comparison of the observed samples against the samples generated in more prolate DM halos ($q_z = 1.3$ and $q_z = 1.4$; cyan and blue histograms, respectively); the third one corresponds to the comparison against a less prolate DM halo ($q_z = 1.1$; magenta histogram). The number of overlapping distributions is thus larger (three instead of two) than in the case of the spherical DM halo illustrated in Fig. 2.11; furthermore, the overlapping area of the distributions is also larger than in Fig. 2.11 for the same Δq_z. Consequently, when the HVS observed sample traveled in a markedly prolate DM halo with $q_z = 1.2$, we get a larger number of erroneous shape associations for this halo than in the case of HVSs traveling in a spherical halo.

We note that, while the larger number of overlapping distributions is only a characteristics of the $p_{\rm med}$ distributions associated with markedly prolate ($q_z \geq 1.2$) DM halos, the larger overlapping area is a property shared by all the oblate and markedly prolate

DM halos. The excess in the number of overlapping distributions, where present, determines erroneous associations of the shape of the DM halo with spheroids whose q_z differs by 0.2 from the true q_z; however, it negligibly affects the success rate S of our method ($\lesssim 0.02\%$). On the other hand, the larger overlapping area of the $p_{\rm med}$ distributions associated to DM halos whose q_z differs by 0.1 from the true q_z is the main responsible for the shape dependence of S, because the larger area increases the probability that a DM halo is assigned a shape whose q_z is off by 0.1. Summarizing, in the infrequent cases of erroneous shape associations, the recovered axis ratio q_z is typically off by $|\Delta q_z| = 0.1$, although $|\Delta q_z| = 0.2$ can seldom occur ($\lesssim 0.04\%$ of the cases) when the DM halo crossed by the HVS sample is markedly prolate.

As illustrated at the beginning of this section, the weak dependence of the success rate S on the shape of the DM halo crossed by the HVS observed sample manifests itself with a slightly higher S for spherical and mildly prolate DM halos, and a slightly lower S for markedly prolate than for markedly oblate DM halos. This weak shape dependence is a direct consequence of the following facts: (i) the difference between the $D_{|v_\vartheta|}$'s of HVSs that traveled in a spherical or in a mildly prolate DM halo ($q_z = 1.0 - 1.1$) and the $D_{|v_\vartheta|}$'s generated in DM halos with $q_z' = q_z \pm 0.1$ is more pronounced than the difference between the $D_{|v_\vartheta|}$'s generated in DM halos that are either oblate ($q_z = 0.7 - 0.9$) or markedly prolate ($q_z = 1.2 - 1.4$) and the $D_{|v_\vartheta|}$'s produced in DM halos with $q_z' = q_z \pm 0.1$; (ii) the differences among the $D_{|v_\vartheta|}$'s of markedly prolate halos are milder than those among oblate halos. We ascribe these two effects to a combination of (a) the choice of a fixed resolution in q_z of our mock catalogs (i.e., $\Delta q_z = 0.1$), and (b) to the superposition of the gravitational actions of the disk and of the DM halo.

Specifically, effect (i) is mostly due to reason (a), that is the resolution in q_z of our mock catalogs. Indeed, more and more prolate (oblate) DM halos, obtained from the spherical halo ($q_z = 1.0$) by progressively increasing (decreasing) q_z by $\Delta q_z = 0.1$, generate a response in the $D_{|v_\vartheta|}$'s that is stronger when q_z is closer to 1. This is true independently of the presence of the axisymmetric disk potential.

On the other hand, effect (ii) is due to a combination of reasons (a) and (b). Reason (a) causes the markedly prolate DM halos considered in our mock catalogs to have q_z's (1.2, 1.3, and 1.4) that render their shapes more similar to one another than the q_z's of the oblate DM halos considered in this work (0.7, 0.8, and 0.9); indeed, the DM halos whose axis ratios are the reciprocals of the axis ratios of these oblate halos would be characterized by q_z's equal to $\simeq 1.1, 1.25$ and 1.4, respectively. Thus, the $D_{|v_\vartheta|}$'s generated by the markedly prolate DM halos are expected to be less different from one another than the corresponding distributions obtained for the oblate DM halos.

On top of this effect, the gravitational pull of the disk makes the $D_{|v_\vartheta|}$'s generated by the markedly prolate DM halos even less different from one another. Indeed, in a prolate DM halo the gravitational pull of the halo is opposed to the pull of the disk. For $q_z \leq 1.2$, the presence of the DM halo increases the fraction of HVSs with low $|v_\vartheta|$'s, rendering the distributions $D_{|v_\vartheta|}$'s more left-skewed than that of a spherical DM halo. However, for $q_z \geq 1.3$, the action of the DM halo not only compensates the gravitational pull of the disk, but it overcomes this pull, by bending the HVS trajectories towards the z-axis: consequently the fraction of low $|v_\vartheta|$'s drop - because v_ϑ increases in magnitudes and changes sign - and renders the $D_{|v_\vartheta|}$'s less left-skewed and more similar to those of the less prolate DM halos.

The above effects are responsible for a slightly higher success rate S for oblate DM halos. While the effects of the choice of a fixed Δq_z to build the mock catalogs can easily be overcome, the effect of the combined gravitational actions of the disk and of the DM halo is inherent to the problem.

Overall, in an axisymmetric Galactic potential, our method recovers the axis ratio q_z of the DM halo crossed by an observed sample of HVSs with a success rate $S \gtrsim 89\%$, and the erroneous shape association imply q_z that is off by ± 0.1 in the overwhelming majority ($\gtrsim 99.96\%$) of the cases. In a negligible fraction ($\lesssim 0.04\%$ [6]) of the cases, and for markedly prolate DM halos only, q_z can be off by 0.2.

2.5 Constraining the shape of the DM halo in a non-axisymmetric Galactic potential

If our Galaxy has either a fully triaxial DM halo (i.e., triaxiality parameters $q_y \neq q_z$, with $q_y \neq 1$ and $q_z \neq 1$) or a spheroidal DM halo with a symmetry axis misaligned with respect to the z-axis (i.e. triaxiality parameters $q_y \neq q_z = 1$, or $q_y = q_z \neq 1$), the total gravitational potential of the Galaxy (Eq. 2.1) is non-axisymmetric. For a non-axisymmetric Galactic potential, we show that the method presented in Sect. 2.3 can effectively recover the axial ratios q_y and q_z from the distribution $\tilde{D}_\omega$ of the shape indicators ω of an observed sample of HVSs (Sect. 2.5.2). We also present the evaluation of the success rate of the method (Sect. 2.5.3).

As anticipated in Sect. 2.2.1, in a non-axisymmetric Galactic potential both components of the tangential velocity $\vec{v}_t = (v_\vartheta, v_\varphi)$ are affected by the halo triaxiality, and can thus be used as indicators of the shape of the DM halo. Specifically, we identify two shape indicators ω: the magnitude of the latitudinal velocity of the HVSs, $|v_\vartheta|$, and a function $\bar{v}_\varphi$ of the azimuthal velocity v_φ, that we define in Sect. 2.5.1. Hereafter, the distributions of the two shape indicators $|v_\vartheta|$ and $\bar{v}_\varphi$ will be referred to as $D_{|v_\vartheta|}$ and $D_{\bar{v}_\varphi}$, respectively. The corresponding two-dimensional distribution will be referred to as $D_{|v_\vartheta|,\bar{v}_\varphi}$.

2.5.1 $|v_\vartheta|$ and $\bar{v}_\varphi$: two indicators of the shape of the DM halo

In a Galaxy with a non-axisymmetric gravitational potential, $D_{|v_\vartheta|}$ and $D_{\bar{v}_\varphi}$ are both affected by each of the two triaxiality parameters, q_y and q_z.

The behavior of $D_{|v_\vartheta|}$ in the case of a non-axisymmetric Galactic potential is similar to the behavior of $D_{|v_\vartheta|}$ in an axisymmetric Galactic potential (Sect. 2.2.1).

Figure 2.13 shows $D_{|v_\vartheta|}$ for a sample of HVSs that traveled in a Galaxy with DM halos of different shapes: the comparison of different distributions in each of the two panels shows that increasing q_z at fixed q_y leads to $D_{|v_\vartheta|}$'s that are generally more skewed towards low values of $|v_\theta|$. This effect was already shown in Fig. 2.4 for the case of spheroidal DM halos axisymmetric about the z axis (i.e., with $q_y = 1$): the gravitational pull of the disk, that drives the HVSs towards the x-y plane, is more and more compensated by a DM distribution which is more and more elongated in the direction of the z-axis. We note that the increase of skewness with increasing q_z depends on the value of q_y and stops when the action of the DM halo overcomes that of the disk, making v_ϑ change sign and increase in magnitude. This effect can be noticed in the left panel of Fig. 2.13, where the $D_{|v_\vartheta|}$'s are comparable for $q_z = 1.0$ and $q_z = 1.4$.

On the other hand, a comparison of the distributions corresponding to the same value of q_z (i.e., the distributions drawn with the same color) in the two panels in Fig. 2.13 shows the dependence of $D_{|v_\vartheta|}$ on q_y, at fixed q_z: DM halos with lower q_y at fixed q_z

[6] The reported fraction of erroneous shape association with q_z off by 0.2 was computed without taking into account the cases corresponding to $q_z = 0.7$ and $q_z = 1.4$: indeed, computing this fraction also for these extreme cases would have required the use of mock samples generated in a DM halo with $q_z = 0.5$ and $q_z = 1.6$.

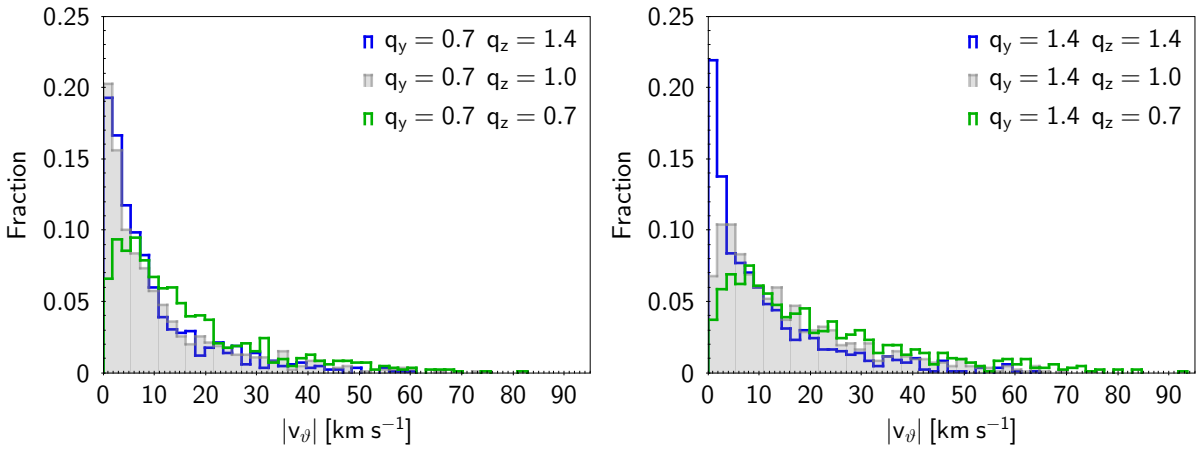

Figure 2.13. Distributions of the magnitude of the galactocentric tangential velocity $|v_\vartheta|$ for HVSs that have traveled in DM halos with $q_z = \{1.4, 1.0, 0.7\}$, and with $q_y = 0.7$ (left panel) and $q_y = 1.4$ (right panel). The distributions were generated with the same initial conditions (mock catalogs A), to highlight the effect of the different geometries of the DM halo.

imply larger concentration of dark matter away from the x-y plane, and thus generate (i) $D_{|v_\vartheta|}$'s that are more skewed towards lower $|v_\vartheta|$'s, as long as q_z is not too high and the DM halo only compensates the $|v_\vartheta|$'s induced by the disk, (see, e.g., the green and grey histograms, corresponding to $q_z = 0.7$ and $q_z = 1.0$); (ii) $D_{|v_\vartheta|}$'s that are less skewed towards lower $|v_\vartheta|$'s, for large values of q_z, when the pull of the DM halo overcomes the pull of the disk, and the increase in $|v_\vartheta|$ previously discussed is enhanced by a dark matter distribution more concentrated about the z-axis (see, e.g., the blue histograms, corresponding to $q_z = 1.4$).

A non-null distribution of v_φ is a distinctive characteristic of non-axisymmetric Galactic potentials: because in our model the gravitational potential is axially symmetric for the Galactic disk and spherically symmetric for the bulge, the only source of non-zero v_φ is the triaxial DM halo with $q_y \neq 1$. This DM halo can be either a fully triaxial DM halo or a spheroidal DM halo with a symmetry axis misaligned with respect to the z-axis (see Sect. 2.1.2).[7]

Even though the distribution of v_φ is extremely sensitive to the triaxiality parameters of the DM halo, using the very value of v_φ as a shape indicator leads to a degeneracy problem: a triaxial ellipsoid with a given $q_y = q_{y,1}$ and $q_z = q_{z,1}$ is equivalent, in terms of geometric shape, to a triaxial ellipsoid characterized by $q_y = q_{y,2} = 1/q_{y,1}$ and $q_z = q_{z,2} = q_{z,1}/q_{y,1}$; indeed, the role of the semi-major axes a and b is swapped in these two ellipsoids, and a rotation of 90° about the z-axis would make one of the two ellipsoids coincide with the other. As a consequence, the resulting distributions of v_φ are statistically indistinguishable. This effect can be seen in the left panel of Fig. 2.14, where we show the case of two samples of HVSs that traveled in two triaxial gravitational potentials whose semi-major axes a and b are swapped: one potential has $(q_{y,1}, q_{z,1}) = (0.7,1.0)$ and the other has $(q_{y,2}, q_{z,2}) = (1.4,1.4) \simeq (1/q_{y,1}, q_{z,1}/q_{y,1})$.

We note that two DM halos which are degenerate in v_φ are also degenerate in $|v_\vartheta|$. This effect can be seen in Fig. 2.13, where the $D_{|v_\vartheta|}$'s corresponding to a DM halo with $(q_y, q_z) = (0.7, 1.0)$ (left panel, grey histogram) and to a DM halo with $(q_y, q_z) = (1.4,1.4)$

[7] An additional baryonic component of the MW that could in principle contribute to v_φ is the MW hot gaseous halo (e.g., Fang et al., 2013; Gatto et al., 2013). However, we recently showed that its effect on the HVS azimuthal velocities is negligible with respect to that of a triaxial DM halo with $q_y \neq 1$ (Chakrabarty et al., 2022). Therefore, we do not consider the contribution of the hot gaseous halo in this work.

(right panel, blue histogram) are indistinguishable.

This degeneracy problem does not limit our understanding of the halo geometric shape in a strict sense; it rather hampers our ability of discriminating, for a DM halo with a given geometry, between two halo orientations that differ by 90° within the adopted reference frame. Breaking this degeneracy would thus enable to constrain not only the degree of triaxiality of the DM halo, but also the orientation of the halo.

The degeneracy might be broken by considering only the HVSs that are traveling in one of the four quadrants of the x-y plane. Indeed, when $q_y > 1$, the mass distribution is elongated in the direction of the y-axis; thus, the stars acquire a v_φ that drives them towards the y-axis; conversely, when $q_y < 1$, the stars are attracted towards the x-axis. Therefore, when the stars are located in the first quadrant (i.e. they have azimuthal coordinate $0° < \varphi < 90°$) they have positive v_φ when $q_y > 1$ and negative v_φ when $q_y < 1$, in our sign convention. As shown in the right panel of Fig. 2.14, the distributions of v_φ for the HVSs located in the first quadrant are manifestly different and not overlapping: for $q_y = 0.7$ the v_φ's are all negative, while they are all positive for $q_y = 1.4$.

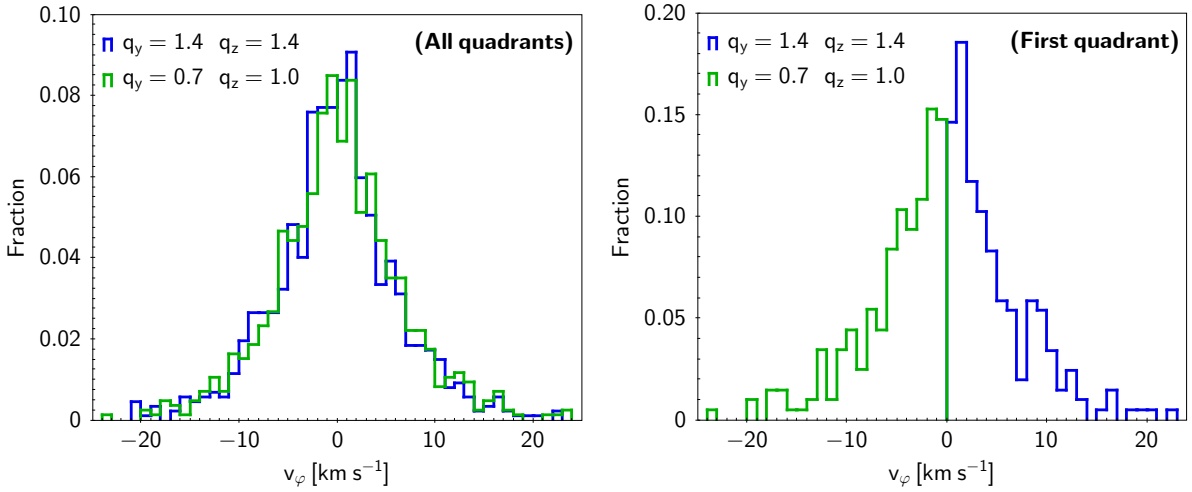

Figure 2.14. Distributions of the azimuthal velocity v_φ of two samples of HVSs that have traveled in gravitational potentials whose DM halos have the same geometrical shape but differ by 90° in azimuthal orientation. *Left panel:* The distributions of v_φ are indistinguishable from one another, when the stars from all the quadrants are considered. *Right panel:* The distributions of v_φ become manifestly different when we consider the HVSs located in the first quadrant of the x-y plane ($0° < \varphi < 90°$) only. The HVSs in the first quadrant have positive (negative) v_φ when $q_y = 1.4$ (0.7). The distributions were generated with the same initial conditions (mock catalogs A), to highlight the effect of the different geometries of the DM halo.

Choosing only the HVSs located in one quadrant is however not the best solution to break the above mentioned degeneracy, because the size of the sample is reduced by a factor ~ 4, lowering the success rate of our method (see Sect. 2.6). To recover the original sample size, we defined as shape indicator the variable $\bar{v}_\varphi \equiv v_\varphi \frac{\tan\varphi}{|\tan\varphi|}$, where the factor $\frac{\tan\varphi}{|\tan\varphi|}$ is a sign plus or minus that renders the value of v_φ positive when the star is moving towards the y axis ($q_y > 1$), and negative when the star is moving towards the x axis ($q_y < 1$), independently of the quadrant where the star is located.

Figure 2.15 shows the distributions of $\bar{v}_\varphi$ for two pairs of HVS samples that traveled through DM halos with the same geometric shape but azimuthal orientations that differ by 90°. One pair is composed of the HVS samples that traveled in DM halos with $(q_y, q_z) = (0.7,1.0)$ (green histogram) and $(q_y, q_z) = (1.4,1.4)$ (blue histogram) (i.e. the same samples investigated in Fig. 2.14); the other pair is composed of the HVS samples

that traveled in DM halos with $(q_y, q_z) = (0.9,1.0)$ (yellow histogram) and $(q_y, q_z) = (1.1,1.1)$ (magenta histogram). The figure shows how the use of the variable $\bar{v}_\varphi$ instead of v_φ enables us to easily distinguish distributions of azimuthal velocities generated in pairs of DM halos that have the semi-major axes a and b swapped. Using the two-dimensional distribution $D_{|v_\vartheta|,\bar{v}_\varphi}$ thus enables us to overcome the degeneracy problem.

We note that the HVSs represented in Fig. 2.15 attain values of $\bar{v}_\varphi$ that are of a few km s^{-1} for mild q_y deviations (i.e, $|\Delta q_y| = 0.1$) from unity, but may reach $\sim \mathcal{O}(10)$ km s^{-1} for the most extreme values of q_y considered in our study (i.e., $q_y = 0.7$ and $q_y = 1.4$). This result is a consequence of the extreme flattening of the DM halo along either the x-axis or the y-axis for values of q_y that are extremely large or extremely small, respectively.

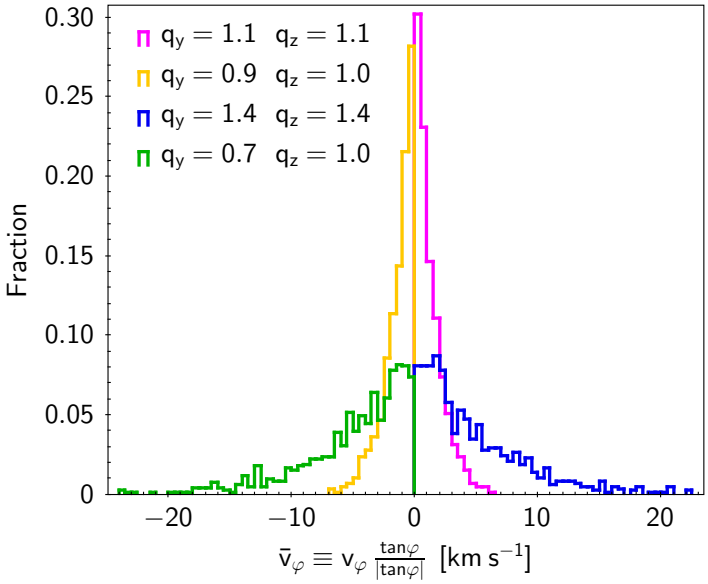

Figure 2.15. Distributions of $\bar{v}_\varphi \equiv v_\varphi \frac{\tan\varphi}{|\tan\varphi|}$ for samples of HVSs that traveled in gravitational potentials whose DM halo has different triaxiality parameters. The use of the variable $\bar{v}_\varphi$ instead of v_φ enables to easily distinguish distributions of azimuthal velocities generated in DM halos with the same geometry but whose semi-major axes a and b are swapped. The distributions were generated with the same initial conditions (mock catalogs A), to highlight the effect of the different geometries of the DM halo.

The distributions of $|v_\vartheta|$ and $\bar{v}_\varphi$ are both very sensitive to the triaxiality parameters of the DM halo. Therefore, their combination can provide a powerful tool to detect non-sphericity of the DM halo and constrain the triaxiality parameters of the corresponding gravitational potential, as we show below.

We compared the two-dimensional distributions $D_{|v_\vartheta|,\bar{v}_\varphi}$'s of the shape indicators obtained for HVSs that traveled in DM halos of different shapes. We generated the distributions by using mock catalogs A, which were produced with HVS samples characterized by the same random set of ejection conditions, as we did in Sect. 2.2.1 for the case of spheroidal DM halos. We defined a series of $n_\mathrm{s} = 56$ total reference shapes by varying both q_y and q_z in steps of 0.1 in the range $[0.7; 1.4]$ and imposing $q_y \neq 1$. These reference DM halos have either a fully triaxial shape or a spheroidal shape which is symmetric about the x-axis or the y-axis, and lead to a non-axisymmetric Galactic potential. For all these reference shapes, we generated the corresponding HVS mock catalogs.

We compared the $D_{|v_\vartheta|,\bar{v}_\varphi}$'s obtained from each of this n_s HVS samples against the $D_{|v_\vartheta|,\bar{v}_\varphi}$ obtained for a spherical DM halo, where $q_y = q_z = 1$, and $D_{\bar{v}_\varphi}$ is a distribution of null values. For this comparison, we used the two-sample, two-dimensional KS test (Press

et al., 2007, and references therein), hereafter referred to as "2D KS test". For all the 2D KS test comparisons, we found null p-values, implying that the $D_{|v_\vartheta|,\bar{v}_\varphi}$'s are significantly different from each other even for the smallest differences in triaxiality parameters with respect to the spherical DM halo. The null p-value results from the fact that, in a spherical DM halo, the HVSs do not acquire any azimuthal velocity; any non null $D_{\bar{v}_\varphi}$ is thus a proof that the HVS sample has traveled in a non-axisymmetric gravitational potential. This result proves that the distribution of $|v_\vartheta|$ and $\bar{v}_\varphi$ can effectively detect non-spherical shapes of the DM halo.

A 2D KS test comparison of pairs of $D_{|v_\vartheta|,\bar{v}_\varphi}$ obtained for DM halos characterized by the same value of q_z but different values of q_y yielded p-values always smaller than 5% even for differences in q_y as small as $\Delta q_y = 0.1$. The high sensitivity of the $D_{|v_\vartheta|,\bar{v}_\varphi}$ to small differences in q_y at fixed q_z is the result of the high sensitivity of $D_{\bar{v}_\varphi}$ to q_y. In turn, this sensitivity comes from the fact that $q_y \neq 1$ is the only source of non-null v_φ in triaxial DM halos.

Conversely, small differences in q_z at fixed q_y can lead to comparable $D_{|v_\vartheta|,\bar{v}_\varphi}$, according to a 2D KS test, with p-values that can exceed 5%. These larger values of p originates from the fact that differences in q_z affect v_ϑ, but v_ϑ is also affected by the gravitational pull of the disk. This effect was already discussed for the case of an axisymmetric Galactic potential, with a DM halo which is either spherical or spheroidal about the z-axis, (Sect. 2.2.1). Overall, $\bar{v}_\varphi$ is a more powerful shape indicator than $|v_\vartheta|$, and the combination of the two shape indicators is the appropriate tool to constrain the triaxiality parameters of a DM halo with the HVSs.

We note that, in our model of the gravitational potential of the MW, we assumed the DM halo to have its principal axes aligned with the axes of our Cartesian reference frame, x, y, and z, where x indicates the direction from the Sun to the Galactic center and z is orthogonal to the Galactic plane (see Sect. 2.1.2). Releasing this assumption has an effect on the shape indicator $\bar{v}_\varphi$. Indeed, let us assume that one of the principal axes of the DM halo still coincide with the z axis, while the remaining two principal axes lie on the Galactic plane, but are misaligned with respect to our x and y axes by an angle $0 < \phi_0 \leq 45°$. In this case, the HVS $\bar{v}_\varphi$'s would no longer be all negative or all positive. Specifically, for $0° < \phi_0 \lesssim 45°$, higher ϕ_0 would correspond to higher degrees of mixing of negative and positive values, while for $\phi_0 \simeq 45°$, the $\bar{v}_\varphi$ distribution will be about half positive and half negative.

For very small misalignments, the very low degree of mixing of the $\bar{v}_\varphi$ distribution would not prevent us from breaking the degeneracy in the orientation of the DM halo. On the other hand, for large misalignments, we would not be able to distinguish two DM halos with the same geometrical shape but with orientations that differs by 90°. However, we stress that even in those cases the degree of triaxiality of the DM halo could still be determined from the distribution of v_φ. Law et al. (2009) find that the axes of the DM halo on the plane of the Galactic disk are aligned with the x and y axes within 15°. In this case, our method would not encounter degeneracy problems.

2.5.2 Shape recovery

To recover the shape of the DM halo by means of the distribution $\tilde{D}_{|v_\vartheta|,\bar{v}_\varphi}$ of the shape indicators $|v_\vartheta|$ and $\bar{v}_\varphi$, we made use of the series of $n_\mathrm{s} = 56$ reference shapes for a non-axisymmetric Galactic potential obtained, as described above, by varying both q_y and q_z in steps of 0.1 in the range $0.7 - 1.4$, and imposing $q_y \neq 1$. For each shape, we generated an ensemble of $n_\mathrm{t} = 5{,}000$ mock catalogs B, one per different set of initial conditions of the stars' trajectories. From each mock catalog, we obtained one two-dimensional

distribution $D_{|v_\vartheta|,\bar{v}_\varphi}$ of the shape indicators, for a total of n_t distribution $D_{|v_\vartheta|,\bar{v}_\varphi}$'s per shape of the DM halo.

As an example, we chose as the HVS observed sample one random mock sample of HVSs that traveled in a DM halo with $q_y = 1.2$ and $q_z = 0.9$. We show here that our method successfully recovers the correct triaxiality parameters q_y and q_z.

Following a procedure similar to that described in Sect. 2.4.1, for each of the $n_\mathrm{s} = 56$ reference shapes (q_y, q_z) of the DM halo we performed the 2D KS test comparisons of the observed sample's $\tilde{D}_{|v_\vartheta|,\bar{v}_\varphi}$ against all of the $n_\mathrm{t} = 5{,}000$ $D_{|v_\vartheta|,v_\varphi}$'s corresponding to each shape. Thus, for each shape of the DM halo, we obtained a distribution of n_t p-values and a corresponding p_med.

Table 2.4 shows the p_med's obtained in this exercise for a selection of DM halos of different triaxiality parameters. We expect that the highest p_med points at the shape of the DM halo that "best matches" the shape of the DM halo actually crossed by the observed sample (see Sect. 2.4.1). Indeed, the highest $p_\mathrm{med} = 0.443$ occurs for the DM halo halo with triaxiality parameters $q_y = 1.2$ and $q_z = 0.9$, namely for the DM halo actually crossed by the observed sample: this result demonstrates that our method effectively recovers the correct shape of the triaxial DM halo crossed by the observed sample.

Table 2.4. Median value, p_med, of the distribution of $n_\mathrm{t} = 5{,}000$ p-values obtained from the n_t 2D KS test comparisons of the observed sample's $\tilde{D}_{|v_\vartheta|,\bar{v}_\varphi}$ against the $D_{|v_\vartheta|,v_\varphi}$'s of the n_t mock samples corresponding to different shapes. The largest p_med indicates the "best match" between the observed sample and the mock sample. The observed sample is generated in a DM halo with $q_y = 1.2$ and $q_z = 0.9$.

(q_y, q_z)	p_med
(1.1,0.8)	6×10^{-22}
(1.1,0.9)	10^{-17}
(1.1,1.0)	9×10^{-16}
(1.2,0.8)	0.006
(1.2,0.9)	0.443
(1.2,1.0)	0.004
(1.3,0.8)	3×10^{-5}
(1.3,0.9)	3×10^{-6}
(1.3,1.0)	3×10^{-11}

2.5.3 Success rate

In this subsection, we illustrate the success rate S of our method for the case of a DM halo with a specific shape (Sect. 2.5.3) and the dependence of S on the shape of the DM halo (Sect. 2.5.3).

The case of the triaxial DM halo with $(q_y, q_z) = (1.2,0.9)$

To evaluate the success rate S of our method, we followed a procedure similar to that of Sect. 2.4.2. We generated a series of $n = n_\mathrm{t}$ HVS observed samples in a DM halo with $q_y = 1.2$ and $q_z = 0.9$, by randomly varying the set of the stars' initial conditions. For each observed sample, we performed the n_t 2D KS test comparisons of the observed sample's $\tilde{D}_{|v_\vartheta|,\bar{v}_\varphi}$ against the $D_{|v_\vartheta|,\bar{v}_\varphi}$'s of all the n_t mock samples corresponding to a given reference shape of the DM halo, and we obtained a p_med. Performing the procedure for $n = n_\mathrm{t}$ observed samples yields a distribution of $n = n_\mathrm{t}$ values of p_med for each given shape of DM halo. Repeating this procedure for each of the $n_\mathrm{s} = 56$ shapes of DM halo yields n_s distributions of p_med's.

We show a representative selection of these distributions in Fig. 2.16. Panels a and b show that the highest $p_{\rm med}$'s correspond to the distribution obtained for the DM halo with triaxiality parameters $q_y = 1.2$ and $q_z = 0.9$ (grey histogram), namely the halo traveled by the observed sample: this proves that our method recovers the correct shape of the triaxial halo in the large majority of the cases.

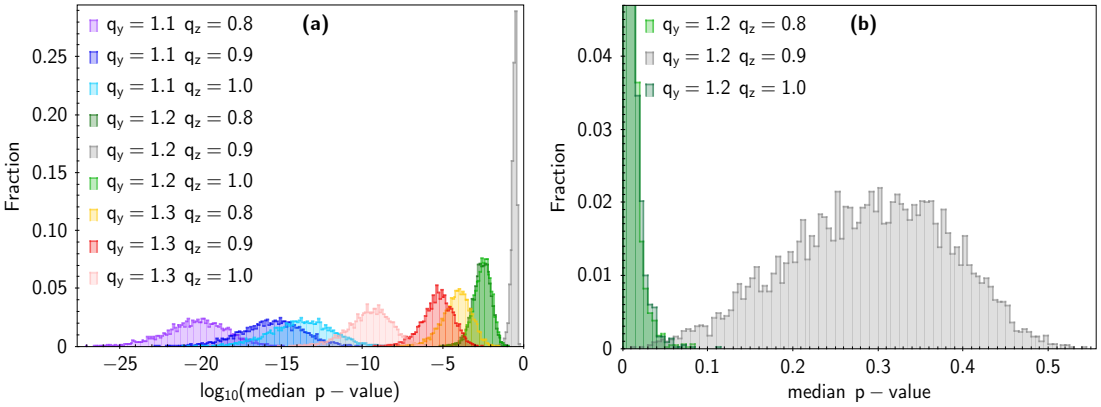

Figure 2.16. *Panel a:* Distributions of the median p-values, $p_{\rm med}$ (in logarithmic scale), obtained from the 2D KS test comparison of the HVS observed sample against a selection of 9 of the $n_{\rm s} = 56$ ensembles of mock HVS samples generated in DM halos with different triaxiality parameters. Each distribution is the result of the 2D KS test comparisons of the $\tilde{D}_{|v_\vartheta|,\bar{v}_\varphi}$'s of the $n = n_{\rm t} = 5{,}000$ observed samples obtained in a DM halo with $q_y = 1.2$ and $q_z = 0.9$ against the $n_{\rm t}$ mock samples generated in a DM halo with a different shape as listed in the panel. *Panel b:* Enlargement of the right-most part of panel a, with the $p_{\rm med}$ axis in linear scale. The green and dark-green distributions are the only distributions with non-null overlap with the grey distribution. The different shapes of the distributions in panels a and b are due to the different size of the histogram bins in the logarithmic and linear scales.

There are, however, cases where an erroneous shape association can occur. As shown in panel a of Fig. 2.16, the distributions of $p_{\rm med}$'s, corresponding to the comparison of the $\tilde{D}_{|v_\vartheta|,\bar{v}_\varphi}$'s of the HVS observed sample against the $D_{|v_\vartheta|,\bar{v}_\varphi}$ of the HVS samples generated in DM halos with the same $q_y = 1.2$ and with $q_z = 0.8$ or $q_z = 0.9$, display a non-null overlap with the distribution corresponding to the comparison of the observed sample against the samples from DM halos with $q_y = 1.2$ and $q_z = 0.9$. This overlap can be better appreciated in the enlargement of panel b. The overlap implies that, for an observed sample generated in a DM halo with $q_y = 1.2$ and $q_z = 0.9$, our method can erroneously associate to the observed sample only the shapes characterized by the same q_y and by a q_z slightly different ($|\Delta q_z| \leq 0.1$) from the correct q_z.

Erroneous shape associations are however very rare, because the overlap between the distributions is very modest. In the above example, the success rate of our method is 99.98%; only in one case over 5,000 the highest $p_{\rm med}$ suggests triaxiality parameters for the DM halo crossed by the observed sample that are not the correct ones, namely $(q_y, q_z) = (1.2, 1.0)$ instead of $(q_y, q_z) = (1.2, 0.9)$. In the analyzed case, any difference $\Delta q_y \geq 0.1$ leads to distributions of $p_{\rm med}$ that do not overlap, namely the rate of erroneous shape associations is equal to zero; the axis ratio q_y is thus correctly recovered in 100% of cases.

Dependence of S on the shape of the DM halo of the observed sample

To investigate the effect of the shape of the DM halo of the observed sample on the success rate of our method in the case of a non-axisymmetric Galactic potential, we explored three additional shapes for the DM halo. Table 2.5 reports the axis ratios q_y and q_z of these

DM halos, and the corresponding success rate, S. The axis ratio and success rate of the case explored in Sect. 2.5.3 are reported in the same table for completeness.

Table 2.5. Success rate S of our method in recovering the axis ratios q_y and q_z of the DM halo of a non-axisymmetric Galactic potential from the two-dimensional distribution $D_{|v_\vartheta|,\bar{v}_\varphi}$ of an observed sample of HVSs.

(q_y, q_z)	S
(0.8,0.8)	100.00%
(1.3,0.8)	99.64%
(1.2,0.9)	99.98%
(1.2,1.3)	96.24%

We obtained success rates $S > 96\%$ in all the explored cases. Thus, for a non-axisymmetric Galactic potential, the success rate of our method is less sensitive to the actual shape of the DM halo than for an axisymmetric Galactic potential. As in the case of an axisymmetric Galactic potential, illustrated in Sect. 2.4.2, for a non-axisymmetric Galactic potential we found that the DM halo with the largest q_z, namely the case $(q_y, q_z = (1.2,1.3)$, yields the smallest success rate, albeit still larger than 96%.

Even though we investigated only four shapes of DM halos, we selected them to appropriately cover the axis-ratio space. We thus expect $S \gtrsim 95\%$ also for different combinations of axis ratios. In particular, less extreme axis ratios are expected to increase the success rate of the method: this tendency, already shown in Sect. 2.4.2 for the DM halo yielding an axisymmetric Galactic potential, is enhanced in the case of a DM halo that generates a non-axisymmetric Galactic potential, because of the presence of a non-null distribution of $\bar{v}_\varphi$. Therefore, a 2D distribution of shape indicators makes the constraining power of our method higher and more effective against the actual shape of the DM halo that we want to recover.

2.6 Sample size and method success rate

In Sects. 2.4 and 2.5 we investigated the efficiency of our method in recovering the shape of the DM halo, in both an axisymmetric and a non-axisymmetric Galactic potential, from a mock observed sample of HVSs composed of ~ 800 4 $M_\odot$ stars. The size of the mock sample, dictated by the combination of the HVS ejection rate and the lifetime of the stars (see Sect. 2.1.3), as well as by our selection criteria (see Sect. 2.2.1), represents the optimal situation, that would occur if the HVSs were actually ejected according to the Hills mechanism with the assumed rate, and if we were able to observe all of them.

Here, we present our investigation of the dependence of the success rate S of our method on the size of the HVS observed sample. In Sect. 2.6.1, we show the results obtained when repeating the analysis performed in Sect. 2.4 on a series of mock HVS observed samples that traveled in a spherical DM halo and whose size is 50%, 25%, 10%, and 5% of the original sample size. In Sect. 2.6.2, we illustrate the generalization of our results to different shapes of the DM halo.

2.6.1 Spherical DM halos

We applied our method to an HVS observed sample that traveled in a spherical DM halo. For the case of an observed sample whose size is 50% the original size, panel *a* of Fig. 2.17 shows the distributions of the median p-values obtained by comparing

each observed sample with the 5,000 mock samples generated in spheroidal DM halos axisymmetric about the z-axis. This figure is the analog of Fig. 2.11, with the exception of the reduced sample size of the observed sample and of the smaller number of $p_{\rm med}$ distributions.

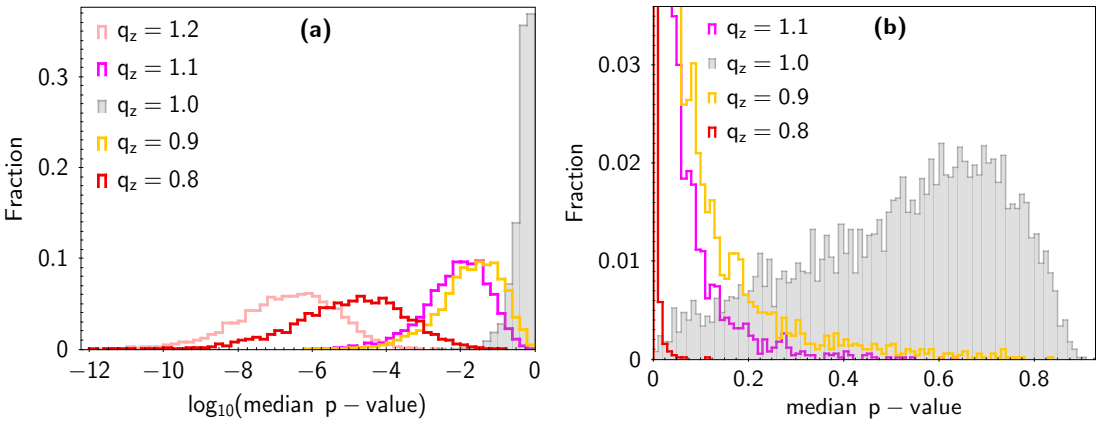

Figure 2.17. *Panel a*: Distributions of the median p-values, $p_{\rm med}$ (in logarithmic scale), obtained by comparing each of the 5,000 observed samples with $\simeq 400$ HVS generated in a spherical DM halo, with the 5,000 mock samples generated in spheroidal DM halos axisymmetric about the z-axis with different q_z, as listed in the panel. *Panel b*: Enlargement of the right-most part of panel a with the $p_{\rm med}$ axis in linear scale. The different shape of the distributions in panels a and b are due to the different size of the histogram bins in the logarithmic and linear scales.

Panel b is the enlargement of panel a. It shows that the distributions of the median p-values obtained from the comparison of the mock observed samples with the mock samples generated in the spherical DM halo with $q_z = 1.0$ (the grey histogram) is flatter than the corresponding histogram in panel b of Fig. 2.11. Indeed, all the distributions of Fig. 2.17 are flatter than the corresponding distributions of Fig. 2.11. As a consequence, there is a larger superposition of the grey distribution with the $p_{\rm med}$ distributions obtained from the KS test comparisons of the observed samples and the samples that crossed the mildly oblate ($q_z = 0.9$) and mildly prolate ($q_z = 1.1$) DM halos. Unlike Fig. 2.11, Fig. 2.17 also shows a non-null overlap of the grey distribution with the red distribution obtained from the comparison of the observed sample against the sample that crossed an oblate DM halo with $q_z = 0.8$; however, this non-null overlap does not correspond to any actual erroneous associations of the observed sample with an oblate DM halo with $q_z = 0.8$, because no comparison yields a $p_{\rm med}$ of the red distribution higher than the $p_{\rm med}$ of the grey distribution (see Sect. 2.4.2).

Summarizing, a 50% smaller HVS sample implies a higher probability of assigning a DM halo with an incorrect axial ratio q_z to an observed sample of HVSs. This corresponds to a lower success rate S of the method: while for the original HVS observed sample we obtain $S = 98.4\%$, for the 50% smaller sample we obtain $S = 91.8\%$. However, the axial ratio can be off by $|\Delta q_z| = 0.1$ only, as for the full-size sample.

The flattening of the distributions of the median p-values keeps on increasing with decreasing size of the observed sample. Figure 2.18 shows the change in the distribution of the median p-values obtained from the KS test comparison of the HVS observed samples against the mock samples generated in a spherical DM halo, when the size of the HVS observed samples drops from 100% (grey histogram; $N \simeq 800$ stars) to 50% (brown histogram; $N \simeq 400$ stars) and to 5% (black histogram; $N \simeq 40$ stars). The increasing flattening of the $p_{\rm med}$ distributions for smaller HVS samples occurs because deviations of the distribution of the p-values from the uniform distribution increase with decreasing

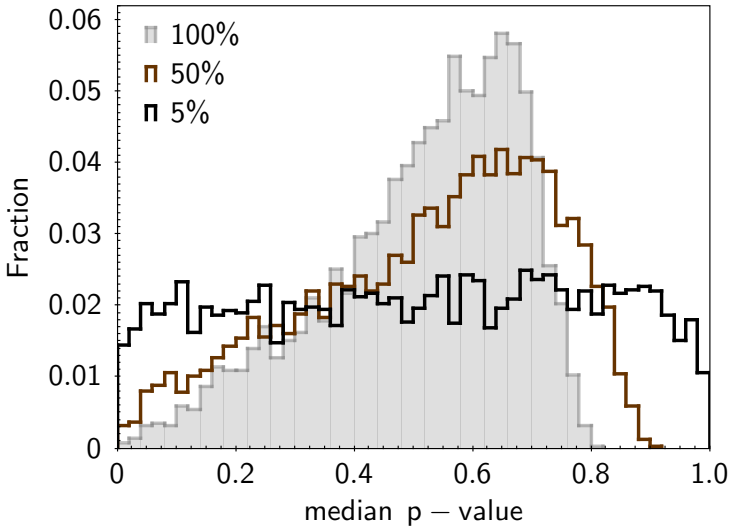

Figure 2.18. Distributions of the median p-values obtained from the KS test comparison of the $\tilde{D}_{|v_\vartheta|}$ of each observed sample, generated in a spherical DM halo, with the 5,000 mock samples generated in a spherical DM halo. The size of the compared samples is 100% (grey histogram; $N \simeq 800$ stars), 50% (brown histogram; $N \simeq 400$ stars), and 5% (black histogram; $N \simeq 40$ stars), respectively, of the original HVS sample size.

size of the HVS sample. In turn, the difference between $p_{\rm med}$ and the expected value 0.5 increases and the distributions of $p_{\rm med}$'s thus have higher tails.

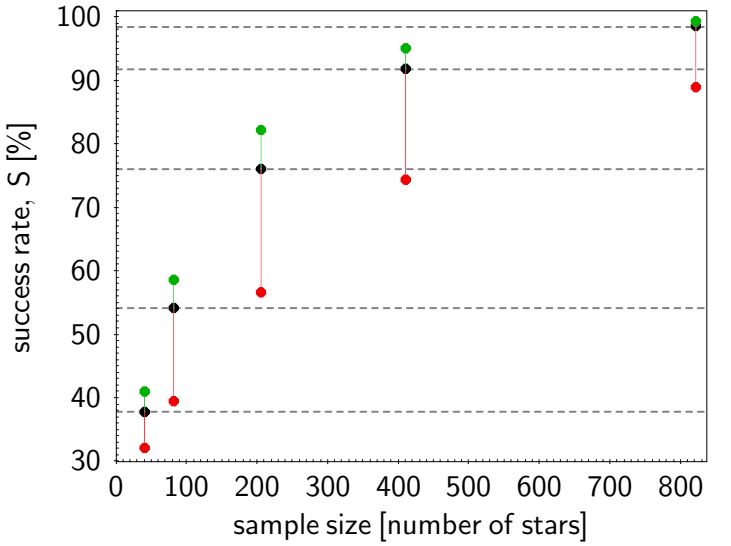

Figure 2.19. Success rate S of our method in recovering the correct shape of a DM halo as a function of the size of the HVS observed sample, for a spherical DM halo ($q_z = 1.0$; black dots) and for two spheroidal DM halos axisymmetric about the z-axis with $q_z = 1.1$ (green dots) and $q_z = 1.4$ (red dots). The sample size reported on the x-axis is the average size of the 5,000 HVS observed samples used to estimate the success rate in the spherical DM halo scenario. S is shown for sample sizes of 100% ($N \simeq 800$ stars), 50% ($N \simeq 400$ stars), 25% ($N \simeq 200$ stars), 10% ($N \simeq 80$ stars), and 5% ($N \simeq 40$ stars) of the original sample size.

For the case of a spherical DM halo, the black dots in Fig. 2.19 show the success rate of our method as a function of the size of the HVS observed sample. A success rate $S \gtrsim 90\%$ requires an HVS sample of $N \gtrsim 400$ HVSs, while $S \gtrsim 75\%$ is achieved with $N \gtrsim 200$ HVSs, $S \gtrsim 55\%$ is obtained with a sample of $N \gtrsim 80$ HVSs, and $S \gtrsim 40\%$ is

obtained with a sample of $N \gtrsim 40$ HVSs.

When the HVS sample size is $N \simeq 400$, the unsuccessful cases yield axial ratios that can be off by $|\Delta q_z| = 0.1$ at most, as it is for the case of the optimal sample size, $N \simeq 800$. On the other hand, when the sample size is $N \simeq 200$, the axial ratio can be off by $|\Delta q_z| \leq 0.2$. For the smallest sample sizes considered here (i.e., for $N \simeq 80$ and $N \simeq 40$), the axial ratio can be off by $|\Delta q_z| \leq 0.4$. For any sample size, the probability to associate a given erroneous shape with the DM halo crossed by the observed sample decreases with increasing difference $|\Delta q_z|$ between the erroneous and the actual axis ratio.

2.6.2 Non-spherical DM halos

For spheroidal DM halos that are axisymmetric about the z-axis, the dependence of the success rate S of our method on the sample size is comparable to the dependence found for spherical DM halos, illustrated in Sect. 2.6.1. However, the shape dependence of S discussed in Sects. 2.4.2 and 2.5.3 is responsible for fluctuations of the value of S for any given HVS sample size.

Figure 2.19 shows the dependence of the success rate S on the HVS sample size for the spheroidal DM halos axisymmetric about the z-axis that yield the most extreme success rates, namely those with $q_z = 1.1$ (green dots) and $q_z = 1.4$ (red dots), superimposed to the same dependence for spherical DM halos (black dots). The different S's between each of the two spheroidal cases and the spherical case are represented by the vertical green and red bars superimposed to the black dots. The spheroidal DM halo with $q_z = 1.4$ yields the lowest success rate for each sample size, and the difference in S between this case and the spherical case can be as high as $\sim 25\%$. On the other hand, the spheroidal DM halo with $q_z = 1.1$ yields the largest success rate for each sample size, with differences in S from the spherical case always smaller than 10%.

For fully triaxial DM halos or for spheroidal DM halos non-axisymmetric about the z-axis, we refrain from performing a detailed analysis: for the optimal sample size of ~ 800 HVSs, our method recovers the correct shape of the DM halo with a success rate $S = 96\% - 100\%$ for the explored scenarios, depending on the actual shape of the DM halo (see Sect. 2.5.3). This success rate is always higher than the success rate obtained, for the optimal sample size, for a spheroidal DM halo axisymmetric about the z-axis and with $q_z = 1.4$; for some shapes of the non-axisymmetric DM halo, S can also be higher than that obtained for a spheroidal DM halo axisymmetric about the z-axis and with $q_z = 1.1$. We thus expect that, for the case of non-axisymmetric DM halos, S will be generally larger than for the axisymmetric cases with the same sample size.

2.7 Discussion

The HVSs are ejected from the Galactic center and cross a large range of distances during their journey across the Galaxy. As shown in Sect. 2.2.1, their use as tracers of the DM halo of the MW is appropriate in any region where the DM halo is expected to dominate their kinematics, namely at galactocentric distances $r \gtrsim 10$ kpc. However, the phase space coordinates of the HVSs at any radius r stores the information on the triaxiality parameters of the dark halo within r. Therefore, the HVSs appear to be a promising probe of the triaxiality of the DM halo of the MW over a large range of spatial scales.

Conversely, other observational probes can constrain the shape of the DM halo over more limited spatial scales (see Sect. 1.4.3). Our HVS-based method is thus a powerful tool to complement the currently available constraints on the shape of the Galactic DM halo provided by different tracers on different, limited scales.

Clearly, the applicability of the presented method depends on a few working hypotheses, that we discuss below. In addition, the size of the available HVS samples with measured velocity is still an issue both for the success rate of the method and for the magnitude of the offset between the recovered and the actual axis ratio. However, even though our method was developed in the framework of a specific model of HVS production and with a set of assumptions, our working hypotheses do not limit the validity of the method, as we illustrate in the following.

As for the HVS production, we considered here the Hills mechanism, because of its unique ability in generating both a large number of unbound main-sequence HVSs and B-type stars in close orbit about SgrA* (see Sect. 1.5.1). However, our method can be applied to any mechanism that can eject stars from the Galactic center on a purely radial direction with a velocity $v_{\rm ej} \gtrsim 730$ km s^{-1}, thus enabling them to reach $r > 10$ kpc with non-null outward radial velocity.

All our simulated HVSs have a mass of 4 $M_\odot$. The large majority of the HVS candidates are B-type stars with mass in the range $\sim 2 - 4\,M_\odot$, while other candidates are classified as A, F, G, or K type stars. The generation of a realistic sample of ejected stars would require sampling the masses of the binary stars that encounter the SMBH from a mass distribution. However, under the simplifying assumption that the population of binary stars were entirely composed of equal-mass binaries, the distribution of the ejection velocities of a sample of HVSs with different masses would be the sum of the independent distributions of the ejection velocities of equal-mass HVSs. Thus, our simulated mock HVS sample of $4\,M_\odot$ stars has the same fractional distribution of ejection velocities that would be obtained for the subsample of $4\,M_\odot$ stars in a simulated extended spectrum of masses for equal-mass binaries. As a consequence, our mock observed sample would mirror a real sample limited to $4\,M_\odot$ HVSs.

In fact, in a realistic scenario, unequal mass binaries are likely. For hyperbolic encounters, as those simulated in this work, the primary member of each binary is usually ejected as an HVS; its ejection velocity depends on the mass m_2 of the secondary star. Thus, in a distribution of binaries whose primary member is a 4 $M_\odot$ star, the velocity of the ejected 4 $M_\odot$ HVS depends on the mass of the companion star, $m_2 \leq 4\,M_\odot$. Nevertheless, Bromley et al. (2006) show that the fractional velocity distribution of 4 $M_\odot$ HVSs located at $r = 10 - 120$ kpc is insensitive to m_2, when $m_2 = 0.5$, 1, 2, and 4 $M_\odot$. Our simulations confirm this result for binaries with m_2 uniformly sampled in the range $0.1 - 4\,M_\odot$. The insensitivity of the velocity distribution to m_2 follows from the fact that the stars that reach $r > 10$ kpc populate the high velocity tail of the distribution of ejection velocities ($v_{\rm ej} \gtrsim 730$ km s^{-1}); the high speed tail of the ejection velocity distribution obtained in the case of 4+4 $M_\odot$ binaries is statistically indistinguishable from the high speed tail of the corresponding distribution obtained when m_2 is sampled in the range $0.1 - 4$ $M_\odot$. Thus, limiting our mock HVS sample to $4\,M_\odot$ stars ejected from equal mass binaries returns, for stars in the region of interest ($r > 10$ kpc), final velocity distributions that are statistically consistent with those we would obtain by fixing the mass of the primary star to $4\,M_\odot$ and by varying the mass of the secondary star in the range $0.1 - 4$ $M_\odot$. However, the normalization of the latter distributions is smaller than the normalization we obtain by simulating $4 + 4\,M_\odot$ binaries. Indeed, when $m_2 = 0.1 - 4\,M_\odot$, the ejection velocity distribution peaks at lower values, implying that a lower number of HVSs can reach $r > 10$ kpc.

The size of the HVS sample also decreases with decreasing ejection rate R. By adopting $R = 10^{-4}$ yr^{-1} (see Sect. 2.1.3), we generated an optimal sample of ~ 800 $4\,M_\odot$ stars. We investigated the effect of different sizes of the HVS samples on the method success rate in Sect. 2.6, and showed that the success rate decreases for smaller sample sizes.

This analysis is suggestive of the effect of a lower ejection rate on the success rate of our method. Indeed, the ejection rate depends on a number of assumptions and it is still poorly constrained (see, e.g., Hills, 1988; Yu and Tremaine, 2003; Bromley et al., 2012; Zhang et al., 2013; Brown, 2015). Bromley et al. (2012) assume continuous star formation in the Galactic center and estimate $R \approx 1 - 2 \times 10^{-3}$ yr^{-1} when integrating over all the mass spectrum of the ejected stars considered. Our adopted $R = 10^{-4}$ yr^{-1} for $4\,M_\odot$ stars appears roughly consistent with this analysis of Bromley et al. (2012). However, by dropping the assumption of continuous star formation, Bromley et al. (2012) find substantial smaller values: $R \sim 2 - 8 \times 10^{-5}$ yr^{-1}. This range partly overlaps with the range $\sim 10^{-5}-$ a few 10^{-4} yr^{-1} found by Zhang et al. (2013) who consider different origins of the injected binaries and different models of the Initial Mass Function of the primary stars (see also Yu and Tremaine, 2003).

The decrease of the success rate with the decreasing size of the HVS sample illustrated in Sect. 2.6 also mimics the effect of the reduction of the HVS sample because of observational limitations, like the star magnitude or the star position within the Galaxy.

The dependence of the size of the HVS sample on the mass of the stars is more intricate: the larger number of stars with $M < 4\,M_\odot$ and lifetime $\tau_{\rm L} > 160$ Myr would determine a larger number of HVSs that are alive at the observation time compared to our $4\,M_\odot$ star sample. However, longer-lived, lower-mass stars can reach larger Galactocentric distances after experiencing the inner turnaround (Sect. 2.2.2); therefore, the lower limit $r = 10$ kpc we adopted here for the $4\,M_\odot$ stars will be larger for lower mass stars, thus potentially reducing the number of HVSs suitable for our method. Opposite effects would be determined by the moderate number of stars with $M > 4\,M_\odot$, and lifetime $\tau_{\rm L} < 160$ Myr. We plan to investigate in future work how these effects combine to determine the optimal sample size and, in turn, the success rate of the method.

Our HVS mock samples include both unbound and bound HVSs, that are HVSs whose ejection velocity does not exceed the escape velocity of the MW. The bound HVSs that satisfy the selection criteria that we defined in Sect. 2.2.2 are indicators of the shape of the DM halo as good as the unbound HVSs. Therefore, the observation of bound HVSs is of fundamental importance to increase the HVS sample size and the success rate of the method.

As highlighted by Marchetti (2021), bound HVSs may be the best candidate stars ejected from the Galactic center that can be observed in the *Gaia* catalogs, while the majority of the unbound HVS population is expected to be too far from the Sun's position (Kenyon et al., 2014) for its radial velocity to be measured by the *Gaia* Radial Velocity Spectrometer (RVS). In the current sample of HVS candidates, $\sim 70\%$ of the stars are located at a galactocentric distance $r > 10$ kpc, at the 3σ level. The possibility to measure the radial velocities of fainter objects in the outer halo will be of fundamental importance to identify new bound and unbound HVS candidates that satisfy our selection criteria. For example, the forthcoming 4-metre Multi-Object Spectroscopic Telescope (4MOST; de Jong et al., 2019) will be able to increase the volume of the spectroscopic sample provided by *Gaia*; specifically, it will measure the radial velocities of *Gaia* photometric sources with magnitude $G < 20.5$, while the *Gaia* RVS will provide radial velocities for sources with $G_{\rm RVS} \leq 16.2$ mag, corresponding to $G \leq 15.9$ for B0V stars and $G \leq 17.4$ mag for K4V stars (Jordi et al., 2010; Fitzgerald, 1970).

If our sample of 4 $M_\odot$ HVSs reached the optimal size of ~ 800 stars, in the ideal case of null uncertainties, our method would be able to recover the correct axis ratios of the DM halo in $\gtrsim 90\%$ of cases, while being off by 0.1 in the remaining $\lesssim 10\%$. The offset of 0.1 found in the minority of unsuccessful cases is set by the resolution in triaxiality parameters that we choose in our simulations, $\Delta q_{y,z} = 0.1$.

Here, we did not investigate the effect of any observational limitations on our HVS observed sample, nor the effect of the uncertainties on the HVS distances and galactocentric tangential velocities on the success rate of our method. This investigation will be pursued elsewhere.

The main contribution to the uncertainty on the tangential velocity of distant HVSs comes from their proper motion. The proper motion measurements currently available in the *Gaia* Early Data Release 3 (EDR3; Gaia Collaboration, 2016c, 2021) are affected by uncertainties that can lead to relative uncertainties on the tangential velocities larger than 100%. On the other hand, for nearby HVS candidates, the largest contribution to the uncertainties on the tangential velocities comes from the star distances inferred from *Gaia* parallaxes: in the Gaia EDR3, the uncertainties on the parallaxes range from $0.02 - 0.03$ mas, for sources with $G < 15$ mag, to 1.3 mas, for sources with $G = 21$ mag (Gaia Collaboration, 2021). The relative uncertainties on the parallax-inferred distances of an HVS candidate at 10 kpc from the Sun can thus vary from $20-30\%$ for the brightest stars to 1300% for the faintest stars. To preserve the high success rate of our method, it clearly is of utmost importance to reduce the uncertainties on both the star distances and proper motions.

A future *Theia*-like mission (Malbet et al., 2016; The Theia Collaboration et al., 2017; Malbet et al., 2019, 2021), designed for unprecedented high precision astrometry, may achieve an end-of-mission uncertainty on proper motions of a few micro-arcseconds per year (i.e., $\sim$100 times smaller than the uncertainty of *Gaia*), opening up the possibility for significantly constraining the shape of the DM halo. The availability of more precise measurements of proper motions will also make it possible to better constrain the birth place of the current HVS candidates.

The confirmation of the galactocentric origin of the trajectories of HVS candidates and their use to constrain the Galactic gravitational potential requires a final cautionary note. This research program is far from obvious, and can suffer from a circularity problem. The galactocentric origin of an HVS candidate can be assessed through a backtracking of the star trajectory (e.g. Brown et al., 2014, 2018; Marchetti et al., 2019; Irrgang et al., 2018; Koposov et al., 2020; Kreuzer et al., 2020; Irrgang et al., 2021); in turn, the backtracking requires an assumption on the gravitational potential that one aims to constrain. In addition to the matter distribution of the Galaxy, the gravitational potential is set by the distribution of the satellites of the Galaxy (e.g., Kenyon et al., 2018). Moreover, the gravitational potential of the Galaxy is time dependent because of the interaction of the Galaxy with its satellites (Boubert et al., 2020). On a wider perspective, the galactocentric origin of an HVS candidate also depends on the theory of gravity (Chakrabarty et al., 2022). Therefore, a solid confirmation of the galactocentric origin is currently limited to high-speed stars that are close to the Galactic center, where the effects mentioned above are negligible (e.g., Koposov et al., 2020). An appropriate method for constraining the gravitational potential with slower and more distant HVS candidates would require, for example, an iterative approach. In the absence of a self-consistent procedure, constraints on the Galaxy mass model with HVS candidates remain questionable.

2.8 Conclusions

We presented a new method to infer the shape of the DM halo of the MW from the distribution of the components of the galactocentric tangential velocities of a sample of HVSs. We applied our method to an ideal optimal sample of $\sim$ 800 4 $M_\odot$ simulated

HVSs. We referred to this sample as the observed sample. We illustrated the method for both axisymmetric and non-axisymmetric Galactic potentials.

In the axisymmetric scenario, we recovered the axial ratio of the DM halo from the one-dimensional distribution of one shape indicator only: the magnitude of the latitudinal velocity, $|v_\vartheta|$, of the HVSs of the observed sample. In the non-axisymmetric scenario, we recovered the axial ratios from the two-dimensional distribution of two shape indicators: $|v_\vartheta|$ and a function $\bar{v}_\varphi$ of the azimuthal velocity, v_φ, of the HVSs of the observed sample.

The method is based on the use of the one- or two-dimensional KS test to compare the distribution of the shape indicator(s) of the observed sample's, $D_{|v_\vartheta|}$ or $D_{|v_\vartheta|,\bar{v}_\varphi}$, against the corresponding distributions of HVS mock samples that traveled in DM halos with different shapes. The resolution in axial ratios of our ensemble of mock catalogs is $\Delta q_{y,z} = 0.1$.

For each shape of the DM halo, we compared the observed sample with a set of 5,000 $D_{|v_\vartheta|}$'s or $D_{|v_\vartheta|,\bar{v}_\varphi}$'s, which account for the different ejection initial conditions of the HVSs. A distribution of 5,000 p-values was thus obtained for each shape. We used the median, $p_{\rm med}$, of these p-value distributions to identify the shape of the DM halo that best matched the shape of the DM halo crossed by the observed sample: the highest $p_{\rm med}$ value comes from the p-value distribution associated with the correct shape of the DM halo.

In our ideal case of galactocentric velocities with null uncertainties and no observational limitations, the method has a success rate $S \gtrsim 89\%$ in recovering the correct shape of the DM halo of an axisymmetric Galactic potential, and a success rate $S > 96\%$ in recovering the correct shape of the DM halo of the non-axisymmetric Galactic potentials that we explored in this work.

The higher success rate of our method for a non-axisymmetric Galactic potential is due to (i) the availability of two shape indicators, $|v_\vartheta|$ and $\bar{v}_\varphi$, compared to one shape indicator alone for an axisymmetric Galactic potential; and (ii) the sensitivity of the azimuthal velocity v_φ to the shape of the DM halo. In the small fraction of unsuccessful cases, an erroneous shape association occurs; however, the discrepancy from the correct axial ratio is small. Indeed, in the axisymmetric Galactic potential scenario, the erroneous DM halo axis ratio q_z typically differs from the correct ratio by $|\Delta q_z| = 0.1$; an offset $|\Delta q_z| = 0.2$ is very rare ($\lesssim 0.04\%$ of cases). In the case of a non-axisymmetric Galactic potential, the incorrect shape associations are expected to be even rarer, because our method has a higher constraining power for a non-axisymmetric than for an axisymmetric Galactic potential.

The success rate of our method depends on the size of the HVS sample, and is higher for larger HVS samples. In the case of an axisymmetric Galactic potential, a decrease in the sample size corresponds to a decrease of the success rate that depends on the actual shape of the DM halo: for a spherical halo, a decrease of the sample size from 800 to 40 mock observed HVSs implies a drop of S from $\sim 98\%$ to $\sim 38\%$; for a spheroidal halo axisymmetric about the z-axis with $q_z = 1.1$, which yields the highest S, S drops from $\sim 99\%$ to $\sim 41\%$ for the same decrease of the sample size; for a spheroidal halo with $q_z = 1.4$, which yields the lowest S, S drops from $\sim 89\%$ to $\sim 32\%$.

On the other hand, for any non-axisymmetric Galactic potential, and for any given sample size, S is expected to be always larger than the rate obtained in the most unfavorable axisymmetric case ($q_z = 1.4$) and typically also larger than the rate obtained in the most favorable axisymmetric case ($q_z = 1.1$).

In addition to increase the success rate S, increasing the size of the HVSs sample decreases the discrepancy between the inferred shape and the correct shape.

Accurate estimates of the success rate of our method when applied to real data require the generation of more realistic mock observed HVS samples, that account for (i)

the uncertainties on the distances and velocities of the HVSs, (ii) the observational limitations of the HVS sample, and (iii) an appropriate mass distribution of the ejected stars. Nevertheless, our analysis suggests that a robust determination of the shape of the DM potential requires measuring the galactocentric velocities of a few hundred HVSs whose galactocentric origin is robustly confirmed.

We will assess elsewhere the sensitivity that is required for our method and that might be reached with future astrometric space missions (Malbet et al., 2016; The Theia Collaboration et al., 2017; Malbet et al., 2019, 2021). Similarly, we will investigate the success rate of our method with expected realistic HVS samples that might come from upcoming spectroscopic surveys (de Jong et al., 2019).

2.9 Appendix

2.9.1 Mock catalogs and observed sample

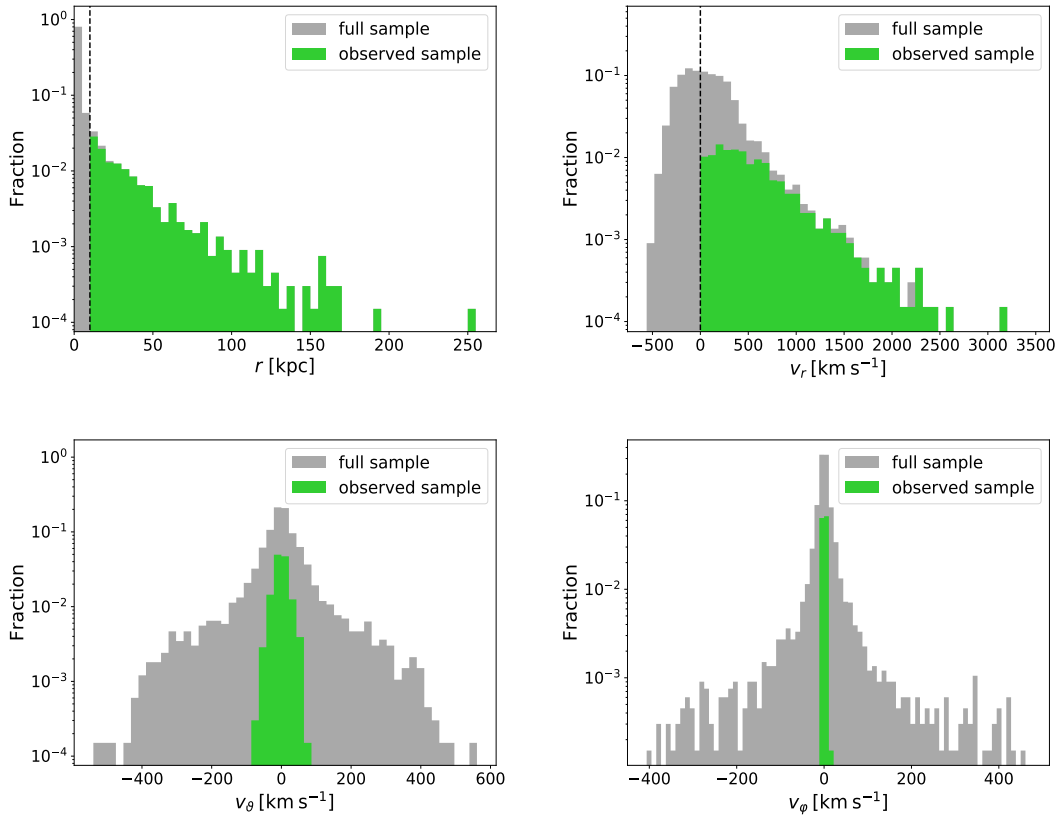

Figure 2.20. Kinematic properties of the HVSs of one of our mock catalogs, corresponding to a Galaxy whose DM halo has a triaxial gravitational potential with $(q_y, q_z) = (1.2,0.9)$. The grey histograms represent the full sample of HVSs; the green histograms represent our observed sample, derived from the full sample by requiring $r > 10$ kpc and $v_r > 0$. *Top left panel*: Distribution of galactocentric distances; the vertical, dashed line corresponds to our threshold radius $r > 10$ kpc. *Top right panel*: Distribution of the radial velocities; the vertical, dashed line corresponds to $v_r = 0$. *Bottom left panel*: Distribution of the latitudinal velocities. *Bottom right panel*: Distribution of the azimuthal velocities.

Fig. 2.20 shows the distributions of the distances to the Galactic center, and of the galactocentric radial, latitudinal, and azimuthal velocities of our simulated HVSs at the steady state (i.e., at the observation time $t_{\rm obs}$; see Sect. 2.1.3) for a mock catalog (see

Sect. 2.1.4) generated in a gravitational potential where the DM halo is triaxial with axis ratios $(q_y, q_z) = (1.2, 0.9)$. The grey histograms correspond to the full sample of simulated HVSs, while the green histograms represent our "observed sample" of ~ 800 HVSs, namely the ideal optimal sample of HVSs that we derived from the full sample by applying the selection criteria $r > 10$ kpc and $v_r > 0$ (see Sects. 2.2.1, 2.2.2, and 2.3). The distributions of the kinematic properties of the stars in the other Galactic potentials we investigated in this work are qualitatively similar to those shown in Fig. 2.20.

2.9.2 Transformation of coordinates and velocities

The Galactic heliocentric position of a star is (d, ℓ, b), with d the heliocentric distance to the star, ℓ its Galactic longitude, and b its Galactic latitude; the Galactic heliocentric velocity is (v_d, v_ℓ, v_b), with v_d the radial velocity of the star, and v_ℓ and v_b the longitudinal and latitudinal components of the heliocentric tangential velocity. The Galactic heliocentric position and velocity components are

$$d = \sqrt{(x + R_\odot)^2 + y^2 + z^2}\,, \tag{2.8}$$

$$l = \arctan\left(\frac{x\,\tan\varphi}{x + R_\odot}\right)\,, \tag{2.9}$$

$$b = \arcsin\left(\frac{z}{d}\right)\,, \tag{2.10}$$

and

$$\begin{aligned} v_d = \quad & (v_x - U_\odot)\,\mathrm{cos}l\,\mathrm{cos}b + [v_y - (V_\odot + \Theta_0)]\,\mathrm{sin}l\,\mathrm{cos}b \\ & + (v_z - W_\odot)\,\mathrm{sin}b\,, \end{aligned} \tag{2.11}$$

$$v_l = \; [v_y - (V_\odot + \Theta_0)]\,\mathrm{cos}l - (v_x - U_\odot)\,\mathrm{sin}l\,, \tag{2.12}$$

$$\begin{aligned} v_b = \quad & (U_\odot - v_x)\,\mathrm{cos}l\,\mathrm{sin}b - [v_y - (V_\odot + \Theta_0)]\,\mathrm{sin}l\,\mathrm{sin}b \\ & + (v_z - W_\odot)\,\mathrm{cos}b\,. \end{aligned} \tag{2.13}$$

The longitudinal component of the proper motion μ is $\mu_\ell = v_\ell/(d\,\mathrm{cos}b)$, and its latitudinal component is $\mu_b = v_b/d$.

We transformed the Galactic heliocentric star position and proper motion to the equatorial system. In this system, the star position is (d, α, δ), with α the right ascension and δ the declination; the star velocity is $(v_d, v_\alpha, v_\delta)$, with v_d still the radial velocity of the star, and v_α and v_δ the components of the star tangential velocity along the right ascension and declination, respectively; the star proper motion is $\mu = (\mu_\alpha, \mu_\delta)$, with $\mu_\alpha = v_\alpha/(d\,\mathrm{cos}\delta)$, and $\mu_\delta = v_\delta/d$.

For the star position, we adopted the transformation equations (Duffett-Smith, 1979)

$$\alpha = \arctan\left[\frac{\mathrm{cos}b\,\mathrm{cos}(\ell - \ell_{\rm asc})}{\mathrm{sin}b\,\mathrm{cos}\delta_G - \mathrm{cos}b\,\mathrm{sin}\delta_G\,\mathrm{sin}(\ell - \ell_{\rm asc})}\right] + \alpha_G\,, \tag{2.14}$$

$$\delta = \arcsin[\mathrm{cos}b\,\mathrm{cos}\delta_G\,\mathrm{sin}(\ell - \ell_{\rm asc}) + \mathrm{sin}b\,\mathrm{sin}\delta_G]\,, \tag{2.15}$$

where α_G and δ_G are the equatorial coordinates of the North Galactic Pole, and $\ell_{\rm asc}$ is the Galactic longitude of the ascending node of the Galactic plane, related to the Galactic longitude of the North Celestial Pole by $\ell_{\rm asc} = \ell_{\rm NCP} - 90^\circ$. We chose J2000.0 as

a reference point for the coordinate conversion. This choice yields $\alpha_G = 192.85948123°$, $\delta_G = 27.12825120°$ (Cox, 2000), and $\ell_{\rm asc} = 32.93192°$ (Poleski, 2013).

For the components of the proper motion μ, we adopted the transformation equations (Poleski, 2013)

$$\mu_\delta = \left(\frac{C_2 \cos b}{C_1^2 + C_2^2} \right) \left({\mu_\ell}^* + \frac{C_1}{C_2} \mu_b \right) , \tag{2.16}$$

$$\mu_\alpha^* = -\frac{1}{C_1} \left(C_2 \mu_\delta - \mu_\ell \cos b \right) , \tag{2.17}$$

with

$$C_1 = \sin\delta_G \cos\delta - \cos\delta_G \sin\delta \cos(\alpha - \alpha_G) , \tag{2.18}$$

$$C_2 = \cos\delta_G \sin(\alpha - \alpha_G) , \tag{2.19}$$

and $\mu_\ell^* = \mu_\ell \cos b$, $\mu_\alpha^* = \mu_\alpha \cos\delta$, and $\mu_\alpha^{*2} + \mu_\delta^2 = \mu_\ell^{*2} + \mu_b^2 = \mu^2$.

Chapter 3

Probing MOdified Newtonian Dynamics with hypervelocity stars [1]

The most popular and widely investigated solution to the problem of the mass discrepancy in the Universe is to assume the presence of cold dark matter that is non-baryonic and interacts with the baryons only via gravity (Peebles, 1982; Bond et al., 1982; Blumenthal et al., 1982, 1984; Spergel et al., 2007; Frenk and White, 2012; Strigari, 2013; Planck Collaboration et al., 2020a), as illustrated in Sect. 1.1. However, to date, none of the elementary particles suggested as candidates of dark matter has been detected (Tanabashi et al., 2018).

In principle, the mass discrepancy problem can be solved with a modification of the theory of gravity rather than with dark matter (Sanders, 1990; Sanders and McGaugh, 2002; Clifton et al., 2012; Nojiri et al., 2017). Modified Newtonian dynamics (MOND; Milgrom, 1983a,b,c) is one of the most investigated modifications of Newtonian gravity (e.g., Famaey and McGaugh, 2012; McGaugh, 2020), and proved to be predictive and successful on galaxy scales, as detailed in Sect. 1.3.3.

However, a number of MOND predictions concerning the Milky Way (MW; Famaey and McGaugh, 2012) and the nearby dwarfs (Hodson et al., 2020) still need to be tested with upcoming astrometric data. Indeed, when interpreted in Newtonian gravity, the MOND gravitational field requires the presence of "phantom dark matter" in addition to the baryonic matter (Milgrom, 1983b; Bekenstein and Milgrom, 1984). Specifically, MOND predicts the existence of a disk of phantom dark matter in the MW (Bienaymé et al., 2009); therefore, the acceleration of the stars perpendicular to the plane of the disk can constrain the total surface density of the baryonic and phantom disks (Nipoti et al., 2007). At 1.1 kpc above the Galactic plane at the distance of the Sun from the Galactic center, the total surface density in MOND is expected to be 60% larger than the surface density of the baryonic disk, whereas this enhancement is predicted to be 51% in Newtonian gravity with a spherical dark matter halo (Bienaymé et al., 2009; Famaey and McGaugh, 2012). Similarly, the scale length of the "baryonic + phantom" disk can be constrained by the vertical acceleration profiles at different radii. In the formulation of MOND suggested by Bekenstein and Milgrom (1984), this scale length should be 1.25 times the scale length of the visible stellar disk (Bienaymé et al., 2009; Famaey and McGaugh, 2012). Moreover, the angle between the minor axis of the velocity ellipsoid of the stars in the solar neighborhood and the vertical direction depends on the shape of the gravitational potential (Cuddeford and Amendt, 1991): for axisymmetric potentials,

[1] The results presented in this chapter are published in our work Chakrabarty et al. (2022)

the angles expected in MOND and Newtonian gravity with a spherical dark matter halo differ by 2 degrees at the distance of the Sun from the MW center and at 2 kpc above the MW disk (Bienaymé et al., 2009).

In this Chapter we propose a novel prediction of MOND concerning the positions and proper motions of hypervelocity stars (HVSs; see Sect. 1.5) within the MW. The HVSs are ejected from the Galactic center with a speed of several hundred km s^{-1} or higher. These stars are sometimes separated into samples of bound and unbound stars. This distinction is irrelevant for our purpose here, and we consider as an HVS any star that is ejected from the Galactic center on a purely radial orbit with null tangential velocity in the galactocentric reference frame. Hypervelocity stars obtain nonzero tangential velocities due to the non-spherical components of the Galaxy gravitational potential. As they travel to large distances from the center, the distribution of their positions and velocities carries signatures of the gravitational field of the Galaxy.

As illustrated in Chpt. 2, several schemes to constrain the shape of the DM halo required in Newtonian gravity (Gnedin et al., 2005; Rossi et al., 2017; Contigiani et al., 2019; Gallo et al., 2022) and to measure the virial mass of the MW (Fragione and Loeb, 2017) using HVSs have been proposed. However, prior to our work, the only attempt to investigate MOND with HVSs was carried out by Perets et al. (2009) who suggested a novel method to discriminate between various models of Galactic potential within CDM and MOND paradigms using the asymmetry of the velocity distributions of incoming and outgoing HVSs. The asymmetry is likely generated by both the structure of the Galactic potential and the finite lifetime of the stars and can be used to probe the Galactic potential. They explored five dark matter (CDM) potentials and one MOND potential and found that two out of the five CDM models of the gravitational potential are disfavored, while the remaining three models and the MOND potential all give similar results.

Here, we simulate the kinematics of the HVSs in MOND as well as in Newtonian gravity. We show that the azimuthal components, v_ϕ, of the tangential velocities of the HVSs may distinguish MOND from Newtonian gravity. Section 3.1 illustrates the quasi-linear formulation of MOND (QUMOND) that we adopt in this work. Section 3.2 describes our model of the distribution of the MW baryonic matter that generates the QUMOND gravitational potential. In Sect. 3.3 we illustrate the model of the dark matter halo we adopt for comparison with the QUMOND predictions. In Sect. 3.4 we illustrate and discuss our simulations. In Sect. 3.5 we show the galactocentric tangential velocities of the HVSs in QUMOND and detail our QUMOND predictions. We conclude in Sect. 3.6.

3.1 Quasi-linear modified Newtonian dynamics

Throughout this work, we adopted QUMOND, the quasi-linear formulation of MOND (Milgrom, 2010), where the gravitational field is

$$\vec{g} = \nu\left(\frac{|\vec{g}_{\rm N}|}{a_0}\right)\ \vec{g}_{\rm N} \tag{3.1}$$

and $\vec{g}_{\rm N}$ is the Newtonian gravitational field due to the baryonic matter alone. The interpolating function $\nu(x)$ satisfies the limits $\nu(x) \to 1$ when $x \gg 1$, and $\nu(x) \to x^{-1/2}$ when $x \ll 1$. We adopt

$$\nu(x) = \left[\frac{1}{2}\left(1+\sqrt{1+4x^{-\gamma}}\right)\right]^{\frac{1}{\gamma}}\ , \tag{3.2}$$

with $\gamma = 1$ or $\gamma = 2$ (Famaey and McGaugh, 2012). The function with $\gamma = 1$ is known as the simple interpolation function. The acceleration scale, below which Newtonian gravity modifies, is set by a_0. The value of a_0 is found by fitting the rotation curve data (Begeman et al., 1991; Bottema et al., 2002), the observed correlation between the mass discrepancy and the acceleration (McGaugh, 2004), and the baryonic Tully-Fisher relation (McGaugh, 2011). The best-fit value of a_0 varies from 3000 to 4000 km^2 s^{-2} kpc^{-1} and also slightly depends on the chosen interpolation function $\nu(x)$ (Eq. 3.2). We chose an intermediate value: $a_0 = 3600$ km^2 s^{-2} kpc^{-1} $= 1.2 \times 10^{-10}$ m s^{-2}.

For the Galaxy, we first assumed a simple model with three baryonic components: a central SMBH, a stellar disk and a stellar bulge. With this model, the Newtonian acceleration entering Eq. (3.1) is

$$\vec{g}_{\rm N} = -\vec{\nabla}(\Phi_{\rm BH} + \Phi_{\rm Bulge} + \Phi_{\rm Disk})\,, \tag{3.3}$$

where $\Phi_{\rm BH}$, $\Phi_{\rm Bulge}$, and $\Phi_{\rm Disk}$ are the Newtonian gravitational potentials that we provide in the next section. A more sophisticated model that includes the additional baryonic component of a hot gaseous (HG) halo will be discussed in Sect. 3.5.1.

3.2 Newtonian gravitational potentials

We investigated two variants of the model for the baryonic gravitational potential that enters Eq. (3.3): an axisymmetric model and a non-axisymmetric model. In the latter model, the deviation from the axial symmetry originates only from the presence of a triaxial bulge. We used the reference frame of the Galaxy with the origin at the Galaxy center. We used cylindrical coordinates (R, ϕ, z) for the axisymmetric model and Cartesian coordinates (x, y, z) for the triaxial model; R lies on the x-y plane, which we take as the equatorial plane of the Galactic disk. For the spherically symmetric components, we used spherical polar coordinates (r, θ, ϕ).

3.2.1 The axisymmetric model

We adopted simple analytical potentials for the three MW components. For the stellar disk, we used the Miyamoto-Nagai model (Miyamoto and Nagai, 1975)

$$\Phi_{\rm Disk}(R, z) = -\frac{GM_{\rm D}}{\sqrt{R^2 + \left(a_{\rm D} + \sqrt{z^2 + b_{\rm D}^2}\right)^2}}\,, \tag{3.4}$$

with $M_{\rm D} = 1.0 \times 10^{11}\ M_\odot$, $a_{\rm D} = 6.5$ kpc, and $b_{\rm D} = 0.26$ kpc (Kafle et al., 2014; Price-Whelan et al., 2014; Rossi et al., 2017; Contigiani et al., 2019).

For the bulge, we took the Hernquist sphere (Hernquist, 1990)

$$\Phi_{\rm Bulge}(r) = -\frac{GM_{\rm B}}{r_{\rm B} + r}\,, \tag{3.5}$$

with $M_{\rm B} = 3.4 \times 10^{10}\ M_\odot$, $r_{\rm B} = 0.7$ kpc (Kafle et al., 2014; Price-Whelan et al., 2014; Rossi et al., 2017; Contigiani et al., 2019), and a total bulge mass of $3.0 \times 10^{10} M_\odot$.

Finally, the gravitational potential of the central SMBH is

$$\Phi_{\rm BH}(r) = -\frac{GM_{\rm BH}}{r}\,, \tag{3.6}$$

with $M_{\rm BH} = 4.0 \times 10^6\ M_\odot$. This mass of the SMBH is comparable to various estimates reported in the literature (e.g., Eisenhauer et al., 2005; Ghez et al., 2008; Boehle et al., 2016; Gillessen et al., 2017).

In this model, the axial symmetry of the MW originates only from the stellar disk because the gravitational potentials of the SMBH and the bulge are spherically symmetric.

3.2.2 The non-axisymmetric model: The triaxial bulge

To estimate the impact of a non-axisymmetric distribution of the baryonic matter on the HVSs kinematics in QUMOND, we considered the effects of a triaxial bulge and kept unaltered the gravitational potentials of the SMBH and the stellar disk of the axisymmetric model. A triaxial bulge is the primary source of azimuthal angular momentum within the Galaxy (Gardner et al., 2020). Our adopted density profile of the triaxial bulge is (Binney et al., 1997; McGaugh, 2008):

$$\rho_{\rm Bulge}(x,y,z) = \frac{M_0}{\eta\zeta b_{\rm m}^3}\ \frac{e^{-(b/b_{\rm m})^2}}{\left(1+\frac{b}{b_0}\right)^{1.8}}\,, \tag{3.7}$$

where

$$b = \sqrt{x^2 + \frac{y^2}{\eta^2} + \frac{z^2}{\zeta^2}}\,, \tag{3.8}$$

$\eta = 0.5$, $\zeta = 0.6$, $b_{\rm m} = 1.9$ kpc, and $b_0 = 0.1$ kpc (Binney et al., 1997). The parameters are determined from the observed luminosity distribution (Binney et al., 1997) and indicate that the largest axis of the bulge, the x axis, is in the plane of the disk, and the second largest axis, the z axis, is in the vertical direction. It follows that two principal axes of the bulge are in the plane of the disk and, therefore, the bulge is not tilted with respect to the plane of the disk. We chose the value of M_0 so that the Newtonian accelerations due to the triaxial and the spherical bulges are comparable at $R \gtrsim 0.5$ kpc in the plane of the disk; in other words, the axisymmetric and non-axisymmetric models yield comparable rotation curves beyond ~ 0.5 kpc and the dynamical differences between the two models are limited to the central region. We set $M_0 = 5.7 \times 10^{11} M_\odot$, which yields a total mass of the bulge of $2.1 \times 10^{10} M_\odot$. Figure 3.1 compares the density profiles of the spherical and triaxial bulges in our two models.

We derived the Newtonian gravitational potential of the triaxial bulge, $\Phi_{\rm Bulge}$, by solving the standard Poisson's equation in three dimensions within a box of volume (16 kpc)^3 about the center. Figure 3.2 shows that the magnitudes of the Newtonian radial acceleration for the triaxial bulge are comparable to the Newtonian radial acceleration generated by the spherical bulge of Eq. (3.5) at $R \gtrsim 0.5$ kpc, as we require with our choice of M_0. Within a distance of 0.1 kpc from the center, the spherical bulge generates a larger acceleration due to its steeper density profile shown in Fig. 3.1. In the intermediate regions between 0.1 kpc and ~ 0.5 kpc, the density profile of the spherical bulge is smaller than the density profile of the triaxial bulge; however, the radial acceleration of the spherical bulge is still larger than the acceleration of the triaxial case in any direction because, due to the steeper central density, the spherical bulge encloses a larger mass within ~ 0.5 kpc. At large distances, $r \gtrsim 5$ kpc, the triaxiality is not effective and the mass distribution within the bulge can be treated as spherically symmetric.

McGaugh (2008) investigates the mass model of the MW in the context of MOND by matching the predicted rotation curve against observations. The scale length of the stellar disk and the mass of the bulge determine the relative contributions of these two

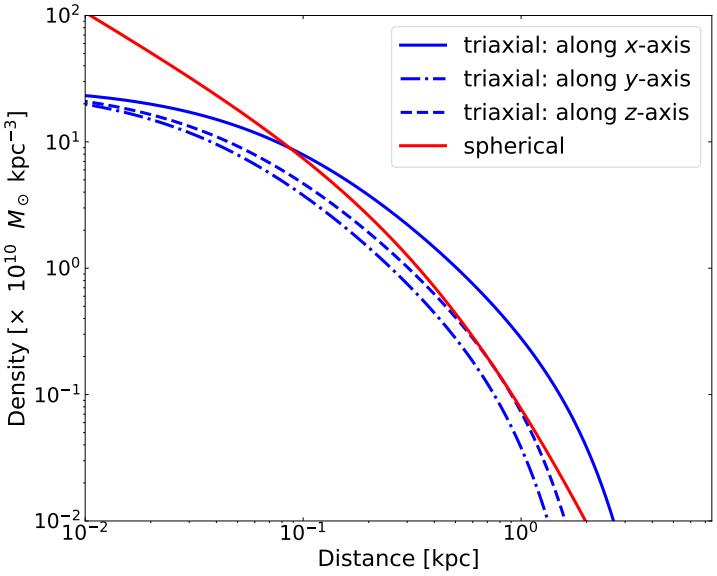

Figure 3.1. Density profiles of the spherical (red) and triaxial (blue) bulges as functions of the distance from the center. For the triaxial bulge, we show the density profiles along the x, y, and z axes.

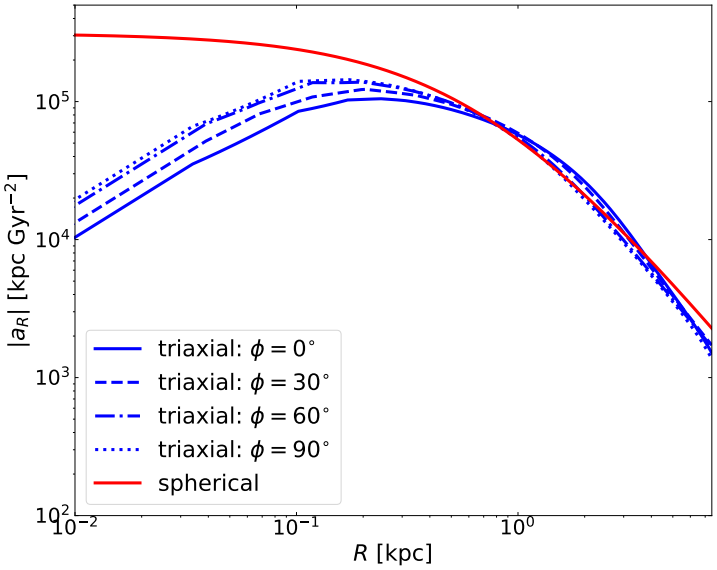

Figure 3.2. Magnitude of the radial acceleration in the plane of the disk, $|a_R|$, due to the bulge alone in Newtonian gravity: spherical bulge (red) and triaxial bulge (blue). For the triaxial bulge, the acceleration varies with the azimuthal angle, ϕ, which is the angle with respect to the x axis in the plane of the disk. We show the results for various values of ϕ; $\phi = 0°$ and $\phi = 90°$ correspond to the x and y axes, respectively.

components of the Galaxy to the total rotation curve. Our model is roughly comparable to the model of McGaugh (2008) that has the stellar disk with scale length $R_\mathrm{d} = 4$ kpc and bulge mass within 1% of the bulge mass in our model. Indeed, the circular velocity v_circ in the McGaugh model is within 5% of our v_circ within $r = 3$ kpc, and $\sim 10\%$ smaller at $r > 3$ kpc. For different values of R_d, the agreement slightly worsens. For example, in McGaugh's model with $R_\mathrm{d} = 2.3$ kpc, v_circ is $\sim 30\%$ smaller than our v_circ within $r = 3$ kpc, but remains within $\sim 5\%$ at $r > 3$ kpc.

3.3 The dark matter halo in Newtonian gravity

We needed to compare the dynamics of HVSs in QUMOND with the corresponding expectations in Newtonian gravity. We thus also considered a Newtonian model of the MW with the same axisymmetric baryonic components described in the previous section, but with an additional surrounding dark matter halo.

For the dark matter halo, we adopted the triaxial generalization suggested by Vogelsberger et al. (2008) of the spherical NFW gravitational potential (Navarro et al., 1997):

$$\Phi_{\rm Halo} = -\frac{GM_{200}}{f(C_{200})}\,\frac{1}{\tilde{r}}\,\ln\left(1+\frac{\tilde{r}}{r_{\rm s}}\right)\,, \tag{3.9}$$

where $f(u) = \ln(1+u) - u/(1+u)$. $M_{200} = 8.35 \times 10^{11} M_{\odot}$ is the mass within r_{200},[2] $C_{200} = r_{200}/r_{\rm s} = 10.82$ is the concentration parameter, and $r_{\rm s} = 18$ kpc is the scale radius. Our adopted values of the parameters are those used in Hesp and Helmi (2018). They are consistent with the estimates from the kinematics of halo stars (Xue et al., 2008; Deason et al., 2012b). The generalized radius is

$$\tilde{r} = \frac{r_E(r+r_{\rm a})}{r_E + r_{\rm a}}\,, \tag{3.10}$$

where the ellipsoidal radius r_E is

$$r_E = \sqrt{\left(\frac{x}{a}\right)^2 + \left(\frac{y}{b}\right)^2 + \left(\frac{z}{c}\right)^2} \tag{3.11}$$

and $r_{\rm a} = 1.2 r_{\rm s}$ (Hesp and Helmi, 2018) is the length scale that determines the transition from the triaxial to the spherical shape: In the inner region ($r \ll r_{\rm a}$) the halo is triaxial ($\tilde{r} \approx r_E$), whereas in the outer region ($r \gg r_{\rm a}$) the halo is almost spherical ($\tilde{r} \approx r$). This transition in the shape of the halo is a generic prediction of ΛCDM simulations (see, e.g., Hayashi et al., 2007). The parameters a, b and c satisfy the relation $a^2 + b^2 + c^2 = 3$.

We defined the two triaxiality parameters $q_y = b/a$ and $q_z = c/a$. Once q_y and q_z are specified, a is given by

$$a = \sqrt{\frac{3}{1+q_y^2+q_z^2}}\,. \tag{3.12}$$

Since the shape of the halo is currently poorly constrained (Bland-Hawthorn and Gerhard, 2016), we varied either q_y or q_z within 40% from unity.

In this work we did not use a triaxial dark matter halo. We only explored spheroidal halos with different axes of symmetry (see Fig. 3.3). To study the effects of the dark matter halo shape on the azimuthal component of the HVS velocity, v_ϕ (see Fig. 3.4), we chose a spheroidal halo that is axisymmetric about the y axis lying in the plane of the disk (case (b) of Fig. 3.3) whereas the baryonic components are axisymmetric about the vertical z axis. In this model, we set $q_y > 1$ and $q_z = 1$. To study the effects of the dark matter halo shape on the latitudinal component v_θ of the HVS velocities, we considered a spheroidal halo that is axisymmetric about the z axis (i.e., $q_y = 1$ and $q_z \neq 1$). The halo is oblate if $q_z < 1$ and prolate if $q_z > 1$ (cases (c) and (d) of Fig. 3.3). Indeed, the kinematics of halo stars from the Sloan Digital Sky Survey suggests that the dark matter halo might be oblate within ~ 20 kpc, with $q_z = 0.7 \pm 0.1$, based on the estimate of constant potential surfaces (Loebman et al., 2014).

[2] r_{200} is the radius of a spherical volume within which the mean mass density is 200 times the critical density of the Universe.

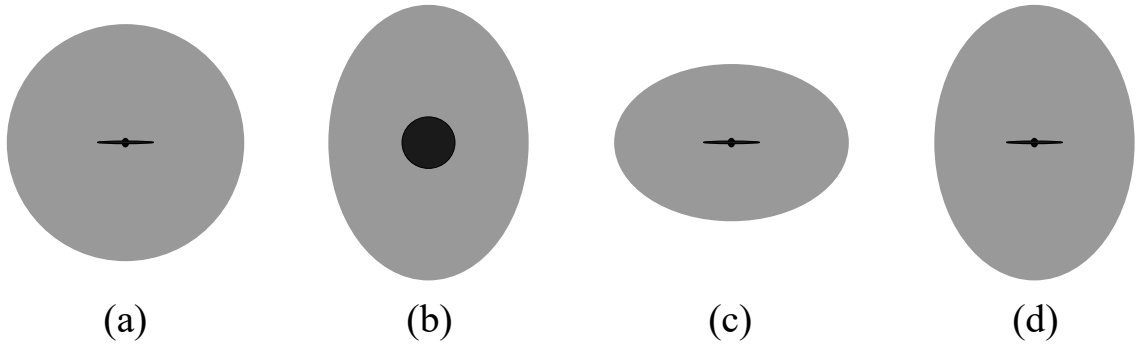

Figure 3.3. Schematic diagrams of our models of the Galaxy in Newtonian gravity. The baryonic components, the bulge and the disk, are shown in black and the dark matter halo in gray. Different shapes of the dark matter halo are shown: (a) spherical (edge-on view of the disk), (b) prolate with the major axis on the plane of disk (face-on view of the disk), (c) oblate with the minor axis perpendicular to the disk (edge-on view of the disk), and (d) prolate with the major axis perpendicular to the disk (edge-on view of the disk). Only in case (b) are the axes of symmetry of the disk and the halo not aligned.

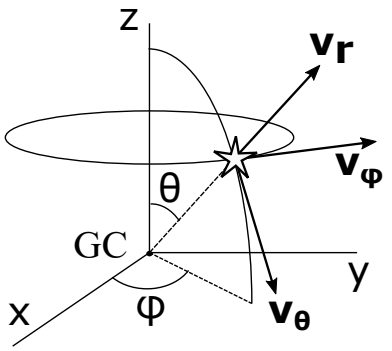

Figure 3.4. Components of the velocity of a star in the spherical polar coordinates with origin at the Galactic center (GC): $\vec{v} = \vec{v}_r + \vec{v}_\theta + \vec{v}_\phi$.

At the solar neighborhood ($R = 8$ kpc), our models yield a circular velocity of 235 km s^{-1} in Newtonian gravity and 240 (210) km s^{-1} in QUMOND with $\gamma = 1$ ($\gamma = 2$). In addition, in our Newtonian model, the total mass enclosed within 120 pc is in perfect agreement with the observed value reported in Table 3 of Kenyon et al. (2008), derived from the estimate of the mass of the central region of the stellar disk of Launhardt et al. (2002). The MW central region is where the HVSs experience the largest deceleration. We verified that varying the radial acceleration profile of the MW central region within the observational uncertainties does not affect our conclusions on the tangential velocities of the HVSs.

3.4 Simulations of the kinematics of the HVSs

In this section we describe our simulations and our synthetic samples of HVSs. Section 3.4.1 illustrates the initial conditions of the equations of motion of the HVSs that we adopted. In Sect. 3.4.2 we show that only stars beyond a minimum galactocentric distance, corresponding to a minimum ejection velocity, are relevant to discriminate between

QUMOND and Newtonian gravity. This threshold depends on the star mass: for 4 $M_\odot$ stars, the minimum galactocentric distance is 15 kpc, which corresponds to the minimum ejection velocity $\sim$ 750 km s^{-1} for models in Newtonian gravity and QUMOND with $\gamma = 1$. For QUMOND with $\gamma = 2$, the ejection velocity threshold is $\sim$ 710 km s^{-1}, which also corresponds to a minimum distance of 15 kpc.

3.4.1 Simulation setup

We assumed that the HVSs are generated through Hills' mechanism (Hills, 1988): In a three-body interaction between the SMBH associated with SgrA* and a binary star, one star of the binary is ejected and the other is captured by the black hole. We emphasize that the assumption of Hills' mechanism for the ejection of the HVSs does not affect our conclusions, as detailed at the end of this section.

In Hills' ejection scenario, we simulated the velocity distribution of the HVSs ejected from the Galactic center by means of a three-body numerical code that reproduces the encounter of a set of equal-mass binary stars with the SMBH. The binaries' orbital parameters and minimum approach distance to the SMBH are drawn from appropriate distributions (Bromley et al. (2006) and references therein). More details on the numerical code and on the ejection velocity distribution will be provided in Gallo et al. (2022) (see Sect. 2.1.1) and in an additional, separate paper. Here, we only report the information that is instrumental to the present analysis.

We adopted a mass $M_{\rm BH} = 4 \times 10^6 M_\odot$ for the black hole (as in our model in Sect. 3.2.1) and a mass of 4 $M_\odot$ for each star in the binary. The choice of mass for the binary stars is consistent with the fact that most of the observed unbound HVSs have masses between 2.5 and 4 $M_\odot$ (Brown, 2015). In addition, choosing the upper limit of this mass range is a conservative choice that is appropriate for our investigation, as we clarify in Sect. 3.5. We obtained a distribution of ejection speeds that displays a prominent peak at $v_{\rm ej} \sim 510$ km s^{-1}, extends to velocities of $\sim$ 4000 km s^{-1}, and has a positive skewness; 16% (12%) of the ejected stars have speed $v_{\rm ej} \gtrsim 710$ (750) km s^{-1}, a value that will be relevant for the present analysis (see Sect. 3.4.2). Our results on the ejection velocities are comparable to the results obtained from the analytical prescriptions provided by Bromley et al. (2006).

The distribution of ejection speeds formally corresponds to the distribution of velocities that the ejected stars would have at infinite distance from the SMBH in absence of other sources of gravitational potential. However, in the context of the Galactic center, this distribution can be taken as the velocity distribution of the ejected stars at the starting point of their trajectories across the MW, which we set as the radius of the sphere of influence of the SMBH (i.e., $r = 3$ pc; Genzel et al., 2010). Although the distribution of ejection velocities weakly depends on the binary mass (Bromley et al., 2006), our results regarding the kinematics of the HVSs are independent of their mass, because the gravitational acceleration acting on the HVSs is mass-independent.

The direction $\hat{n}(\theta, \phi)$ of the ejection velocity is assigned randomly to each star, because Hills' mechanism yields isotropic ejections. We used the fourth order Runge-Kutta method with adaptive step-size to integrate the equation of motion of each star. We started with a predefined time-step of 5 kyr and the time-step was adjusted so that, at each step, the position and velocity of the star were determined with an accuracy of 1 pc and 0.01 km s^{-1}, respectively. For stars with ejection velocities higher than 600 km s^{-1}, the conservation of total energy holds with a relative accuracy of 10^{-12} for each time-step as well as over the entire simulation. Stars with ejection velocities lower than 600 km s^{-1} are not relevant for our study.

The typical lifetime of an isolated star of 4 $M_\odot$ on the main sequence is $\tau_{\rm L} \simeq 160$ Myr, for Solar metallicities (Schaller et al., 1992; Brown et al., 2006b). We assumed this lifetime as the total lifetime of our simulated stars. At the time of ejection, each star was assigned a random age of $\tau_{\rm ej} = \epsilon\tau_{\rm L}$, where ϵ is a random number drawn from a uniform density distribution between 0 and 1. We took the average ejection rate to be 10^{-4} yr^{-1}, which is consistent with the estimates by Yu and Tremaine (2003) and Zhang et al. (2013) (see also Hills, 1988). Therefore, in the simulation, we ejected stars in intervals of $\Delta t = 0.01$ Myr. For our chosen lifetime and ejection rate, the distribution of ejected stars in the MW reaches a steady state after 160 Myr. We started the simulation at $t = 0$ and the i-th star was ejected at $t = (i-1)\Delta t$ with its age $\tau^i_{\rm ej}$ at the time of ejection. We chose the time of observation, which is the total run-time of the simulation, to be $t_{\rm obs} = 400$ Myr when the distribution of the HVSs is in the stationary regime. For each star, we tested the condition of its survival: A star survives long enough to be observed if $[t_{\rm obs} - (i-1)\Delta t] < (\tau_{\rm L} - \tau^i_{\rm ej})$. If a star satisfies this condition, its travel time is determined by $[t_{\rm obs} - (i-1)\Delta t]$.

We simulated the kinematics of the HVSs through the Galaxy (i) for QUMOND, with the baryonic components only, and (ii) for Newtonian gravity, with the baryonic components and the dark matter halo. For each model of the Galactic potential, we determined positions and velocities of the HVSs at the time of observation, $t = t_{\rm obs}$. Tables 3.1 and 3.2 summarize the simulations that we performed in QUMOND and in Newtonian gravity. The tables list both the simulations of our simpler model for the baryonic Galactic components considered in Eq. (3.3) and described in Sect. 3.2 and the simulations that include the additional non-spherical HG halo surrounding the MW (see Sect. 3.5.1).

Table 3.1. List of the simulations for QUMOND.

γ	Bulge	Hot gaseous halo	Number of stars
1	spherical	no	40000
1	triaxial	no	individual stars
2	spherical	no	40000
2	triaxial	no	individual stars
1	spherical	yes	40000
2	spherical	yes	40000

Notes. To find the upper limit of $|v_\phi|$ for QUMOND with a triaxial bulge, we performed many simulations of individual stars. In this case, we used the gravitational field of the triaxial bulge within 5 kpc of the Galactic center and that of the spherical bulge at larger radii.

Table 3.2. List of the simulations for Newtonian gravity.

q_y	q_z	Panel of Fig. 3.3	Hot gaseous halo
1	0.9	c	no
1	1	a	no
1	1.1	d	no
1.1	1	b	no
1.2	1	b	no
1.2	1	b	yes
1.4	1	b	yes

Notes. Simulations in Newtonian gravity were performed with a spherical bulge. Each simulation contains 40000 stars.

We compared the final phase-space distributions of the HVSs obtained in QUMOND with the distributions obtained in Newtonian gravity. Due to the large radial velocities

of the HVSs, their phase-space distributions in the (r, v_r) or (z, v_z) space in QUMOND are virtually indistinguishable from those in Newtonian gravity (left and middle panels of Fig. 3.5). However, the distributions of the galactocentric tangential velocity components, the latitudinal component $v_\theta = r(\mathrm{d}\theta/\mathrm{d}t)$, and the azimuthal component $v_\phi = r\sin\theta(\mathrm{d}\phi/\mathrm{d}t)$, are distinctive and can be used, in principle, to discriminate between QUMOND and Newtonian gravity (right panel of Fig. 3.5). Our result is independent of the mechanism responsible for the ejection of the HVSs from the Galactic center: any mechanism that can expel stars from the Galactic center with radial velocities $v_{\rm ej} \gtrsim 710$ km s^{-1}, as we discuss below, and null tangential velocities would be suitable to perform the analysis presented in this work, leading to the same conclusions.

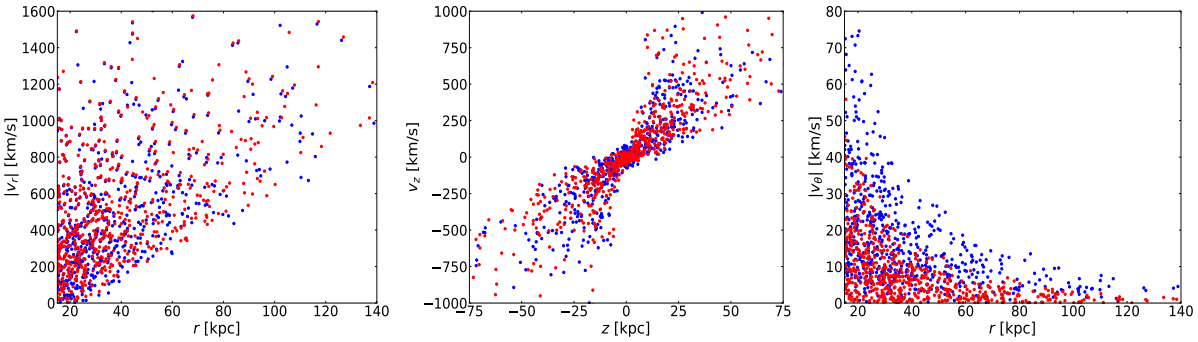

Figure 3.5. Distributions of HVSs in three sections of phase space in QUMOND with $\gamma = 1.0$ (blue dots) and Newtonian gravity with a prolate ($q_y = 1, q_z = 1.1$) dark matter halo (red dots). The left, middle, and right panels show the r-v_r, z-v_z, and r-v_θ sections, respectively. Here, r is the galactocentric distance, z is the vertical coordinate, and v_r, v_z, v_θ are the radial, vertical, and latitudinal components of the velocity, respectively.

3.4.2 Evolution of the tangential velocity components

The tangential velocity components of the HVSs are excellent probes of the non-spherical components of the Galactic gravitational potential. However, this distinctive ability only holds for HVSs with ejection speeds higher than a threshold: for stars with lower ejection speed, the tangential velocity components may indeed be disproportionately high.

To find the threshold ejection velocity, we simulated the dynamics of 200 HVS with mass 4 $M_\odot$, ejection velocities $v_{\rm ej}$ between 650 and 850 km s^{-1}, and random initial directions. For each star, the simulation time was taken to be its lifetime, namely 160 Myr for 4 $M_\odot$ stars. This time is the maximum possible travel time. For each star, we determined the maximum values of the magnitudes of the tangential velocity components, $|v_\theta|$ and $|v_\phi|$.

We considered both Newtonian gravity with different shapes of the dark matter halo and QUMOND with $\gamma = 1$ and $\gamma = 2$. For both the Newtonian and the QUMOND scenarios, the baryonic components (Eqs. 3.4 - 3.6) were taken to be axisymmetric about the z axis. Due to the pull of the disk, the stars obtain nonzero v_θ values for all the models. However, in QUMOND with a spherical bulge, the stars do not obtain any $|v_\phi|$ because the baryonic matter, the only component present, is axisymmetric. In our models of Newtonian gravity, the stars acquire nonzero values of v_ϕ only when the two axes of symmetry of the baryonic and dark matter components are misaligned: for example, for $(q_y, q_z) = (1.1, 1)$ (panel (b) in Fig. 3.3), the dark halo is symmetric about the y axis whereas the baryonic matter is symmetric about the z axis. When no such misalignment is present, as in the cases sketched in panels (a), (c), and (d) of Fig. 3.3, v_ϕ vanishes, and the only non-null component of the tangential velocity is the latitudinal velocity, v_θ.

The left panel of Fig. 3.6 shows that $|v_\theta|$ can be as large as 600 km s^{-1} for stars with $v_{\rm ej} < 710$ km s^{-1} in QUMOND with $\gamma = 2$, and for stars with $v_{\rm ej} < 750$ km s^{-1} in all the other models. In contrast, for stars with ejection speed higher than these thresholds, the maximum values of $|v_\theta|$ are consistently lower than ~ 100 km s^{-1}. The right panel of Fig. 3.6 shows qualitatively similar results for $|v_\phi|$ in the Newtonian models with the misaligned axes of symmetry ($q_y \neq 1$): in these models, $|v_\phi|$ is lower than ~ 20 km s^{-1} when $v_{\rm ej} \gtrsim 750$ km s^{-1}. In these Newtonian models with $q_y \neq 1$, the vertical scatter in the maximum values of $|v_\theta|$ (left panel) is large. The stars ejected with smaller angle with respect to the disk (i.e., $(90^\circ - \theta) \lesssim 30^\circ$) undergo larger deflection and attain larger $|v_\theta|$. On the other hand, the stars ejected almost perpendicular to the disk do not bend significantly, hence have smaller $|v_\theta|$. Conversely, in the same Newtonian models, the stars always attain a $|v_\phi| \gtrsim 350$ km s^{-1} (right panel) irrespective of the direction of the HVS ejection velocity.

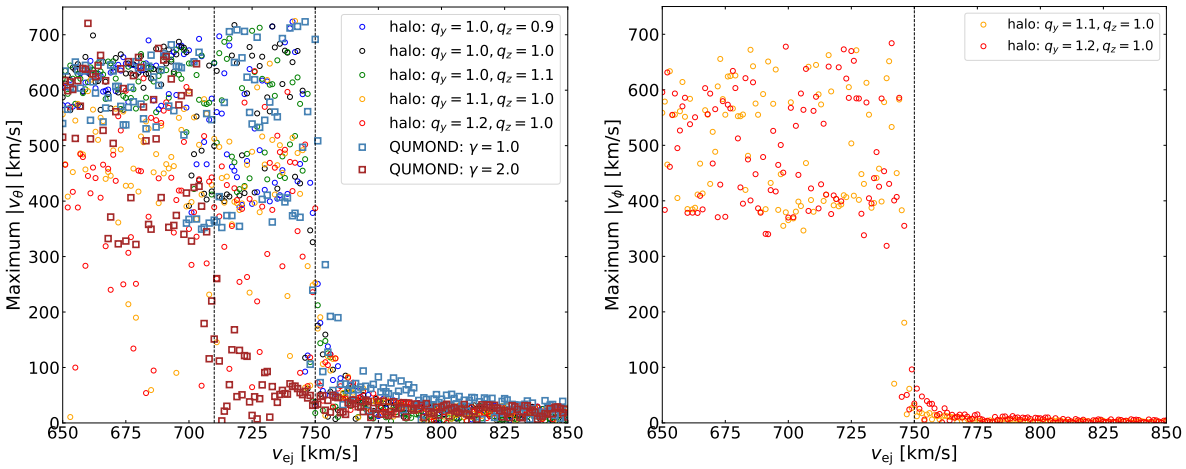

Figure 3.6. *Left panel:* Maximum values of the latitudinal velocity components, $|v_\theta|$, of 4 $M_\odot$ HVSs as a function of their ejection velocities, $v_{\rm ej}$, in Newtonian gravity with different shapes of the dark matter halo and in QUMOND with $\gamma = 1$ and $\gamma = 2$; symbols and models are detailed in the inset. The vertical scatter in the plot originates from the random directions of the star ejection. The vertical dotted lines indicate $v_{\rm ej} = 710$ and $v_{\rm ej} = 750$ km s^{-1}. In all the models except QUMOND with $\gamma = 2$, the maximum $|v_\theta|$ substantially drops for stars with $v_{\rm ej} \gtrsim 750$ km s^{-1}. For QUMOND with $\gamma = 2$, the maximum $|v_\theta|$ drops for stars with $v_{\rm ej} \gtrsim 710$ km s^{-1}. *Right panel:* Maximum values of the azimuthal velocity components, $|v_\phi|$, of 4 $M_\odot$ HVSs as a function of their ejection velocities, $v_{\rm ej}$, in two Newtonian gravity models where the axes of symmetry of the baryonic matter and of the dark matter halo are misaligned. The other models considered in the left panel do not appear because they are axisymmetric and have zero $|v_\phi|$ values. The vertical scatter originates from the random directions of the star ejection. The vertical dotted line indicates $v_{\rm ej} = 750$ km s^{-1}.

High tangential velocities of the stars with lower ejection speed are caused by the exchange of kinetic energy between radial and angular degrees of freedom, especially when the stars undergo an inner turnaround. Figure 3.7 illustrates that the inner turnaround does occur for stars with low ejection velocity. In Fig. 3.7 we show v_ϕ as a function of the radial component v_r for three stars with ejection velocity $v_{\rm ej} = \{745, 747, 749\}$ km s^{-1} in the Newtonian models with the misaligned axes, with $(q_y, q_z) = (1.1, 1)$. In each case, $v_r = v_{\rm ej}$ and $v_\phi = 0$, initially; at later times, v_ϕ starts increasing as v_r decreases. When $v_r = 0$ for the first time, as indicated by the vertical dotted lines, the star undergoes the outer turnaround, namely it reaches its maximum distance from the MW center and starts moving inward. Therefore, v_r becomes negative while v_ϕ keeps increasing. When v_r becomes zero for the second time, the star undergoes the inner turnaround, namely the star reaches the closest approach to the center and starts again moving outward.

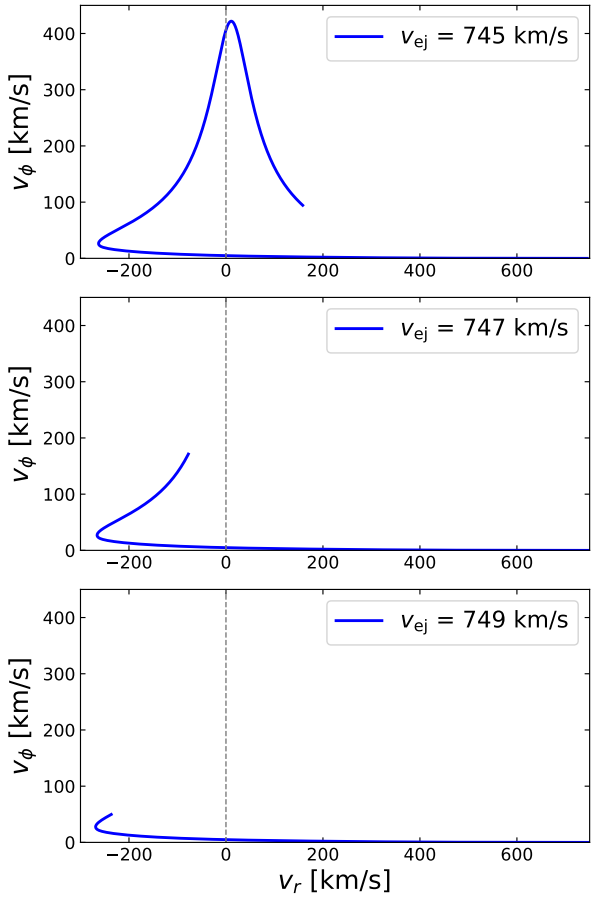

Figure 3.7. Azimuthal velocity component, v_ϕ, as a function of the radial velocity component, v_r, for three HVSs with mass 4 $M_\odot$ and ejection velocity $v_{\rm ej} = \{745, 747, 749\}$ km s^{-1} in Newtonian gravity with $(q_y, q_z) = (1.1, 1)$. In each case, the star starts with $v_r = v_{\rm ej}$ and $v_\phi = 0$. The maxima of v_ϕ are quite different in the three cases. The stars with $v_{\rm ej} = 747$ and 749 km s^{-1} do not live long enough to undergo the inner turnaround, that is, they do not encounter $v_r = 0$ for the second time. On the contrary, the inner turnaround occurs for the star with $v_{\rm ej} = 745$ km s^{-1}.

Around this phase of the inner turnaround, $|v_\phi|$ reaches its maximum, as shown for $v_{\rm ej} = 745$ km s^{-1}. Stars with higher ejection speeds take longer time to undergo the outer turnaround and may not live long enough to experience the inner turnaround, as illustrated by the other two stars shown in Fig. 3.7. As a result, the maximum of $|v_\phi|$ falls sharply around $v_{\rm ej} \approx 750$ km s^{-1} (right panel of Fig. 3.6).

We conclude that for stars with ejection velocities higher than a threshold velocity, the maximum values of the magnitudes of the latitudinal and azimuthal velocity components, $|v_\theta|$ and $|v_\phi|$, are proportionate to the departure from the spherical symmetry of the potential. For stars with ejection speeds lower than the threshold, this proportionality disappears because these stars may experience the inner turnaround. Our simulations suggest that, for 4 $M_\odot$ stars, this threshold ejection velocity is ~ 710 km s^{-1} for QUMOND with $\gamma = 2$ and ~ 750 km s^{-1} for all the other models we investigate.

The ejection velocity is not observable but it is correlated with the outer turnaround, namely the maximum distance from the MW center that the star can travel. Figure 3.8 shows the outer turnaround as a function of the ejection velocity of a star in different models of the Galactic potential. This figure shows that neither in the Newtonian models nor in QUMOND with $\gamma = 1$ can stars with $v_{\rm ej} \lesssim 750$ km s^{-1} travel beyond a distance of about 15 kpc from the Galactic center. Similarly, in QUMOND with $\gamma = 2$, the stars

with $v_{\rm ej} \lesssim 710$ km s^{-1} cannot travel beyond 15 kpc. Therefore, identifying the 4 $M_\odot$ stars that have not experienced the inner turnaround, and thus have tangential velocities proportionate to the deviation of the gravitational potential from axial symmetry, requires considering only 4 $M_\odot$ HVSs at galactocentric distance $r > 15$ kpc.

The threshold ejection velocity increases with decreasing HVS mass, because of the longer lifetimes of lower-mass HVSs: longer-lived stars do not experience the inner turnaround only if they travel to larger galactocentric distances; in other words, only if they have larger ejection speeds. For example, for 3 $M_\odot$ or 2.5 $M_\odot$ stars with lifetimes on the main sequence ~ 350 Myr and ~ 580 Myr, respectively (Schaller et al., 1992), the threshold ejection velocities are ~ 790 km s^{-1} and ~ 815 km s^{-1} in Newtonian models; these threshold ejection speeds correspond to outer turnaround radii of ~ 30 kpc and ~ 50 kpc, respectively (Fig. 3.8). In QUMOND with $\gamma = 1$ ($\gamma = 2$), for 3 $M_\odot$ or 2.5 $M_\odot$ stars, the threshold ejection velocity is ~ 800 (755) km s^{-1} and ~ 830 (785) km s^{-1}, respectively; the corresponding turnaround radius is ~ 30 (30) kpc and ~ 50 (50) kpc, respectively. Therefore, the 3 $M_\odot$ or 2.5 $M_\odot$ stars are of interest for our test only if they are at galactocentric distance r larger than 30 kpc and 50 kpc, respectively.

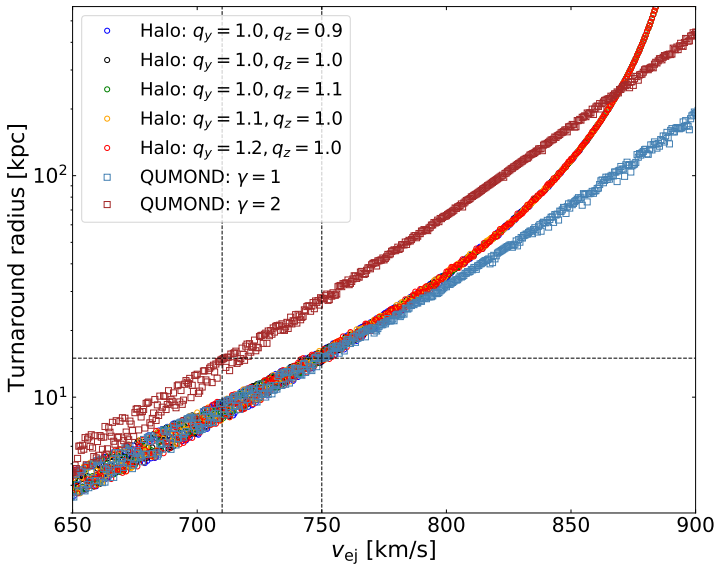

Figure 3.8. HVS outer turnaround as a function of the ejection speed, $v_{\rm ej}$, in Newtonian gravity with different shapes of the dark matter halo and in QUMOND with $\gamma = 1$ and $\gamma = 2$; models and symbols are detailed in the inset. The scatter of the points originates from the random initial directions of the HVS ejection velocities. The Newtonian gravitational potential is dominated by the dark matter halo that becomes approximately spherical at large radii and makes the scatter of the points decrease with increasing $v_{\rm ej}$. The vertical dotted lines mark the thresholds $v_{\rm ej} = 710$ km s^{-1} for QUMOND with $\gamma = 2$ and $v_{\rm ej} = 750$ km s^{-1} for all the other models; the horizontal line marks the minimum galactocentric distance of 15 kpc, appropriate for 4 $M_\odot$ HVSs. Less massive stars have larger velocity thresholds and larger minimum galactocentric distances.

3.5 Tangential velocity in QUMOND and Newtonian gravity

In this section we show the distributions of the azimuthal and latitudinal components of the tangential velocity, v_ϕ and v_θ respectively, in both QUMOND and Newtonian gravity. We show that, for HVSs within ~ 60 kpc, QUMOND yields upper limits for $|v_\phi|$ values that are substantially lower than the values that non-axisymmetric gravitational potentials can generate in Newtonian gravity. The QUMOND scenario might thus be

challenged if values of $|v_\phi|$ higher than those upper limits are observed.

In QUMOND, the symmetry of the Galactic potential is determined by the distribution of the baryonic components alone, unlike the case of Newtonian gravity, where the shape of the dark matter halo plays a crucial and dominant role. In QUMOND, if the baryonic distribution is axially symmetric, the pull of the stellar disk generates non-null v_θ values, whereas v_ϕ is always zero. Non-null values of v_ϕ only appear in a non-axisymmetric distribution of baryons, which mostly originates from a triaxial bulge (Eq. 3.7) or from a non-spherical HG halo (Sect. 3.5.1).

In Newtonian gravity with a perfectly axisymmetric distribution of the baryonic matter, as we adopt here (Eqs. 3.4-3.6), non-null values of v_ϕ can still appear if the halo of dark matter is not axially symmetric about the same axis of symmetry of the baryonic distribution, which is the z axis in our models. More importantly, a tilted or triaxial dark matter halo acts on the variation in v_ϕ for most of the HVS trajectory, whereas in QUMOND the action of the triaxiality of the bulge is limited to the initial phase of the HVS trajectory within ~ 5 kpc of the center.

This fundamental difference suggests that we might expect substantially higher values of v_ϕ in Newtonian gravity than in QUMOND, unless in Newtonian gravity either the dark matter halo is perfectly spherical or the halo is axisymmetric and its axis of symmetry is aligned with the axis of symmetry of the baryonic components. These possibilities, however, appear unlikely in the current dark matter scenarios (Hayashi et al., 2007; Debattista et al., 2013).

A detailed study on how the shape of the dark matter halo in Newtonian gravity affects the velocity components of the HVSs is presented in Gallo et al. (2022) (see Chpt. 2). Here, we briefly discuss the distributions of the azimuthal and latitudinal velocity components v_ϕ and v_θ in QUMOND and Newtonian gravity, and how v_ϕ can discriminate between the two theories of gravity.

3.5.1 The upper limit of the azimuthal component, v_ϕ, in QUMOND

In QUMOND, if the baryonic components are non-axisymmetric, the HVSs may have non-null v_ϕ values. To estimate these values of $|v_\phi|$, in Sect. 3.5.1 we consider the effects of a triaxial bulge, which is the Galactic baryonic component that is expected to play the major role in affecting $|v_\phi|$ (Gardner et al., 2020). In Sect. 3.5.1, we illustrate the effects of including a non-spherical halo of hot gas surrounding a MW with a spherical bulge.

The role of a triaxial bulge

Finding the gravitational field of the triaxial bulge over the entire numerical domain requires a demanding amount of computational time. We thus adopted a simplified approach that uses the fact that the triaxiality of the bulge is not effective at distances $r \gtrsim 5$ kpc, according to the density profile in Eq. (3.7) and the acceleration profile shown in Fig. 3.2. For our purpose, at these large radii, the gravitational potential of the bulge is well approximated by the potential generated by a spherically symmetric source. Therefore, we only used the field of a triaxial bulge to simulate the motion of the HVSs within 5 kpc of the Galactic center; at larger radii, we adopted the gravitational field of a spherical bulge. We matched the two regimes by setting the components of the velocity at $r = 5$ kpc from the inner region as the initial conditions for the outer region. The gravitational acceleration at $r = 5$ kpc due to the triaxial bulge is about 7% smaller than the gravitational acceleration at $r = 5$ kpc due to the spherical bulge, suggesting that our approach introduces a limited error in the integration of the equation of motion of the HVSs. In fact, this approximation does not affect our main result: it produces a slight

overestimate of the QUMOND upper limit we discuss below, because the acceleration of the spherical bulge is higher than the actual triaxal bulge acceleration.

As argued in Sect. 3.4.2, 4 $M_\odot$ stars with ejection velocity $v_{\rm ej} \lesssim 710$ km s^{-1} in QUMOND with $\gamma = 2$, or with $v_{\rm ej} \lesssim 750$ km s^{-1} in the other QUMOND and Newtonian models, tend to have disproportionately high tangential velocity components and cannot be used to probe the non-spherical components in the Galaxy potential. The maximum value of v_ϕ is inversely proportional to the ejection velocity, as expected by the argument illustrated in Sect. 3.4.2.

In order to find the maximum $|v_\phi|$ in QUMOND, we chose the lowest ejection velocity relevant for our analysis. Figure 3.9 shows $|v_\phi|$ as a function of the galactocentric distance r for three different ejection velocities: $v_{\rm ej} = 710$ km s^{-1} in QUMOND with $\gamma = 2$ (red curves), $v_{\rm ej} = 750$ km s^{-1} and 1000 km s^{-1} in QUMOND with $\gamma = 1$ (red and orange curves). All the stars shown in Fig. 3.9 are ejected at a polar angle $\theta = 45°$; the solid lines show v_ϕ for an azimuthal angle $\phi = 45°$, whereas the dashed and dot-dashed lines show v_ϕ for the slowest stars for different ϕ. We remind the reader that the largest semimajor axis of the triaxial bulge is along the x axis (see Eq. 3.7 and Fig. 3.4). According to Fig. 3.9, at $r = 5$ kpc, the maximum v_ϕ we should expect is ~ 8 km s^{-1}. We note that this result is not sensitive to the choice of the interpolating function ν (Eq. 3.2), because within 5 kpc the gravitational field is mostly Newtonian.

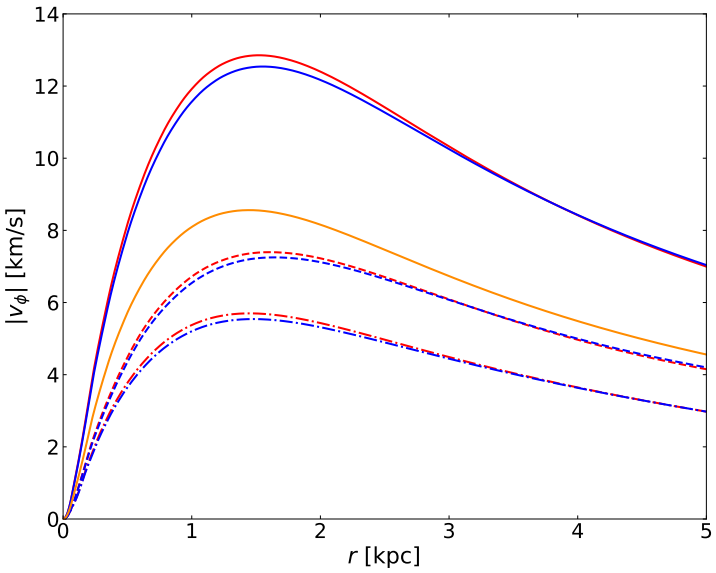

Figure 3.9. Magnitude of the azimuthal velocity component, v_ϕ, in QUMOND as a function of the galactocentric distance, r, for three 4 $M_\odot$ HVSs with different ejection velocities: $v_{\rm ej} = 710$ km s^{-1} in QUMOND with $\gamma = 2$ (red), $v_{\rm ej} = 750$ km s^{-1} in QUMOND with $\gamma = 1$ (blue), and $v_{\rm ej} = 1000$ km s^{-1} in QUMOND with $\gamma = 1$ (orange). The solid lines are for the stars ejected along $\theta = 45°$ and $\phi = 45°$, whereas the dashed (dash-dotted) line is for $\theta = 45°$ and $\phi = 15°$ (75°). In these examples, the QUMOND field is due to the triaxial bulge and the axisymmetric disk. The stars acquire v_ϕ only due to the triaxiality of the bulge.

Assuming that the angular momentum per unit mass $|\ell_z| = r \sin\theta |v_\phi|$ is conserved at larger radii, and $|v_\phi|$ thus falls off as r^{-1}, we obtain

$$|v_\phi^{\rm max}(r)| \sim 4 \left(\frac{10 \text{ kpc}}{r}\right) \text{km s}^{-1} \tag{3.13}$$

for 4 $M_\odot$ stars. The upper-limit radial profile of $|v_\phi|$ reported in Eq. (3.13) is shown by the black solid line in Fig. 3.10. The above equation provides a conservative upper limit

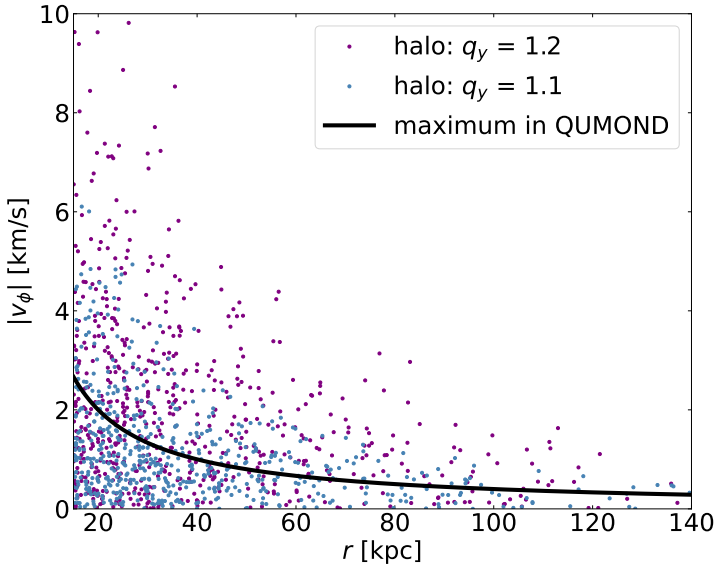

Figure 3.10. Magnitudes of the azimuthal velocity components v_ϕ of 4 $M_\odot$ HVSs in Newtonian gravity as a function of their radial coordinates, r, at the time of observation for a prolate dark matter halo with axis of symmetry in the plane of the disk. The light blue and purple dots show the HVSs for a halo with $(q_y, q_z) = (1.1, 1)$ and $(q_y, q_z) = (1.2, 1)$, respectively. The black line shows the upper limit of $|v_\phi|$ in QUMOND due to the triaxial bulge. The upper limit also holds for HVSs with masses lower than 4 $M_\odot$, provided they are beyond a certain galactocentric distance, e.g., $r \gtrsim 30$ kpc (50 kpc) for 3 $M_\odot$ (2.5 $M_\odot$) HVSs.

for two reasons. First, the equation was derived using the 4 $M_\odot$ HVSs with the lowest ejection velocities relevant for our analysis, namely 710 and 750 km s^{-1}. Any HVS that travels beyond 15 kpc (see Fig. 3.8) has higher ejection velocity, hence lower azimuthal velocity. Secondly, the star trajectories bend toward the Galactic disk located in the x-y plane ($\theta = 90°$; see Fig. 3.4), so that θ approaches 90°.[3] As a result, $\sin\theta$ always increases and causes a further decrease in $|v_\phi|$, because $|\ell_z| = r\sin\theta|v_\phi|$ remains constant. Therefore, using the HVS with the lowest ejection velocity and taking $\sin\theta$ as a constant yield the conservative upper limit of $|v_\phi|$ given in Eq. (3.13).

The radial profile $|v_\phi^{\rm max}(r)|$ of Eq. (3.13) also provides a conservative upper limit for stars with masses lower than 4 $M_\odot$. Indeed, as discussed in Sect. 3.4.2, stars with lower mass, and thus longer lifetimes, must be ejected with higher speeds in order to avoid the inner turnaround. Therefore, for higher ejection speeds, the normalization of the azimuthal velocity radial profile, $|v_\phi(r)|$ in Eq. (3.13), will be lower.

In Newtonian gravity with an axisymmetric distribution of baryons (Eqs. 3.4-3.6), the HVSs obtain non-null $|v_\phi|$ values only when the dark matter halo is non-axisymmetric about the z axis, as in our models with $q_y \neq 1$. Figure 3.10 shows the values of $|v_\phi|$ and r of the HVSs for two different shapes of the halo: $(q_y, q_z) = (1.1, 1)$, and $(q_y, q_z) = (1.2, 1)$. In both cases, the halo is prolate with the semimajor axis along the y axis in the plane of the disk. The halo becomes more spherical at larger radii, $r \gtrsim r_a = 21.6$ kpc. Thus, the azimuthal angular momentum, $\ell_z = r\sin\theta\ v_\phi$, of each HVS becomes a constant as the star travels beyond $r \sim r_a = 21.6$ kpc and $|v_\phi|$ decreases as r^{-1}. Near $r \sim 21.6$ kpc, $|v_\phi|$ of an HVS can be as high as 10 km s^{-1} for $q_y = 1.2$, and 6 km s^{-1} for $q_y = 1.1$

[3] As the disk is located on $\theta = 90°$, θ always approaches 90°. For an HVS ejected above the disk, the initial value of θ is between 0° and 90°, and θ increases. When the HVS is ejected below the disk, the initial θ is between 90° and 180°, and θ decreases.

(see Fig. 3.10). These values are substantially higher than the QUMOND upper limit $v_\phi^{\max}(r) \sim 1.8$ km s^{-1} derived with Eq. (3.13) at that distance and shown by the solid line in Fig. 3.10.

The effect of a hot gaseous halo

In addition to the baryonic components considered in the previous section, we included in our MW model a reservoir of baryons in the form of an HG halo extending up to the virial radius of the MW. The existence of this HG halo with a temperature $\sim 10^6$ K is suggested by the O VII and O VIII emission and absorption lines in the soft X-ray band (Paerels and Kahn, 2003; Gupta et al., 2012; Fang et al., 2013; Gatto et al., 2013; Salem et al., 2015). The presence of such diffuse hot gas may alleviate the missing baryon problem [4] (Fukugita et al., 1998; Gupta et al., 2012; Shull et al., 2012; Fang et al., 2013; Planck Collaboration et al., 2020a). An oblate gaseous halo with the smallest principal axis lying on the Galactic plane may be part of the Vast Polar Structure of the MW (Pawlowski et al., 2011; Zhao et al., 2013; Hammer et al., 2013).

We modeled the HG halo using the density profile (Thomas et al., 2017):

$$\rho_{\rm HG}(m) = \rho_{0,\rm HG}\left(1+\frac{m}{r_{0,\rm HG}}\right)^{-3}\exp\left(-\frac{m^2}{r_{\rm t,HG}^2}\right), \tag{3.14}$$

where $r_{0,\rm HG} = 100$ kpc is the core radius and $r_{\rm t,HG} = 200$ kpc is the truncation radius. The elliptical radius m for the oblate halo is

$$m = \sqrt{\frac{x^2}{a_{\rm HG}^2}+y^2+z^2}\,. \tag{3.15}$$

Currently, the shape of the halo has no observational constraints; we thus varied $a_{\rm HG}$ from 0.4 to 0.8. Similarly, its total mass is uncertain by a factor of ten (Miller and Bregman, 2013; Gatto et al., 2013; Salem et al., 2015), and we thus explored two different values of $\rho_{0,\rm HG}$: 3.0×10^5 and 3.0×10^4 $M_\odot$ kpc^{-3}. These values yield a total mass of $1.5\times10^{11}M_\odot$ and $1.5\times10^{10}M_\odot$, respectively, within 100 kpc.

We explored the effects of the HG halo on the azimuthal velocities of the HVSs in both the Newtonian and QUMOND scenarios (Figs. 3.11-3.12). In both cases, we considered the axisymmetric models for the central black hole, bulge and disk of Eqs. (3.4-3.6).

In Newtonian gravity, we considered the non-axisymmetric dark matter halos with $(q_y, q_z) = (1.2, 1)$ and $(q_y, q_z) = (1.4, 1)$ and assumed that the principal axes of the dark halo coincided with that of the HG halo. Whereas the dark halo is nearly spherical at large radii ($r \gtrsim 21.6$ kpc) and its contribution to the $|v_\phi|$ values thus falls as r^{-1} at large distances, the constant oblateness of the HG halo increases the $|v_\phi|$ values at all radii. Nevertheless the $|v_\phi|$ values are dominated by the shape of the non-axisymmetric dark matter halo, because its mass is at least 10 times the mass of the HG halo.

On the contrary, in QUMOND, the gravitational field is substantially enhanced at large distances by the presence of the HG halo and its mass and shape have a relevant effect on the values of $|v_\phi|$. Therefore, for the HG halo with the highest mass $M(<100\,\text{kpc}) = 1.5\times10^{11}\,M_\odot$ (Fig. 3.11), although the $|v_\phi|$'s in Newtonian scenario can still exceed the values in QUMOND at distances between 15 kpc and 60 kpc irrespective of

[4] The baryonic census in the Local Group appears to add up to only $\sim 15\%$ (Fukugita et al., 1998) of the baryonic mass expected from the estimated baryonic abundance ($\Omega_b h^2 \approx 0.022$) (Planck Collaboration et al., 2020a) from the Big Bang nucleosynthesis and the CMB anisotropies.

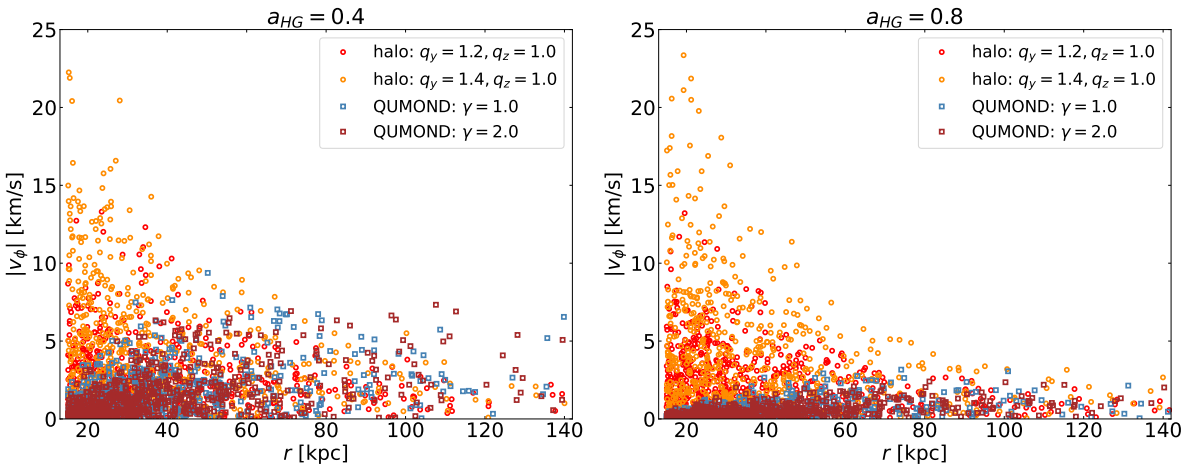

Figure 3.11. Magnitudes of the azimuthal velocity components, v_ϕ, of 4 $M_\odot$ HVSs as a function of their radial coordinates, r, at the time of observation in the presence of an HG halo with total mass of $1.5 \times 10^{11} M_\odot$ within 100 kpc in both Newtonian and QUMOND scenarios. The left and right panels show the results for two different oblatenesses, $a_{\rm HG} = 0.4$ and 0.8, of the HG halo (see Eqs. 3.14-3.15).

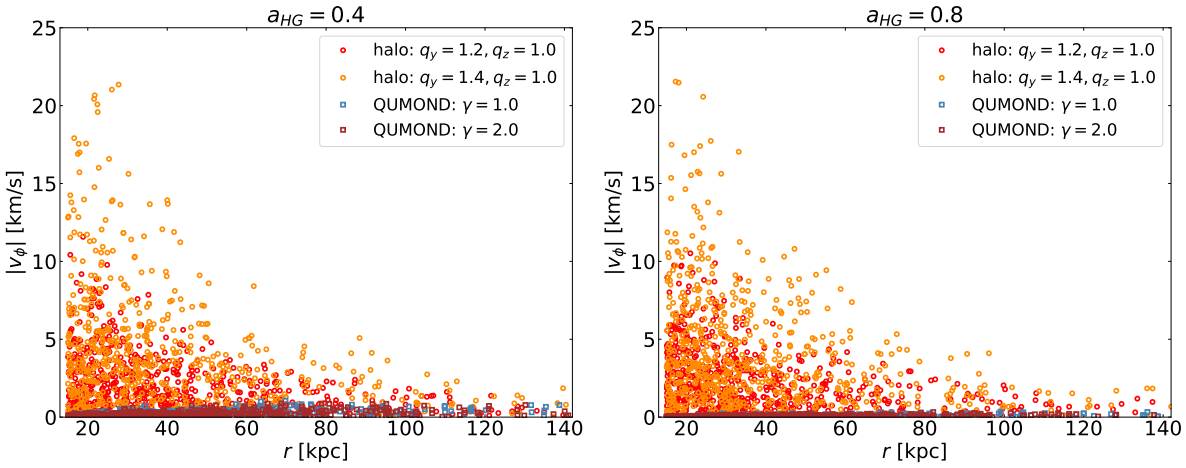

Figure 3.12. Same as Fig. 3.11 except for the HG halo with a lower mass: $1.5 \times 10^{10} M_\odot$ within 100 kpc.

the shape of the HG halo, at larger distances, the maximum possible values of $|v_\phi|$ in QUMOND are higher than or comparable to the maximum possible values in Newtonian gravity, depending on the shape of the HG halo. On the contrary, for the HG halo with the lowest mass $M(< 100\,\mathrm{kpc}) = 1.5 \times 10^{10}\,M_\odot$ (Fig. 3.12), the $|v_\phi|$ values in Newtonian gravity can be significantly higher than the values in QUMOND at distances between 15 kpc and 100 kpc.

In summary, the presence of an oblate HG halo increases the upper limit of the $|v_\phi|$'s in QUMOND at all distances, compared to the presence of a triaxial bulge alone. However, at smaller distances (15 kpc $\lesssim r \lesssim$ 60 kpc), the $|v_\phi|$ values in Newtonian gravity due to a non-axisymmetric dark matter halo may still substantially exceed the QUMOND values.

3.5.2 Latitudinal component, v_θ

The difference in the latitudinal component v_θ of the velocity in QUMOND and in Newtonian gravity is subtler than the difference in v_ϕ. In QUMOND, the source of the

gravitational field is concentrated in the plane of the disk and it bends the HVSs trajectories toward this plane. In Newtonian gravity, the main role is played by the spheroidal dark matter halo: A prolate halo, with its major axis perpendicular to the stellar disk, is likely to generate v_θ lower than in QUMOND; on the contrary, an oblate halo with its major axis in the plane of the disk will generate v_θ comparable or even higher than in QUMOND. Accurate predictions of these differences clearly depend on the exact values of the axial ratios, in addition to the actual mass and size of the dark matter halo.

From our knowledge of the baryonic components, we can predict the distribution of $|v_\theta|$ in Newtonian gravity, assuming that the dark matter halo is spherical and therefore it does not affect v_θ. Similarly, in our adopted model, the SMBH and the bulge have spherically symmetric potential and do not contribute to v_θ. The shaded histogram in the left panel of Fig. 3.13 shows the distribution of $|v_\theta|$ in this Newtonian model, effectively caused by the disk alone. In QUMOND, at larger distances, where the Newtonian gravitational field approaches a_0, the gravitational pull of the disk gets enhanced compared to Newtonian gravity. Consequently, the HVSs have larger $|v_\theta|$ in QUMOND than in Newtonian gravity.

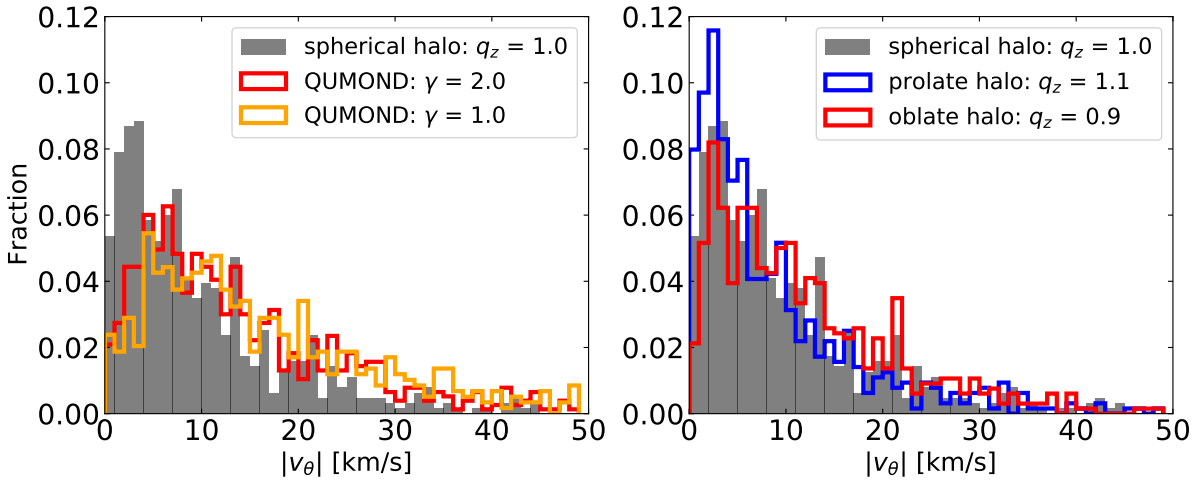

Figure 3.13. Distributions of the latitudinal component of the velocity, $|v_\theta|$, in Newtonian gravity and in QUMOND for 4 $M_\odot$ HVSs. The left panel shows the distributions of $|v_\theta|$ for different models of the Galactic potential: Newtonian gravity with a spherical dark matter halo (gray shaded histogram) and QUMOND with $\gamma = 1$ (orange histogram) and $\gamma = 2$ (red histogram). As the gravitational pull of the baryonic disk is enhanced in QUMOND, the fraction of HVSs with high $|v_\theta|$ is larger than in Newtonian gravity with a spherical halo. The right panel shows the distributions of $|v_\theta|$ for three different shapes of the dark matter halo in Newtonian gravity. The three halos have $q_y = 1$ but different q_z: a spherical halo with $q_z = 1$ (gray shaded histogram), a prolate halo with $q_z = 1.1$ (blue histogram), and an oblate halo with $q_z = 0.9$ (red histogram). An oblate halo enhances the gravitational pull of the baryonic disk, as shown by the larger fraction of HVSs with high $|v_\theta|$ and the smaller fraction of HVSs with low $|v_\theta|$ (compare the shaded and red histograms). The opposite occurs with a prolate halo (compare the shaded and blue histograms).

Figure 3.14 shows the magnitude of v_θ as a function of the galactocentric distance r due to the baryonic components in QUMOND with $\gamma = 1$ and 2 (orange and red dots, respectively), and in Newtonian gravity with a spherical halo (black dots). In both models, the maximum possible values of $|v_\theta|$ decrease as $\sim r^{-1}$, because, as each star travels beyond the length scale of the stellar disk, its angular momentum, $\sim r v_\theta$, becomes a constant. Because of the enhanced pull of QUMOND, the maximum value of v_θ is higher than in Newtonian gravity at all radii. Unfortunately, unlike the case of v_ϕ, these differences cannot be used to distinguish QUMOND from Newtonian gravity, because these same differences can be generated by an appropriate shape of the dark

matter halo, as we illustrate below.

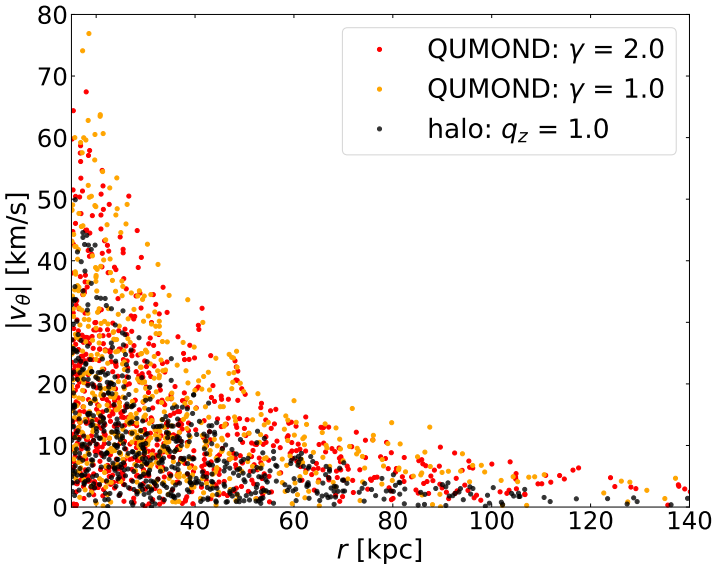

Figure 3.14. Latitudinal velocity components, $|v_\theta|$, as a function of the galactocentric distance, r, of 4 $M_\odot$ HVSs in QUMOND with $\gamma = 1$ (orange dots) and $\gamma = 2$ (red dots), and in Newtonian gravity with a spherical dark matter halo ($q_z = 1$) (black dots).

In Newtonian gravity with a dark matter halo, non-null v_θ values are caused by the Galactic disk and by the halo with $q_z \neq 1$ (models sketched in panels (c) and (d) of Fig. 3.3). For an oblate halo ($q_z < 1$), the gravitational pull of the halo enhances the pull of the disk. Hence, the number of HVSs with high $|v_\theta|$ is larger than in the case of a spherical halo, as shown by the comparison of the red and shaded histograms in the right panel of Fig. 3.13. The reverse happens for a prolate halo with $q_z > 1$. Therefore, the difference between the QUMOND and the Newtonian distributions shown in the left panel of Fig. 3.13 can be easily mimicked in Newtonian gravity by an appropriate oblate dark matter halo.

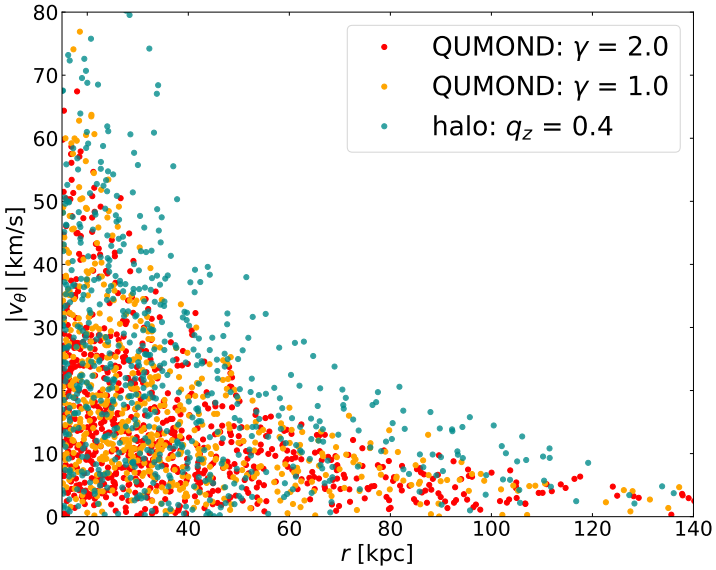

Figure 3.15. Latitudinal velocity components, $|v_\theta|$, as a function of the galactocentric distance, r, of 4 $M_\odot$ HVSs in QUMOND with $\gamma = 1$ (orange dots) and $\gamma = 2$ (red dots), and in Newtonian gravity with an oblate dark matter halo with $q_z = 0.4$ (dark cyan dots).

This degeneracy was emphasized by Read and Moore in 2005 when they attempted to distinguish MOND from Newtonian gravity using the stellar streams of the Sagittarius dwarf. The degeneracy between an oblate halo and QUMOND can be broken if q_z is sufficiently small. Indeed, similar to the case of v_ϕ, QUMOND sets an upper limit to $|v_\theta|$; on the contrary, in Newtonian gravity, $|v_\theta|$ may be higher than this upper limit if q_z is sufficiently small. In our models, the Newtonian $|v_\theta|$ values are higher than the QUMOND upper limit if $q_z \lesssim 0.6$. However, the difference between the QUMOND and Newtonian $|v_\theta|$ values is not as prominent as for $|v_\phi|$ values: In our model, the transition scale of the halo shape from oblate to spherical is $r_\mathrm{a} = 21.6$ kpc; therefore, the size of the portion of the halo that is actually oblate is comparable to the size of the baryonic disk. On the contrary, the size of the triaxial bulge causing nonzero $|v_\phi|$ values in QUMOND is much smaller than the scale length of the non-axisymmetric halo responsible for non-null $|v_\phi|$'s in Newtonian gravity. Therefore, v_θ is less effective than v_ϕ at distinguishing QUMOND from Newtonian gravity. Figure 3.15 quantifies this difficulty by showing $|v_\theta|$ versus r for QUMOND with $\gamma = 1$ and $\gamma = 2$, and for Newtonian gravity with an oblate halo with $q_z = 0.4$; this dark matter halo is a rather extreme case, when compared to the current estimates of the shape of the MW dark matter halo (Loebman et al., 2014).

3.5.3 Azimuthal velocities: A comparison with real data

We attempted a first comparison of the QUMOND upper limit $|v_\phi^{\max}(r)|$ (Eq. 3.13) with the measured $|v_\phi^{\mathrm{obs}}|$ of nine stars drawn from the HVS survey sample of Brown et al. (2014). These nine stars have masses in the range $\sim 2.5 - 4\ M_\odot$. Their galactocentric distances are larger than the minimum mass-dependent radii required for our test (see Sect. 3.4.2). In addition, Kenyon et al. (2018) show that HVSs ejected within 25° from the line joining the MW center and the LMC are affected by the LMC when they reach a galactocentric distance of 35 to 65 kpc. The nine HVSs of our sample are all located more than $\sim 84°$ away from the LMC, and the LMC pull should thus be irrelevant.

To be used for our test, these stars must originate from the Galactic center rather than being disk runaway stars. In principle, we could distinguish the two kinds of stars by tracing their trajectories back in time, if we knew the correct theory of gravity and the correct MW gravitational potential. When this information is unknown, and it is actually what we wish to constrain, this approach clearly generates a circularity problem. We can solve this problem by tracing back the star trajectories in different gravitational potentials and different theories of gravity to select those stars, if any, that appear to be HVSs in all models. We will investigate this self-consistent treatment, and thus the actual feasibility of our test, elsewhere. Here, we simply wished to see whether, if we assumed that the observed allegedly HVSs were indeed HVSs in all the models, the current data would have sufficed to distinguish between QUMOND and Newtonian gravity.

We relied on the analysis of Brown et al. (2018) who, in Newtonian gravity, assume an axisymmetric disk and a spherical dark matter halo (Kenyon et al., 2014) to estimate a larger probability for the nine stars mentioned above to come from the Galactic center than to be disk runaway stars.

We computed the azimuthal components, v_ϕ^{obs}, of their galactocentric velocities from the proper motions available in the Gaia Early Data Release 3 (EDR3; Gaia Collaboration, 2016c, 2021). We adopted the heliocentric distances derived from Brown et al. (2018), and the radial velocities of Brown et al. (2014). We found that the magnitudes of the azimuthal velocities are in the range $|v_\phi^{\mathrm{obs}}| \simeq 37 - 452$ km s^{-1}. For eight of these stars, the uncertainties on the azimuthal velocities are dominated by the errors on the proper motions, whereas the errors on the stars' distances and radial velocities, as well

as on the position and velocity of the Sun in the galactocentric reference frame, appear to be negligible. For these stars, the relative uncertainties on the azimuthal velocities are in the range $\sim 50 - 340\%$. For the ninth star, B329, neglecting the error on its distance is inappropriate. B329 is a (3.21 ± 0.24) $M_\odot$ star at galactocentric distance $r = (61 \pm 13)$ kpc; by ignoring the uncertainty on the distance, we derived $|v_\phi^{\rm obs}| = (371 \pm 74)$ km s^{-1}, whereas including the uncertainty on the distance yields $|v_\phi^{\rm obs}| = (371 \pm 131)$ km s^{-1}.

We conclude that the current uncertainties on $|v_\phi^{\rm obs}|$ make the azimuthal components consistent with zero within 3σ for all of the nine stars of our sample. We are thus unable to verify whether these measures would be in principle consistent with the QUMOND limit. Indeed, even in Newtonian gravity, the large values of $|v_\phi^{\rm obs}|$ would probably imply an unrealistically large flatness or triaxiality of the dark matter halo (Fig. 3.10). Therefore, even if these nine stars were HVSs in both QUMOND and Newtonian gravity, the comparison of their azimuthal components with the QUMOND upper limit, $|v_\phi^{\rm max}(r)|$, would still be inconclusive.

3.6 Discussion and conclusions

We showed that measuring the galactocentric tangential velocity of HVSs in the MW can effectively allow us to discriminate between MOND, in its QUMOND formulation, and Newtonian gravity. Specifically, we demonstrated that HVSs with sufficiently high ejection speed possess galactocentric azimuthal velocities whose magnitude, $|v_\phi|$, cannot exceed a velocity threshold in QUMOND, while $|v_\phi|$ has no upper bounds in Newtonian gravity. This result could naturally translate into an observational test to discriminate between these two theories of gravity.

Our findings follow from the fact that the HVSs ejected from the Galaxy center on radial orbits acquire non-null azimuthal tangential speeds, v_ϕ, due to the non-axisymmetric components of the Galactic gravitational potential. Hypervelocity stars with low ejection velocity can turn back toward the Galactic center and move outward again, acquiring a high $|v_\phi|$ that is not proportionate to the deviation from the axial symmetry of the potential. In contrast, HVSs with high ejection velocities reach larger galactocentric distances before turning back and thus die before experiencing the inner turnaround. These HVSs acquire a substantially lower $|v_\phi|$, which is proportional to the deviation from the axial symmetry of the potential.

In our models of the Galactic gravitational potential, the ejection velocity threshold for 4 $M_\odot$ stars is ~ 710 km s^{-1} in QUMOND with $\gamma = 2$, and it is ~ 750 km s^{-1} both in QUMOND with $\gamma = 1$ and in the Newtonian gravity models that we investigated here. Hypervelocity stars with ejection velocities higher than this value reach galactocentric distances larger than ~ 15 kpc if they live long enough. We thus expect that the $|v_\phi|$ component of 4 $M_\odot$ HVSs beyond this distance can be used to probe the deviation from the axial symmetry of the Galactic potential.

The ejection velocity threshold and the corresponding minimum galactocentric distance increase with decreasing HVS mass. For example, in Newtonian gravity, 3 $M_\odot$ and 2.5 $M_\odot$ HVSs have ejection velocity thresholds of ~ 790 km s^{-1} and ~ 815 km s^{-1}, which correspond to the minimum galactocentric distances of 30 kpc and 50 kpc, respectively. In QUMOND with $\gamma = 1$ ($\gamma = 2$), 3 $M_\odot$ and 2.5 $M_\odot$ HVSs have ejection velocity thresholds of ~ 800 (755) km s^{-1} and ~ 830 (785) km s^{-1}, which correspond to the minimum galactocentric distances of 30 (30) kpc and 50 (50) kpc, respectively (see Sect. 3.4.2). Therefore, the mass of the star sets the minimum distances beyond which the star must be located if we wish to use it for the test we suggested here.

In Newtonian gravity, the symmetric features of the baryonic distribution can be overcome by those of the dark matter halo surrounding the Galaxy. Here, we explored the case where both the baryonic components and the dark matter halo are axisymmetric but their axes are misaligned; the shape of the halo depends on the distance from the Galactic center, and the halo approaches the spherical symmetry at distances larger than ~ 21.6 kpc. It follows that v_ϕ is affected by the non-axisymmetric features of the potential up to this radius.

Among the baryonic components, only a triaxial bulge as well as the possible presence of a non-spherical HG halo can affect v_ϕ. Additional variations in v_ϕ might derive from massive external objects, such as the LMC (Kenyon et al., 2018), whereas other non-axisymmetric components within the disk, such as spiral arms or density inhomogeneities, are expected to affect only the stars within ~ 1 kpc of the disk (Gardner et al., 2020). The contribution from the HG halo in $|v_\phi|$ strongly depends on its shape and total mass, which are poorly constrained by observations.

In our QUMOND model with a triaxial bulge, the triaxiality of the bulge is effective up to $r \sim 5$ kpc; beyond this radius, the bulge can be approximated to be spherical and, because of the conservation of angular momentum, the maximum value of $|v_\phi|$ is proportional to r^{-1} (Eq. 3.13). Therefore, when compared with the Newtonian model affecting $|v_\phi|$ out to ~ 21.6 kpc, the values of $|v_\phi|$ of HVSs at $r \gtrsim 15$ kpc in QUMOND are substantially lower than the values allowed for a non-axisymmetric potential in Newtonian gravity. For example, at $r \sim 20$ kpc, we find $|v_\phi| \lesssim 2$ km s^{-1} in QUMOND, whereas $|v_\phi|$ can be as high as 6 or 10 km s^{-1} for a dark matter halo with axial ratios $q_y = 1.1$ or 1.2, respectively (see Fig. 3.10).

If a non-spherical HG halo is included in the MW model, it dominates the $|v_\phi|$ values of the HVSs in QUMOND, and the $|v_\phi|$ values in this case may be higher than those generated by the triaxial bulge alone. On the contrary, in Newtonian gravity, the $|v_\phi|$ values are still dominated by the dark matter halo and can still largely exceed the QUMOND values for HVSs at distances of up to 60 kpc from the center.

We conclude that precise measurements of v_ϕ for a few 4 $M_\odot$ HVSs at galactocentric distances larger than ~ 15 kpc (or 3 $M_\odot$ HVSs at $r \gtrsim 30$ kpc, or 2.5 $M_\odot$ HVSs at $r \gtrsim 50$ kpc) and smaller than ~ 60 kpc may in principle test the validity of QUMOND. Finding a few HVSs with azimuthal components, $|v_\phi|$, above the QUMOND upper limits, $|v_\phi^{\max}|$, given by Eq. (3.13) (black line in Fig. 3.10) or shown in Figs. 3.11-3.12 in the presence of the HG halo, would suggest that MOND may not be the correct theory of gravity, at least in its QUMOND formulation. Such tests clearly require that the HVSs are confirmed to originate from the Galactic center and that their trajectories are not perturbed by external objects, such as the LMC.

Assessing the HVS nature of observed stars is far from trivial, however, because we need to trace their trajectories back in time with the theory of gravity and in the gravitational potential that we wish to constrain. In addition, in QUMOND the perturbation of the trajectories by objects beyond the MW is complicated by the external field effect that is absent in Newtonian gravity (e.g., Haghi et al., 2016; Famaey et al., 2018; Hodson et al., 2020). The external field effect is expected to be more relevant for the most distant stars and needs to be quantified. We plan to tackle these issues elsewhere.

If we assume that the stars currently identified as HVSs are indeed HVSs in both QUMOND and Newtonian gravity, we conclude that the current uncertainties on their azimuthal velocities, v_ϕ, mostly due to the large relative uncertainties on the proper motion measurements, are too large to provide a conclusive comparison of the data with our QUMOND limit. Indeed, in the subsample of nine HVSs drawn from the sample of Brown et al. (2014) that we considered here, the azimuthal velocities have relative

uncertainties in the range 35-340%. The precision on the estimates of v_ϕ thus needs to be improved by at least a factor of ~ 10 to make our test decisive. Future measurements from space-borne astrometric missions with expected microarcsecond precision on star positions, such as Theia (The Theia Collaboration et al., 2017; Malbet et al., 2019, 2021), are expected to allow us to discriminate between the two theories of gravity.

Chapter 4

Final remarks and future prospects

In this Thesis, we reviewed the challenges of the ΛCDM cosmological model on galaxy scales, and explored the gravitational potential of our own Galaxy by means of hypervelocity stars (HVSs).

The cosmological parameters of the ΛCDM model are measured at an accuracy of $\sim 1\%$ or smaller (Hinshaw et al., 2013; Planck Collaboration et al., 2020a), effectively confirming the capability of the model to describe the homogeneous and isotropic Universe and the dynamics of cosmic structures. In this model, dark matter is $\sim 85\%$ of the total matter density of the Universe, but its fundamental nature is still unknown. As reviewed in Chpt. 1 and, more extensively, in our work de Martino et al. (2020), the lack of a direct detection of the DM particles is not the only issue encountered by the CDM model. Indeed, this model faces several challenges on galactic scales, as the cusp/core problem, the missing satellites problem, the too-big-to-fail problem, and the planes of satellite galaxies problem (see Sect. 1.3.1). Possible solutions to these challenges can be found accounting for physical processes that involve baryons and that were previously neglected in CDM simulations, as feedback from supernovae and dynamical friction from baryonic clumps. However, the effectiveness of baryonic feedback is still under debate. Alternatively, a change of the dark matter paradigm (see Sect. 1.3.2) or a modified gravity model that does not require DM (see, e.g., Sect. 1.3.3) can help to solve some of the issues, although none of the models offers a definitive answer to all the questions yet.

In this context, investigating the gravitational potential of the Milky Way (MW) by means of appropriate probes can help to test the predictions of the ΛCDM model on galaxy scales. With this aim, as illustrated in Chpts. 2 and 3, we carried out a project that uses HVSs as gravitational probes to (i) determine the shape of the DM halo of our Galaxy, and (ii) test the viability of a model where MOdified Newtonian Dynamics (MOND) holds on galaxy scales and no DM halo is present. HVSs are ejected from the Galactic center and cross a large range of distances during their journey across the Galaxy: they are thus powerful tracers of the MW mass distribution. During their travel through the MW, the initially purely radial trajectories of the HVSs are bent by the non-spherical components of the Galactic potential. As a consequence, the HVSs acquire non-null tangential velocities, whose components turn out to be the key quantities for both our halo-shape method and our gravity test.

We presented our new method to constrain the shape of the DM halo of the MW in Chpt. 2 and in our work Gallo et al. (2022). This method determines the shape of the MW DM halo by means of a new statistical approach based on the distribution of the components of the galactocentric tangential velocities of a sample of HVSs. We applied the method to an ideal optimal sample of ~ 800 4 $M_\odot$ simulated HVSs, which we referred to as the observed sample, in both axisymmetric and non-axisymmetric Galactic

potentials. In the case of an axisymmetric Galactic potential, we recovered the axial parameters of the DM halo from the one-dimensional distribution of the magnitude of the latitudinal velocity, $|v_\vartheta|$, of the HVSs of the observed sample. In the non-axisymmetric scenario, the axial ratios of the DM halo are recovered from the two-dimensional distribution of $|v_\vartheta|$ and a function $\bar{v}_\varphi$ of the azimuthal velocity, v_φ, of the HVSs of the observed sample. In our ideal case of no observational limitations and galactocentric velocities with null uncertainties, the method has a success rate $S \gtrsim 89\%$ in recovering the correct shape of the DM halo in an axisymmetric Galactic gravitational potential, and $S > 96\%$ in recovering the halo shape in the non-axisymmetric potentials explored in this work. However, the success rate of our method depends on the size of the HVS sample, and is lower for smaller HVS samples.

Even though our method was developed in a ΛCDM framework, with the gravitational potential of the DM halos modeled with the triaxial generalization of the Navarro-Frenk-White DM potential, the method can in principle be used not only to test the predictions of ΛCDM on galactic DM halos, but also to constrain the still unknown nature of the DM particles. Indeed, as discussed in Sect. 1.4.2, the shape of the Galactic DM halo may depend on the nature of the DM particles. DM particle candidates different from WIMPs may yield DM halos systematically different from those predicted by ΛCDM. In this case, our method would virtually be able to reveal those differences.

Going beyond DM models, and with the aim to test whether a gravity theory that does not include the contribution of any DM particles is a viable alternative to describe the MW potential, in Chpt. 3 and in our work Chakrabarty et al. (2022) we proposed a novel test to discriminate between a scenario in which Newtonian gravity holds on galactic scales, and a scenario where MOND (in its quasi-linear QUMOND formulation) is the correct theory of gravity on these scales. We compared HVS velocities simulated in a MW ruled by Newtonian gravity and embedded in a DM halo and those obtained in a MW ruled by MOND. We showed that measuring the galactocentric tangential velocity of HVSs in the MW can effectively allow us to discriminate between MOND, in its QUMOND formulation, and Newtonian gravity. Specifically, we demonstrated that, in QMOND, HVSs with sufficiently high ejection speed and located within 60 kpc from the Galactic center have azimuthal velocities smaller than a distance-dependent upper limit, not met by Newtonian velocities. This result translates into an observational test to discriminate between these two theories of gravity. Precise measurements of v_ϕ for a few 4 $M_\odot$ HVSs at galactocentric distances larger than $\sim$ 15 kpc (or 3 $M_\odot$ HVSs at $r \gtrsim 30$ kpc, or 2.5 $M_\odot$ HVSs at $r \gtrsim 50$ kpc) and smaller than $\sim$ 60 kpc may test the validity of QUMOND: finding a few HVSs with azimuthal components, $|v_\phi|$, above the QUMOND upper limits, would suggest that MOND may not be the correct theory of gravity, at least in its QUMOND formulation.

Both our proposed gravity test and our halo-shape method are conceived to be applied to real observed HVSs. The current sample of HVS candidates consists of a few tens of stars. This number of HVSs is sufficiently large for our gravity test: indeed, this test can discriminate between the two theories of gravity with sufficiently precise v_ϕ measurements of even a few HVSs. On the other hand, the current number of HVS candidates is too low to make our halo-shape method sufficiently successful. To ensure a high success rate, it is of fundamental importance to measure the galactocentric velocities of a few hundred genuine HVSs.

The possibility to measure the radial velocities of fainter objects in the outer halo, for example by means of the forthcoming 4-metre Multi-Object Spectroscopic Telescope (de Jong et al., 2019), will enable us to identify new HVS candidates that satisfy our selection criteria (see Sects. 2.2.2 and 3.4.2).

A criticality of both our new method to constrain the MW DM halo shape and our new gravity test is the problem of the uncertainties on the HVS tangential velocities. Indeed, the high success rate of our new halo-shape method is obtained under the assumption of tangential velocities with null uncertainties and it is expected to decrease for increasingly high uncertainties. Similarly, for our novel gravity test, we find that the current uncertainties on tangential velocities need to be reduced by at least a factor ~ 10 to make the test decisive.

Proper motions are, together with the stars' distances, the main source of error on the tangential velocities. A future *Theia*-like mission (Malbet et al., 2016; The Theia Collaboration et al., 2017; Malbet et al., 2019, 2021), designed for unprecedented high precision astrometry, may achieve an end-of-mission uncertainty on HVS proper motions of a few micro-arcseconds per year (e.g., $\sim 0.12\ \mu$as/yr for a star of $R = 10$ mag and $\sim 4.4\ \mu$as/yr for a star of $R = 20$ mag). Such a low uncertainty, ~ 100 times smaller than that of *Gaia*, will open up the possibility for significantly constraining the shape of the DM halo of the MW and for discriminating between MOND and Newtonian gravity.

Our investigations of the Milky Way gravity by means of HVSs were conducted in the framework of preparatory studies for this future astrometric mission, and are contributing to the definition of its scientific goals. Furthermore, follow-up projects, that we are already pursuing, will enable us to determine the precision that a *Theia*-like mission should achieve on proper motions to make our method powerful and our gravity test decisive. These results will contribute to the definition of the technical requirements of this mission.

More precise measurements of proper motions will also make it possible to better constrain the birth place of the current HVS candidates, helping to solve the circularity problem that currently affects the possibility to apply both our halo-shape method and our gravity test to real HVS data (see Sects. 2.7 and 3.5.3). It is indeed of the utmost importance to build samples of HVS candidates with a high probability to originate from the Galactic center, independently of the model of gravitational potential chosen to backtrack their position at the time of ejection. However, in recent works that investigate the origin of the HVS candidates (e.g., Irrgang et al., 2018; Kreuzer et al., 2020; Irrgang et al., 2021), the backtracking of the star trajectories is derived only for a specific Galactic potential that include a spherical DM halo. In our halo-shape method, HVSs are used to constrain the axial parameters of the DM halo; thus, their genuine HVS nature must not depend on the shape of the DM halo that we want to determine. More generally, a highly likely galactocentric origin of the sample of HVS candidates is required to test the viability of alternative theories of gravity. To be used for our gravity test, the stars must be HVSs in all the MW gravity models.

Once the above mentioned issues will be solved, our method to constrain the shape of the Galactic DM halo and our novel gravity test will be powerful tools to shed light on the Milky Way gravity.

Bibliography

M. Aaronson. Accurate radial velocities for carbon stars in Draco and Ursa Minor: the first hint of a dwarf spheroidal mass-to-light ratio. *ApJ*, 266:L11–L15, March 1983. doi: 10.1086/183969.

M. G. Abadi, J. F. Navarro, and M. Steinmetz. An Alternative Origin for Hypervelocity Stars. *ApJ*, 691(2): L63–L66, Feb 2009. doi: 10.1088/0004-637X/691/2/L63.

M. G. Abadi, J. F. Navarro, M. Fardal, A. Babul, and M. Steinmetz. Galaxy-induced transformation of dark matter haloes. *MNRAS*, 407(1):435–446, Sept. 2010. doi: 10.1111/j.1365-2966.2010.16912.x.

K. Abazajian. Linear cosmological structure limits on warm dark matter. *Phys. Rev. D*, 73(6):063513, March 2006. doi: 10.1103/PhysRevD.73.063513.

L. F. Abbott and P. Sikivie. A cosmological bound on the invisible axion. *Phys. Lett. B*, 120(1-3):133–136, Jan 1983. doi: 10.1016/0370-2693(83)90638-X.

E. Abdalla, G. F. Abellán, A. Aboubrahim, A. Agnello, O. Akarsu, Y. Akrami, G. Alestas, D. Aloni, L. Amendola, L. A. Anchordoqui, R. I. Anderson, N. Arendse, M. Asgari, M. Ballardini, V. Barger, S. Basilakos, R. C. Batista, E. S. Battistelli, R. Battye, M. Benetti, D. Benisty, A. Berlin, P. de Bernardis, E. Berti, B. Bidenko, S. Birrer, J. P. Blakeslee, K. K. Boddy, C. R. Bom, A. Bonilla, N. Borghi, F. R. Bouchet, M. Braglia, T. Buchert, E. Buckley-Geer, E. Calabrese, R. R. Caldwell, D. Camarena, S. Capozziello, S. Casertano, G. C. F. Chen, J. Chluba, A. Chen, H.-Y. Chen, A. Chudaykin, M. Cicoli, C. J. Copi, F. Courbin, F.-Y. Cyr-Racine, B. Czerny, M. Dainotti, G. D'Amico, A.-C. Davis, J. de Cruz Pérez, J. de Haro, J. Delabrouille, P. B. Denton, S. Dhawan, K. R. Dienes, E. Di Valentino, P. Du, D. Eckert, C. Escamilla-Rivera, A. Ferté, F. Finelli, P. Fosalba, W. L. Freedman, N. Frusciante, E. Gaztañaga, W. Giarè, E. Giusarma, A. Gómez-Valent, W. Handley, I. Harrison, L. Hart, D. K. Hazra, A. Heavens, A. Heinesen, H. Hildebrandt, J. C. Hill, N. B. Hogg, D. E. Holz, D. C. Hooper, N. Hosseininejad, D. Huterer, M. Ishak, M. M. Ivanov, A. H. Jaffe, I. S. Jang, K. Jedamzik, R. Jimenez, M. Joseph, S. Joudaki, M. Kamionkowski, T. Karwal, L. Kazantzidis, R. E. Keeley, M. Klasen, E. Komatsu, L. V. E. Koopmans, S. Kumar, L. Lamagna, R. Lazkoz, C.-C. Lee, J. Lesgourgues, J. Levi Said, T. R. Lewis, B. L'Huiller, M. Lucca, R. Maartens, L. M. Macri, D. Marfatia, V. Marra, C. J. A. P. Martins, S. Masi, S. Matarrese, A. Mazumdar, A. Melchiorri, O. Mena, L. Mersini-Houghton, J. Mertens, D. Milakovic, Y. Minami, V. Miranda, C. Moreno-Pulido, M. Moresco, D. F. Mota, E. Mottola, S. Mozzon, J. Muir, A. Mukherjee, S. Mukherjee, P. Naselsky, P. Nath, S. Nesseris, F. Niedermann, A. Notari, R. C. Nunes, E. Ó. Colgáin, K. A. Owens, E. Ozulker, F. Pace, A. Paliathanasis, A. Palmese, S. Pan, D. Paoletti, S. E. Perez Bergliaffa, L. Perivolaropoulos, D. W. Pesce, V. Pettorino, O. H. E. Philcox, L. Pogosian, V. Poulin, G. Poulot, M. Raveri, M. J. Reid, F. Renzi, A. G. Riess, V. I. Sabla, P. Salucci, V. Salzano, E. N. Saridakis, B. S. Sathyaprakash, M. Schmaltz, N. Schöneberg, D. Scolnic, A. A. Sen, N. Sehgal, A. Shafieloo, M. M. Sheikh-Jabbari, J. Silk, A. Silvestri, F. Skara, M. S. Sloth, M. Soares-Santos, J. Solà Peracaula, Y.-Y. Songsheng, J. F. Soriano, D. Staicova, G. D. Starkman, I. Szapudi, E. M. Teixera, B. Thomas, T. Treu, E. Trott, C. van de Bruck, J. A. Vazquez, L. Verde, L. Visinelli, D. Wang, J.-M. Wang, S.-J. Wang, R. Watkins, S. Watson, J. K. Webb, N. Weiner, A. Weltman, S. J. Witte, R. Wojtak, A. K. Yadav, W. Yang, G.-B. Zhao, and M. Zumalacárregui. Cosmology Intertwined: A Review of the Particle Physics, Astrophysics, and Cosmology Associated with the Cosmological Tensions and Anomalies. *arXiv e-prints*, art. arXiv:2203.06142, Mar. 2022.

I. Ablimit, G. Zhao, C. Flynn, and S. A. Bird. The Rotation Curve, Mass Distribution, and Dark Matter Content of the Milky Way from Classical Cepheids. *ApJ*, 895(1):L12, May 2020. doi: 10.3847/2041-8213/ab8d45.

A. A. Aguilar-Arevalo, B. C. Brown, L. Bugel, G. Cheng, J. M. Conrad, R. L. Cooper, R. Dharmapalan, A. Diaz, Z. Djurcic, D. A. Finley, R. Ford, F. G. Garcia, G. T. Garvey, J. Grange, E. C. Huang, W. Huelsnitz, C. Ignarra, R. A. Johnson, G. Karagiorgi, T. Katori, T. Kobilarcik, W. C. Louis, C. Mariani, W. Marsh, G. B. Mills, J. Mirabal, J. Monroe, C. D. Moore, J. Mousseau, P. Nienaber, J. Nowak, B. Osmanov, Z. Pavlovic, D. Perevalov, H. Ray, B. P. Roe, A. D. Russell, M. H. Shaevitz, J. Spitz, I. Stancu, R. Tayloe, R. T. Thornton, M. Tzanov, R. G. Van de Water, D. H. White, D. A. Wickremasinghe, E. D. Zimmerman, and MiniBooNE Collaboration. Significant Excess of Electronlike Events in the MiniBooNE Short-Baseline Neutrino Experiment. *Phys. Rev. Lett.*, 121(22):221801, Nov. 2018. doi: 10.1103/PhysRevLett.121.221801.

R. J. Allen and F. H. Shu. The extrapolated central surface brightness of galaxies. *ApJ*, 227:67–72, 1979. doi: 10.1086/156705.

R. Amanullah, C. Lidman, D. Rubin, G. Aldering, P. Astier, K. Barbary, M. S. Burns, A. Conley, K. S. Dawson, S. E. Deustua, M. Doi, S. Fabbro, L. Faccioli, H. K. Fakhouri, G. Folatelli, A. S. Fruchter, H. Furusawa, G. Garavini, G. Goldhaber, A. Goobar, D. E. Groom, I. Hook, D. A. Howell, N. Kashikawa, A. G. Kim, R. A. Knop, M. Kowalski, E. Linder, J. Meyers, T. Morokuma, S. Nobili, J. Nordin, P. E. Nugent, L. Östman, R. Pain, N. Panagia, S. Perlmutter, J. Raux, P. Ruiz-Lapuente, A. L. Spadafora, M. Strovink, N. Suzuki, L. Wang, W. M. Wood-Vasey, N. Yasuda, and T. Supernova Cosmology Project. Spectra and Hubble Space Telescope Light Curves of Six Type Ia Supernovae at $0.511 < z < 1.12$ and the Union2 Compilation. *ApJ*, 716 (1):712–738, 2010. doi: 10.1088/0004-637X/716/1/712.

L. Amendola and R. Barbieri. Dark matter from an ultra-light pseudo-Goldsone-boson. *Phys. Lett. B*, 642(3): 192–196, Nov. 2006. doi: 10.1016/j.physletb.2006.08.069.

D. Anderhalden, J. Diemand, G. Bertone, A. V. Macciò, and A. Schneider. The galactic halo in mixed dark matter cosmologies. *J. Cosmol. Astropart. Phys.*, 2012(10):047, Oct 2012. doi: 10.1088/1475-7516/2012/10/047.

T. W. Anderson and D. A. Darling. Asymptotic theory of certain "goodness of fit" criteria based on stochastic processes. *The Annals of Mathematical Statistics*, 23(2):193–212, 1952.

T. W. Anderson and D. A. Darling. A test of goodness of fit. *Journal of the American Statistical Association*, 49(268):765–769, 1954.

R. E. Angulo, O. Hahn, and T. Abel. The warm dark matter halo mass function below the cut-off scale. *MNRAS*, 434(4):3337–3347, Oct. 2013. doi: 10.1093/mnras/stt1246.

G. W. Angus. Dwarf spheroidals in MOND. *MNRAS*, 387(4):1481–1488, July 2008. doi: 10.1111/j.1365-2966.2008.13351.x.

G. W. Angus. Is an 11eV sterile neutrino consistent with clusters, the cosmic microwave background and modified Newtonian dynamics? *MNRAS*, 394(1):527–532, 2009. doi: 10.1111/j.1365-2966.2008.14341.x.

G. W. Angus and A. Diaferio. The abundance of galaxy clusters in modified Newtonian dynamics: cosmological simulations with massive neutrinos. *MNRAS*, 417(2):941–949, 2011. doi: 10.1111/j.1365-2966.2011.19321.x.

G. W. Angus, A. Diaferio, B. Famaey, and K. J. van der Heyden. Cosmological simulations in MOND: the cluster scale halo mass function with light sterile neutrinos. *MNRAS*, 436(1):202–211, 2013. doi: 10.1093/mnras/stt1564.

G. W. Angus, A. Diaferio, B. Famaey, G. Gentile, and K. J. van der Heyden. Modified Baryonic Dynamics: two-component cosmological simulations with light sterile neutrinos. *J. Cosmol. Astropart. Phys.*, 2014(10): 079, 2014. doi: 10.1088/1475-7516/2014/10/079.

A. Arvanitaki, S. Dimopoulos, S. Dubovsky, N. Kaloper, and J. March-Russell. String axiverse. *Phys. Rev. D*, 81(12):123530, June 2010. doi: 10.1103/PhysRevD.81.123530.

P. Astier, J. Guy, N. Regnault, R. Pain, E. Aubourg, D. Balam, S. Basa, R. G. Carlberg, S. Fabbro, D. Fouchez, I. M. Hook, D. A. Howell, H. Lafoux, J. D. Neill, N. Palanque-Delabrouille, K. Perrett, C. J. Pritchet, J. Rich, M. Sullivan, R. Taillet, G. Aldering, P. Antilogus, V. Arsenijevic, C. Balland, S. Baumont, J. Bronder, H. Courtois, R. S. Ellis, M. Filiol, A. C. Gonçalves, A. Goobar, D. Guide, D. Hardin, V. Lusset, C. Lidman, R. McMahon, M. Mouchet, A. Mourao, S. Perlmutter, P. Ripoche, C. Tao, and N. Walton. The Supernova Legacy Survey: measurement of Ω_M, Ω_Λ and w from the first year data set. *A&A*, 447(1):31–48, Feb. 2006. doi: 10.1051/0004-6361:20054185.

J. Bailin and M. Steinmetz. Internal and External Alignment of the Shapes and Angular Momenta of ΛCDM Halos. *ApJ*, 627(2):647–665, July 2005. doi: 10.1086/430397.

A. Banerjee and C. J. Jog. Progressively More Prolate Dark Matter Halo in the Outer Galaxy as Traced by Flaring H I Gas. *ApJ*, 732(1):L8, May 2011. doi: 10.1088/2041-8205/732/1/L8.

I. Banik, M. Milgrom, and H. Zhao. Toomre stability of disk galaxies in quasi-linear MOND. *arXiv e-prints*, art. arXiv:1808.10545, 2018.

N. Bar, K. Blum, J. Eby, and R. Sato. Ultralight dark matter in disk galaxies. *Phys. Rev. D*, 99(10):103020, May 2019. doi: 10.1103/PhysRevD.99.103020.

K. G. Begeman, A. H. Broeils, and R. H. Sanders. Extended rotation curves of spiral galaxies : dark haloes and modified dynamics. *MNRAS*, 249:523, April 1991. doi: 10.1093/mnras/249.3.523.

J. Bekenstein and M. Milgrom. Does the missing mass problem signal the breakdown of Newtonian gravity? *ApJ*, 286:7–14, Nov 1984. doi: 10.1086/162570.

J. D. Bekenstein. Relativistic gravitation theory for the modified Newtonian dynamics paradigm. *Phys. Rev. D*, 70(8):083509, Oct. 2004. doi: 10.1103/PhysRevD.70.083509.

G. Bertone and D. Hooper. History of dark matter. *Rev. Mod. Phys*, 90(4):045002, Oct 2018. doi: 10.1103/RevModPhys.90.045002.

G. Bertone, D. Hooper, and J. Silk. Particle dark matter: evidence, candidates and constraints. *Phys. Rep.*, 405 (5-6):279–390, Jan 2005. doi: 10.1016/j.physrep.2004.08.031.

P. Bhattacharjee, S. Chaudhury, and S. Kundu. Rotation Curve of the Milky Way out to ~200 kpc. *ApJ*, 785 (1):63, April 2014. doi: 10.1088/0004-637X/785/1/63.

B. Bhattacharya and D. Habtzghi. Median of the p value under the alternative hypothesis. *The American Statistician*, 56(3):202–206, 2002. doi: 10.1198/000313002146.

O. Bienaymé, B. Famaey, X. Wu, H. S. Zhao, and D. Aubert. Galactic kinematics with modified Newtonian dynamics. *A&A*, 500(2):801–805, June 2009. doi: 10.1051/0004-6361/200809978.

J. Binney, O. Gerhard, and D. Spergel. The photometric structure of the inner Galaxy. *MNRAS*, 288(2):365–374, June 1997. doi: 10.1093/mnras/288.2.365.

A. Biviano. From Messier to Abell: 200 Years of Science with Galaxy Clusters. In F. Durret and D. Gerbal, editors, *Constructing the Universe with Clusters of Galaxies*, page 1, Jan. 2000.

A. Blaauw. On the origin of the O- and B-type stars with high velocities (the "run-away" stars), and some related problems. *Bull. Astron. Inst. Netherlands*, 15:265, May 1961.

J. Bland-Hawthorn and O. Gerhard. The Galaxy in Context: Structural, Kinematic, and Integrated Properties. *ARA&A*, 54:529–596, Sept. 2016. doi: 10.1146/annurev-astro-081915-023441.

G. R. Blumenthal, H. Pagels, and J. R. Primack. Galaxy formation by dissipationless particles heavier than neutrinos. *Nature*, 299(5878):37–38, Sept. 1982. doi: 10.1038/299037a0.

G. R. Blumenthal, S. M. Faber, J. R. Primack, and M. J. Rees. Formation of galaxies and large-scale structure with cold dark matter. *Nature*, 311:517–525, Oct. 1984. doi: 10.1038/311517a0.

V. V. Bobylev. Kinematics of the galaxy from Cepheids with proper motions from the Gaia DR1 catalogue. *Astron. Lett*, 43(3):152–158, March 2017. doi: 10.1134/S106377371703001X.

V. V. Bobylev and A. T. Bajkova. Kinematic analysis of solar-neighborhood stars based on RAVE4 data. *Astron. Lett*, 42(2):90–99, Feb. 2016. doi: 10.1134/S1063773716020018.

P. Bode, J. P. Ostriker, and N. Turok. Halo Formation in Warm Dark Matter Models. *ApJ*, 556(1):93–107, July 2001. doi: 10.1086/321541.

A. Boehle, A. M. Ghez, R. Schödel, L. Meyer, S. Yelda, S. Albers, G. D. Martinez, E. E. Becklin, T. Do, J. R. Lu, K. Matthews, M. R. Morris, B. Sitarski, and G. Witzel. An Improved Distance and Mass Estimate for Sgr A* from a Multistar Orbit Analysis. *ApJ*, 830(1):17, Oct. 2016. doi: 10.3847/0004-637X/830/1/17.

H. Böhringer and N. Werner. X-ray spectroscopy of galaxy clusters: studying astrophysical processes in the largest celestial laboratories. *A&AR*, 18(1-2):127–196, Feb. 2010. doi: 10.1007/s00159-009-0023-3.

J. S. Bolton, M. Viel, T.-S. Kim, M. G. Haehnelt, and R. F. Carswell. Possible evidence for an inverted temperaturedensity relation in the intergalactic medium from the flux distribution of the Lyα forest. *MNRAS*, 386(2):1131–1144, April 2008. doi: 10.1111/j.1365-2966.2008.13114.x.

J. R. Bond, J. Silk, and E. W. Kolb. The generation of isothermal perturbations in the very early universe. *ApJ*, 255:341–360, April 1982. doi: 10.1086/159835.

A. Bosma. *The distribution and kinematics of neutral hydrogen in spiral galaxies of various morphological types*. PhD thesis, Jan. 1978.

R. Bottema, J. L. G. Pestaña, B. Rothberg, and R. H. Sand ers. MOND rotation curves for spiral galaxies with Cepheid-based distances. *A&A*, 393:453–460, Oct. 2002. doi: 10.1051/0004-6361:20021021.

D. Boubert and N. W. Evans. A Dipole on the Sky: Predictions for Hypervelocity Stars from the Large Magellanic Cloud. *ApJ*, 825(1):L6, July 2016. doi: 10.3847/2041-8205/825/1/L6.

D. Boubert, D. Erkal, N. W. Evans, and R. G. Izzard. Hypervelocity runaways from the Large Magellanic Cloud. *MNRAS*, 469(2):2151–2162, Aug. 2017. doi: 10.1093/mnras/stx848.

D. Boubert, J. Guillochon, K. Hawkins, I. Ginsburg, N. W. Evans, and J. Strader. Revisiting hypervelocity stars after Gaia DR2. *MNRAS*, 479(2):2789–2795, Sep 2018. doi: 10.1093/mnras/sty1601.

D. Boubert, D. Erkal, and A. Gualandris. Deflection of the hypervelocity stars by the pull of the Large Magellanic Cloud on the Milky Way. *MNRAS*, 497(3):2930–2940, Sept. 2020. doi: 10.1093/mnras/staa2211.

F. Bournaud and P. A. Duc. From tidal dwarf galaxies to satellite galaxies. *A&A*, 456(2):481–492, 2006. doi: 10.1051/0004-6361:20065248.

J. Bovy, A. Bahmanyar, T. K. Fritz, and N. Kallivayalil. The Shape of the Inner Milky Way Halo from Observations of the Pal 5 and GD–1 Stellar Streams. *ApJ*, 833(1):31, Dec. 2016. doi: 10.3847/1538-4357/833/1/31.

A. Boyarsky, O. Ruchayskiy, and M. Shaposhnikov. The Role of Sterile Neutrinos in Cosmology and Astrophysics. *Annual Review of Nuclear and Particle Science*, 59(1):191–214, Nov 2009. doi: 10.1146/annurev.nucl.010909.083654.

M. Boylan-Kolchin, J. S. Bullock, and M. Kaplinghat. Too big to fail? The puzzling darkness of massive Milky Way subhaloes. *MNRAS*, 415(1):L40–L44, July 2011. doi: 10.1111/j.1745-3933.2011.01074.x.

M. Boylan-Kolchin, J. S. Bullock, and M. Kaplinghat. The Milky Way's bright satellites as an apparent failure of ΛCDM. *MNRAS*, 422(2):1203–1218, May 2012. doi: 10.1111/j.1365-2966.2012.20695.x.

R. Brada and M. Milgrom. Stability of Disk Galaxies in the Modified Dynamics. *ApJ*, 519(2):590–598, 1999. doi: 10.1086/307402.

B. C. Bromley, S. J. Kenyon, M. J. Geller, E. Barcikowski, W. R. Brown, and M. J. Kurtz. Hypervelocity Stars: Predicting the Spectrum of Ejection Velocities. *ApJ*, 653(2):1194–1202, Dec 2006. doi: 10.1086/508419.

B. C. Bromley, S. J. Kenyon, W. R. Brown, and M. J. Geller. Runaway Stars, Hypervelocity Stars, and Radial Velocity Surveys. *ApJ*, 706(2):925–940, Dec. 2009. doi: 10.1088/0004-637X/706/2/925.

B. C. Bromley, S. J. Kenyon, M. J. Geller, and W. R. Brown. Binary Disruption by Massive Black Holes: Hypervelocity Stars, S Stars, and Tidal Disruption Events. *ApJ*, 749(2):L42, April 2012. doi: 10.1088/2041-8205/749/2/L42.

B. C. Bromley, S. J. Kenyon, W. R. Brown, and M. J. Geller. Nearby High-speed Stars in Gaia DR2. *ApJ*, 868 (1):25, Nov 2018. doi: 10.3847/1538-4357/aae83e.

A. M. Brooks and A. Zolotov. Why Baryons Matter: The Kinematics of Dwarf Spheroidal Satellites. *ApJ*, 786 (2):87, 2014. doi: 10.1088/0004-637X/786/2/87.

M. M. Brouwer, K. A. Oman, E. A. Valentijn, M. Bilicki, C. Heymans, H. Hoekstra, N. R. Napolitano, N. Roy, C. Tortora, A. H. Wright, M. Asgari, J. L. van den Busch, A. Dvornik, T. Erben, B. Giblin, A. W. Graham, H. Hildebrandt, A. M. Hopkins, A. Kannawadi, K. Kuijken, J. Liske, H. Shan, T. Tröster, E. Verlinde, and M. Visser. The weak lensing radial acceleration relation: Constraining modified gravity and cold dark matter theories with KiDS-1000. *A&A*, 650:A113, June 2021. doi: 10.1051/0004-6361/202040108.

W. R. Brown. Hypervelocity Stars. *ARA&A*, 53:15–49, Aug. 2015. doi: 10.1146/annurev-astro-082214-122230.

W. R. Brown, M. J. Geller, S. J. Kenyon, and M. J. Kurtz. Discovery of an Unbound Hypervelocity Star in the Milky Way Halo. *ApJ*, 622(1):L33–L36, March 2005. doi: 10.1086/429378.

W. R. Brown, M. J. Geller, S. J. Kenyon, and M. J. Kurtz. A Successful Targeted Search for Hypervelocity Stars. *ApJ*, 640(1):L35–L38, March 2006a. doi: 10.1086/503279.

W. R. Brown, M. J. Geller, S. J. Kenyon, and M. J. Kurtz. Hypervelocity Stars. I. The Spectroscopic Survey. *ApJ*, 647(1):303–311, Aug 2006b. doi: 10.1086/505165.

W. R. Brown, M. J. Geller, S. J. Kenyon, M. J. Kurtz, and B. C. Bromley. Hypervelocity Stars. II. The Bound Population. *ApJ*, 660(1):311–318, May 2007a. doi: 10.1086/513595.

W. R. Brown, M. J. Geller, S. J. Kenyon, M. J. Kurtz, and B. C. Bromley. Hypervelocity Stars. III. The Space Density and Ejection History of Main-Sequence Stars from the Galactic Center. *ApJ*, 671(2):1708–1716, Dec. 2007b. doi: 10.1086/523642.

W. R. Brown, M. J. Geller, and S. J. Kenyon. MMT Hypervelocity Star Survey. *ApJ*, 690(2):1639–1647, Jan. 2009. doi: 10.1088/0004-637X/690/2/1639.

W. R. Brown, M. J. Geller, and S. J. Kenyon. MMT Hypervelocity Star Survey. II. Five New Unbound Stars. *ApJ*, 751(1):55, May 2012. doi: 10.1088/0004-637X/751/1/55.

W. R. Brown, M. J. Geller, and S. J. Kenyon. MMT Hypervelocity Star Survey. III. The Complete Survey. *ApJ*, 787(1):89, May 2014. doi: 10.1088/0004-637X/787/1/89.

W. R. Brown, M. G. Lattanzi, S. J. Kenyon, and M. J. Geller. Gaia and the Galactic Center Origin of Hypervelocity Stars. *ApJ*, 866(1):39, Oct 2018. doi: 10.3847/1538-4357/aadb8e.

S. E. Bryan, S. T. Kay, A. R. Duffy, J. Schaye, C. Dalla Vecchia, and C. M. Booth. The impact of baryons on the spins and shapes of dark matter haloes. *MNRAS*, 429(4):3316–3329, March 2013. doi: 10.1093/mnras/sts587.

J. Buch, S. C. J. Leung, and J. Fan. Using Gaia DR2 to Constrain Local Dark Matter Density and Thin Dark Disk. *J. Cosmol. Astropart. Phys.*, 1904:026, 2019. doi: 10.1088/1475-7516/2019/04/026.

T. Buck, A. V. Macciò, A. A. Dutton, A. Obreja, and J. Frings. NIHAO XV: the environmental impact of the host galaxy on galactic satellite and field dwarf galaxies. *MNRAS*, 483(1):1314–1341, 2019. doi: 10.1093/mnras/sty2913.

J. S. Bullock and M. Boylan-Kolchin. Small-Scale Challenges to the ΛCDM Paradigm. *ARA&A*, 55(1):343–387, Aug 2017. doi: 10.1146/annurev-astro-091916-055313.

I. Butsky, A. V. Macciò, A. A. Dutton, L. Wang, A. Obreja, G. S. Stinson, C. Penzo, X. Kang, B. W. Keller, and J. Wadsley. NIHAO project II: halo shape, phase-space density and velocity distribution of dark matter in galaxy formation simulations. *MNRAS*, 462(1):663–680, Oct. 2016. doi: 10.1093/mnras/stw1688.

E. Calabrese and D. N. Spergel. Ultra-light dark matter in ultra-faint dwarf galaxies. *MNRAS*, 460(4):4397–4402, Aug 2016. doi: 10.1093/mnras/stw1256.

M. Cappellari. Structure and Kinematics of Early-Type Galaxies from Integral Field Spectroscopy. *ARA&A*, 54: 597–665, Sept. 2016. doi: 10.1146/annurev-astro-082214-122432.

M. Cappellari, R. Bacon, M. Bureau, M. C. Damen, R. L. Davies, P. T. de Zeeuw, E. Emsellem, J. Falcón-Barroso, D. Krajnović, H. Kuntschner, R. M. McDermid, R. F. Peletier, M. Sarzi, R. C. E. van den Bosch, and G. van de Ven. The SAURON project - IV. The mass-to-light ratio, the virial mass estimator and the Fundamental Plane of elliptical and lenticular galaxies. *MNRAS*, 366(4):1126–1150, March 2006. doi: 10.1111/j.1365-2966.2005.09981.x.

V. F. Cardone and N. Radicella. Can MONDian vector theories explain the cosmic speed up? *Phys. Rev. D*, 80 (6):063515, 2009. doi: 10.1103/PhysRevD.80.063515.

E. D. Carlson, M. E. Machacek, and L. J. Hall. Self-interacting dark matter. *ApJ*, 398:43–52, 1992. doi: 10.1086/171833.

B. J. Carr and S. W. Hawking. Black holes in the early Universe. *MNRAS*, 168:399–416, Aug. 1974. doi: 10.1093/mnras/168.2.399.

M. Cautun, C. S. Frenk, R. van de Weygaert, W. A. Hellwing, and B. J. T. Jones. Milky Way mass constraints from the Galactic satellite gap. *MNRAS*, 445(2):2049–2060, Dec. 2014. doi: 10.1093/mnras/stu1849.

S. S. Chakrabarty, L. Ostorero, A. Gallo, S. Ebagezio, and A. Diaferio. Probing modified Newtonian dynamics with hypervelocity stars. *A&A*, 657:A115, Jan. 2022. doi: 10.1051/0004-6361/202141136.

D.-M. Chen and S. McGaugh. Contradiction between strong lensing statistics and a feedback solution to the cusp/core problem. *Research in Astronomy and Astrophysics*, 10(12):1215–1222, Dec 2010. doi: 10.1088/1674-4527/10/12/003.

S.-R. Chen, H.-Y. Schive, and T. Chiueh. Jeans analysis for dwarf spheroidal galaxies in wave dark matter. *MNRAS*, 468(2):1338–1348, June 2017. doi: 10.1093/mnras/stx449.

K. T. E. Chua, K. Dibert, M. Vogelsberger, and J. Zavala. The impact of inelastic self-interacting dark matter on the dark matter structure of a milky way halo. *MNRAS*, Oct 2020. doi: 10.1093/mnras/staa3315.

S. J. Clark, B. Dutta, Y. Gao, L. E. Strigari, and S. Watson. Planck constraint on relic primordial black holes. *Phys. Rev. D*, 95(8):083006, 2017. doi: 10.1103/PhysRevD.95.083006.

N. Clerc, C. C. Kirkpatrick, A. Finoguenov, R. Capasso, J. Comparat, S. Damsted, K. Furnell, A. E. Kukkola, J. Ider Chitham, A. Merloni, M. Salvato, A. Gueguen, T. Dwelly, C. Collins, A. Saro, G. Erfanianfar, D. P. Schneider, J. Brownstein, G. A. Mamon, N. Padilla, E. Jullo, and D. Bizyaev. SPIDERS: overview of the X-ray galaxy cluster follow-up and the final spectroscopic data release. *MNRAS*, 497(3):3976–3992, Sept. 2020. doi: 10.1093/mnras/staa2066.

T. Clifton, P. G. Ferreira, A. Padilla, and C. Skordis. Modified gravity and cosmology. *Phys. Rep.*, 513(1):1–189, March 2012. doi: 10.1016/j.physrep.2012.01.001.

D. Clowe, M. Bradač, A. H. Gonzalez, M. Markevitch, S. W. Randall, C. Jones, and D. Zaritsky. A Direct Empirical Proof of the Existence of Dark Matter. *ApJ*, 648(2):L109–L113, Sept. 2006. doi: 10.1086/508162.

S. Cole and C. Lacey. The structure of dark matter haloes in hierarchical clustering models. *MNRAS*, 281:716, July 1996. doi: 10.1093/mnras/281.2.716.

P. Colin, V. Avila-Reese, O. Valenzuela, and C. Firmani. Structure and subhalo population of halos in a selfinteracting dark matter cosmology. *ApJ*, 581:777–793, 2002. doi: 10.1086/344259.

O. Contigiani, E. M. Rossi, and T. Marchetti. On measuring the Galactic dark matter halo with hypervelocity stars. *MNRAS*, 487(3):4025–4036, Aug. 2019. doi: 10.1093/mnras/stz1547.

A. N. Cox. *Allen's astrophysical quantities*. 2000.

P. Cuddeford and P. Amendt. Extended stellar hydrodynamics for galactic discs. II. *MNRAS*, 253:427–444, Dec. 1991. doi: 10.1093/mnras/253.3.427.

J. J. Dalcanton, D. N. Spergel, and F. J. Summers. The Formation of Disk Galaxies. *ApJ*, 482(2):659–676, 1997. doi: 10.1086/304182.

R. Dave, D. N. Spergel, P. J. Steinhardt, and B. D. Wandelt. Halo properties in cosmological simulations of selfinteracting cold dark matter. *ApJ*, 547:574–589, 2001. doi: 10.1086/318417.

L. P. David, K. A. Arnaud, W. Forman, and C. Jones. Einstein Observations of the Hydra A Cluster and the Efficiency of Galaxy Formation in Groups and Clusters. *ApJ*, 356:32, June 1990. doi: 10.1086/168812.

M. Davis, G. Efstathiou, C. S. Frenk, and S. D. M. White. The evolution of large-scale structure in a universe dominated by cold dark matter. *ApJ*, 292:371–394, May 1985. doi: 10.1086/163168.

T. M. Davis, E. Mörtsell, J. Sollerman, A. C. Becker, S. Blondin, P. Challis, A. Clocchiatti, A. V. Filippenko, R. J. Foley, P. M. Garnavich, S. Jha, K. Krisciunas, R. P. Kirshner, B. Leibundgut, W. Li, T. Matheson, G. Miknaitis, G. Pignata, A. Rest, A. G. Riess, B. P. Schmidt, R. C. Smith, J. Spyromilio, C. W. Stubbs, N. B. Suntzeff, J. L. Tonry, W. M. Wood-Vasey, and A. Zenteno. Scrutinizing Exotic Cosmological Models Using ESSENCE Supernova Data Combined with Other Cosmological Probes. *ApJ*, 666(2):716–725, 2007. doi: 10.1086/519988.

W. J. G. de Blok and A. Bosma. High-resolution rotation curves of low surface brightness galaxies. *A&A*, 385: 816–846, April 2002. doi: 10.1051/0004-6361:20020080.

R. S. de Jong, O. Agertz, A. A. Berbel, J. Aird, D. A. Alexander, A. Amarsi, F. Anders, R. Andrae, B. Ansarinejad, W. Ansorge, P. Antilogus, H. Anwand-Heerwart, A. Arentsen, A. Arnadottir, M. Asplund, M. Auger, N. Azais, D. Baade, G. Baker, S. Baker, E. Balbinot, I. K. Baldry, M. Banerji, S. Barden, P. Barklem, E. Barthélémy-Mazot, C. Battistini, S. Bauer, C. P. M. Bell, O. Bellido-Tirado, S. Bellstedt, V. Belokurov, T. Bensby, M. Bergemann, J. M. Bestenlehner, R. Bielby, M. Bilicki, C. Blake, J. Bland-Hawthorn, C. Boeche, W. Boland, T. Boller, S. Bongard, A. Bongiorno, P. Bonifacio, D. Boudon, D. Brooks, M. J. I. Brown, R. Brown, M. Brüggen, J. Brynnel, J. Brzeski, T. Buchert, P. Buschkamp, E. Caffau, P. Caillier, J. Carrick, L. Casagrande, S. Case, A. Casey, I. Cesarini, G. Cescutti, D. Chapuis, C. Chiappini, M. Childress, N. Christlieb, R. Church, M. R. L. Cioni, M. Cluver, M. Colless, T. Collett, J. Comparat, A. Cooper, W. Couch, F. Courbin, S. Croom, D. Croton, E. Daguisé, G. Dalton, L. J. M. Davies, T. Davis, P. de Laverny, A. Deason, F. Dionies, K. Disseau, P. Doel, D. Döscher, S. P. Driver, T. Dwelly, D. Eckert, A. Edge, B. Edvardsson, D. E. Youssoufi, A. Elhaddad, H. Enke, G. Erfanianfar, T. Farrell, T. Fechner, C. Feiz, S. Feltzing, I. Ferreras, D. Feuerstein, D. Feuillet, A. Finoguenov, D. Ford, S. Fotopoulou, M. Fouesneau, C. Frenk, S. Frey, W. Gaessler, S. Geier, N. Gentile Fusillo, O. Gerhard, T. Giannantonio, D. Giannone, B. Gibson, P. Gillingham, C. González-Fernández, E. Gonzalez-Solares, S. Gottloeber, A. Gould, E. K. Grebel, A. Gueguen, G. Guiglion, M. Haehnelt, T. Hahn, C. J. Hansen, H. Hartman, K. Hauptner, K. Hawkins, D. Haynes, R. Haynes, U. Heiter, A. Helmi, C. H. Aguayo, P. Hewett, S. Hinton, D. Hobbs, S. Hoenig, D. Hofman, I. Hook, J. Hopgood, A. Hopkins, A. Hourihane, L. Howes, C. Howlett, T. Huet, M. Irwin, O. Iwert, P. Jablonka, T. Jahn, K. Jahnke, A. Jarno, S. Jin, P. Jofre, D. Johl, D. Jones, H. Jönsson, C. Jordan, I. Karovicova, A. Khalatyan, A. Kelz, R. Kennicutt, D. King, F. Kitaura, J. Klar, U. Klauser, J. P. Kneib, A. Koch, S. Koposov, G. Kordopatis, A. Korn, J. Kosmalski, R. Kotak, M. Kovalev, K. Kreckel, Y. Kripak, M. Krumpe, K. Kuijken, A. Kunder, I. Kushniruk, M. I. Lam, G. Lamer, F. Laurent, J. Lawrence, M. Lehmitz, B. Lemasle, J. Lewis, B. Li, C. Lidman, K. Lind, J. Liske, J. L. Lizon, J. Loveday, H. G. Ludwig, R. M. McDermid, K. Maguire, V. Mainieri, S. Mali, H. Mandel, K. Mandel, L. Mannering, S. Martell, D. Martinez Delgado, G. Matijevic, H. McGregor, R. McMahon, P. McMillan, O. Mena, A. Merloni, M. J. Meyer, C. Michel, G. Micheva, J. E. Migniau, I. Minchev, G. Monari,

R. Muller, D. Murphy, D. Muthukrishna, K. Nandra, R. Navarro, M. Ness, V. Nichani, R. Nichol, H. Nicklas, F. Niederhofer, P. Norberg, D. Obreschkow, S. Oliver, M. Owers, N. Pai, S. Pankratow, D. Parkinson, J. Paschke, R. Paterson, A. Pecontal, I. Parry, D. Phillips, A. Pillepich, L. Pinard, J. Pirard, N. Piskunov, V. Plank, D. Plüschke, E. Pons, P. Popesso, C. Power, J. Pragt, A. Pramskiy, D. Pryer, M. Quattri, A. B. d. A. Queiroz, A. Quirrenbach, S. Rahurkar, A. Raichoor, S. Ramstedt, A. Rau, A. Recio-Blanco, R. Reiss, F. Renaud, Y. Revaz, P. Rhode, J. Richard, A. D. Richter, H. W. Rix, A. S. G. Robotham, R. Roelfsema, M. Romaniello, D. Rosario, F. Rothmaier, B. Roukema, G. Ruchti, G. Rupprecht, J. Rybizki, N. Ryde, A. Saar, E. Sadler, M. Sahlén, M. Salvato, B. Sassolas, W. Saunders, A. Saviauk, L. Sbordone, T. Schmidt, O. Schnurr, R. D. Scholz, A. Schwope, W. Seifert, T. Shanks, A. Sheinis, T. Sivov, Á. Skúladóttir, S. Smartt, S. Smedley, G. Smith, R. Smith, J. Sorce, L. Spitler, E. Starkenburg, M. Steinmetz, I. Stilz, J. Storm, M. Sullivan, W. Sutherland, E. Swann, A. Tamone, E. N. Taylor, J. Teillon, E. Tempel, R. ter Horst, W. F. Thi, E. Tolstoy, S. Trager, G. Traven, P. E. Tremblay, L. Tresse, M. Valentini, R. van de Weygaert, M. van den Ancker, J. Veljanoski, S. Venkatesan, L. Wagner, K. Wagner, C. J. Walcher, L. Waller, N. Walton, L. Wang, R. Winkler, L. Wisotzki, C. C. Worley, G. Worseck, M. Xiang, W. Xu, D. Yong, C. Zhao, J. Zheng, F. Zscheyge, and D. Zucker. 4MOST: Project overview and information for the First Call for Proposals. *The Messenger*, 175: 3–11, March 2019. doi: 10.18727/0722-6691/5117.

A. A. de Laix, R. J. Scherrer, and R. K. Schaefer. Constraints of selfinteracting dark matter. *ApJ*, 452:495, 1995. doi: 10.1086/176322.

I. de Martino, S. S. Chakrabarty, V. Cesare, A. Gallo, L. Ostorero, and A. Diaferio. Dark Matters on the Scale of Galaxies. *Universe*, 6(8):107, Aug. 2020. doi: 10.3390/universe6080107.

A. J. Deason, V. Belokurov, N. W. Evans, and J. An. Broken degeneracies: the rotation curve and velocity anisotropy of the Milky Way halo. *MNRAS*, 424(1):L44–L48, July 2012a. doi: 10.1111/j.1745-3933.2012.01283.x.

A. J. Deason, V. Belokurov, N. W. Evans, S. E. Koposov, R. J. Cooke, J. Peñarrubia, C. F. P. Laporte, M. Fellhauer, M. G. Walker, and E. W. Olszewski. The cold veil of the Milky Way stellar halo. *MNRAS*, 425(4): 2840–2853, Oct. 2012b. doi: 10.1111/j.1365-2966.2012.21639.x.

V. P. Debattista, R. Roškar, M. Valluri, T. Quinn, B. Moore, and J. Wadsley. What's up in the Milky Way? The orientation of the disc relative to the triaxial halo. *MNRAS*, 434(4):2971–2981, Oct. 2013. doi: 10.1093/mnras/stt1217.

W. Dehnen and J. Binney. Mass models of the Milky Way. *MNRAS*, 294(3):429–438, March 1998. doi: 10.1046/j.1365-8711.1998.01282.x.

A. Del Popolo and M. Le Delliou. Small Scale Problems of the ΛCDM Model: A Short Review. *Galaxies*, 5(1): 17, Feb 2017. doi: 10.3390/galaxies5010017.

A. Diaferio and G. W. Angus. The Acceleration Scale, Modified Newtonian Dynamics, and Sterile Neutrinos. *arXiv e-prints*, art. arXiv:1206.6231, 2012.

A. Diaferio, S. Schindler, and K. Dolag. Clusters of Galaxies: Setting the Stage. *Space Sci. Rev.*, 134(1-4):7–24, Feb. 2008. doi: 10.1007/s11214-008-9324-5.

M. Dine and W. Fischler. The Not So Harmless Axion. *Phys. Lett.*, 120B:137–141, 1983. doi: 10.1016/0370-2693(83)90639-1.

S. Dodelson and L. M. Widrow. Sterile neutrinos as dark matter. *Phys. Rev. Lett.*, 72(1):17–20, Jan 1994. doi: 10.1103/PhysRevLett.72.17.

A. D. Dolgov and S. H. Hansen. Massive sterile neutrinos as warm dark matter. *Astropart. Phys.*, 16(3):339–344, Jan 2002. doi: 10.1016/S0927-6505(01)00115-3.

R. M. J. Donahue. A note on information seldom reported via the p value. *The American Statistician*, 53(4): 303–306, 1999. doi: 10.1080/00031305.1999.10474481.

G. A. Dooley, A. H. G. Peter, M. Vogelsberger, J. Zavala, and A. Frebel. Enhanced Tidal Stripping of Satellites in the Galactic Halo from Dark Matter Self-Interactions. *MNRAS*, 461(1):710–727, 2016. doi: 10.1093/mnras/stw1309.

C. Du, H. Li, Y. Yan, H. J. Newberg, J. Shi, J. Ma, Y. Chen, and Z. Wu. New Nearby Hypervelocity Stars and Their Spatial Distribution from Gaia DR2. *ApJS*, 244(1):4, Sept. 2019. doi: 10.3847/1538-4365/ab328c.

X. Du, C. Behrens, and J. C. Niemeyer. Substructure of fuzzy dark matter haloes. *MNRAS*, 465(1):941–951, Feb 2017. doi: 10.1093/mnras/stw2724.

J. Dubinski. The Effect of Dissipation on the Shapes of Dark Halos. *ApJ*, 431:617, Aug. 1994. doi: 10.1086/174512.

J. Dubinski and R. G. Carlberg. The Structure of Cold Dark Matter Halos. *ApJ*, 378:496, Sept. 1991. doi: 10.1086/170451.

P. Duffett-Smith. *Practical astronomy with your calculator*. 1979.

A. A. Dutton, A. V. Macciò, J. Frings, L. Wang, G. S. Stinson, C. Penzo, and X. Kang. NIHAO V: too big does not fail - reconciling the conflict between ΛCDM predictions and the circular velocities of nearby field galaxies. *MNRAS*, 457(1):L74–L78, 2016. doi: 10.1093/mnrasl/slv193.

H. Edelmann, R. Napiwotzki, U. Heber, N. Christlieb, and D. Reimers. HE 0437-5439: An Unbound Hypervelocity Main-Sequence B-Type Star. *ApJ*, 634(2):L181–L184, Dec 2005. doi: 10.1086/498940.

F. Eisenhauer, R. Genzel, T. Alexander, R. Abuter, T. Paumard, T. Ott, A. Gilbert, S. Gillessen, M. Horrobin, S. Trippe, H. Bonnet, C. Dumas, N. Hubin, A. Kaufer, M. Kissler-Patig, G. Monnet, S. Ströbele, T. Szeifert, A. Eckart, R. Schödel, and S. Zucker. SINFONI in the Galactic Center: Young Stars and Infrared Flares in the Central Light-Month. *ApJ*, 628(1):246–259, July 2005. doi: 10.1086/430667.

A. El-Zant, I. Shlosman, and Y. Hoffman. Dark Halos: The Flattening of the Density Cusp by Dynamical Friction. *ApJ*, 560(2):636–643, Oct. 2001. doi: 10.1086/322516.

O. D. Elbert, J. S. Bullock, S. Garrison-Kimmel, M. Rocha, J. Oorbe, and A. H. G. Peter. Core formation in dwarf haloes with self-interacting dark matter: no fine-tuning necessary. *MNRAS*, 453(1):29–37, 2015. doi: 10.1093/mnras/stv1470.

D. Erkal, D. Boubert, A. Gualandris, N. W. Evans, and F. Antonini. A hypervelocity star with a Magellanic origin. *MNRAS*, 483(2):2007–2013, Feb. 2019. doi: 10.1093/mnras/sty2674.

S. M. Fall and G. Efstathiou. Formation and rotation of disc galaxies with haloes. *MNRAS*, 193:189–206, Oct. 1980. doi: 10.1093/mnras/193.2.189.

B. Famaey and S. S. McGaugh. Modified Newtonian Dynamics (MOND): Observational Phenomenology and Relativistic Extensions. *Living Reviews in Relativity*, 15(1):10, 2012. doi: 10.12942/lrr-2012-10.

B. Famaey, S. McGaugh, and M. Milgrom. MOND and the dynamics of NGC 1052-DF2. *MNRAS*, 480(1): 473–476, Oct. 2018. doi: 10.1093/mnras/sty1884.

T. Fang, J. Bullock, and M. Boylan-Kolchin. On the Hot Gas Content of the Milky Way Halo. *ApJ*, 762(1):20, Jan. 2013. doi: 10.1088/0004-637X/762/1/20.

M. Fellhauer, V. Belokurov, N. W. Evans, M. I. Wilkinson, D. B. Zucker, G. Gilmore, M. J. Irwin, D. M. Bramich, S. Vidrih, R. F. G. Wyse, T. C. Beers, and J. Brinkmann. The Origin of the Bifurcation in the Sagittarius Stream. *ApJ*, 651(1):167–173, Nov. 2006. doi: 10.1086/507128.

J. L. Feng. Dark Matter Candidates from Particle Physics and Methods of Detection. *ARA&A*, 48:495–545, Sep 2010. doi: 10.1146/annurev-astro-082708-101659.

I. Ferrero, M. G. Abadi, J. F. Navarro, L. V. Sales, and S. Gurovich. The dark matter haloes of dwarf galaxies: a challenge for the Λ cold dark matter paradigm? *MNRAS*, 425(4):2817–2823, Oct 2012. doi: 10.1111/j.1365-2966.2012.21623.x.

A. Finzi. On the validity of Newton's law at a long distance. *MNRAS*, 127:21, 1963. doi: 10.1093/mnras/127.1.21.

C. Firmani, E. D'Onghia, V. Avila-Reese, G. Chincarini, and X. Hernandez. Evidence of self-interacting cold dark matter from galactic to galaxy cluster scales. *MNRAS*, 315:L29, 2000. doi: 10.1046/j.1365-8711.2000.03555.x.

C. Firmani, E. D'Onghia, G. Chincarini, X. Hernandez, and V. Avila-Reese. Constraints on dark matter physics from dwarf galaxies through galaxy cluster haloes. *MNRAS*, 321:713, 2001. doi: 10.1046/j.1365-8711.2001.04030.x.

M. P. Fitzgerald. The Intrinsic Colours of Stars and Two-Colour Reddening Lines. *A&A*, 4:234, Feb. 1970.

R. A. Flores and J. R. Primack. Observational and Theoretical Constraints on Singular Dark Matter Halos. *ApJ*, 427:L1, May 1994. doi: 10.1086/187350.

R. Foot and Z. K. Silagadze. Thin disk of co-rotating dwarfs: A fingerprint of dissipative (mirror) dark matter? *Phys. Dark Univ.*, 2:163–165, 2013. doi: 10.1016/j.dark.2013.10.001.

G. Fragione and R. Capuzzo-Dolcetta. High-velocity stars from the interaction of a globular cluster and a massive black hole binary. *MNRAS*, 458(3):2596–2603, May 2016. doi: 10.1093/mnras/stw531.

G. Fragione and A. Loeb. Constraining the Milky Way mass with hypervelocity stars. *New A*, 55:32–38, Aug. 2017. doi: 10.1016/j.newast.2017.03.002.

M. Franx, G. Illingworth, and T. de Zeeuw. The Ordered Nature of Elliptical Galaxies: Implications for Their Intrinsic Angular Momenta and Shapes. *ApJ*, 383:112, Dec. 1991. doi: 10.1086/170769.

K. C. Freeman. On the Disks of Spiral and S0 Galaxies. *ApJ*, 160:811, June 1970. doi: 10.1086/150474.

C. S. Frenk and S. D. M. White. Dark matter and cosmic structure. *Annalen der Physik*, 524(9-10):507–534, Oct. 2012. doi: 10.1002/andp.201200212.

C. S. Frenk, S. D. M. White, M. Davis, and G. Efstathiou. The Formation of Dark Halos in a Universe Dominated by Cold Dark Matter. *ApJ*, 327:507, April 1988. doi: 10.1086/166213.

D. Frenkel and B. Smit. *Understanding Molecular Simulation: From Algorithms to Applications*. Computational science. Elsevier Science, 2001. ISBN 9780080519982.

M. Fukugita, C. J. Hogan, and P. J. E. Peebles. The Cosmic Baryon Budget. *ApJ*, 503(2):518–530, Aug. 1998. doi: 10.1086/306025.

Gaia Collaboration. VizieR Online Data Catalog: Gaia DR1 (Gaia Collaboration, 2016). *VizieR Online Data Catalog*, art. I/337, June 2016a.

Gaia Collaboration. Gaia Data Release 1. Summary of the astrometric, photometric, and survey properties. *A&A*, 595:A2, Nov. 2016b. doi: 10.1051/0004-6361/201629512.

Gaia Collaboration. The Gaia mission. *A&A*, 595:A1, Nov. 2016c. doi: 10.1051/0004-6361/201629272.

Gaia Collaboration. VizieR Online Data Catalog: Gaia DR2 (Gaia Collaboration, 2018). *VizieR Online Data Catalog*, art. I/345, April 2018a.

Gaia Collaboration. Gaia Data Release 2. Summary of the contents and survey properties. *A&A*, 616:A1, Aug. 2018b. doi: 10.1051/0004-6361/201833051.

Gaia Collaboration. Gaia Early Data Release 3. Summary of the contents and survey properties. *A&A*, 649:A1, May 2021. doi: 10.1051/0004-6361/202039657.

A. Gallo, L. Ostorero, S. S. Chakrabarty, S. Ebagezio, and A. Diaferio. Probing the shape of the Milky Way dark matter halo with hypervelocity stars: a new method. *A&A, in press*, arXiv:2111.09657, 2022.

S. Gardner, A. Hinkel, and B. Yanny. Applying Noether's Theorem to Matter in the Milky Way: Evidence for External Perturbations and Non-steady-state Effects from Gaia Data Release 2. *ApJ*, 890(2):110, Feb. 2020. doi: 10.3847/1538-4357/ab66c8.

S. Garrison-Kimmel, M. Boylan-Kolchin, J. S. Bullock, and E. N. Kirby. Too big to fail in the Local Group. *MNRAS*, 444(1):222–236, 2014. doi: 10.1093/mnras/stu1477.

A. Garzilli, A. Magalich, T. Theuns, C. S. Frenk, C. Weniger, O. Ruchayskiy, and A. Boyarsky. The Lyman-α forest as a diagnostic of the nature of the dark matter. *MNRAS*, 489(3):3456–3471, Aug 2019. doi: 10.1093/mnras/stz2188.

A. Gatto, F. Fraternali, J. I. Read, F. Marinacci, H. Lux, and S. Walch. Unveiling the corona of the Milky Way via ram-pressure stripping of dwarf satellites. *MNRAS*, 433(4):2749–2763, Aug. 2013. doi: 10.1093/mnras/stt896.

M. J. Geller, A. Diaferio, K. J. Rines, and A. L. Serra. Measuring the Mass Distribution in Galaxy Clusters. *ApJ*, 764(1):58, Feb. 2013. doi: 10.1088/0004-637X/764/1/58.

A. Genina, A. Benítez-Llambay, C. S. Frenk, S. Cole, A. Fattahi, J. F. Navarro, K. A. Oman, T. Sawala, and T. Theuns. The core-cusp problem: a matter of perspective. *MNRAS*, 474(1):1398–1411, Feb 2018. doi: 10.1093/mnras/stx2855.

R. T. Génova-Santos. *The Establishment of the Standard Cosmological Model Through Observations*, pages 311–347. 2020. doi: 10.1007/978-3-030-38509-5_11.

R. Genzel, F. Eisenhauer, and S. Gillessen. The Galactic Center massive black hole and nuclear star cluster. *Rev. Mod. Phys.*, 82(4):3121–3195, Oct 2010. doi: 10.1103/RevModPhys.82.3121.

A. Ghari, B. Famaey, C. Laporte, and H. Haghi. Dark matter-baryon scaling relations from Einasto halo fits to SPARC galaxy rotation curves. *A&A*, 623:A123, Mar. 2019. doi: 10.1051/0004-6361/201834661.

A. M. Ghez, G. Duchêne, K. Matthews, S. D. Hornstein, A. Tanner, J. Larkin, M. Morris, E. E. Becklin, S. Salim, T. Kremenek, D. Thompson, B. T. Soifer, G. Neugebauer, and I. McLean. The First Measurement of Spectral Lines in a Short-Period Star Bound to the Galaxy's Central Black Hole: A Paradox of Youth. *ApJ*, 586(2): L127–L131, April 2003. doi: 10.1086/374804.

A. M. Ghez, S. Salim, S. D. Hornstein, A. Tanner, J. R. Lu, M. Morris, E. E. Becklin, and G. Duchêne. Stellar Orbits around the Galactic Center Black Hole. *ApJ*, 620(2):744–757, Feb. 2005. doi: 10.1086/427175.

A. M. Ghez, S. Salim, N. N. Weinberg, J. R. Lu, T. Do, J. K. Dunn, K. Matthews, M. R. Morris, S. Yelda, E. E. Becklin, T. Kremenek, M. Milosavljevic, and J. Naiman. Measuring Distance and Properties of the Milky Way's Central Supermassive Black Hole with Stellar Orbits. *ApJ*, 689(2):1044–1062, Dec. 2008. doi: 10.1086/592738.

S. Gillessen, F. Eisenhauer, S. Trippe, T. Alexand er, R. Genzel, F. Martins, and T. Ott. Monitoring Stellar Orbits Around the Massive Black Hole in the Galactic Center. *ApJ*, 692(2):1075–1109, Feb. 2009. doi: 10.1088/0004-637X/692/2/1075.

S. Gillessen, P. M. Plewa, F. Eisenhauer, R. Sari, I. Waisberg, M. Habibi, O. Pfuhl, E. George, J. Dexter, S. von Fellenberg, T. Ott, and R. Genzel. An Update on Monitoring Stellar Orbits in the Galactic Center. *ApJ*, 837 (1):30, March 2017. doi: 10.3847/1538-4357/aa5c41.

S. Giodini, D. Pierini, A. Finoguenov, G. W. Pratt, H. Boehringer, A. Leauthaud, L. Guzzo, H. Aussel, M. Bolzonella, P. Capak, M. Elvis, G. Hasinger, O. Ilbert, J. S. Kartaltepe, A. M. Koekemoer, S. J. Lilly, R. Massey, H. J. McCracken, J. Rhodes, M. Salvato, D. B. Sanders, N. Z. Scoville, S. Sasaki, V. Smolcic, Y. Taniguchi, D. Thompson, and COSMOS Collaboration. Stellar and Total Baryon Mass Fractions in Groups and Clusters Since Redshift 1. *ApJ*, 703(1):982–993, Sept. 2009. doi: 10.1088/0004-637X/703/1/982.

M. Girardi, P. Manzato, M. Mezzetti, G. Giuricin, and F. Limboz. Observational Mass-to-Light Ratio of Galaxy Systems from Poor Groups to Rich Clusters. *ApJ*, 569(2):720–741, April 2002. doi: 10.1086/339360.

O. Y. Gnedin and J. P. Ostriker. Limits on collisional dark matter from elliptical galaxies in clusters. *ApJ*, 561: 61, 2001. doi: 10.1086/323211.

O. Y. Gnedin and H. Zhao. Maximum feedback and dark matter profiles of dwarf galaxies. *MNRAS*, 333(2): 299–306, 2002. doi: 10.1046/j.1365-8711.2002.05361.x.

O. Y. Gnedin, A. V. Kravtsov, A. A. Klypin, and D. Nagai. Response of Dark Matter Halos to Condensation of Baryons: Cosmological Simulations and Improved Adiabatic Contraction Model. *ApJ*, 616(1):16–26, Nov. 2004. doi: 10.1086/424914.

O. Y. Gnedin, A. Gould, J. Miralda-Escudé, and A. R. Zentner. Probing the Shape of the Galactic Halo with Hypervelocity Stars. *ApJ*, 634(1):344–350, Nov 2005. doi: 10.1086/496958.

A. Goldstein, P. Veres, E. Burns, M. S. Briggs, R. Hamburg, D. Kocevski, C. A. Wilson-Hodge, R. D. Preece, S. Poolakkil, O. J. Roberts, and et al. An ordinary short gamma-ray burst with extraordinary implications: Fermi-gbm detection of grb 170817a. *ApJ*, 848(2):L14, Oct 2017. doi: 10.3847/2041-8213/aa8f41.

Y. Gong, S. Hou, D. Liang, and E. Papantonopoulos. Gravitational waves in einstein-æther and generalized teves theory after gw170817. *Phys. Rev. D*, 97:084040, April 2018. doi: 10.1103/PhysRevD.97.084040.

A. X. González-Morales, D. J. E. Marsh, J. Peñarrubia, and L. A. Ureña-López. Unbiased constraints on ultralight axion mass from dwarf spheroidal galaxies. *MNRAS*, 472(2):1346–1360, Dec 2017. doi: 10.1093/mnras/stx1941.

Gravity Collaboration, R. Abuter, N. Aimar, A. Amorim, J. Ball, M. Bauböck, J. P. Berger, H. Bonnet, G. Bourdarot, W. Brandner, V. Cardoso, Y. Clénet, Y. Dallilar, R. Davies, P. T. de Zeeuw, J. Dexter, A. Drescher, F. Eisenhauer, N. M. Förster Schreiber, A. Foschi, P. Garcia, F. Gao, E. Gendron, R. Genzel, S. Gillessen, M. Habibi, X. Haubois, G. Heißel, T. Henning, S. Hippler, M. Horrobin, L. Jochum, L. Jocou, A. Kaufer, P. Kervella, S. Lacour, V. Lapeyrère, J. B. Le Bouquin, P. Léna, D. Lutz, T. Ott, T. Paumard, K. Perraut, G. Perrin, O. Pfuhl, S. Rabien, J. Shangguan, T. Shimizu, S. Scheithauer, J. Stadler, A. W. Stephens, O. Straub, C. Straubmeier, E. Sturm, L. J. Tacconi, K. R. W. Tristram, F. Vincent, S. von Fellenberg, F. Widmann, E. Wieprecht, E. Wiezorrek, J. Woillez, S. Yazici, and A. Young. Mass distribution in the Galactic Center based on interferometric astrometry of multiple stellar orbits. *A&A*, 657:L12, Jan. 2022. doi: 10.1051/0004-6361/202142465.

A. Gupta, S. Mathur, Y. Krongold, F. Nicastro, and M. Galeazzi. A Huge Reservoir of Ionized Gas around the Milky Way: Accounting for the Missing Mass? *ApJ*, 756(1):L8, Sept. 2012. doi: 10.1088/2041-8205/756/1/L8.

M. Gustafsson, M. Fairbairn, and J. Sommer-Larsen. Baryonic pinching of galactic dark matter halos. *Phys. Rev. D*, 74(12):123522, Dec. 2006. doi: 10.1103/PhysRevD.74.123522.

H. Haghi, A. E. Bazkiaei, A. H. Zonoozi, and P. Kroupa. Declining rotation curves of galaxies as a test of gravitational theory. *MNRAS*, 458(4):4172–4187, June 2016. doi: 10.1093/mnras/stw573.

F. Hammer, Y. Yang, S. Fouquet, M. S. Pawlowski, P. Kroupa, M. Puech, H. Flores, and J. Wang. The vast thin plane of M31 corotating dwarfs: an additional fossil signature of the M31 merger and of its considerable impact in the whole Local Group. *MNRAS*, 431(4):3543–3549, June 2013. doi: 10.1093/mnras/stt435.

E. Hayashi, J. F. Navarro, and V. Springel. The shape of the gravitational potential in cold dark matter haloes. *MNRAS*, 377(1):50–62, May 2007. doi: 10.1111/j.1365-2966.2007.11599.x.

A. Helmi. Velocity Trends in the Debris of Sagittarius and the Shape of the Dark Matter Halo of Our Galaxy. *ApJ*, 610(2):L97–L100, Aug. 2004. doi: 10.1086/423340.

X. Hernandez, R. A. Sussman, and L. Nasser. Approaching the Dark Sector through a bounding curvature criterion. *MNRAS*, 483(1):147–151, Feb. 2019. doi: 10.1093/mnras/sty3073.

L. Hernquist. An Analytical Model for Spherical Galaxies and Bulges. *ApJ*, 356:359, June 1990. doi: 10.1086/168845.

C. Hesp and A. Helmi. On the feasibility of constraining the triaxiality of the Galactic dark halo with orbital resonances using nearby stars. *arXiv e-prints*, art. arXiv:1804.03670, April 2018.

J. G. Hills. Hyper-velocity and tidal stars from binaries disrupted by a massive Galactic black hole. *Nature*, 331 (6158):687–689, Feb 1988. doi: 10.1038/331687a0.

G. Hinshaw, D. Larson, E. Komatsu, D. N. Spergel, C. L. Bennett, J. Dunkley, M. R. Nolta, M. Halpern, R. S. Hill, N. Odegard, L. Page, K. M. Smith, J. L. Weiland, B. Gold, N. Jarosik, A. Kogut, M. Limon, S. S. Meyer, G. S. Tucker, E. Wollack, and E. L. Wright. Nine-year Wilkinson Microwave Anisotropy Probe (WMAP) Observations: Cosmological Parameter Results. *ApJS*, 208(2):19, Oct 2013. doi: 10.1088/0067-0049/208/2/19.

H. A. Hirsch, U. Heber, S. J. O'Toole, and F. Bresolin. US 708 - an unbound hyper-velocity subluminous O star. *A&A*, 444(3):L61–L64, Dec 2005. doi: 10.1051/0004-6361:200500212.

A. O. Hodson, A. Diaferio, and L. Ostorero. Distribution of phantom dark matter in dwarf spheroidals. *A&A*, 640:A26, Aug. 2020. doi: 10.1051/0004-6361/202037634.

F. Hohl. Numerical Experiments with a Disk of Stars. *ApJ*, 168:343, Sept. 1971. doi: 10.1086/151091.

J. Holmberg and C. Flynn. The local surface density of disc matter mapped byhipparcos. *MNRAS*, 352(2): 440446, Aug 2004. doi: 10.1111/j.1365-2966.2004.07931.x.

C. Hopman and T. Alexander. Resonant Relaxation near a Massive Black Hole: The Stellar Distribution and Gravitational Wave Sources. *ApJ*, 645(2):1152–1163, July 2006. doi: 10.1086/504400.

S. Horiuchi, P. J. Humphrey, J. Oñorbe, K. N. Abazajian, M. Kaplinghat, and S. Garrison-Kimmel. Sterile neutrino dark matter bounds from galaxies of the Local Group. *Phys. Rev. D*, 89(2):025017, 2014. doi: 10.1103/PhysRevD.89.025017.

J.-W. Hsueh, W. Enzi, S. Vegetti, M. W. Auger, C. D. Fassnacht, G. Despali, L. V. E. Koopmans, and J. P. McKean. SHARP VII. New constraints on the dark matter free-streaming properties and substructure abundance from gravitationally lensed quasars. *MNRAS*, 492(2):3047–3059, Nov. 2019. doi: 10.1093/mnras/stz3177.

W. Hu, R. Barkana, and A. Gruzinov. Fuzzy Cold Dark Matter: The Wave Properties of Ultralight Particles. *Phys. Rev. Lett.*, 85(6):1158–1161, Aug. 2000. doi: 10.1103/PhysRevLett.85.1158.

Y. Huang, X. W. Liu, H. W. Zhang, B. Q. Chen, M. S. Xiang, C. Wang, H. B. Yuan, Z. J. Tian, Y. B. Li, and B. Wang. Discovery of Two New Hypervelocity Stars from the LAMOST Spectroscopic Surveys. *ApJ*, 847(1): L9, Sep 2017. doi: 10.3847/2041-8213/aa894b.

Y. Huang, Q. Li, H. Zhang, X. Li, W. Sun, J. Chang, X. Dong, and X. Liu. Discovery of a Candidate Hypervelocity Star Originating from the Sagittarius Dwarf Spheroidal Galaxy. *ApJ*, 907(2):L42, Feb. 2021. doi: 10.3847/2041-8213/abd413.

L. Hui, J. P. Ostriker, S. Tremaine, and E. Witten. Ultralight scalars as cosmological dark matter. *Phys. Rev. D*, 95(4):043541, Feb 2017. doi: 10.1103/PhysRevD.95.043541.

H. M. Hung, R. T. O'Neill, P. Bauer, and K. Khne. The Behavior of the P-Value When the Alternative Hypothesis is True. *Biometrics*, 53(1):11–22, 1997. doi: 10.2307/2533093.

R. Ibata, G. F. Lewis, M. Irwin, E. Totten, and T. Quinn. Great Circle Tidal Streams: Evidence for a Nearly Spherical Massive Dark Halo around the Milky Way. *ApJ*, 551(1):294–311, April 2001. doi: 10.1086/320060.

A. Irrgang, S. Kreuzer, and U. Heber. Hypervelocity stars in the Gaia era. Runaway B stars beyond the velocity limit of classical ejection mechanisms. *A&A*, 620:A48, Dec. 2018. doi: 10.1051/0004-6361/201833874.

A. Irrgang, M. Dimpel, U. Heber, and R. Raddi. Blue extreme disk-runaway stars with Gaia EDR3. *A&A*, 646: L4, Feb. 2021. doi: 10.1051/0004-6361/202040178.

V. Iršič, M. Viel, M. G. Haehnelt, J. S. Bolton, S. Cristiani, G. D. Becker, V. D'Odorico, G. Cupani, T.-S. Kim, T. A. M. Berg, S. López, S. Ellison, L. Christensen, K. D. Denney, and G. Worseck. New constraints on the free-streaming of warm dark matter from intermediate and small scale Lyman-α forest data. *Phys. Rev. D*, 96 (2):023522, July 2017. doi: 10.1103/PhysRevD.96.023522.

M. Irwin and D. Hatzidimitriou. Structural parameters for the Galactic dwarf spheroidals. *MNRAS*, 277(4): 1354–1378, Dec. 1995. doi: 10.1093/mnras/277.4.1354.

J. R. Jardel and J. A. Sellwood. Halo Density Reduction by Baryonic Settling? *ApJ*, 691(2):1300–1306, Feb. 2009. doi: 10.1088/0004-637X/691/2/1300.

M. A. Jiménez and X. Hernandez. Disk stability under MONDian gravity. *arXiv e-prints*, art. arXiv:1406.0537, 2014.

R. Jimenez, L. Verde, T. Treu, and D. Stern. Constraints on the Equation of State of Dark Energy and the Hubble Constant from Stellar Ages and the Cosmic Microwave Background. *ApJ*, 593(2):622–629, Aug. 2003. doi: 10.1086/376595.

Y. P. Jing and Y. Suto. Triaxial Modeling of Halo Density Profiles with High-Resolution N-Body Simulations. *ApJ*, 574(2):538–553, Aug. 2002. doi: 10.1086/341065.

K. V. Johnston, D. R. Law, and S. R. Majewski. A Two Micron All Sky Survey View of the Sagittarius Dwarf Galaxy. III. Constraints on the Flattening of the Galactic Halo. *ApJ*, 619(2):800–806, Feb. 2005. doi: 10.1086/426777.

C. Jones and W. Forman. The structure of clusters of galaxies observed with Einstein. *ApJ*, 276:38–55, Jan. 1984. doi: 10.1086/161591.

C. Jordi, M. Gebran, J. M. Carrasco, J. de Bruijne, H. Voss, C. Fabricius, J. Knude, A. Vallenari, R. Kohley, and A. Mora. Gaia broad band photometry. *A&A*, 523:A48, Nov. 2010. doi: 10.1051/0004-6361/201015441.

G. Jungman, M. Kamionkowski, and K. Griest. Supersymmetric dark matter. *Phys. Rep.*, 267:195–373, March 1996. doi: 10.1016/0370-1573(95)00058-5.

P. R. Kafle, S. Sharma, G. F. Lewis, and J. Bland-Hawthorn. On the Shoulders of Giants: Properties of the Stellar Halo and the Milky Way Mass Distribution. *ApJ*, 794(1):59, Oct. 2014. doi: 10.1088/0004-637X/794/1/59.

N. Katz and J. E. Gunn. Dissipational Galaxy Formation. I. Effects of Gasdynamics. *ApJ*, 377:365, Aug. 1991. doi: 10.1086/170367.

N. Katz and S. D. M. White. Hierarchical Galaxy Formation: Overmerging and the Formation of an X-Ray Cluster. *ApJ*, 412:455, Aug. 1993. doi: 10.1086/172935.

G. Kauffmann, S. D. M. White, and B. Guiderdoni. The formation and evolution of galaxies within merging dark matter haloes. *MNRAS*, 264:201–218, 1993. doi: 10.1093/mnras/264.1.201.

S. Kazantzidis, A. V. Kravtsov, A. R. Zentner, B. Allgood, D. Nagai, and B. Moore. The Effect of Gas Cooling on the Shapes of Dark Matter Halos. *ApJ*, 611(2):L73–L76, Aug. 2004. doi: 10.1086/423992.

R. Kennedy, C. Frenk, S. Cole, and A. Benson. Constraining the warm dark matter particle mass with Milky Way satellites. *MNRAS*, 442(3):2487–2495, Aug 2014. doi: 10.1093/mnras/stu719.

S. J. Kenyon, B. C. Bromley, M. J. Geller, and W. R. Brown. Hypervelocity Stars: From the Galactic Center to the Halo. *ApJ*, 680(1):312–327, June 2008. doi: 10.1086/587738.

S. J. Kenyon, B. C. Bromley, W. R. Brown, and M. J. Geller. Predicted Space Motions for Hypervelocity and Runaway Stars: Proper Motions and Radial Velocities for the Gaia Era. *ApJ*, 793(2):122, Oct. 2014. doi: 10.1088/0004-637X/793/2/122.

S. J. Kenyon, B. C. Bromley, W. R. Brown, and M. J. Geller. Impact of the Galactic Disk and Large Magellanic Cloud on the Trajectories of Hypervelocity Stars Ejected from the Galactic Center. *ApJ*, 864(2):130, Sept. 2018. doi: 10.3847/1538-4357/aada04.

A. Klypin, A. V. Kravtsov, O. Valenzuela, and F. Prada. Where Are the Missing Galactic Satellites? *ApJ*, 522 (1):82–92, Sept. 1999. doi: 10.1086/307643.

J. P. Kneib, R. S. Ellis, I. Smail, W. J. Couch, and R. M. Sharples. Hubble Space Telescope Observations of the Lensing Cluster Abell 2218. *ApJ*, 471:643, Nov. 1996. doi: 10.1086/177995.

S. E. Koposov, H.-W. Rix, and D. W. Hogg. Constraining the Milky Way Potential with a Six-Dimensional Phase-Space Map of the GD-1 Stellar Stream. *ApJ*, 712(1):260–273, March 2010. doi: 10.1088/0004-637X/712/1/260.

S. E. Koposov, D. Boubert, T. S. Li, D. Erkal, G. S. Da Costa, D. B. Zucker, A. P. Ji, K. Kuehn, G. F. Lewis, D. Mackey, J. D. Simpson, N. Shipp, Z. Wan, V. Belokurov, J. Bland-Hawthorn, S. L. Martell, T. Nordlander, A. B. Pace, G. M. De Silva, M.-Y. Wang, and S5 Collaboration. Discovery of a nearby 1700 km s^{-1} star ejected from the Milky Way by Sgr A*. *MNRAS*, 491(2):2465–2480, Jan. 2020. doi: 10.1093/mnras/stz3081.

J. Kormendy. Dark Matter in Dwarf Galaxies. In J. Kormendy and G. R. Knapp, editors, *Dark matter in the universe*, volume 117, page 139, Jan. 1987.

M. Kowalski, D. Rubin, G. Aldering, R. J. Agostinho, A. Amadon, R. Amanullah, C. Balland , K. Barbary, G. Blanc, P. J. Challis, A. Conley, N. V. Connolly, R. Covarrubias, K. S. Dawson, S. E. Deustua, R. Ellis, S. Fabbro, V. Fadeyev, X. Fan, B. Farris, G. Folatelli, B. L. Frye, G. Garavini, E. L. Gates, L. Germany, G. Goldhaber, B. Goldman, A. Goobar, D. E. Groom, J. Haissinski, D. Hardin, I. Hook, S. Kent, A. G. Kim, R. A. Knop, C. Lidman, E. V. Linder, J. Mendez, J. Meyers, G. J. Miller, M. Moniez, A. M. Mourão, H. Newberg, S. Nobili, P. E. Nugent, R. Pain, O. Perdereau, S. Perlmutter, M. M. Phillips, V. Prasad, R. Quimby, N. Regnault, J. Rich, E. P. Rubenstein, P. Ruiz-Lapuente, F. D. Santos, B. E. Schaefer, R. A. Schommer, R. C. Smith, A. M. Soderberg, A. L. Spadafora, L. G. Strolger, M. Strovink, N. B. Suntzeff, N. Suzuki, R. C. Thomas, N. A. Walton, L. Wang, W. M. Wood-Vasey, and J. L. Yun. Improved Cosmological Constraints from New, Old, and Combined Supernova Data Sets. *ApJ*, 686(2):749–778, 2008. doi: 10.1086/589937.

S. Kreuzer, A. Irrgang, and U. Heber. Hypervelocity stars in the Gaia era. Revisiting the most extreme stars from the MMT HVS survey. *A&A*, 637:A53, May 2020. doi: 10.1051/0004-6361/202037747.

M. Kuhlen, M. Vogelsberger, and R. Angulo. Numerical simulations of the dark universe: State of the art and the next decade. *Physics of the Dark Universe*, 1(1-2):50–93, Nov. 2012. doi: 10.1016/j.dark.2012.10.002.

K. Kuijken and G. Gilmore. The mass distribution in the galactic disc -II. Determination of the surface mass density of the galactic disc near the Sun. *MNRAS*, 239:605–649, 1989a. doi: 10.1093/mnras/239.2.605.

K. Kuijken and G. Gilmore. The mass distribution in the galactic disc -III. The local volume mass density. *MNRAS*, 239:651–664, 1989b. doi: 10.1093/mnras/239.2.651.

A. H. W. Küpper, E. Balbinot, A. Bonaca, K. V. Johnston, D. W. Hogg, P. Kroupa, and B. X. Santiago. Globular Cluster Streams as Galactic High-Precision Scales—the Poster Child Palomar 5. *ApJ*, 803(2):80, April 2015. doi: 10.1088/0004-637X/803/2/80.

R. Kuzio de Naray, S. S. McGaugh, W. J. G. de Blok, and A. Bosma. High-Resolution Optical Velocity Fields of 11 Low Surface Brightness Galaxies. *ApJS*, 165(2):461–479, Aug 2006. doi: 10.1086/505345.

T. Lasserre, C. Afonso, J. N. Albert, J. Andersen, R. Ansari, É. Aubourg, P. Bareyre, F. Bauer, J. P. Beaulieu, G. Blanc, A. Bouquet, S. Char, X. Charlot, F. Couchot, C. Coutures, F. Derue, R. Ferlet, J. F. Glicenstein, B. Goldman, A. Gould, D. Graff, M. Gros, J. Haissinski, J. C. Hamilton, D. Hardin, J. de Kat, A. Kim, É. Lesquoy, C. Loup, C. Magneville, B. Mansoux, J. B. Marquette, É. Maurice, A. Milsztajn, M. Moniez, N. Palanque-Delabrouille, O. Perdereau, L. Prévot, N. Regnault, J. Rich, M. Spiro, A. Vidal-Madjar, L. Vigroux, S. Zylberajch, and EROS Collaboration. Not enough stellar mass Machos in the Galactic halo. *A&A*, 355:L39–L42, March 2000.

R. Launhardt, R. Zylka, and P. G. Mezger. The nuclear bulge of the Galaxy. III. Large-scale physical characteristics of stars and interstellar matter. *A&A*, 384:112–139, March 2002. doi: 10.1051/0004-6361:20020017.

D. R. Law and S. R. Majewski. The Sagittarius Dwarf Galaxy: A Model for Evolution in a Triaxial Milky Way Halo. *ApJ*, 714(1):229–254, May 2010. doi: 10.1088/0004-637X/714/1/229.

D. R. Law, S. R. Majewski, and K. V. Johnston. Evidence for a Triaxial Milky Way Dark Matter Halo from the Sagittarius Stellar Tidal Stream. *ApJ*, 703(1):L67–L71, Sept. 2009. doi: 10.1088/0004-637X/703/1/L67.

F. Lelli, F. Fraternali, and M. Verheijen. A scaling relation for disc galaxies: circular-velocity gradient versus central surface brightness. *MNRAS*, 433:L30–L34, 2013. doi: 10.1093/mnrasl/slt053.

F. Lelli, S. S. McGaugh, and J. M. Schombert. The Small Scatter of the Baryonic Tully-Fisher Relation. *ApJ*, 816(1):L14, Jan. 2016a. doi: 10.3847/2041-8205/816/1/L14.

F. Lelli, S. S. McGaugh, and J. M. Schombert. The Small Scatter of the Baryonic Tully-Fisher Relation. *ApJ*, 816(1):L14, Jan. 2016b. doi: 10.3847/2041-8205/816/1/L14.

P. J. T. Leonard. The Maximum Possible Velocity of Dynamically Ejected Runaway Stars. *AJ*, 101:562, Feb. 1991. doi: 10.1086/115704.

Y. Li, A. Luo, G. Zhao, Y. Lu, J. Ren, and F. Zuo. Metal-poor Hypervelocity Star Candidates from the Sloan Digital Sky Survey. *ApJ*, 744(2):L24, Jan. 2012. doi: 10.1088/2041-8205/744/2/L24.

Y.-B. Li, A. L. Luo, G. Zhao, Y.-J. Lu, P. Wei, B. Du, X. Li, Y.-H. Zhao, Z.-W. Han, B. Wang, Y. Wu, Y. Zhang, Y.-H. Hou, Y.-F. Wang, and M. Yang. 19 low mass hypervelocity star candidates from the first data release of the LAMOST survey. *Research in Astronomy and Astrophysics*, 15(8):1364, Aug. 2015. doi: 10.1088/1674-4527/15/8/018.

Y.-B. Li, A. L. Luo, Y.-J. Lu, X.-S. Zhang, J. Li, R. Wang, F. Zuo, M. Xiang, Y.-S. Ting, T. Marchetti, S. Li, Y.-F. Wang, S. Zhang, K. Hattori, Y.-H. Zhao, H.-W. Zhang, and G. Zhao. 591 High-velocity Stars in the Galactic Halo Selected from LAMOST DR7 and Gaia DR2. *ApJS*, 252(1):3, Jan. 2021. doi: 10.3847/1538-4365/abc16e.

N. I. Libeskind, A. Knebe, Y. Hoffman, and S. Gottlöber. The universal nature of subhalo accretion. *MNRAS*, 443(2):1274–1280, Sept. 2014. doi: 10.1093/mnras/stu1216.

N. I. Libeskind, Y. Hoffman, R. B. Tully, H. M. Courtois, D. Pomarède, S. Gottlöber, and M. Steinmetz. Planes of satellite galaxies and the cosmic web. *MNRAS*, 452(1):1052–1059, Sept. 2015. doi: 10.1093/mnras/stv1302.

LIGO Scientific Collaboration and Virgo Collaboration. Gw170817: Observation of gravitational waves from a binary neutron star inspiral. *Phys. Rev. Lett.*, 119:161101, Oct 2017. doi: 10.1103/PhysRevLett.119.161101.

A. Loeb and N. Weiner. Cores in Dwarf Galaxies from Dark Matter with a Yukawa Potential. *Phys. Rev. Lett.*, 106(17):171302, 2011. doi: 10.1103/PhysRevLett.106.171302.

S. R. Loebman, Ž. Ivezić, T. R. Quinn, J. Bovy, C. R. Christensen, M. Jurić, R. Roškar, A. M. Brooks, and F. Governato. The Milky Way Tomography with Sloan Digital Sky Survey. V. Mapping the Dark Matter Halo. *ApJ*, 794(2):151, Oct. 2014. doi: 10.1088/0004-637X/794/2/151.

E. L. Łokas and G. A. Mamon. Dark matter distribution in the Coma cluster from galaxy kinematics: breaking the mass-anisotropy degeneracy. *MNRAS*, 343(2):401–412, Aug. 2003. doi: 10.1046/j.1365-8711.2003.06684.x.

M. R. Lovell, V. Eke, C. S. Frenk, L. Gao, A. Jenkins, T. Theuns, J. Wang, S. D. M. White, A. Boyarsky, and O. Ruchayskiy. The haloes of bright satellite galaxies in a warm dark matter universe. *MNRAS*, 420(3): 2318–2324, Feb. 2012. doi: 10.1111/j.1365-2966.2011.20200.x.

A. Luna, D. Minniti, and J. Alonso-García. Candidate Hypervelocity Red Clump Stars in the Galactic Bulge Found Using the VVV and Gaia Surveys. *ApJ*, 887(2):L39, Dec. 2019. doi: 10.3847/2041-8213/ab5c27.

H. N. Luu, S. H. H. Tye, and T. Broadhurst. Multiple ultralight axionic wave dark matter and astronomical structures. *Physics of the Dark Universe*, 30:100636, Dec. 2020. doi: 10.1016/j.dark.2020.100636.

A. V. Macció, S. Paduroiu, D. Anderhalden, A. Schneider, and B. Moore. Cores in warm dark matter haloes: a Catch 22 problem. *MNRAS*, 424(2):1105–1112, Aug. 2012. doi: 10.1111/j.1365-2966.2012.21284.x.

M. E. Machacek. Growth of Adiabatic Perturbations in Self-interacting Dark Matter. *ApJ*, 431:41, 1994. doi: 10.1086/174465.

F. Malbet, A. Léger, G. Anglada Escudé, A. Sozzetti, D. Spolyar, L. Labadie, M. Shao, B. Holl, R. Goullioud, A. Crouzier, C. Boehm, and A. Krone-Martins. Microarcsecond astrometric observatory Theia: from dark matter to compact objects and nearby earths. In H. A. MacEwen, G. G. Fazio, M. Lystrup, N. Batalha, N. Siegler, and E. C. Tong, editors, *Space Telescopes and Instrumentation 2016: Optical, Infrared, and Millimeter Wave*, volume 9904 of *Society of Photo-Optical Instrumentation Engineers (SPIE) Conference Series*, page 99042F, July 2016. doi: 10.1117/12.2234425.

F. Malbet, U. Abbas, J. Alves, C. Boehm, W. Brown, L. Chemin, A. Correia, F. Courbin, J. Darling, A. Diaferio, M. Fortin, M. Fridlund, O. Gnedin, B. Holl, A. Krone-Martins, A. Léger, L. Labadie, J. Laskar, G. Mamon, B. McArthur, D. Michalik, A. Moitinho, M. Oertel, L. Ostorero, J. Schneider, P. Scott, M. Shao, A. Sozzetti, J. Tomsick, M. Valluri, and R. Wyse. ESA Voyage 2050 white paper – Faint objects in motion: the new frontier of high precision astrometry. *arXiv e-prints*, art. arXiv:1910.08028, Oct. 2019.

F. Malbet, C. Boehm, A. Krone-Martins, A. Amorim, G. Anglada-Escudé, A. Brandeker, F. Courbin, T. Enßlin, A. Falcão, K. Freese, B. Holl, L. Labadie, A. Léger, G. A. Mamon, B. McArthur, A. Mora, M. Shao, A. Sozzetti, D. Spolyar, E. Villaver, U. Abbas, C. Albertus, J. Alves, R. Barnes, A. S. Bonomo, H. Bouy, W. R. Brown, V. Cardoso, M. Castellani, L. Chemin, H. Clark, A. C. M. Correia, M. Crosta, A. Crouzier, M. Damasso, J. Darling, M. B. Davies, A. Diaferio, M. Fortin, M. Fridlund, M. Gai, P. Garcia, O. Gnedin, A. Goobar, P. Gordo, R. Goullioud, D. Hall, N. Hambly, D. Harrison, D. Hobbs, A. Holland, E. Høg, C. Jordi, S. Klioner, A. Lançon, J. Laskar, M. Lattanzi, C. Le Poncin-Lafitte, X. Luri, D. Michalik, A. M. de Almeida, A. Mourão, L. Moustakas, N. J. Murray, M. Muterspaugh, M. Oertel, L. Ostorero, J. Portell, J.-P. Prost, A. Quirrenbach, J. Schneider, P. Scott, A. Siebert, A. d. Silva, M. Silva, P. Thébault, J. Tomsick, W. Traub, M. de Val-Borro, M. Valluri, N. A. Walton, L. L. Watkins, G. White, L. Wyrzykowski, R. Wyse, and Y. Yamada. Faint objects in motion: the new frontier of high precision astrometry. *Experimental Astronomy*, Sept. 2021. doi: 10.1007/s10686-021-09781-1.

K. Malhan and R. A. Ibata. Constraining the Milky Way halo potential with the GD-1 stellar stream. *MNRAS*, 486(3):2995–3005, July 2019. doi: 10.1093/mnras/stz1035.

D. Malyshev, A. Neronov, and D. Eckert. Constraints on 3.55 kev line emission from stacked observations of dwarf spheroidal galaxies. *Phys. Rev. D*, 90(10), Nov 2014. doi: 10.1103/physrevd.90.103506.

C. Maraston. Evolutionary population synthesis: models, analysis of the ingredients and application to high-z galaxies. *MNRAS*, 362(3):799–825, 2005. doi: 10.1111/j.1365-2966.2005.09270.x.

T. Marchetti. Gaia EDR3 in 6D: searching for unbound stars in the galaxy. *MNRAS*, 503(1):1374–1389, May 2021. doi: 10.1093/mnras/stab599.

T. Marchetti, E. M. Rossi, G. Kordopatis, A. G. A. Brown, A. Rimoldi, E. Starkenburg, K. Youakim, and R. Ashley. An artificial neural network to discover hypervelocity stars: candidates in Gaia DR1/TGAS. *MNRAS*, 470(2):1388–1403, Sep 2017. doi: 10.1093/mnras/stx1304.

T. Marchetti, O. Contigiani, E. M. Rossi, J. G. Albert, A. G. A. Brown, and A. Sesana. Predicting the hypervelocity star population in Gaia. *MNRAS*, 476(4):4697–4712, June 2018. doi: 10.1093/mnras/sty579.

T. Marchetti, E. M. Rossi, and A. G. A. Brown. Gaia DR2 in 6D: searching for the fastest stars in the Galaxy. *MNRAS*, 490(1):157–171, Nov 2019. doi: 10.1093/mnras/sty2592.

D. J. E. Marsh and A.-R. Pop. Axion dark matter, solitons and the cusp-core problem. *MNRAS*, 451(3): 2479–2492, Aug 2015. doi: 10.1093/mnras/stv1050.

D. J. E. Marsh and J. Silk. A model for halo formation with axion mixed dark matter. *MNRAS*, 437(3):2652–2663, Jan. 2014. doi: 10.1093/mnras/stt2079.

S. P. Martin. *A Supersymmetry Primer*, pages 1–98. 1998. doi: 10.1142/9789812839657_0001.

T. P. K. Martinsson, M. A. W. Verheijen, K. B. Westfall, M. A. Bershady, D. R. Andersen, and R. A. Swaters. The DiskMass Survey. VII. The distribution of luminous and dark matter in spiral galaxies. *A&A*, 557:A131, Sept. 2013. doi: 10.1051/0004-6361/201321390.

S. Mashchenko, H. M. P. Couchman, and J. Wadsley. The removal of cusps from galaxy centres by stellar feedback in the early Universe. *Nature*, 442(7102):539–542, 2006. doi: 10.1038/nature04944.

S. Mashchenko, J. Wadsley, and H. M. P. Couchman. Stellar feedback in dwarf galaxy formation. *Science*, 319 (5860):174177, Jan 2008. doi: 10.1126/science.1148666.

M. Mateo, E. Olszewski, D. L. Welch, P. Fischer, and W. Kunkel. A Kinematic Study of the Fornax Dwarf Spheroid Galaxy. *AJ*, 102:914, Sept. 1991. doi: 10.1086/115923.

M. L. Mateo. Dwarf Galaxies of the Local Group. *ARA&A*, 36:435–506, Jan. 1998. doi: 10.1146/annurev.astro.36.1.435.

S. McGaugh. Predictions and Outcomes for the Dynamics of Rotating Galaxies. *Galaxies*, 8(2):35, April 2020. doi: 10.3390/galaxies8020035.

S. S. McGaugh. The Mass Discrepancy-Acceleration Relation: Disk Mass and the Dark Matter Distribution. *ApJ*, 609(2):652–666, July 2004. doi: 10.1086/421338.

S. S. McGaugh. Milky Way Mass Models and MOND. *ApJ*, 683(1):137–148, 2008. doi: 10.1086/589148.

S. S. McGaugh. Novel Test of Modified Newtonian Dynamics with Gas Rich Galaxies. *Phys. Rev. Lett.*, 106(12): 121303, March 2011. doi: 10.1103/PhysRevLett.106.121303.

S. S. McGaugh. The Baryonic Tully-Fisher Relation of Gas-rich Galaxies as a Test of ΛCDM and MOND. *AJ*, 143(2):40, Feb 2012. doi: 10.1088/0004-6256/143/2/40.

S. S. McGaugh and W. J. G. de Blok. Testing the Hypothesis of Modified Dynamics with Low Surface Brightness Galaxies and Other Evidence. *ApJ*, 499(1):66–81, 1998a. doi: 10.1086/305629.

S. S. McGaugh and W. J. G. de Blok. Testing the Dark Matter Hypothesis with Low Surface Brightness Galaxies and Other Evidence. *ApJ*, 499(1):41–65, May 1998b. doi: 10.1086/305612.

S. S. McGaugh, G. D. Bothun, and J. M. Schombert. Galaxy Selection and the Surface Brightness Distribution. *AJ*, 110:573, 1995. doi: 10.1086/117543.

S. S. McGaugh, J. M. Schombert, G. D. Bothun, and W. de Blok. The Baryonic Tully-Fisher relation. *Astrophys. J. Lett.*, 533:L99–L102, 2000. doi: 10.1086/312628.

S. S. McGaugh, V. C. Rubin, and W. J. G. de Blok. High-Resolution Rotation Curves of Low Surface Brightness Galaxies. I. Data. *AJ*, 122(5):2381–2395, Nov 2001. doi: 10.1086/323448.

S. S. McGaugh, F. Lelli, and J. M. Schombert. Radial Acceleration Relation in Rotationally Supported Galaxies. *Phys. Rev. Lett.*, 117(20):201101, Nov 2016. doi: 10.1103/PhysRevLett.117.201101.

M. Meneghetti, N. Yoshida, M. Bartelmann, L. Moscardini, V. Springel, G. Tormen, and S. D. M. White. Giant cluster arcs as a constraint on the scattering cross-section of dark matter. *MNRAS*, 325:435, 2001. doi: 10.1046/j.1365-8711.2001.04477.x.

M. Meneghetti, G. Davoli, P. Bergamini, P. Rosati, P. Natarajan, C. Giocoli, G. B. Caminha, R. B. Metcalf, E. Rasia, S. Borgani, F. Calura, C. Grillo, A. Mercurio, and E. Vanzella. An excess of small-scale gravitational lenses observed in galaxy clusters. *Science*, 369(6509):1347–1351, Sept. 2020. doi: 10.1126/science.aax5164.

D. Merritt. *A Philosophical Approach to MOND: Assessing the Milgromian Research Program in Cosmology*. 2020.

D. Merritt and M. Y. Poon. Chaotic Loss Cones and Black Hole Fueling. *ApJ*, 606(2):788–798, May 2004. doi: 10.1086/382497.

L. Meyer, A. M. Ghez, R. Schödel, S. Yelda, A. Boehle, J. R. Lu, T. Do, M. R. Morris, E. E. Becklin, and K. Matthews. The Shortest-Known-Period Star Orbiting Our Galaxy's Supermassive Black Hole. *Science*, 338 (6103):84, Oct. 2012. doi: 10.1126/science.1225506.

M. Milgrom. A modification of the Newtonian dynamics as a possible alternative to the hidden mass hypothesis. *ApJ*, 270:365–370, July 1983a. doi: 10.1086/161130.

M. Milgrom. A modification of the Newtonian dynamics - Implications for galaxies. *ApJ*, 270:371–389, July 1983b. doi: 10.1086/161131.

M. Milgrom. A modification of the newtonian dynamics : implications for galaxy systems. *ApJ*, 270:384–389, July 1983c. doi: 10.1086/161132.

M. Milgrom. On Stability of Galactic Disks in the Modified Dynamics and the Distribution of Their Mean Surface-Brightness. *ApJ*, 338:121, 1989. doi: 10.1086/167184.

M. Milgrom. Dynamics with a Nonstandard Inertia-Acceleration Relation: An Alternative to Dark Matter in Galactic Systems. *Annals of Physics*, 229(2):384–415, Feb. 1994. doi: 10.1006/aphy.1994.1012.

M. Milgrom. The modified dynamics as a vacuum effect. *Phys. Lett. A*, 253(5-6):273–279, 1999. doi: 10.1016/S0375-9601(99)00077-8.

M. Milgrom. MOND as modified inertia. In G. A. Mamon, F. Combes, C. Deffayet, and B. Fort, editors, *EAS Publications Series*, volume 20 of *EAS Publications Series*, pages 217–224, Jan. 2006. doi: 10.1051/eas:2006074.

M. Milgrom. Bimetric mond gravity. *Phys. Rev. D*, 80:123536, Dec 2009. doi: 10.1103/PhysRevD.80.123536.

M. Milgrom. Quasi-linear formulation of MOND. *MNRAS*, 403(2):886–895, April 2010. doi: 10.1111/j.1365-2966.2009.16184.x.

M. C. Miller, M. Freitag, D. P. Hamilton, and V. M. Lauburg. Binary Encounters with Supermassive Black Holes: Zero-Eccentricity LISA Events. *ApJ*, 631(2):L117–L120, Oct. 2005. doi: 10.1086/497335.

M. J. Miller and J. N. Bregman. The Structure of the Milky Way's Hot Gas Halo. *ApJ*, 770(2):118, June 2013. doi: 10.1088/0004-637X/770/2/118.

M. Miyamoto and R. Nagai. Three-dimensional models for the distribution of mass in galaxies. *PASJ*, 27:533–543, Jan 1975.

B. Moore. Evidence against dissipation-less dark matter from observations of galaxy haloes. *Nature*, 370(6491):629–631, Aug 1994. doi: 10.1038/370629a0.

M. Moresco, A. Cimatti, R. Jimenez, L. Pozzetti, G. Zamorani, M. Bolzonella, J. Dunlop, F. Lamareille, M. Mignoli, H. Pearce, P. Rosati, D. Stern, L. Verde, E. Zucca, C. M. Carollo, T. Contini, J.-P. Kneib, O. Le Fèvre, S. J. Lilly, V. Mainieri, A. Renzini, M. Scodeggio, I. Balestra, R. Gobat, R. McLure, S. Bardelli, A. Bongiorno, K. Caputi, O. Cucciati, S. de la Torre, L. de Ravel, P. Franzetti, B. Garilli, A. Iovino, P. Kampczyk, C. Knobel, K. Kovač, J.-F. Le Borgne, V. Le Brun, C. Maier, R. Pelló, Y. Peng, E. Perez-Montero, V. Presotto, J. D. Silverman, M. Tanaka, L. A. M. Tasca, L. Tresse, D. Vergani, O. Almaini, L. Barnes, R. Bordoloi, E. Bradshaw, A. Cappi, R. Chuter, M. Cirasuolo, G. Coppa, C. Diener, S. Foucaud, W. Hartley, M. Kamionkowski, A. M. Koekemoer, C. López-Sanjuan, H. J. McCracken, P. Nair, P. Oesch, A. Stanford, and N. Welikala. Improved constraints on the expansion rate of the Universe up to z ~1.1 from the spectroscopic evolution of cosmic chronometers. *J. Cosmol. Astropart. Phys.*, 2012(8):006, 2012a. doi: 10.1088/1475-7516/2012/08/006.

M. Moresco, L. Verde, L. Pozzetti, R. Jimenez, and A. Cimatti. New constraints on cosmological parameters and neutrino properties using the expansion rate of the Universe to z ~1.75. *J. Cosmol. Astropart. Phys.*, 2012(7):053, July 2012b. doi: 10.1088/1475-7516/2012/07/053.

H. Motohashi and W. Hu. Primordial black holes and slow-roll violation. *Phys. Rev. D*, 96(6):063503, Sept. 2017. doi: 10.1103/PhysRevD.96.063503.

V. K. Narayanan, D. N. Spergel, R. Davé, and C.-P. Ma. Constraints on the mass of warm dark matter particles and the shape of the linear power spectrum from the lyα forest. *ApJ*, 543(2):L103–L106, Nov. 2000. doi: 10.1086/317269.

J. F. Navarro, V. R. Eke, and C. S. Frenk. The cores of dwarf galaxy haloes. *MNRAS*, 283(3):L72–L78, Dec. 1996a. doi: 10.1093/mnras/283.3.L72.

J. F. Navarro, C. S. Frenk, and S. D. M. White. The Structure of Cold Dark Matter Halos. *ApJ*, 462:563, May 1996b. doi: 10.1086/177173.

J. F. Navarro, C. S. Frenk, and S. D. M. White. A Universal Density Profile from Hierarchical Clustering. *ApJ*, 490(2):493–508, Dec. 1997. doi: 10.1086/304888.

K. F. Neugent, P. Massey, N. I. Morrell, B. Skiff, and C. Georgy. A Runaway Yellow Supergiant Star in the Small Magellanic Cloud. *AJ*, 155(5):207, May 2018. doi: 10.3847/1538-3881/aab964.

K. C. Ng, S. Horiuchi, J. M. Gaskins, M. Smith, and R. Preece. Improved limits on sterile neutrino dark matter using full-sky fermi gamma-ray burst monitor data. *Phys. Rev. D*, 92(4), Aug 2015. doi: 10.1103/physrevd.92.043503.

C. Nipoti, P. Londrillo, H. Zhao, and L. Ciotti. Vertical dynamics of disc galaxies in modified Newtonian dynamics. *MNRAS*, 379(2):597–604, Aug. 2007. doi: 10.1111/j.1365-2966.2007.11835.x.

S. Nojiri, S. D. Odintsov, and V. K. Oikonomou. Modified gravity theories on a nutshell: Inflation, bounce and late-time evolution. *Phys. Rep.*, 692:1–104, June 2017. doi: 10.1016/j.physrep.2017.06.001.

R. M. O'Leary and A. Loeb. Production of hypervelocity stars through encounters with stellar-mass black holes in the Galactic Centre. *MNRAS*, 383(1):86–92, Jan 2008. doi: 10.1111/j.1365-2966.2007.12531.x.

R. P. Olling and M. R. Merrifield. Two measures of the shape of the dark halo of the Milky Way. *MNRAS*, 311(2):361–369, Jan 2000. doi: 10.1046/j.1365-8711.2000.03053.x.

K. A. Oman, J. F. Navarro, A. Fattahi, C. S. Frenk, T. Sawala, S. D. M. White, R. Bower, R. A. Crain, M. Furlong, M. Schaller, J. Schaye, and T. Theuns. The unexpected diversity of dwarf galaxy rotation curves. *MNRAS*, 452(4):3650–3665, Oct. 2015. doi: 10.1093/mnras/stv1504.

J. H. Oort. The force exerted by the stellar system in the direction perpendicular to the galactic plane and some related problems. *Bulletin of the Astronomical Institutes of the Netherlands*, 6:249, Aug 1932.

J. P. Ostriker and P. J. E. Peebles. A Numerical Study of the Stability of Flattened Galaxies: or, can Cold Galaxies Survive? *ApJ*, 186:467–480, Dec. 1973. doi: 10.1086/152513.

J. P. Ostriker and P. J. Steinhardt. The observational case for a low-density Universe with a non-zero cosmological constant. *Nature*, 377(6550):600–602, 1995. doi: 10.1038/377600a0.

F. B. S. Paerels and S. M. Kahn. High-Resolution X-Ray Spectroscopy with CHANDRA and XMM-NEWTON. *ARA&A*, 41:291–342, Jan. 2003. doi: 10.1146/annurev.astro.41.071601.165952.

E. Papastergis, A. M. Martin, R. Giovanelli, and M. P. Haynes. The Velocity Width Function of Galaxies from the 40% ALFALFA Survey: Shedding Light on the Cold Dark Matter Overabundance Problem. *ApJ*, 739(1): 38, 2011. doi: 10.1088/0004-637X/739/1/38.

E. Papastergis, R. Giovanelli, M. P. Haynes, and F. Shankar. Is there a "too big to fail" problem in the field? *A&A*, 574:A113, 2015. doi: 10.1051/0004-6361/201424909.

S. Passaglia, W. Hu, and H. Motohashi. Primordial black holes and local non-Gaussianity in canonical inflation. *Phys. Rev. D*, 99(4):043536, Feb. 2019. doi: 10.1103/PhysRevD.99.043536.

M. S. Pawlowski. The planes of satellite galaxies problem, suggested solutions, and open questions. *Mod. Phys. Lett. A*, 33(6):1830004, Feb. 2018. doi: 10.1142/S0217732318300045.

M. S. Pawlowski, P. Kroupa, and K. S. de Boer. Making counter-orbiting tidal debris. The origin of the Milky Way disc of satellites? *A&A*, 532:A118, Aug. 2011. doi: 10.1051/0004-6361/201015021.

M. S. Pawlowski, B. Famaey, H. Jerjen, D. Merritt, P. Kroupa, J. Dabringhausen, F. Lüghausen, D. A. Forbes, G. Hensler, F. Hammer, M. Puech, S. Fouquet, H. Flores, and Y. Yang. Co-orbiting satellite galaxy structures are still in conflict with the distribution of primordial dwarf galaxies. *MNRAS*, 442(3):2362–2380, Aug. 2014. doi: 10.1093/mnras/stu1005.

R. D. Peccei and H. R. Quinn. CP Conservation in the Presence of Instantons. *Phys. Rev. Lett.*, 38:1440–1443, 1977a. doi: 10.1103/PhysRevLett.38.1440. [,328(1977)].

R. D. Peccei and H. R. Quinn. Constraints Imposed by CP Conservation in the Presence of Instantons. *Phys. Rev.*, D16:1791–1797, 1977b. doi: 10.1103/PhysRevD.16.1791.

P. J. E. Peebles. Large-scale background temperature and mass fluctuations due to scale-invariant primeval perturbations. *ApJ*, 263:L1–L5, Dec. 1982. doi: 10.1086/183911.

W. J. Percival, C. M. Baugh, J. Bland-Hawthorn, T. Bridges, R. Cannon, S. Cole, M. Colless, C. Collins, W. Couch, G. Dalton, R. De Propris, S. P. Driver, G. Efstathiou, R. S. Ellis, C. S. Frenk, K. Glazebrook, C. Jackson, O. Lahav, I. Lewis, S. Lumsden, S. Maddox, S. Moody, P. Norberg, J. A. Peacock, B. A. Peterson, W. Sutherland, and K. Taylor. The 2dF Galaxy Redshift Survey: the power spectrum and the matter content of the Universe. *MNRAS*, 327(4):1297–1306, Nov. 2001. doi: 10.1046/j.1365-8711.2001.04827.x.

C. B. Pereira, E. G. Jilinski, N. A. Drake, V. G. Ortega, and F. Roig. A study of two high-velocity red horizontal branch stars. *A&A*, 559:A12, Nov. 2013. doi: 10.1051/0004-6361/201221012.

H. B. Perets, C. Hopman, and T. Alexander. Massive Perturber-driven Interactions between Stars and a Massive Black Hole. *ApJ*, 656(2):709–720, Feb. 2007. doi: 10.1086/510377.

H. B. Perets, X. Wu, H. S. Zhao, B. Famaey, G. Gentile, and T. Alexander. The Galactic Potential and the Asymmetric Distribution of Hypervelocity Stars. *ApJ*, 697(2):2096–2101, June 2009. doi: 10.1088/0004-637X/697/2/2096.

S. Perlmutter, G. Aldering, G. Goldhaber, R. A. Knop, P. Nugent, P. G. Castro, S. Deustua, S. Fabbro, A. Goobar, D. E. Groom, I. M. Hook, A. G. Kim, M. Y. Kim, J. C. Lee, N. J. Nunes, R. Pain, C. R. Pennypacker, R. Quimby, C. Lidman, R. S. Ellis, M. Irwin, R. G. McMahon, P. Ruiz-Lapuente, N. Walton, B. Schaefer, B. J. Boyle, A. V. Filippenko, T. Matheson, A. S. Fruchter, N. Panagia, H. J. M. Newberg, W. J. Couch, and T. S. C. Project. Measurements of Ω and Λ from 42 High-Redshift Supernovae. *ApJ*, 517(2):565–586, 1999. doi: 10.1086/307221.

M. Persic, P. Salucci, and F. Stel. The universal rotation curve of spiral galaxies — I. The dark matter connection. *MNRAS*, 281(1):27–47, July 1996. doi: 10.1093/mnras/278.1.27.

Planck Collaboration, N. Aghanim, Y. Akrami, M. Ashdown, J. Aumont, C. Baccigalupi, M. Ballardini, A. J. Banday, R. B. Barreiro, N. Bartolo, S. Basak, R. Battye, K. Benabed, J. P. Bernard, M. Bersanelli, P. Bielewicz, J. J. Bock, J. R. Bond, J. Borrill, F. R. Bouchet, F. Boulanger, M. Bucher, C. Burigana, R. C. Butler, E. Calabrese, J. F. Cardoso, J. Carron, A. Challinor, H. C. Chiang, J. Chluba, L. P. L. Colombo, C. Combet, D. Contreras, B. P. Crill, F. Cuttaia, P. de Bernardis, G. de Zotti, J. Delabrouille, J. M. Delouis, E. Di Valentino, J. M. Diego, O. Doré, M. Douspis, A. Ducout, X. Dupac, S. Dusini, G. Efstathiou, F. Elsner, T. A. Enßlin, H. K. Eriksen, Y. Fantaye, M. Farhang, J. Fergusson, R. Fernandez-Cobos, F. Finelli, F. Forastieri, M. Frailis, A. A. Fraisse, E. Franceschi, A. Frolov, S. Galeotta, S. Galli, K. Ganga, R. T. Génova-Santos, M. Gerbino, T. Ghosh, J. González-Nuevo, K. M. Górski, S. Gratton, A. Gruppuso, J. E. Gudmundsson, J. Hamann, W. Handley, F. K. Hansen, D. Herranz, S. R. Hildebrandt, E. Hivon, Z. Huang, A. H. Jaffe, W. C. Jones, A. Karakci, E. Keihänen, R. Keskitalo, K. Kiiveri, J. Kim, T. S. Kisner, L. Knox, N. Krachmalnicoff, M. Kunz, H. Kurki-Suonio, G. Lagache, J. M. Lamarre, A. Lasenby, M. Lattanzi, C. R. Lawrence, M. Le Jeune, P. Lemos, J. Lesgourgues, F. Levrier, A. Lewis, M. Liguori, P. B. Lilje, M. Lilley, V. Lindholm, M. López-Caniego, P. M. Lubin, Y. Z. Ma, J. F. Macías-Pérez, G. Maggio, D. Maino, N. Mandolesi, A. Mangilli, A. Marcos-Caballero, M. Maris, P. G. Martin, M. Martinelli, E. Martínez-González, S. Matarrese, N. Mauri, J. D. McEwen, P. R. Meinhold, A. Melchiorri, A. Mennella, M. Migliaccio, M. Millea, S. Mitra, M. A. Miville-Deschênes, D. Molinari, L. Montier, G. Morgante, A. Moss, P. Natoli, H. U. Nørgaard-Nielsen, L. Pagano, D. Paoletti, B. Partridge, G. Patanchon, H. V. Peiris, F. Perrotta, V. Pettorino, F. Piacentini, L. Polastri, G. Polenta, J. L. Puget, J. P. Rachen, M. Reinecke, M. Remazeilles, A. Renzi, G. Rocha, C. Rosset, G. Roudier, J. A. Rubiño-Martín, B. Ruiz-Granados, L. Salvati, M. Sandri, M. Savelainen, D. Scott, E. P. S. Shellard, C. Sirignano, G. Sirri, L. D. Spencer, R. Sunyaev, A. S. Suur-Uski, J. A. Tauber, D. Tavagnacco, M. Tenti, L. Toffolatti, M. Tomasi, T. Trombetti, L. Valenziano, J. Valiviita, B. Van Tent, L. Vibert, P. Vielva, F. Villa, N. Vittorio, B. D. Wandelt, I. K. Wehus, M. White, S. D. M. White, A. Zacchei, and A. Zonca. Planck 2018 results. VI. Cosmological parameters. *A&A*, 641:A6, Sept. 2020a. doi: 10.1051/0004-6361/201833910.

Planck Collaboration, N. Aghanim, Y. Akrami, M. Ashdown, J. Aumont, C. Baccigalupi, M. Ballardini, A. J. Banday, R. B. Barreiro, N. Bartolo, S. Basak, K. Benabed, J. P. Bernard, M. Bersanelli, P. Bielewicz, J. J. Bock, J. R. Bond, J. Borrill, F. R. Bouchet, F. Boulanger, M. Bucher, C. Burigana, R. C. Butler, E. Calabrese, J. F. Cardoso, J. Carron, B. Casaponsa, A. Challinor, H. C. Chiang, L. P. L. Colombo, C. Combet, B. P. Crill, F. Cuttaia, P. de Bernardis, A. de Rosa, G. de Zotti, J. Delabrouille, J. M. Delouis, E. Di Valentino, J. M. Diego, O. Doré, M. Douspis, A. Ducout, X. Dupac, S. Dusini, G. Efstathiou, F. Elsner, T. A. Enßlin, H. K. Eriksen, Y. Fantaye, R. Fernandez-Cobos, F. Finelli, M. Frailis, A. A. Fraisse, E. Franceschi, A. Frolov, S. Galeotta, S. Galli, K. Ganga, R. T. Génova-Santos, M. Gerbino, T. Ghosh, Y. Giraud-Héraud, J. González-Nuevo, K. M. Górski, S. Gratton, A. Gruppuso, J. E. Gudmundsson, J. Hamann, W. Handley, F. K. Hansen, D. Herranz, E. Hivon, Z. Huang, A. H. Jaffe, W. C. Jones, E. Keihänen, R. Keskitalo, K. Kiiveri, J. Kim, T. S. Kisner, N. Krachmalnicoff, M. Kunz, H. Kurki-Suonio, G. Lagache, J. M. Lamarre, A. Lasenby, M. Lattanzi, C. R. Lawrence, M. Le Jeune, F. Levrier, A. Lewis, M. Liguori, P. B. Lilje, M. Lilley, V. Lindholm, M. López-Caniego, P. M. Lubin, Y. Z. Ma, J. F. Macías-Pérez, G. Maggio, D. Maino, N. Mandolesi, A. Mangilli, A. Marcos-Caballero, M. Maris, P. G. Martin, E. Martínez-González, S. Matarrese, N. Mauri, J. D. McEwen, P. R. Meinhold, A. Melchiorri, A. Mennella, M. Migliaccio, M. Millea, M. A. Miville-Deschênes, D. Molinari, A. Moneti, L. Montier, G. Morgante, A. Moss, P. Natoli, H. U. Nørgaard-Nielsen, L. Pagano, D. Paoletti, B. Partridge, G. Patanchon, H. V. Peiris, F. Perrotta, V. Pettorino, F. Piacentini, G. Polenta, J. L. Puget, J. P. Rachen, M. Reinecke, M. Remazeilles, A. Renzi, G. Rocha, C. Rosset, G. Roudier, J. A. Rubiño-Martín, B. Ruiz-Granados, L. Salvati, M. Sandri, M. Savelainen, D. Scott, E. P. S. Shellard, C. Sirignano, G. Sirri, L. D. Spencer, R. Sunyaev, A. S. Suur-Uski, J. A. Tauber, D. Tavagnacco, M. Tenti, L. Toffolatti, M. Tomasi, T. Trombetti, J. Valiviita, B. Van Tent, P. Vielva, F. Villa, N. Vittorio, B. D. Wandelt, I. K. Wehus, A. Zacchei, and A. Zonca. Planck 2018 results. V. CMB power spectra and likelihoods. *A&A*, 641:A5, Sept. 2020b. doi: 10.1051/0004-6361/201936386.

Planck Collaboration, Y. Akrami, F. Arroja, M. Ashdown, J. Aumont, C. Baccigalupi, M. Ballardini, A. J. Banday, R. B. Barreiro, N. Bartolo, S. Basak, K. Benabed, J. P. Bernard, M. Bersanelli, P. Bielewicz, J. J. Bock, J. R. Bond, J. Borrill, F. R. Bouchet, F. Boulanger, M. Bucher, C. Burigana, R. C. Butler, E. Calabrese, J. F. Cardoso, J. Carron, A. Challinor, H. C. Chiang, L. P. L. Colombo, C. Combet, D. Contreras, B. P. Crill, F. Cuttaia, P. de Bernardis, G. de Zotti, J. Delabrouille, J. M. Delouis, E. Di Valentino, J. M. Diego, S. Donzelli, O. Doré, M. Douspis, A. Ducout, X. Dupac, S. Dusini, G. Efstathiou, F. Elsner, T. A. Enßlin, H. K. Eriksen, Y. Fantaye, J. Fergusson, R. Fernandez-Cobos, F. Finelli, F. Forastieri, M. Frailis, E. Franceschi, A. Frolov, S. Galeotta, S. Galli, K. Ganga, C. Gauthier, R. T. Génova-Santos, M. Gerbino, T. Ghosh, J. González-Nuevo, K. M. Górski, S. Gratton, A. Gruppuso, J. E. Gudmundsson, J. Hamann, W. Handley, F. K. Hansen, D. Herranz, E. Hivon, D. C. Hooper, Z. Huang, A. H. Jaffe, W. C. Jones, E. Keihänen, R. Keskitalo, K. Kiiveri, J. Kim, T. S. Kisner, N. Krachmalnicoff, M. Kunz, H. Kurki-Suonio, G. Lagache, J. M. Lamarre, A. Lasenby, M. Lattanzi, C. R. Lawrence, M. Le Jeune, J. Lesgourgues, F. Levrier, A. Lewis, M. Liguori, P. B. Lilje, V. Lindholm, M. López-Caniego, P. M. Lubin, Y. Z. Ma, J. F. Macías-Pérez, G. Maggio, D. Maino, N. Mandolesi, A. Mangilli, A. Marcos-Caballero, M. Maris, P. G. Martin, E. Martínez-González, S. Matarrese, N. Mauri, J. D. McEwen, P. D. Meerburg, P. R. Meinhold, A. Melchiorri, A. Mennella, M. Migliaccio, S. Mitra,

M. A. Miville-Deschênes, D. Molinari, A. Moneti, L. Montier, G. Morgante, A. Moss, M. Münchmeyer, P. Natoli, H. U. Nørgaard-Nielsen, L. Pagano, D. Paoletti, B. Partridge, G. Patanchon, H. V. Peiris, F. Perrotta, V. Pettorino, F. Piacentini, L. Polastri, G. Polenta, J. L. Puget, J. P. Rachen, M. Reinecke, M. Remazeilles, A. Renzi, G. Rocha, C. Rosset, G. Roudier, J. A. Rubiño-Martín, B. Ruiz-Granados, L. Salvati, M. Sandri, M. Savelainen, D. Scott, E. P. S. Shellard, M. Shiraishi, C. Sirignano, G. Sirri, L. D. Spencer, R. Sunyaev, A. S. Suur-Uski, J. A. Tauber, D. Tavagnacco, M. Tenti, L. Toffolatti, M. Tomasi, T. Trombetti, J. Valiviita, B. Van Tent, P. Vielva, F. Villa, N. Vittorio, B. D. Wandelt, I. K. Wehus, S. D. M. White, A. Zacchei, J. P. Zibin, and A. Zonca. Planck 2018 results. X. Constraints on inflation. *A&A*, 641:A10, Sept. 2020d. doi: 10.1051/0004-6361/201833887.

Planck Collaboration, Y. Akrami, F. Arroja, M. Ashdown, J. Aumont, C. Baccigalupi, M. Ballardini, A. J. Banday, R. B. Barreiro, N. Bartolo, S. Basak, K. Benabed, J. P. Bernard, M. Bersanelli, P. Bielewicz, J. R. Bond, J. Borrill, F. R. Bouchet, M. Bucher, C. Burigana, R. C. Butler, E. Calabrese, J. F. Cardoso, B. Casaponsa, A. Challinor, H. C. Chiang, L. P. L. Colombo, C. Combet, B. P. Crill, F. Cuttaia, P. de Bernardis, A. de Rosa, G. de Zotti, J. Delabrouille, J. M. Delouis, E. Di Valentino, J. M. Diego, O. Doré, M. Douspis, A. Ducout, X. Dupac, S. Dusini, G. Efstathiou, F. Elsner, T. A. Enßlin, H. K. Eriksen, Y. Fantaye, J. Fergusson, R. Fernandez-Cobos, F. Finelli, M. Frailis, A. A. Fraisse, E. Franceschi, A. Frolov, S. Galeotta, S. Galli, K. Ganga, R. T. Génova-Santos, M. Gerbino, J. González-Nuevo, K. M. Górski, S. Gratton, A. Gruppuso, J. E. Gudmundsson, J. Hamann, W. Handley, F. K. Hansen, D. Herranz, E. Hivon, Z. Huang, A. H. Jaffe, W. C. Jones, G. Jung, E. Keihänen, R. Keskitalo, K. Kiiveri, J. Kim, N. Krachmalnicoff, M. Kunz, H. Kurki-Suonio, J. M. Lamarre, A. Lasenby, M. Lattanzi, C. R. Lawrence, M. Le Jeune, F. Levrier, A. Lewis, M. Liguori, P. B. Lilje, V. Lindholm, M. López-Caniego, Y. Z. Ma, J. F. Macías-Pérez, G. Maggio, D. Maino, N. Mandolesi, A. Marcos-Caballero, M. Maris, P. G. Martin, E. Martínez-González, S. Matarrese, N. Mauri, J. D. McEwen, P. D. Meerburg, P. R. Meinhold, A. Melchiorri, A. Mennella, M. Migliaccio, M. A. Miville-Deschênes, D. Molinari, A. Moneti, L. Montier, G. Morgante, A. Moss, M. Münchmeyer, P. Natoli, F. Oppizzi, L. Pagano, D. Paoletti, B. Partridge, G. Patanchon, F. Perrotta, V. Pettorino, F. Piacentini, G. Polenta, J. L. Puget, J. P. Rachen, B. Racine, M. Reinecke, M. Remazeilles, A. Renzi, G. Rocha, J. A. Rubiño-Martín, B. Ruiz-Granados, L. Salvati, M. Savelainen, D. Scott, E. P. S. Shellard, M. Shiraishi, C. Sirignano, G. Sirri, K. Smith, L. D. Spencer, L. Stanco, R. Sunyaev, A. S. Suur-Uski, J. A. Tauber, D. Tavagnacco, M. Tenti, L. Toffolatti, M. Tomasi, T. Trombetti, J. Valiviita, B. Van Tent, P. Vielva, F. Villa, N. Vittorio, B. D. Wandelt, I. K. Wehus, A. Zacchei, and A. Zonca. Planck 2018 results. IX. Constraints on primordial non-Gaussianity. *A&A*, 641:A9, Sept. 2020c. doi: 10.1051/0004-6361/201935891.

Planck Collaboration, Y. Akrami, M. Ashdown, J. Aumont, C. Baccigalupi, M. Ballardini, A. J. Banday, R. B. Barreiro, N. Bartolo, S. Basak, K. Benabed, M. Bersanelli, P. Bielewicz, J. J. Bock, J. R. Bond, J. Borrill, F. R. Bouchet, F. Boulanger, M. Bucher, C. Burigana, R. C. Butler, E. Calabrese, J. F. Cardoso, B. Casaponsa, H. C. Chiang, L. P. L. Colombo, C. Combet, D. Contreras, B. P. Crill, P. de Bernardis, G. de Zotti, J. Delabrouille, J. M. Delouis, E. Di Valentino, J. M. Diego, O. Doré, M. Douspis, A. Ducout, X. Dupac, G. Efstathiou, F. Elsner, T. A. Enßlin, H. K. Eriksen, Y. Fantaye, R. Fernandez-Cobos, F. Finelli, M. Frailis, A. A. Fraisse, E. Franceschi, A. Frolov, S. Galeotta, S. Galli, K. Ganga, R. T. Génova-Santos, M. Gerbino, T. Ghosh, J. González-Nuevo, K. M. Górski, A. Gruppuso, J. E. Gudmundsson, J. Hamann, W. Handley, F. K. Hansen, D. Herranz, E. Hivon, Z. Huang, A. H. Jaffe, W. C. Jones, E. Keihänen, R. Keskitalo, K. Kiiveri, J. Kim, N. Krachmalnicoff, M. Kunz, H. Kurki-Suonio, G. Lagache, J. M. Lamarre, A. Lasenby, M. Lattanzi, C. R. Lawrence, M. Le Jeune, F. Levrier, M. Liguori, P. B. Lilje, V. Lindholm, M. López-Caniego, Y. Z. Ma, J. F. Macías-Pérez, G. Maggio, D. Maino, N. Mandolesi, A. Mangilli, A. Marcos-Caballero, M. Maris, P. G. Martin, E. Martínez-González, S. Matarrese, N. Mauri, J. D. McEwen, P. R. Meinhold, A. Mennella, M. Migliaccio, M. A. Miville-Deschênes, D. Molinari, A. Moneti, L. Montier, G. Morgante, A. Moss, P. Natoli, L. Pagano, D. Paoletti, B. Partridge, F. Perrotta, V. Pettorino, F. Piacentini, G. Polenta, J. L. Puget, J. P. Rachen, M. Reinecke, M. Remazeilles, A. Renzi, G. Rocha, C. Rosset, G. Roudier, J. A. Rubiño-Martín, B. Ruiz-Granados, L. Salvati, M. Savelainen, D. Scott, E. P. S. Shellard, C. Sirignano, R. Sunyaev, A. S. Suur-Uski, J. A. Tauber, D. Tavagnacco, M. Tenti, L. Toffolatti, M. Tomasi, T. Trombetti, L. Valenziano, J. Valiviita, B. Van Tent, P. Vielva, F. Villa, N. Vittorio, B. D. Wandelt, I. K. Wehus, A. Zacchei, J. P. Zibin, and A. Zonca. Planck 2018 results. VII. Isotropy and statistics of the CMB. *A&A*, 641:A7, Sept. 2020e. doi: 10.1051/0004-6361/201935201.

R. Poleski. Transformation of the equatorial proper motion to the Galactic system. *arXiv e-prints*, art. arXiv:1306.2945, June 2013.

E. Polisensky and M. Ricotti. Constraints on the dark matter particle mass from the number of milky way satellites. *Phys. Rev. D*, 83:043506, Feb 2011. doi: 10.1103/PhysRevD.83.043506.

A. C. Pope, T. Matsubara, A. S. Szalay, M. R. Blanton, D. J. Eisenstein, J. Gray, B. Jain, N. A. Bahcall, J. Brinkmann, T. Budavari, A. J. Connolly, J. A. Frieman, J. E. Gunn, D. Johnston, S. M. Kent, R. H. Lupton, A. Meiksin, R. C. Nichol, D. P. Schneider, R. Scranton, M. A. Strauss, I. Szapudi, M. Tegmark,

M. S. Vogeley, D. H. Weinberg, I. Zehavi, and SDSS Collaboration. Cosmological Parameters from Eigenmode Analysis of Sloan Digital Sky Survey Galaxy Redshifts. *ApJ*, 607(2):655–660, June 2004. doi: 10.1086/383533.

L. Posti and A. Helmi. Mass and shape of the Milky Way's dark matter halo with globular clusters from Gaia and Hubble. *A&A*, 621:A56, Jan 2019. doi: 10.1051/0004-6361/201833355.

M. Postman, D. Coe, N. Benítez, L. Bradley, T. Broadhurst, M. Donahue, H. Ford, O. Graur, G. Graves, S. Jouvel, A. Koekemoer, D. Lemze, E. Medezinski, A. Molino, L. Moustakas, S. Ogaz, A. Riess, S. Rodney, P. Rosati, K. Umetsu, W. Zheng, A. Zitrin, M. Bartelmann, R. Bouwens, N. Czakon, S. Golwala, O. Host, L. Infante, S. Jha, Y. Jimenez-Teja, D. Kelson, O. Lahav, R. Lazkoz, D. Maoz, C. McCully, P. Melchior, M. Meneghetti, J. Merten, J. Moustakas, M. Nonino, B. Patel, E. Regös, J. Sayers, S. Seitz, and A. Van der Wel. The Cluster Lensing and Supernova Survey with Hubble: An Overview. *ApJS*, 199(2):25, April 2012. doi: 10.1088/0067-0049/199/2/25.

A. Poveda, J. Ruiz, and C. Allen. Run-away Stars as the Result of the Gravitational Collapse of Proto-stellar Clusters. *Boletin de los Observatorios Tonantzintla y Tacubaya*, 4:86–90, April 1967.

J. Preskill, M. B. Wise, and F. Wilczek. Cosmology of the invisible axion. *Phys. Lett. B*, 120(1-3):127–132, Jan 1983. doi: 10.1016/0370-2693(83)90637-8.

W. H. Press, S. A. Teukolsky, W. T. Vetterling, and B. P. Flannery. *Numerical Recipes 3rd Edition: The Art of Scientific Computing*. Cambridge University Press, USA, 3 edition, 2007. ISBN 0521880688.

A. M. Price-Whelan, D. W. Hogg, K. V. Johnston, and D. Hendel. Inferring the Gravitational Potential of the Milky Way with a Few Precisely Measured Stars. *ApJ*, 794(1):4, Oct 2014. doi: 10.1088/0004-637X/794/1/4.

R. N. Proctor, C. Mendes de Oliveira, L. Azanha, R. Dupke, and R. Overzier. A derivation of masses and total luminosities of galaxy groups and clusters in the maxBCG catalogue. *MNRAS*, 449(3):2345–2352, May 2015. doi: 10.1093/mnras/stv371.

C. Pulsoni, O. Gerhard, M. Arnaboldi, L. Coccato, A. Longobardi, N. R. Napolitano, E. Moylan, C. Narayan, V. Gupta, A. Burkert, M. Capaccioli, A. L. Chies-Santos, A. Cortesi, K. C. Freeman, K. Kuijken, M. R. Merrifield, A. J. Romanowsky, and C. Tortora. The extended Planetary Nebula Spectrograph (ePN.S) early-type galaxy survey: The kinematic diversity of stellar halos and the relation between halo transition scale and stellar mass. *A&A*, 618:A94, Oct. 2018. doi: 10.1051/0004-6361/201732473.

L. Randall and J. Scholtz. Dissipative Dark Matter and the Andromeda Plane of Satellites. *J. Cosmol. Astropart. Phys.*, 1509(09):057, 2015. doi: 10.1088/1475-7516/2015/09/057.

A. Rasskazov, G. Fragione, N. W. C. Leigh, H. Tagawa, A. Sesana, A. Price-Whelan, and E. M. Rossi. Hypervelocity Stars from a Supermassive Black Hole-Intermediate-mass Black Hole Binary. *ApJ*, 878(1):17, June 2019. doi: 10.3847/1538-4357/ab1c5d.

J. I. Read and D. Erkal. Abundance matching with the mean star formation rate: there is no missing satellites problem in the Milky Way above $M_{200} \sim 10^9$ $M_\odot$. *MNRAS*, 487(4):5799–5812, Aug 2019. doi: 10.1093/mnras/stz1320.

J. I. Read and B. Moore. Tidal streams in a MOND potential: constraints from Sagittarius. *MNRAS*, 361(3):971–976, Aug. 2005. doi: 10.1111/j.1365-2966.2005.09232.x.

J. I. Read, M. I. Wilkinson, N. W. Evans, G. Gilmore, and J. T. Kleyna. The importance of tides for the Local Group dwarf spheroidals. *MNRAS*, 367(1):387–399, 2006. doi: 10.1111/j.1365-2966.2005.09959.x.

M. J. Reid and A. Brunthaler. The Proper Motion of Sagittarius A*. II. The Mass of Sagittarius A*. *ApJ*, 616(2):872–884, Dec. 2004. doi: 10.1086/424960.

F. Renaud, B. Famaey, and P. Kroupa. Star formation triggered by galaxy interactions in modified gravity. *MNRAS*, 463(4):3637–3652, 2016. doi: 10.1093/mnras/stw2331.

A. G. Riess, A. V. Filippenko, P. Challis, A. Clocchiatti, A. Diercks, P. M. Garnavich, R. L. Gilliland, C. J. Hogan, S. Jha, R. P. Kirshner, B. Leibundgut, M. M. Phillips, D. Reiss, B. P. Schmidt, R. A. Schommer, R. C. Smith, J. Spyromilio, C. Stubbs, N. B. Suntzeff, and J. Tonry. Observational Evidence from Supernovae for an Accelerating Universe and a Cosmological Constant. *AJ*, 116(3):1009–1038, 1998. doi: 10.1086/300499.

A. G. Riess, L.-G. Strolger, J. Tonry, S. Casertano, H. C. Ferguson, B. Mobasher, P. Challis, A. V. Filippenko, S. Jha, W. Li, R. Chornock, R. P. Kirshner, B. Leibundgut, M. Dickinson, M. Livio, M. Giavalisco, C. C. Steidel, T. Benítez, and Z. Tsvetanov. Type Ia Supernova Discoveries at $z > 1$ from the Hubble Space Telescope: Evidence for Past Deceleration and Constraints on Dark Energy Evolution. *ApJ*, 607(2):665–687, June 2004. doi: 10.1086/383612.

K. Rines, M. J. Geller, A. Diaferio, M. J. Kurtz, and T. H. Jarrett. CAIRNS: The Cluster and Infall Region Nearby Survey. II. Environmental Dependence of Infrared Mass-to-Light Ratios. *AJ*, 128(3):1078–1111, Sept. 2004. doi: 10.1086/423218.

K. Rines, M. J. Geller, A. Diaferio, and M. J. Kurtz. Measuring the Ultimate Halo Mass of Galaxy Clusters: Redshifts and Mass Profiles from the Hectospec Cluster Survey (HeCS). *ApJ*, 767(1):15, April 2013. doi: 10.1088/0004-637X/767/1/15.

M. S. Roberts and A. H. Rots. Comparison of Rotation Curves of Different Galaxy Types. *A&A*, 26:483–485, Aug. 1973.

M. Rocha, A. H. G. Peter, J. S. Bullock, M. Kaplinghat, S. Garrison-Kimmel, J. Onorbe, and L. A. Moustakas. Cosmological Simulations with Self-Interacting Dark Matter I: Constant Density Cores and Substructure. *MNRAS*, 430:81–104, 2013. doi: 10.1093/mnras/sts514.

D. H. Rogstad and G. S. Shostak. Gross Properties of Five Scd Galaxies as Determined from 21-CENTIMETER Observations. *ApJ*, 176:315, Sept. 1972. doi: 10.1086/151636.

E. Romano-Díaz, I. Shlosman, Y. Hoffman, and C. Heller. Erasing dark matter cusps in cosmological galactic halos with baryons. *ApJ*, 685(2):L105–L108, Sept. 2008. doi: 10.1086/592687.

P. Rosati, S. Borgani, and C. Norman. The Evolution of X-ray Clusters of Galaxies. *ARA&A*, 40:539–577, Jan. 2002. doi: 10.1146/annurev.astro.40.120401.150547.

E. M. Rossi, T. Marchetti, M. Cacciato, M. Kuiack, and R. Sari. Joint constraints on the Galactic dark matter halo and Galactic Centre from hypervelocity stars. *MNRAS*, 467(2):1844–1856, May 2017. doi: 10.1093/mnras/stx098.

A. Růžička, J. Palouš, and C. Theis. Is the dark matter halo of the Milky Way flattened? *A&A*, 461(1):155–169, Jan. 2007. doi: 10.1051/0004-6361:20065538.

V. C. Rubin and J. Ford, W. Kent. Rotation of the Andromeda Nebula from a Spectroscopic Survey of Emission Regions. *ApJ*, 159:379, Feb. 1970. doi: 10.1086/150317.

V. C. Rubin, J. Ford, W. K., N. Thonnard, and D. Burstein. Rotational properties of 23Sb galaxies. *ApJ*, 261:439–456, Oct. 1982. doi: 10.1086/160355.

V. C. Rubin, D. Burstein, J. Ford, W. K., and N. Thonnard. Rotation velocities of 16 SA galaxies and a comparison of Sa, SB and SC rotation properties. *ApJ*, 289:81–104, Feb. 1985. doi: 10.1086/162866.

M. Salem, G. Besla, G. Bryan, M. Putman, R. P. van der Marel, and S. Tonnesen. Ram Pressure Stripping of the Large Magellanic Cloud's Disk as a Probe of the Milky Way's Circumgalactic Medium. *ApJ*, 815(1):77, Dec. 2015. doi: 10.1088/0004-637X/815/1/77.

P. Salucci. The distribution of dark matter in galaxies. *A&AR*, 27(1):2, 2019. doi: 10.1007/s00159-018-0113-1.

F. J. Sánchez-Salcedo, E. Martínez-Gómez, V. M. Aguirre-Torres, and H. M. Hernández-Toledo. Low-mass disc galaxies and the issue of stability: MOND versus dark matter. *MNRAS*, 462(4):3918–3936, 2016. doi: 10.1093/mnras/stw1911.

R. H. Sanders. Alternatives to dark matter. *MNRAS*, 223:539–555, Dec 1986. doi: 10.1093/mnras/223.3.539.

R. H. Sanders. Mass discrepancies in galaxies: dark matter and alternatives. *A&AR*, 2(1):1–28, Jan 1990. doi: 10.1007/BF00873540.

R. H. Sanders. *The Dark Matter Problem: A Historical Perspective*. 2010.

R. H. Sanders and S. S. McGaugh. Modified Newtonian Dynamics as an Alternative to Dark Matter. *ARA&A*, 40:263–317, Jan 2002. doi: 10.1146/annurev.astro.40.060401.093923.

C. L. Sarazin. X-ray emission from clusters of galaxies. *Rev. Mod. Phys.*, 58(1):1–115, Jan. 1986. doi: 10.1103/RevModPhys.58.1.

V. Savchenko, C. Ferrigno, E. Kuulkers, A. Bazzano, E. Bozzo, S. Brandt, J. Chenevez, T. J.-L. Courvoisier, R. Diehl, A. Domingo, and et al. Integral detection of the first prompt gamma-ray signal coincident with the gravitational-wave event gw170817. *ApJ*, 848(2):L15, Oct 2017. doi: 10.3847/2041-8213/aa8f94.

G. Schaller, D. Schaerer, G. Meynet, and A. Maeder. New grids of stellar models from 0.8 to 120 M_solar at Z=0.020 and Z=0.001. *A&AS*, 96:269, Dec. 1992.

H.-Y. Schive, T. Chiueh, and T. Broadhurst. Cosmic structure as the quantum interference of a coherent dark wave. *Nature Physics*, 10(7):496–499, July 2014. doi: 10.1038/nphys2996.

A. Schneider, R. E. Smith, A. V. Macci, and B. Moore. Non-linear evolution of cosmological structures in warm dark matter models. *MNRAS*, 424(1):684–698, July 2012. doi: 10.1111/j.1365-2966.2012.21252.x.

A. Schneider, D. Anderhalden, A. V. Macci, and J. Diemand. Warm dark matter does not do better than cold dark matter in solving small-scale inconsistencies. *MNRAS: Letters*, 441(1):L6L10, March 2014. doi: 10.1093/mnrasl/slu034.

R. Schönrich, J. Binney, and W. Dehnen. Local kinematics and the local standard of rest. *MNRAS*, 403(4): 1829–1833, April 2010. doi: 10.1111/j.1365-2966.2010.16253.x.

K. Schutz, T. Lin, B. R. Safdi, and C.-L. Wu. Constraining a Thin Dark Matter Disk with Gaia. *Phys. Rev. Lett.*, 121(8):081101, 2018. doi: 10.1103/PhysRevLett.121.081101.

U. c. v. Seljak, A. Makarov, P. McDonald, and H. Trac. Can sterile neutrinos be the dark matter? *Phys. Rev. Lett.*, 97:191303, Nov 2006. doi: 10.1103/PhysRevLett.97.191303.

J. A. Sellwood. Secular evolution in disk galaxies. *Rev. Mod. Phys.*, 86(1):1–46, Jan. 2014. doi: 10.1103/RevModPhys.86.1.

M. Sereno, C. Giocoli, L. Izzo, F. Marulli, A. Veropalumbo, S. Ettori, L. Moscardini, G. Covone, A. Ferragamo, R. Barrena, and A. Streblyanska. Gravitational lensing detection of an extremely dense environment around a galaxy cluster. *Nature Astronomy*, 2:744–750, July 2018. doi: 10.1038/s41550-018-0508-y.

A. L. Serra, G. W. Angus, and A. Diaferio. Implications for dwarf spheroidal mass content from interloper removal. *A&A*, 524:A16, 2010. doi: 10.1051/0004-6361/201015180.

A. Sesana, F. Haardt, and P. Madau. Interaction of Massive Black Hole Binaries with Their Stellar Environment. I. Ejection of Hypervelocity Stars. *ApJ*, 651(1):392–400, Nov. 2006. doi: 10.1086/507596.

J. M. Shull, B. D. Smith, and C. W. Danforth. The Baryon Census in a Multiphase Intergalactic Medium: 30% of the Baryons May Still be Missing. *ApJ*, 759(1):23, Nov. 2012. doi: 10.1088/0004-637X/759/1/23.

J. Silk. Fluctuations in the Primordial Fireball. *Nature*, 215(5106):1155–1156, Sept. 1967. doi: 10.1038/2151155a0.

J. Silk, V. Antonuccio-Delogu, Y. Dubois, V. Gaibler, M. R. Haas, S. Khochfar, and M. Krause. Jet interactions with a giant molecular cloud in the Galactic centre and ejection of hypervelocity stars. *A&A*, 545:L11, Sep 2012. doi: 10.1051/0004-6361/201220049.

J. Simon, L. Verde, and R. Jimenez. Constraints on the redshift dependence of the dark energy potential. *Phys. Rev. D*, 71(12):123001, June 2005. doi: 10.1103/PhysRevD.71.123001.

C. Skordis and T. Złośnik. Gravitational alternatives to dark matter with tensor mode speed equaling the speed of light. *Phys. Rev. D*, 100(10):104013, 2019. doi: 10.1103/PhysRevD.100.104013.

C. Skordis and T. Złośnik. New Relativistic Theory for Modified Newtonian Dynamics. *Phys. Rev. Lett.*, 127 (16):161302, Oct. 2021. doi: 10.1103/PhysRevLett.127.161302.

M. C. Smith, N. W. Evans, and J. H. An. The Tilt of the Halo Velocity Ellipsoid and the Shape of the Milky Way Halo. *ApJ*, 698(2):1110–1116, June 2009a. doi: 10.1088/0004-637X/698/2/1110.

M. C. Smith, N. W. Evans, V. Belokurov, P. C. Hewett, D. M. Bramich, G. Gilmore, M. J. Irwin, S. Vidrih, and D. B. Zucker. Kinematics of SDSS subdwarfs: structure and substructure of the Milky Way halo. *MNRAS*, 399(3):1223–1237, Nov. 2009b. doi: 10.1111/j.1365-2966.2009.15391.x.

R. E. Smith and K. Markovic. Testing the warm dark matter paradigm with large-scale structures. *Phys. Rev. D*, 84(6):063507, Sep 2011. doi: 10.1103/PhysRevD.84.063507.

J. Sohn, M. J. Geller, H. J. Zahid, D. G. Fabricant, A. Diaferio, and K. J. Rines. The Velocity Dispersion Function of Very Massive Galaxy Clusters: Abell 2029 and Coma. *ApJS*, 229(2):20, April 2017. doi: 10.3847/1538-4365/aa653e.

J. Sohn, M. J. Geller, and H. J. Zahid. A Spectroscopic Census of X-Ray Systems in the COSMOS Field. *ApJ*, 880(2):142, Aug. 2019. doi: 10.3847/1538-4357/ab2b46.

D. N. Spergel and P. J. Steinhardt. Observational evidence for selfinteracting cold dark matter. *Phys. Rev. Lett.*, 84:3760–3763, 2000. doi: 10.1103/PhysRevLett.84.3760.

D. N. Spergel, R. Bean, O. Doré, M. R. Nolta, C. L. Bennett, J. Dunkley, G. Hinshaw, N. Jarosik, E. Komatsu, L. Page, H. V. Peiris, L. Verde, M. Halpern, R. S. Hill, A. Kogut, M. Limon, S. S. Meyer, N. Odegard, G. S. Tucker, J. L. Weiland, E. Wollack, and E. L. Wright. Three-Year Wilkinson Microwave Anisotropy Probe (WMAP) Observations: Implications for Cosmology. *ApJS*, 170(2):377–408, June 2007. doi: 10.1086/513700.

D. Stern, R. Jimenez, L. Verde, M. Kamionkowski, and S. A. Stanford. Cosmic chronometers: constraining the equation of state of dark energy. I: H(z) measurements. *J. Cosmol. Astropart. Phys.*, 2010(2):008, 2010. doi: 10.1088/1475-7516/2010/02/008.

L. E. Strigari. Galactic searches for dark matter. *Phys. Rep.*, 531(1):1–88, Oct. 2013. doi: 10.1016/j.physrep.2013.05.004.

N. Suzuki, D. Rubin, C. Lidman, G. Aldering, R. Amanullah, K. Barbary, L. F. Barrientos, J. Botyanszki, M. Brodwin, N. Connolly, K. S. Dawson, A. Dey, M. Doi, M. Donahue, S. Deustua, P. Eisenhardt, E. Ellingson, L. Faccioli, V. Fadeyev, H. K. Fakhouri, A. S. Fruchter, D. G. Gilbank, M. D. Gladders, G. Goldhaber, A. H. Gonzalez, A. Goobar, A. Gude, T. Hattori, H. Hoekstra, E. Hsiao, X. Huang, Y. Ihara, M. J. Jee, D. Johnston, N. Kashikawa, B. Koester, K. Konishi, M. Kowalski, E. V. Linder, L. Lubin, J. Melbourne, J. Meyers, T. Morokuma, F. Munshi, C. Mullis, T. Oda, N. Panagia, S. Perlmutter, M. Postman, T. Pritchard, J. Rhodes, P. Ripoche, P. Rosati, D. J. Schlegel, A. Spadafora, S. A. Stanford, V. Stanishev, D. Stern, M. Strovink, N. Takanashi, K. Tokita, M. Wagner, L. Wang, N. Yasuda, H. K. C. Yee, and T. Supernova Cosmology Project. The Hubble Space Telescope Cluster Supernova Survey. V. Improving the Dark-energy Constraints above z $>$ 1 and Building an Early-type-hosted Supernova Sample. *ApJ*, 746(1):85, Feb. 2012. doi: 10.1088/0004-637X/746/1/85.

P. Svrcek and E. Witten. Axions in string theory. *Journal of High Energy Physics*, 2006(6):051, June 2006. doi: 10.1088/1126-6708/2006/06/051.

T. Tamura, R. Iizuka, Y. Maeda, K. Mitsuda, and N. Y. Yamasaki. An x-ray spectroscopic search for dark matter in the perseus cluster with suzaku. *Publications of the Astronomical Society of Japan*, 67(2), March 2015. doi: 10.1093/pasj/psu156.

M. Tanabashi, K. Hagiwara, K. Hikasa, K. Nakamura, Y. Sumino, F. Takahashi, J. Tanaka, K. Agashe, G. Aielli, C. Amsler, M. Antonelli, D. M. Asner, H. Baer, S. Banerjee, R. M. Barnett, T. Basaglia, C. W. Bauer, J. J. Beatty, V. I. Belousov, J. Beringer, S. Bethke, A. Bettini, H. Bichsel, O. Biebel, K. M. Black, E. Blucher, O. Buchmuller, V. Burkert, M. A. Bychkov, R. N. Cahn, M. Carena, A. Ceccucci, A. Cerri, D. Chakraborty, M. C. Chen, R. S. Chivukula, G. Cowan, O. Dahl, G. D'Ambrosio, T. Damour, D. de Florian, A. de Gouvêa, T. DeGrand, P. de Jong, G. Dissertori, B. A. Dobrescu, M. D'Onofrio, M. Doser, M. Drees, H. K. Dreiner, D. A. Dwyer, P. Eerola, S. Eidelman, J. Ellis, J. Erler, V. V. Ezhela, W. Fetscher, B. D. Fields, R. Firestone, B. Foster, A. Freitas, H. Gallagher, L. Garren, H. J. Gerber, G. Gerbier, T. Gershon, Y. Gershtein, T. Gherghetta, A. A. Godizov, M. Goodman, C. Grab, A. V. Gritsan, C. Grojean, D. E. Groom, M. Grünewald, A. Gurtu, T. Gutsche, H. E. Haber, C. Hanhart, S. Hashimoto, Y. Hayato, K. G. Hayes, A. Hebecker, S. Heinemeyer, B. Heltsley, J. J. Hernández-Rey, J. Hisano, A. Höcker, J. Holder, A. Holtkamp, T. Hyodo, K. D. Irwin, K. F. Johnson, M. Kado, M. Karliner, U. F. Katz, S. R. Klein, E. Klempt, R. V. Kowalewski, F. Krauss, M. Kreps, B. Krusche, Y. V. Kuyanov, Y. Kwon, O. Lahav, J. Laiho, J. Lesgourgues, A. Liddle, Z. Ligeti, C. J. Lin, C. Lippmann, T. M. Liss, L. Littenberg, K. S. Lugovsky, S. B. Lugovsky, A. Lusiani, Y. Makida, F. Maltoni, T. Mannel, A. V. Manohar, W. J. Marciano, A. D. Martin, A. Masoni, J. Matthews, U. G. Meißner, D. Milstead, R. E. Mitchell, K. Mönig, P. Molaro, F. Moortgat, M. Moskovic, H. Murayama, M. Narain, P. Nason, S. Navas, M. Neubert, P. Nevski, Y. Nir, K. A. Olive, S. Pagan Griso, J. Parsons, C. Patrignani, J. A. Peacock, M. Pennington, S. T. Petcov, V. A. Petrov, E. Pianori, A. Piepke, A. Pomarol, A. Quadt, J. Rademacker, G. Raffelt, B. N. Ratcliff, P. Richardson, A. Ringwald, S. Roesler, S. Rolli, A. Romaniouk, L. J. Rosenberg, J. L. Rosner, G. Rybka, R. A. Ryutin, C. T. Sachrajda, Y. Sakai, G. P. Salam, S. Sarkar, F. Sauli, O. Schneider, K. Scholberg, A. J. Schwartz, D. Scott, V. Sharma, S. R. Sharpe, T. Shutt, M. Silari, T. Sjöstrand, P. Skands, T. Skwarnicki, J. G. Smith, G. F. Smoot, S. Spanier, H. Spieler, C. Spiering, A. Stahl, S. L. Stone, T. Sumiyoshi, M. J. Syphers, K. Terashi, J. Terning, U. Thoma, R. S. Thorne, L. Tiator, M. Titov, N. P. Tkachenko, N. A. Törnqvist, D. R. Tovey, G. Valencia, R. Van de Water, N. Varelas, G. Venanzoni, L. Verde, M. G. Vincter, P. Vogel, A. Vogt, S. P. Wakely, W. Walkowiak, C. W. Walter, D. Wands, D. R. Ward, M. O. Wascko, G. Weiglein, D. H. Weinberg, E. J. Weinberg, M. White, L. R. Wiencke, S. Willocq, C. G. Wohl, J. Womersley, C. L. Woody, R. L. Workman, W. M. Yao, G. P. Zeller, O. V. Zenin, R. Y. Zhu, S. L. Zhu, F. Zimmermann, P. A. Zyla, J. Anderson, L. Fuller, V. S. Lugovsky, P. Schaffner, and Particle Data Group. Review of Particle Physics*. *Phys. Rev. D*, 98(3):030001, Aug. 2018. doi: 10.1103/PhysRevD.98.030001.

M. Tegmark, M. R. Blanton, M. A. Strauss, F. Hoyle, D. Schlegel, R. Scoccimarro, M. S. Vogeley, D. H. Weinberg, I. Zehavi, A. Berlind, T. Budavari, A. Connolly, D. J. Eisenstein, D. Finkbeiner, J. A. Frieman, J. E. Gunn, A. J. S. Hamilton, L. Hui, B. Jain, D. Johnston, S. Kent, H. Lin, R. Nakajima, R. C. Nichol, J. P. Ostriker, A. Pope, R. Scranton, U. Seljak, R. K. Sheth, A. Stebbins, A. S. Szalay, I. Szapudi, L. Verde, Y. Xu, J. Annis, N. A. Bahcall, J. Brinkmann, S. Burles, F. J. Castander, I. Csabai, J. Loveday, M. Doi, M. Fukugita, I. Gott,

J. Richard, G. Hennessy, D. W. Hogg, Ž. Ivezić, G. R. Knapp, D. Q. Lamb, B. C. Lee, R. H. Lupton, T. A. McKay, P. Kunszt, J. A. Munn, L. O'Connell, J. Peoples, J. R. Pier, M. Richmond, C. Rockosi, D. P. Schneider, C. Stoughton, D. L. Tucker, D. E. Vand en Berk, B. Yanny, D. G. York, and SDSS Collaboration. The Three-Dimensional Power Spectrum of Galaxies from the Sloan Digital Sky Survey. *ApJ*, 606(2):702–740, 2004. doi: 10.1086/382125.

The Theia Collaboration, C. Boehm, A. Krone-Martins, A. Amorim, G. Anglada-Escude, A. Brandeker, F. Courbin, T. Ensslin, A. Falcao, K. Freese, B. Holl, L. Labadie, A. Leger, F. Malbet, G. Mamon, B. McArthur, A. Mora, M. Shao, A. Sozzetti, D. Spolyar, E. Villaver, C. Albertus, S. Bertone, H. Bouy, M. Boylan-Kolchin, A. Brown, W. Brown, V. Cardoso, L. Chemin, R. Claudi, A. C. M. Correia, M. Crosta, A. Crouzier, F.-Y. Cyr-Racine, M. Damasso, A. da Silva, M. Davies, P. Das, P. Dayal, M. de Val-Borro, A. Diaferio, A. Erickcek, M. Fairbairn, M. Fortin, M. Fridlund, P. Garcia, O. Gnedin, A. Goobar, P. Gordo, R. Goullioud, N. Hambly, N. Hara, D. Hobbs, E. Hog, A. Holland, R. Ibata, C. Jordi, S. Klioner, S. Kopeikin, T. Lacroix, J. Laskar, C. Le Poncin-Lafitte, X. Luri, S. Majumdar, V. Makarov, R. Massey, B. Mennesson, D. Michalik, A. Moitinho de Almeida, A. Mourao, L. Moustakas, N. Murray, M. Muterspaugh, M. Oertel, L. Ostorero, A. Perez-Garcia, I. Platais, J. P. i. de Mora, A. Quirrenbach, L. Randall, J. Read, E. Regos, B. Rory, K. Rybicki, P. Scott, J. Schneider, J. Scholtz, A. Siebert, I. Tereno, J. Tomsick, W. Traub, M. Valluri, M. Walker, N. Walton, L. Watkins, G. White, D. W. Evans, L. Wyrzykowski, and R. Wyse. Theia: Faint objects in motion or the new astrometry frontier. *arXiv e-prints*, art. arXiv:1707.01348, July 2017.

I. Thies, P. Kroupa, and B. Famaey. Simulating disk galaxies and interactions in Milgromian dynamics. *arXiv e-prints*, art. arXiv:1606.04942, 2016.

G. F. Thomas, B. Famaey, R. Ibata, F. Lüghausen, and P. Kroupa. Stellar streams as gravitational experiments. I. The case of Sagittarius. *A&A*, 603:A65, July 2017. doi: 10.1051/0004-6361/201730531.

Y. Tian, P.-C. Yu, P. Li, S. S. McGaugh, and C.-M. Ko. Mass-Velocity Dispersion Relation in HIFLUGCS Galaxy Clusters. *ApJ*, 910(1):56, March 2021. doi: 10.3847/1538-4357/abe45c.

A. Tillich, U. Heber, S. Geier, H. Hirsch, P. F. L. Maxted, B. T. Gänsicke, T. R. Marsh, R. Napiwotzki, R. H. Østensen, and R. D. Scholz. The Hyper-MUCHFUSS project: probing the Galactic halo with sdB stars. *A&A*, 527:A137, March 2011. doi: 10.1051/0004-6361/201015539.

O. Tiret and F. Combes. Interacting Galaxies with Modified Newtonian Dynamics. In J. G. Funes and E. M. Corsini, editors, *Formation and Evolution of Galaxy Disks*, volume 396 of *Astronomical Society of the Pacific Conference Series*, page 259, 2008a.

O. Tiret and F. Combes. Evolution of spiral galaxies in modified gravity. II. Gas dynamics. *A&A*, 483(3):719–726, 2008b. doi: 10.1051/0004-6361:200809357.

P. B. Tissera, S. D. M. White, S. Pedrosa, and C. Scannapieco. Dark matter response to galaxy formation. *MNRAS*, 406(2):922–935, Aug. 2010. doi: 10.1111/j.1365-2966.2010.16777.x.

P. Tisserand, L. Le Guillou, C. Afonso, J. N. Albert, J. Andersen, R. Ansari, É. Aubourg, P. Bareyre, J. P. Beaulieu, X. Charlot, C. Coutures, R. Ferlet, P. Fouqué, J. F. Glicenstein, B. Goldman, A. Gould, D. Graff, M. Gros, J. Haissinski, C. Hamadache, J. de Kat, T. Lasserre, É. Lesquoy, C. Loup, C. Magneville, J. B. Marquette, É. Maurice, A. Maury, A. Milsztajn, M. Moniez, N. Palanque-Delabrouille, O. Perdereau, Y. R. Rahal, J. Rich, M. Spiro, A. Vidal-Madjar, L. Vigroux, S. Zylberajch, and EROS-2 Collaboration. Limits on the Macho content of the Galactic Halo from the EROS-2 Survey of the Magellanic Clouds. *A&A*, 469(2): 387–404, July 2007. doi: 10.1051/0004-6361:20066017.

S. Tremaine and J. E. Gunn. Dynamical role of light neutral leptons in cosmology. *Phys. Rev. Lett.*, 42:407–410, Feb 1979. doi: 10.1103/PhysRevLett.42.407.

S. Tulin and H.-B. Yu. Dark matter self-interactions and small scale structure. *Phys. Rep.*, 730:1–57, Feb. 2018. doi: 10.1016/j.physrep.2017.11.004.

J. A. Tyson, F. Valdes, and R. A. Wenk. Detection of Systematic Gravitational Lens Galaxy Image Alignments: Mapping Dark Matter in Galaxy Clusters. *ApJ*, 349:L1, Jan. 1990. doi: 10.1086/185636.

K. Umetsu. Cluster-galaxy weak lensing. *A&AR*, 28(1):7, Dec. 2020. doi: 10.1007/s00159-020-00129-w.

T. S. van Albada and R. Sancisi. Dark Matter in Spiral Galaxies. *Philosophical Transactions of the Royal Society of London Series A*, 320(1556):447–464, Dec. 1986. doi: 10.1098/rsta.1986.0128.

J. M. van der Hulst, E. D. Skillman, T. R. Smith, G. D. Bothun, S. S. McGaugh, and W. J. G. de Blok. Star Formation Thresholds in Low Surface Brightness Galaxies. *AJ*, 106:548, Aug 1993. doi: 10.1086/116660.

P. C. van der Kruit and K. C. Freeman. Galaxy Disks. *ARA&A*, 49(1):301–371, 2011. doi: 10.1146/annurev-astro-083109-153241.

D. Vargya, R. Sanderson, O. Sameie, M. Boylan-Kolchin, P. F. Hopkins, A. Wetzel, and A. Graus. Shapes of Milky-Way-Mass Galaxies with Self-Interacting Dark Matter. *arXiv e-prints*, art. arXiv:2104.14069, April 2021.

H. E. S. Velten, R. F. vom Marttens, and W. Zimdahl. Aspects of the cosmological "coincidence problem". *European Physical Journal C*, 74:3160, Nov. 2014. doi: 10.1140/epjc/s10052-014-3160-4.

C. Vera-Ciro and A. Helmi. Constraints on the Shape of the Milky Way Dark Matter Halo from the Sagittarius Stream. *ApJ*, 773(1):L4, Aug. 2013. doi: 10.1088/2041-8205/773/1/L4.

C. A. Vera-Ciro, L. V. Sales, A. Helmi, C. S. Frenk, J. F. Navarro, V. Springel, M. Vogelsberger, and S. D. M. White. The shape of dark matter haloes in the Aquarius simulations: evolution and memory. *MNRAS*, 416 (2):1377–1391, Sept. 2011. doi: 10.1111/j.1365-2966.2011.19134.x.

M. Viel, J. Lesgourgues, M. G. Haehnelt, S. Matarrese, and A. Riotto. Constraining warm dark matter candidates including sterile neutrinos and light gravitinos with WMAP and the Lyman-α forest. *Phys. Rev. D*, 71(6): 063534, March 2005. doi: 10.1103/PhysRevD.71.063534.

F. Villaescusa-Navarro and N. Dalal. Cores and cusps in warm dark matter halos. *J. Cosmol. Astropart. Phys.*, 2011(3):024, 2011. doi: 10.1088/1475-7516/2011/03/024.

M. Vogelsberger, S. D. M. White, A. Helmi, and V. Springel. The fine-grained phase-space structure of cold dark matter haloes. *MNRAS*, 385(1):236–254, March 2008. doi: 10.1111/j.1365-2966.2007.12746.x.

M. Vogelsberger, J. Zavala, and A. Loeb. Subhaloes in Self-Interacting Galactic Dark Matter Haloes. *MNRAS*, 423:3740, 2012. doi: 10.1111/j.1365-2966.2012.21182.x.

G. M. Voit. Tracing cosmic evolution with clusters of galaxies. *Rev. Mod. Phys.*, 77(1):207–258, April 2005. doi: 10.1103/RevModPhys.77.207.

M. G. Walker, M. Mateo, E. W. Olszewski, J. Peñarrubia, N. W. Evans, and G. Gilmore. A Universal Mass Profile for Dwarf Spheroidal Galaxies? *ApJ*, 704(2):1274–1287, Oct 2009. doi: 10.1088/0004-637X/704/2/1274.

S. Walker, A. Simionescu, D. Nagai, N. Okabe, D. Eckert, T. Mroczkowski, H. Akamatsu, S. Ettori, and V. Ghirardini. The Physics of Galaxy Cluster Outskirts. *Space Sci. Rev.*, 215(1):7, Jan. 2019. doi: 10.1007/s11214-018-0572-8.

S. Wang, Y.-F. Wang, Q.-G. Huang, and T. G. Li. Constraints on the primordial black hole abundance from the first advanced ligo observation run using the stochastic gravitational-wave background. *Phys. Rev. Lett.*, 120 (19), May 2018. doi: 10.1103/physrevlett.120.191102.

Y.-H. Wang, N. Leigh, Y.-F. Yuan, and R. Perna. The fate of close encounters between binary stars and binary supermassive black holes. *MNRAS*, 475(4):4595–4608, April 2018. doi: 10.1093/mnras/sty107.

M. S. Warren, P. J. Quinn, J. K. Salmon, and W. H. Zurek. Dark Halos Formed via Dissipationless Collapse. I. Shapes and Alignment of Angular Momentum. *ApJ*, 399:405, Nov. 1992. doi: 10.1086/171937.

R. H. Wechsler and J. L. Tinker. The Connection Between Galaxies and Their Dark Matter Halos. *ARA&A*, 56: 435–487, Sept. 2018. doi: 10.1146/annurev-astro-081817-051756.

P. M. Weilbacher, P. A. Duc, U. Fritze v. Alvensleben, P. Martin, and K. J. Fricke. Tidal dwarf candidates in a sample of interacting galaxies. *A&A*, 358:819–834, 2000.

D. H. Weinberg, J. S. Bullock, F. Governato, R. Kuzio de Naray, and A. H. G. Peter. Cold dark matter: Controversies on small scales. *Proceedings of the National Academy of Science*, 112(40):12249–12255, Oct 2015. doi: 10.1073/pnas.1308716112.

S. Weinberg. A New Light Boson? *Phys. Rev. Lett.*, 40:223–226, 1978. doi: 10.1103/PhysRevLett.40.223.

S. Weinberg. A new light boson? *Phys. Rev. Lett.*, 40(4):223–226, Jan. 1978. doi: 10.1103/PhysRevLett.40.223.

S. Weinberg. The cosmological constant problem. *Reviews of Modern Physics*, 61(1):1–23, Jan. 1989. doi: 10.1103/RevModPhys.61.1.

M. Wetzstein, T. Naab, and A. Burkert. Do dwarf galaxies form in tidal tails? *MNRAS*, 375(3):805–820, 2007. doi: 10.1111/j.1365-2966.2006.11360.x.

L. M. Widrow and N. Kaiser. Using the Schroedinger Equation to Simulate Collisionless Matter. *ApJ*, 416:L71, Oct 1993. doi: 10.1086/187073.

F. Wilczek. Problem of Strong P and T Invariance in the Presence of Instantons. *Phys. Rev. Lett.*, 40:279–282, 1978. doi: 10.1103/PhysRevLett.40.279.

F. Wilczek. Problem of strong P and T invariance in the presence of instantons. *Phys. Rev. Lett.*, 40(5):279–282, Jan. 1978. doi: 10.1103/PhysRevLett.40.279.

X. X. Xue, H. W. Rix, G. Zhao, P. Re Fiorentin, T. Naab, M. Steinmetz, F. C. van den Bosch, T. C. Beers, Y. S. Lee, E. F. Bell, C. Rockosi, B. Yanny, H. Newberg, R. Wilhelm, X. Kang, M. C. Smith, and D. P. Schneider. The Milky Way's Circular Velocity Curve to 60 kpc and an Estimate of the Dark Matter Halo Mass from the Kinematics of ~2400 SDSS Blue Horizontal-Branch Stars. *ApJ*, 684(2):1143–1158, Sept. 2008. doi: 10.1086/589500.

N. Yoshida, V. Springel, S. D. M. White, and G. Tormen. Weakly self-interacting dark matter and the structure of dark halos. *ApJ*, 544:L87–L90, 2000. doi: 10.1086/317306.

S. Young and C. T. Byrnes. Signatures of non-gaussianity in the isocurvature modes of primordial black hole dark matter. *J. Cosmol. Astropart. Phys.*, 2015(4):034, 2015. doi: 10.1088/1475-7516/2015/04/034.

Q. Yu and P. Madau. Kinematics of hypervelocity stars in the triaxial halo of the Milky Way. *MNRAS*, 379(4): 1293–1301, Aug 2007. doi: 10.1111/j.1365-2966.2007.12034.x.

Q. Yu and S. Tremaine. Ejection of Hypervelocity Stars by the (Binary) Black Hole in the Galactic Center. *ApJ*, 599(2):1129–1138, Dec 2003. doi: 10.1086/379546.

J. Zavala, Y. P. Jing, A. Faltenbacher, G. Yepes, Y. Hoffman, S. Gottlöber, and B. Catinella. The Velocity Function in the Local Environment from ΛCDM and ΛWDM Constrained Simulations. *ApJ*, 700(2):1779–1793, Aug. 2009. doi: 10.1088/0004-637X/700/2/1779.

J. Zavala, M. Vogelsberger, and M. G. Walker. Constraining Self-Interacting Dark Matter with the Milky Way's dwarf spheroidals. *MNRAS*, 431:L20–L24, 2013. doi: 10.1093/mnrasl/sls053.

M. Zemp, O. Y. Gnedin, N. Y. Gnedin, and A. V. Kravtsov. The Impact of Baryon Physics on the Structure of High-redshift Galaxies. *ApJ*, 748(1):54, March 2012. doi: 10.1088/0004-637X/748/1/54.

A. R. Zentner, A. V. Kravtsov, O. Y. Gnedin, and A. A. Klypin. The Anisotropic Distribution of Galactic Satellites. *ApJ*, 629(1):219–232, Aug. 2005. doi: 10.1086/431355.

F. Zhang, Y. Lu, and Q. Yu. The Galactic Center S-stars and the Hypervelocity Stars in the Galactic Halo: Two Faces of the Tidal Breakup of Stellar Binaries by the Central Massive Black Hole? *ApJ*, 768(2):153, May 2013. doi: 10.1088/0004-637X/768/2/153.

H. Zhao, B. Famaey, F. Lüghausen, and P. Kroupa. Local Group timing in Milgromian dynamics. A past Milky Way-Andromeda encounter at z > 0.8. *A&A*, 557:L3, Sept. 2013. doi: 10.1051/0004-6361/201321879.

Z. Zheng, J. L. Carlin, T. C. Beers, L. Deng, C. J. Grillmair, P. Guhathakurta, S. Lépine, H. J. Newberg, B. Yanny, H. Zhang, C. Liu, G. Jin, and Y. Zhang. The First Hypervelocity Star from the LAMOST Survey. *ApJ*, 785(2):L23, April 2014. doi: 10.1088/2041-8205/785/2/L23.

F. Zwicky. Die Rotverschiebung von extragalaktischen Nebeln. *Helvetica Physica Acta*, 6:110–127, Jan. 1933.